VNIVERSITAT DE VALÈNCIA

Departamento de Física Teórica

PhD thesis

NEW MODELS IN PARTICLE AND ASTROPARTICLE PHYSICS:

consequences for dark matter and LHC.

Supervisors: Profs. Martin Hirsch, Fiorenza Donato and Jose W.F.Valle

Author: Valentina De Romeri

IFIC - Universidad de Valencia

ACADEMIC YEAR 2013

MARTIN HIRSCH, Investigador Cientifico de IFIC/CSIC de València,
FIORENZA DONATO, Investigadora Cientifica de INFN y Profesora Adjunta de la Universidad de Torino (Italia) and
JOSÉ W.F. VALLE, Profesor de Investigación de IFIC/CSIC de València,

CERTIFICAN:

Que la presente memoria "New models in particle and astroparticle physics: consequences for dark matter and LHC" ha sido realizada bajo su dirección en el Departamento de Física Teórica de la Universitat de València y en régimen de cotutela en el Departamento de Física Teórica de la Universitá degli Studi di Torino, por VALENTINA DE ROMERI y constituye su Tesis para optar al grado de Doctor en Física.

Y para que así conste, en cumplimiento de la legislación vigente, presentan en el Departamento de Física Teórica de la Universitat de València la referida Tesis Doctoral, y firman el presente certificado.

València, el 20 de Octubre de 2013.

Martin Hirsch, Fiorenza Donato and José W.F. Valle

CONTENTS

Articles upon which this thesis is based:

1 V. De Romeri and M. Hirsch, *Sneutrino Dark Matter in Low-scale Seesaw Scenarios*, JHEP 1212 (2012) 106 [arXiv:1209.3891 [hep-ph]].

2 F. Calore, V. De Romeri and F. Donato, *Conservative upper limits on WIMP annihilation cross section from Fermi-LAT γ-rays*, Phys. Rev. D **85**, 023004 (2012) [arXiv:1105.4230 [astro-ph.CO]].

3 V. De Romeri, M. Hirsch and M. Malinsky, *Soft masses in SUSY SO(10) GUTs with low intermediate scales*, Phys. Rev. D **84**, 053012 (2011) [arXiv:1107.3412 [hep-ph]].

4 F. Calore, V. De Romeri, M. Di Mauro, F. Donato, J. Herpich, A. Maccio, L. Maccione, G. Stinson, *Uncertainties on gamma-ray anisotropy from dark matter in the Milky Way*,
In preparation

CONTRIBUTIONS TO PROCEEDINGS:

5 V. De Romeri, *Right Handed Sneutrino Dark Matter in Inverse and Linear seesaw scenarios*, Contribution to the Proceedings of PASCOS 2012, arXiv:1209.1465 [hep-ph].

6 V. De Romeri, *Soft masses in SUSY SO(10) GUTs with low intermediate scales*, Contribution to the Proceedings of CORFU 2011, PoS CORFU **2011**, 019 (2011)

7 F. Donato, F. Calore and V. De Romeri, *Conservative upper limits on WIMP annihilation cross section from Fermi-LAT γ-rays*, Contribution to the Proceedings of TAUP 2011, 2012 J. Phys.: Conf. Ser. 375 012039, arXiv:1112.4171 [hep-ph].

INTRODUCTION

The Standard Model (SM) of particle physics is the theory which currently best describes the fundamental forces of electromagnetic, weak, and strong nuclear interactions. Nevertheless, it fails in fully being a "theory of everything". Despite its success in explaining a wide variety of experimental results of the last 40 years, it does not provide an explanation for some still unresolved questions, like the nature of dark matter (DM) and neutrino oscillations. These two problems are indeed the main motivations for this doctoral thesis. Therefore, one of the two research lines developed in this manuscript concerns possible extensions of the SM which can correctly describe neutrino physics.

The observation of neutrino oscillations has been one of the major discoveries in particle physics, implying that neutrinos have mass. The improved precision of modern neutrino experiments has led to the accurate measurement of the oscillation parameters and they have firmly demonstrated that the anomalies observed by the experiments are due to this phenomenon. However, in the SM neutrinos are described as massless particles and therefore it is necessary to go beyond this well-established theoretical framework to explain their masses. This can be accomplished through the famous seesaw mechanism. This elegant way to generate neutrino masses and to explain their smallness requires the introduction of new particles. The necessary ingredients to realize this mechanism can naturally occur in Grand Unified (GUT) models, which have been historically introduced to unify the strong, weak and electromagnetic forces. Interestingly enough, this unification is particularly successful once another important theoretical concept, namely the idea of supersymmetry (SUSY) is taken into account. This widely motivated extension of the SM relates the fermionic and bosonic degrees of freedom, predicting the existence of a supersymmetric partner for each of the SM particles.

Motivated by the fact that the masses of SUSY particles encode valuable information about new physics associated with some possible intermediate scale between the electro-weak (TeV) and the GUT scales, we will analyze some SUSY GUT models with low energy-scale seesaws, capable of accomodating neutrino masses and mixings. We will study the SUSY spectra at the TeV scale and we will investigate the possibility of disentangling different models through the measurements of the masses of SUSY particles at colliders like the LHC (Large Hadron Collider). The LHC is indeed the most powerful experiment currently involved in searches for physics beyond the SM.

The second research line of this thesis is motivated by the so-called *dark matter problem*. Indeed manyfold astrophysical and cosmological observations give strong evidences for the

existence of a form of non-luminous and non-baryonic matter, the DM, which should account for almost 27% of the total mass-energy of the Universe. Nevertheless, while numerous measurements have precisely determined the amount of DM in our Universe, its nature is still unknown. While DM cannot be formed by any of the SM particles, good DM candidates can arise in extensions of the SM. For instance, SUSY theories provide a possible candidate for DM, notably the lightest supersymmetric particle of the model. In the context of SUSY models with a low-scale seesaw mechanism, we will focus on the sneutrino, the scalar superpartner of the neutrino. We will discuss phenomenological constraints on the parameter space of the different models, notably we will impose the correct cosmological abundance of sneutrino DM as well as the measured neutrino masses and mixings. We will further consider bounds from lepton flavour violation processes and SUSY searches at colliders. Finally, we will present prospects for the detection of sneutrino DM.

Sneutrino DM features properties that are typical of a class of DM candidates dubbed weakly interacting massive particles (WIMPs). These particles exhibit weak scale interactions and masses near the weak scale. In general, WIMP candidates can be searched for with multiple techniques: detecting their recoil against nuclei in underground direct detection experiments or looking for the products of their annihilations/decays with astrophysical observations (indirect detection). Concerning the latter possibility, γ-rays are one of the most promising messengers of DM annihilations to look at. In fact, current γ-ray experiments, thanks to their increased sensitivity, have started to explore the theoretically favoured regions of the WIMP parameter space. Moreover, γ-rays are almost not deflected during their propagation therefore they carry spatial information about the distribution of their sources. This feature can be exploited to disentangle possible exotic DM signals from the astrophysical background.

In the second part of this thesis, we will employ the γ-ray measurements pursued by the Fermi-LAT telescope, in order to constrain the WIMP parameters. Notably, we will infer bounds on the WIMP annihilation cross section by looking at the energy spectrum of the extragalactic isotropic gamma-ray background (IGRB). Furthermore, we will constrain scenarios in which the DM annihilation cross section is enhanced through a velocity-dependent mechanism, the Sommerfeld enhancement. We will further consider the fluctuations on small angular scales (anisotropies) of the IGRB as a complementary technique to search for WIMP annihilations. In particular, we will study the angular power spectrum of the γ-ray emission due to WIMP annihilations in the halo of our galaxy and we will analyze the impact of some astrophysical uncertainties on these predictions.

The material of this thesis is organized as follows: the first Chapter is a short review about the observational and theoretical motivations for new physics beyond the SM; the second Chapter deals with some remarks about searches for DM, among them the indirect detection of DM through γ-rays. The original part of this thesis will start from the third Chapter, which is dedicated to the study of four basic SUSY SO(10) GUT models [1]. The fourth Chapter is about the phenomenological analysis of SUSY models with and without left-right symmetry, with the sneutrino as DM candidate [2]. The fifth Chapter is entirely devoted to the indirect detection of DM through γ-rays, namely to bounds on the WIMP annihilation

cross section from the IGRB [3] and finally, the sixth Chapter focuses on the study of anisotropies in the γ-ray sky from DM annihilation in the halo of the Milky Way, a work which is still in preparation.

RESUMEN

El modelo estándar (SM) de la física de partículas es la teoría que describe mejor las fuerzas fundamentales de electromagnetismo, débil, y las interacciones nucleares fuerte. Sin embargo, fracasa en ser una completa "teoría del todo". A pesar de su éxito a la hora de explicar una gran variedad de resultados experimentales de los últimos 40 años, no proporciona una explicación para algunas cuestiones aún sin resolver, como la naturaleza de la materia oscura (DM) y oscilación de los neutrinos. Estos dos problemas son, de hecho, las principales motivaciones de esta tesis doctoral. Por lo tanto, una de las dos líneas de investigación que se desarrollan en este manuscrito trata sobre posibles extensiones del SM que describen correctamente la física de los neutrinos.

La observación de la oscilación de los neutrinos ha sido uno de los grandes descubrimientos de la física de las partículas, esto implica que los neutrinos tienen masa. La precisión mejorada de los experimentos modernos para detectar los neutrinos ha dado lugar a una mejor medición de los parámetros de oscilación y han corroborado que las anomalías observadas por los experimentos son debidas a este fenómeno. Sin embargo, en el SM los neutrinos se describen como partículas sin masa y por lo tanto es necesario ir más allá de este (bien establecido) marco teórico para explicar sus masas. Esto se puede lograr a través del conocido mecanismo de *seesaw*. Esta elegante manera de generar las masas de los neutrinos y de explicar su pequeñez requiere la introducción de nuevas partículas. Los ingredientes necesarios para hacer realidad este mecanismo pueden producirse de manera natural en modelos de Gran Unificación (GUT), los cuales han sido históricamente introducidos para unificar las fuerzas débiles, fuerte y electromagnética. Curiosamente, esta unificación es particularmente efectiva cuando otro importante concepto teórico, es decir, la idea de supersimetría (SUSY) es tomada en cuenta. Esta amplia extensión del SM ha sido motivada para introducir una simetría entres los grados de libertad bosónicos y fermiónicos, y predice la existencia de un compañero supersimétrico para cada una de las partículas del SM.

Motivados por el hecho de que las masas de las partículas SUSY codifican información valiosa acerca de nueva física asociada con algunas posibles escalas intermedias entre las escalas electro-débil (TeV) y GUT, analizamos algunos modelos SUSY GUT con seesaw de baja energía, capaz de explicar las masas y mezclas de los neutrinos. Estudiamos los espectros SUSY en la escala TeV y investigamos la posibilidad de diferenciar entre diferentes modelos a través de la medición de las masas de las partículas SUSY en colisionadores como el LHC (Gran Colisionador de Hadrones). El LHC es el experimento más potente que actualmente participa en las búsquedas de la física más allá del SM. Aunque todos los modelos estan basados en el grupo de gauge SO(10) GUT, se diferencian al nivel de grupos

de simetría en la escala intermedios y/o contenido de partículas debajo de la escala GUT. Los grupos gauge suplementarios y/o campos más allá de MSSM cambian la evolución de los parámetros soft con respecto a la expectativa mSugra básica. Las combinaciones de masas invariantes que consideramos convienen sobre todo mostrar los efectos de física más allá de mSugra en los espectros SUSY. Notablemente, mientras los invariantes sólo contienen dependencia logarítmica en las nuevas escalas de la física, su comportamiento es *cualitativamente* distinto en modelos diferentes. Por lo tanto, sostenemos que los invariantes RGE pueden ser buenos discriminadores de modelos.

La segunda línea de investigación de esta tesis está motivada por el *problema de la materia oscura*. De hecho varias observaciones astrofísicas y cosmológicas dan fuertes evidencias de la existencia de una forma de materia no-luminosa y no-bariónica, la DM, que corresponde a casi el 27% de la energía total del universo. No obstante numerosas mediciones hayan determinado la cantidad de DM en nuestro universo, su naturaleza es todavía desconocida. Mientras que la DM no puede estar formada por alguna de las partículas del SM, buenos candidatos a DM pueden surgir en las extensiones del SM. Por ejemplo, SUSY proporciona un posible candidato para la DM, en especial la partícula supersimétrica más ligera del modelo. En el contexto de modelos SUSY con un seesaw a baja escala energética, nos centramos en el sneutrino, el compañero escalar del neutrino. Consideramos dos posibilidades: los modelos con el grupo de gauge de MSSM y un seesaw lineal o inverso y un modelo con el grupo de gauge $SU(3)_c \times SU(2)_L \times U(1)_{B-L} \times U(1)_R$ y un seesaw inverso. Analizamos las limitaciones fenomenológicas en el espacio de parámetros de los diferentes modelos, es decir, imponiendo la correcta abundancia cosmológica del sneutrino DM, así como los valores medidos de masas y mezclas de neutrinos. También estudiamos los límites de procesos de violación del sabor y de la busqueda de particulas SUSY en colliders. Por último, presentamos las perspectivas para la detección de sneutrino DM. El sneutrino puede ser el candidato de materia oscura en ambos casos, realizando todos los límites experimentales conocidos. Mientras el seesaw inverso y lineal lleva a resultados diferentes para violación de sabor leptonico, en general, producen una fenomenología de materia oscura similar.

El sneutrino DM presenta las propiedades de las funciones que son típicos de una clase de DM candidatos denominados partículas masivas débilmente interactuantes (WIMPs). Estas partículas presentan interacciones débiles y masas cerca de la escala débil.
En general, los candidatos WIMP pueden ser buscados mediante varias técnicas: detección de la energía depositada en detectores en experimentos subterráneos o la busqueda de los productos provenientes de sus aniquilaciones y desintegraciones contrastandolas con observaciones astrofísicas (detección indirecta). Con respecto a esta última posibilidad, los rayos gamas son uno de los mensajeros más prometentes en la busqueda de aniquilaciones de DM. De hecho, los experimentos de rayos gama, gracias a su mayor sensibilidad, empiezan a estudiar las regiones en el espacio de parámetros WIMP que son favoritas en distintas teorías. Por otra parte, los rayos gama casi no se desvian durante su propagación, por lo tanto, llevan información espacial sobre la distribución de sus fuentes. Esta característica puede ser aprovechada para desentrañar posibles señales exóticas de DM del fondo astrofísico.

En la segunda parte de esta tesis se emplean las mediciones de rayos gama realizadas por

el telescopio Fermi-LAT, para restringir el espacio de parámetros WIMP. En particular, establecemos límites en la sección eficaz de aniquilación desde el espectro de energía del fondo isotropico de rayos gama (IGRB). Por otra parte, limitamos los escenarios en los que la sección eficaz de aniquilación de DM es aumentada a través de un mecanismo dependiente de la velocidad, el Sommerfeld enhancement. También estudiamos las fluctuaciones en las pequeñas escalas angulares (anisotropías) del IGRB como una técnica complementaria para buscar aniquilaciones de WIMPs. En particular, se estudia el espectro de potencia angular de la emisión en rayos gama debido a WIMPs que aniquilan en el halo de nuestra galaxia y analizamos el impacto de algunas incertidumbres astrofísicas de dichas predicciones. Hablamos de dos tipos de incertidumbres relacionadas con el estudio del espectro de potencia angular (APS) debido a la aniquilación galáctica de materia oscura: en primer lugar, el espectro de potencia angular en $l \gtrsim 100$ necesita el perfil extrapolado de materia oscura a escalas por debajo de la resolución de la simulación numérica. En segundo lugar, diferentes distribuciones espaciales de las sub-estructuras pueden conducir a diferentes APS. Con este fin, consideramos simulaciones de N cuerpos de halones galácticos de tamaño de la Vía Láctea. Encontramos que la extracción de los perfiles de densidad de materia oscura afecta claramente a los APS en multipolos $l \gtrsim 10$. Por último, evaluamos la incertidumbre debido a la presencia de sub-estructuras de 500 realizaciones de sus distribuciones. Mientras para multipolos altos la incertidumbre en el APS total se encoge a aproximadamente pocos %, por el $l \lesssim 100$ puede exceder un orden de magnitud.

Para concluir, en esta tesis doctoral tratamos aspectos diferentes de la fenomenología de nueva física más allá del modelo estándar. Notablemente nos concentramos en dos problemas todavía no resueltos del modelo estándar, las oscilaciones de neutrinos y la materia oscura. Además del estudio inevitable de la literatura acerca de las dos líneas de la investigación presentadas en esta tesis, el trabajo se ha realizado tanto con instrumentos analíticos como numéricos, como SARAH, SPheno, Toolbox, CalcHep, Micromegas, ROOT y Healpix.

Con este objetivo en mente explotamos la interacción entre el estudio de nuevos modelos teóricos y el análisis de resultados experimentales recientes. En particular, vemos que modelos SUSY SO(10) GUT muestran una fenomenología interesante que se puede estudiar con la actividad de LHC con energía del centro de la masa más alta, o con un futuro colisionador lineal. Además, mostramos que los modelos SUSY capaces de acomodar las masas de neutrinos a través de mecanismos de seesaw de baja escala energética también pueden proveer a un candidato de materia oscura bueno, el sneutrino. Finalmente, investigamos el descubrimiento indirecto de materia oscura como un método adicional de probar su naturaleza. La sensibilidad buena del telescopio Fermi-LAT ofrece un instrumento único para identificar señales de materia oscura en el cielo gama.

El progreso constante de técnicas experimentales, tanto con respecto a los aceleradores y búsquedas de materia oscura directas e indirectas, permitirá de dilucidar más sobre los escenarios que hemos estudiado en esta tesis y con suerte finalmente llegar a una descripción correcta de cómo se generan las masas de los neutrinos así como identificar la naturaleza de la física de partículas de materia oscura.

INTRODUZIONE

Il Modello Standard (MS) della fisica delle particelle è la teoria che meglio descrive le forze fondamentali forte, elettromagnetica e debole. Tuttavia, esso non viene accettato come una completa "teoria del tutto". Infatti, nonostante abbia avuto un grosso successo nello spiegare i risultati sperimentali degli ultimi 40 anni, il MS lascia alcune questioni ancora irrisolte, per esempio non prevede l'esistenza della materia oscura (DM) nè l'oscillazione dei neutrini.
Questi due problemi sono, di fatto, i motivi principali di questa tesi di dottorato. Infatti, la prima delle due linee di investigazione che si sviluppano in questo manoscritto tratta di possibili estensioni del MS che descrivano correttamente la fisica dei neutrini.

L'osservazione delle oscillazioni dei neutrini è stata una delle maggiori scoperte in fisica delle particelle, implicando che i neutrini hanno massa. La precisione degli esperimenti moderni ha permesso la misurazione accurata dei parametri di oscillazione permettendo così di dimostrare che le anomalie osservate dagli esperimenti sono realmente dovute a tale fenomeno. Tuttavia, nel MS, i neutrini sono descritti come particelle senza massa ed è perciò necessario andare oltre questo ben fondato modello teorico per spiegare le loro masse. Ad esempio, le masse dei neutrini possono essere generate attraverso il famoso meccanismo del *seesaw*. Questo elegante metodo, che permette di spiegare la piccolezza di tali masse, richiede l'introduzione di nuove particelle. Gli ingredienti necessari per realizzare questo meccanismo possono apparire in maniera naturale in modelli di Grande Unificazione (GUT), che sono stati storicamente introdotti per unificare le forze forte, debole ed elettromagnetica. Curiosamente, questa unificazione riesce particolarmente bene una volta introdotto un altro importante concetto teorico, vale a dire l'idea della supersimmetria (SUSY). Questa estensione ampiamente motivata del MS mette in relazione i gradi di libertà fermionici e bosonici, predicendo l'esistenza di un partner supersimmetrico per ognuna delle particelle del MS.

Motivati dal fatto che le masse delle particelle SUSY contengono informazioni preziose sulla nuova fisica associata a possibili scale intermedie, tra le scale elettro-debole (TeV) e GUT, analizzeremo alcuni modelli SUSY GUT con seesaw a bassa scala energetica, capaci di spiegare le oscillazioni e le masse dei neutrini. Studieremo gli spettri SUSY alla scala TeV e analizzeremo la possibilità di distinguere tra diversi modelli attraverso le misurazioni delle masse delle particelle SUSY presso collisionatori come l'LHC (Large Hadron Collider). L'LHC è infatti il più potente esperimento attualmente coinvolto nelle ricerche di fisica oltre il MS.

La seconda linea di ricerca di questa tesi è motivata dal cosiddetto *problema della materia*

oscura. Infatti, molteplici osservazioni astrofisiche e cosmologiche forniscono forti evidenze dell'esistenza di una forma di materia non barionica e non luminosa, la DM, che rappresenta quasi il 27% del totale di massa-energia dell'universo. Tuttavia, nonostante numerose misurazioni abbiano determinato precisamente la quantitá di DM nel nostro universo, la sua natura risulta ancora sconosciuta. Per quanto la DM non possa essere formata da nessuna delle particelle del MS, buoni candidati di DM possono sorgere in estensioni del MS. Per esempio, le teorie SUSY forniscono un possibile candidato per la DM, ossia la particella supersimmetrica piú leggera del modello. Nel contesto di modelli SUSY con un meccanismo di seesaw a bassa scala energetica, ci concentreremo sullo sneutrino, il superpartner scalare del neutrino. Discuteremo vincoli fenomenologici sullo spazio dei parametri dei diversi modelli, nello specifico imporremo la corretta abbondanza cosmologica dello sneutrino come DM e i valori misurati di masse e mescolanze dei neutrini. Ulteriormente, considereremo limiti da processi di violazione di sapore e ricerche SUSY presso collisionatori. Infine, vi presenteremo le prospettive per la rilevazione dello sneutrino come DM.

Lo sneutrino come DM presenta proprietà tipiche di una classe di candidati di DM soprannominati "particelle massive debolmente interagenti" (WIMPs). Queste particelle esibiscono interazioni deboli e masse dell'ordine della scala debole. In generale, i candidati WIMP possono essere ricercati con varie tecniche: tramite la rivelazione dell'energia depositata in esperimenti sotterranei (rivelazione diretta) o tramite la ricerca di prodotti delle loro annichilazioni/decadimenti con osservazioni astrofisiche (rivelazione indiretta). Per quanto riguarda quest'ultima possibilità i raggi gamma sono uno dei messaggeri più promettenti nella ricerca di annichilazione di DM. Infatti, gli attuali esperimenti di raggi gamma, grazie alla loro sensibilità, hanno iniziato ad esplorare le regioni dello spazio dei parametri WIMP favorite in diversi modelli teorici. Inoltre, i raggi gamma quasi non vengono deviati durante la loro propagazione, pertanto trasportano informazioni spaziali circa la distribuzione delle loro sorgenti. Questa caratteristica può essere sfruttata per districare possibili segnali esotici di DM dal fondo astrofisico.

Nella seconda parte di questa tesi, utilizzeremo le misurazioni di raggi gamma realizzate dal telescopio Fermi-LAT, al fine di vincolare lo spazio dei parametri WIMP. In particolare, poremo limiti sulla sezione d'urto di annichilazione di WIMP esaminando lo spettro di energia del fondo isotropo extragalattico di raggi gamma (IGRB). Inoltre, si vincoleranno gli scenari in cui la sezione d'urto di annichilazione di DM è aumentata attraverso un meccanismo dipendente dalla velocità, il cosiddetto "Sommerfeld enhancement". Considereremo poi le fluttuazioni su piccole scale angolari (anisotropie) della IGRB come tecnica complementare di ricerca di annichilazione di WIMPs. In particolare studieremo lo spettro di potenza angolare dell'emissione in raggi gamma causata da annichilazione di WIMPs nell'alone della nostra galassia e analizzeremo l'impatto di alcune incertezze astrofisiche su tali predizioni.

Il materiale di questa tesi è organizzato come segue: il primo capitolo è una breve recensione sulle motivazioni osservative e teoriche per nuova fisica oltre il MS; il secondo capitolo si occupa delle ricerche di DM, in particolare la rilevazione indiretta di DM attraverso i raggi gamma. La parte originale di questa tesi incomincerá con il terzo capitolo, dedicato allo studio di quattro modelli SUSY SO(10) GUT [1]. Il quarto capitolo tratta l'analisi

fenomenologica di modelli SUSY con e senza simmetria destra-sinistra, con lo sneutrino come candidato di DM [2]. Il quinto capitolo è interamente dedicato alla rilevazione indiretta di DM attraverso i raggi gamma, vale a dire ai limiti sulla sezione d'urto di annichilazione di WIMP ottenuti dal IGRB [3] e, infine, il capitolo sesto si concentra sullo studio delle anisotropie nel cielo in raggi gamma dovute all'annichilazione di DM nell'alone della Via Lattea, un lavoro che è ancora in fase di preparazione.

CHAPTER

ONE

NEW PHYSICS BEYOND THE STANDARD MODEL

The last 40 years have been marked by many important discoveries in particle physics, which lead to perhaps the most triumphant theory (by now) of elementary particle interactions, the *Standard Model* (SM) [4–7]. Beginning with the discovery of weak neutral currents in the Seventies and ending with that of the Higgs boson in 2012, many experimental results have been achieved in these decades. Precision tests have been carried out at colliders such as LEP in the Nineties or Tevatron also later. They tested the initial idea of Glashow, Salam, and Weinberg of unifying the weak nuclear force with quantum electrodynamics resulting in the electroweak theory and led to the successful SM.
However, it has been in the last decades when empirical evidence appeared that the SM is incomplete. The main experimental inconsistency perhaps arises from neutrino physics: neutrinos in the SM are assumed to be massless, but as we will discuss hereafter recent oscillation experiments have shown that neutrinos have mass. Nevertheless, neutrino masses are not the only question left open by the SM. Interestingly enough, most of the observational "limitations" of the SM arise in astroparticle physics:

- the need for non-baryonic dark matter,
- neutrino masses and mixings (not only in astroparticle physics, though),
- dark energy,
- baryon asymmetry,
- inflation.

Motivations for this thesis can be then found in this list: we will deal with theoretical extensions of the SM which try to explain neutrino masses and mixings, and dark matter physics.

1 Observational motivations

1.1 Neutrinos

Perhaps the strongest motivation to go beyond the Standard Model stems from neutrino physics. The SM is constructed in a way that neutrinos are massless particles. This property is related to the V-A character of weak interactions: it is a consequence of the SM as a theory containing only left-handed neutrinos. Dirac neutrino masses are indeed avoided by the absence of the right-handed neutrino partner in the particle spectrum, thus making it impossible to add a renormalizible mass term. A Majorana mass, i.e. a mass term that changes a particle to an antiparticle, for the left-handed neutrino is also forbidden. It would violate the electroweak gauge symmetry, because it is not invariant under the weak isospin symmetry; moreover, it does not conserve the lepton number L, in contrast with the accidental global symmetry B-L of the SM. However, with the discovery of flavor conversion of solar, atmospheric, reactor, and accelerator neutrinos, it has been established that neutrinos do have non-zero mass and that they mix among themselves, thus making the SM incomplete.

Historical highlights of neutrino physics.

Neutrino deficits There are different kinds of experiments that measure neutrinos and their properties. Some experiments measure *solar* neutrinos, that are the neutrinos produced in the nuclear reactions inside the Sun. Historically, the most important were Homestake [8–10], Kamiokande [11], Super-Kamiokande [12–15], SAGE [16, 17], GALLEX-GNO [18–20], and Sudbury Neutrino Observatory - SNO [21–24]. The latter was the one which actually solved the *solar neutrino problem*.
The fluxes experimentally detected can be compared with the theoretical expectations, which however depend on the model for the solar structure and activity. It resulted that all those experiments detected less neutrinos - $\sim (30-50)\%$ less - than predicted by the standard model of the Sun [25–29], a discrepancy which was usually referred to as "the solar neutrino problem".
Besides the neutrinos coming from the Sun, there are also the so called *atmospheric* neutrinos, which are produced in particle showers when a cosmic ray hits the upper atmosphere. The main production channel is through the decay of charged pions, going into μ^+, μ^-:

$$\pi^\pm \to \mu^\pm + \nu_\mu(\bar{\nu}_\mu)$$

followed by the muon decay:

$$\mu^\pm \to e^\pm + \nu_e(\bar{\nu}_e) + \bar{\nu}_\mu(\nu_\mu)$$

which gives a flux consisting of muon-neutrinos (ν_μ) and electron-neutrinos (ν_e) in the ratio of 2:1. These neutrinos travel down to the Earth surface and are eventually detected by underground neutrino telescopes. Again, historically the main experiments for atmospheric

neutrinos were: NUSEX [30, 31], Soudan 2 [32], Frejus [33, 34], IMB [35, 36], MACRO [37] and Kamiokande [38, 39]. Super-Kamiokande [40–42] is the most recent one, currently taking data. MINOS [43] is an accelerator experiment also testing the atmospheric neutrino scale. As for the solar ones, the measured fluxes are compared with theoretical expectations [44–47]. The water Cherenkov detectors (like Kamiokande and IMB) measured an anomalous deficit in muon-neutrinos, while tracking calorimeters (Frejus, NUSEX) saw no discrepancy. However Soudan-2, a tracking calorimeter, later reported results in line with the water Cherenkov detectors, thus making the "atmospheric neutrino anomaly" reliable. Finally, Super-Kamiokande measured the oscillation between muon- and tau- neutrinos $\nu_\mu \to \nu_\tau$.

The anomalies detected in solar and atmospheric neutrino experiments have been explained assuming neutrino oscillations. Over the years, the precision in neutrino physics experiments has increased, and the oscillation solution to the solar and atmospheric neutrino deficits has become solid. Moreover, new reactor and accelerator experiments have been constructed to give support for the interpretation in terms of flavor oscillation [48–55].

In *disappearance* experiments, oscillations are measured in the following way: suppose that a source produces only neutrinos of a given flavor, say μ. If they take part in oscillations, after travelling some distance they cross the detector which measures a smaller flux of muon neutrinos than what expected. Solar neutrino, KamLAND [49], Super-Kamiokande [42], K2K [56] and MINOS [52] experiments have measured disappearance of respectively solar ν_e, reactor $\bar{\nu}_e$ and atmospheric ν_μ and $\bar{\nu}_\mu$ (the latter three experiments in the list). In 2012, Daya Bay [57] and RENO [58] experiments discovered reactor $\bar{\nu}_e$ disappearance. As to *appearance* experiments, in 2011 T2K [55] reported the appearance of electron neutrinos in a beam of muon neutrinos.
All neutrino oscillation data are compatible with a three-flavors neutrino scenario [1], in agreement also with bounds from the invisible decay width of the Z^0 boson. Nevertheless, sterile neutrinos which can mix with light neutrinos may also exist.

Neutrino oscillations Neutrino oscillations were originally conceived by Bruno Pontecorvo between the 50s and the 60s [61–63], and after the experimental proofs the literature on the topic has increased exponentially. Some references are [64–70]. The neutrinos which are produced in association with charged leptons are the *flavor* neutrinos and they are called electron-, muon- and tau-neutrino respectively, according to their flavor. These neutrinos are detected by neutrino telescopes, which are sensitive to charged lepton flavors. In the SM ν_e, ν_μ, ν_τ are described by the weak $SU(2)_L$ doublets and their interactions are mediated by the bosons of the weak force ($W^\pm$ and Z^0). When neutrinos exchange a Z^0 boson the process is described by a neutral current (NC):

$$J_\mu^{NC} = \bar{\nu}_l \gamma_\mu (1 - \gamma_5) \nu_l,$$

being $l = e, \mu, \tau$. When the neutrino interaction is instead mediated by one of the charged weak bosons $W^\pm$, it is described by a charged current (CC):

[1] Except for the results of two experiments, LSND [59] and the MiniBooNE [60] which however need further experimental investigations

$$J_\mu^{CC} = \bar{l}\gamma_\mu(1-\gamma_5)\nu_l,$$

being $l = e, \mu, \tau$.
The flavor neutrinos $\nu_\alpha(\alpha = e, \mu, \tau)$ do not coincide with neutrinos of definite mass $\nu_i(i = 1, 2, 3)$, but they are coherent combinations of the mass eigenstates. Flavor mixing means that the weak charged current processes mix neutrino mass eigenstates. Indeed, the matrix that relates the three eigenstates (of flavor and mass) is named after him : V_{PMNS} is a 3×3 unitary matrix, the Pontecorvo - Maki - Nakagawa - Sakata lepton mixing matrix [71].

For the case of three types of neutrinos the 3×3 V_{PMNS} mixing matrix can be parameterized as [72, 73]

$$V_{PMNS} = \omega_{23}\omega_{13}\omega_{12} \tag{1}$$

where ω_{ij} are effective 3×3 unitary matrices characterized by an angle θ_{ij} and a CP phase ϕ_{ij}, with a 2×2 non-trivial subsector. For example

$$\omega_{12} = \begin{pmatrix} \cos\theta_{12} & e^{i\phi_{12}}\sin\theta_{12} & 0 \\ -e^{-i\phi_{12}}\sin\theta_{12} & \cos\theta_{12} & 0 \\ 0 & 0 & 1 \end{pmatrix} \tag{2}$$

We can expand the product in equation (1), neglecting the CP violating phases:

$$V_{PMNS} = \begin{pmatrix} c_{13}c_{12} & s_{12}c_{13} & s_{13} \\ -s_{12}c_{23} - s_{23}s_{13}c_{12} & c_{23}c_{12} - s_{23}s_{13}s_{12} & s_{23}c_{13} \\ s_{23}s_{12} - s_{13}c_{23}c_{12} & -s_{23}c_{12} - s_{13}s_{12}c_{23} & c_{23}c_{13} \end{pmatrix} \tag{3}$$

where $c_{ij} \equiv \cos\theta_{ij}$ and $s_{ij} \equiv \sin\theta_{ij}$.

The V_{PMNS} mixing matrix connects the two basis, of flavor (Greek index) and mass (latin index):

$$|\nu_\alpha\rangle = V^*_{PMNS\ \alpha i}|\nu_i\rangle \tag{4}$$

and it is the analog of the Cabibbo-Kobayashi-Maskawa (CKM) matrix that describes the mixing in the quark sector. This process of oscillation is a probabilistic consequence of quantum mechanics. Given a neutrino produced as a certain flavor type, after travelling a certain distance, the neutrino will become a mixture of the three types. This is due to the fact that the quantum mechanical evolution is mass diagonal, although the production is flavor diagonal, and as seen before the two basis do not coincide. To see this in more detail, we can consider the state $|\nu_i(t)\rangle$ at an initial time t, and observe it again at a later time t':

$$|\nu_i(t')\rangle = e^{iE_i(t'-t)}|\nu_i(t)\rangle \tag{5}$$

where the energy can be written in terms of the relativistic energy-momentum relation $E_i^2 = p^2 + m_i^2$. We are then interested to compute the probability of a flavor eigenstate ν_α oscillating into another flavor eigenstate ν_β:

$$P(\nu_\alpha \to \nu_\beta) = \langle \nu_\beta | \nu_\alpha \rangle^2 = \left| \sum_{k=1}^{3} V^{*\,\alpha k}_{PMNS} V^{\beta k}_{PMNS}\, e^{\left(-i\frac{m_k^2 L}{2E}\right)} \right|^2 \tag{6}$$
$$= \sum_{j,k=1}^{3} V^{*\,\alpha k}_{PMNS} V^{\beta k}_{PMNS} V^{\alpha j}_{PMNS} V^{*\,\beta j}_{PMNS}\, e^{\left(-i\frac{\Delta m_{kj}^2 L}{2E}\right)}$$

where $L \simeq t' - t$ for ultrarelativistic neutrinos and $\Delta m^2_{kj} \equiv m^2_k - m^2_j$. This equation doesn't take into account matter effects [74], the Mikheyev-Smirnov-Wolfenstein effect (MSW) - the adiabatic conversion of solar neutrinos in the matter of the Sun [75, 76]. This latter effect accounts for the resonant process that enhances the transition probability inside the matter of the Sun, which must be taken into account when calculating solar neutrino fluxes.

Neutrino masses

Neutrino oscillation measurements only give the mass differences squared of the different flavours. Indeed, from Eq. (6) we can see that neutrino oscillations are not sensitive to the absolute value of neutrino masses, but only to their squared mass differences Δm^2_{ij}. Therefore, two kinds of hierarchies can be considered: a *normal* hierarchy (NH: $m_1 < m_2 < m_3$) or an *inverted* hierarchy (IH: $m_3 < m_1 < m_2$), where m_i are mass eigenvalues of the three neutrinos. The determination of the neutrino mass ordering remains an open task.

Constraints and best fit values of the mixing angles and squared mass differences can be inferred from the available experimental data. Tab. (1.1) contains the most recent values according to [77], which includes the very recent measurements of θ_{13}, reported by the reactor experiments Daya Bay [57], Double Chooz [78] and RENO [58].
It is possible to infer the absolute scale of neutrino masses from tritium beta decay experiments and from neutrinoless double beta decay experiments. Upper limits on the neutrino masses can be obtained also from cosmology. Actually, the strongest upper limit on the masses of neutrinos comes from cosmology: the Planck satellite measurements of the cosmic microwave background (CMB) has reported an upper limit on the sum of the three light neutrino masses, under the assumption of three species of degenerate neutrinos and ΛCDM scenario [79]:

$$\sum m_\nu < 0.66 \text{ eV}, \tag{7}$$

at 95% C.L. This bound from the Planck temperature power spectrum is further reduced when combined with a WMAP polarization data, high-resolution CMB experiments and

[2] This is a local minimum in the first octant of θ_{23} with $\Delta\chi^2 = 0.02$ with respect to the global minimum

parameter	best fit	1σ range	2σ range	3σ range
Δm^2_{21} $[10^{-5}\text{eV}^2]$	7.62	7.43–7.81	7.27–8.01	7.12–8.20
$\lvert\Delta m^2_{31}\rvert$ $[10^{-3}\text{eV}^2]$	2.55 2.43	$2.46-2.61$ $2.37-2.50$	$2.38-2.68$ $2.29-2.58$	$2.31-2.74$ $2.21-2.64$
$\sin^2\theta_{12}$	0.320	0.303–0.336	0.29–0.35	0.27–0.37
$\sin^2\theta_{23}$	0.613 (0.427) [2] 0.600	0.400-0.461 & 0.573–0.635 0.569–0.626	0.38–0.66 0.39–0.65	0.36–0.68 0.37–0.67
$\sin^2\theta_{13}$	0.0246 0.0250	0.0218–0.0275 0.0223–0.0276	0.019–0.030 0.020–0.030	0.017–0.033
δ_{CP}	0.80π -0.03π	$0-2\pi$	$0-2\pi$	$0-2\pi$

Table 1.1: Neutrino oscillation parameters summary from [77]. For Δm^2_{31}, $\sin^2\theta_{23}$, $\sin^2\theta_{13}$, and δ_{CP} (the Dirac CP violation phase) the upper (lower) row corresponds to normal (inverted) neutrino mass hierarchy.

baryon acoustic oscillation data:

$$\sum m_\nu < 0.23 \text{ eV}, \tag{8}$$

at 95% C.L. However, these constraints are highly model dependent and can be modified in non minimal cosmological scenarios such as models with a curvature. Other cosmological constraints on the sum of light neutrino masses come from lensing data of galaxy clusters and Ly-α forest [80].
As to laboratory experiments, there are two kinds of searches that can look for the absolute scale of neutrino masses: neutrinoless double beta decay and beta decay experiments. The neutrinoless double beta decay ($0\nu2\beta$) is a rare nuclear process which violates lepton number and it occurs only if neutrinos are Majorana particles. If light neutrinos mediate this process, it is possible to infer an upper bound or a measurement of their effective mass. The KamLAND-Zen [81] experiment in combination with EXO-200 [82] find a Majorana neutrino mass limit of $\langle m_{\beta\beta}\rangle = \mid \sum_i U^2_{ei} m_{\nu_i} \mid < 0.12 - 0.25$ eV at 90% C.L. [83]. The GERDA collaboration [84] suggests an upper limit on the effective electron neutrino mass in the range $0.2 - 0.4$ eV [85].
On the other hand, nuclear beta decay experiments are the best strategy for measuring directly the neutrino mass. The current limits from tritium beta decay (under the assumption of degenerate neutrino masses) is $\sum m_{\nu_i} < 2.05 - 2.3$ eV at 95% C.L. from the Troitsk and Mainz experiments, respectively. In the future, KATRIN will give more precise results [86].

Summarizing, although in the last decades many important results have been achieved, the global picture of neutrino physics is still far from being complete, since some open questions remain: - whether neutrinos are Majorana or Dirac particles (we will address this topic in more details in Section 3.1); - the mechanism of generation of neutrino masses; - the type of mass spectrum (hierarchical/non-hierarchical) and its ordering (normal/inverse); and the CP-violating phase ϕ.

1.2 Dark Matter

Nowadays, it is known that ordinary baryonic matter is not the dominant form of matter in the universe [87]. The bulk of the matter content of the universe is in the form of an unknown non-baryonic type of matter, called dark matter (DM).

Observational evidences for dark matter

Evidence for DM exists on many scales, from galactic up to cosmological scales. It is sustained by galactic rotation curves, namely the velocity dispersions of spiral galaxy satellites and the velocity dispersions of dwarf galaxies, by data from CMB [79,88], weak and strong lensing [89–91], hot gas in clusters [92,93], large scale structures [94] and indirectly also the Big Bang nucleosynthesis (BBN) [95].
Hereafter we will shortly review some of the most striking evidences for DM.

Evidences on the galactic scale From the rotation curve of a spiral galaxy we can infer the mass M(r) enclosed within a radius r. If the whole mass of the galaxy was made up only of the visible stars and gas, one would expect that the rotation velocity curve should decline increasing the distance from the galactic center. Indeed, assuming a spherically symmetric distribution of matter, the mass inside a radius r is given by $M(r) \equiv 4\pi \int \rho(r) r^2 \mathrm{d}r$ where $\rho(r)$, which is the mass density profile, should fall as $\propto 1/\sqrt{r}$ beyond the optical disc, provided that the mass has stopped to increase beyond the optical radius and that in the standard Newtonian description the circular velocity on a stable Keplerian orbit is:

$$v(r) = \sqrt{\frac{GM(r)}{r}}. \tag{9}$$

On the contrary, what one observes is that $v(r)$ remains constant until much larger radii, thus indicating that the mass included within the radius r should be more abundant than the visible one. This result can be interpreted as the existence of a *dark halo*, with $M(r) \propto r$. The local DM density in the solar system is non-trivially estimated by observations such as galactic rotation curves and measuring the kinematics of stars. At the location of the Sun, $r_\odot = 8.33$ kpc [96] it is found $\rho_{loc}^{DM} = (0.4 \pm 0.1)$ GeV/cm^3 [97–100] [3]. For definiteness, we will consider $\rho_{loc}^{DM} = 0.4$ GeV/cm^3.

Evidences from galaxy clusters Galaxy clusters are the largest gravitationally bound objects in the universe. The first observations on these large concentrations of galaxies, in association with the application of the virial theorem $v^2 \sim GM/R$ [103] led to the conclusion that the matter contained in clusters is much more abundant than the visible one. Later, with the discovery that these galaxies are embedded in hot X-ray emitting gas, other methods for providing evidence for the existence of DM in galaxy clusters have been used: X-ray

[3] The typical associated error bar of 0.1 GeV/cm^3 may spread up to $0.2 - 0.8$ GeV/cm^3 [101] although some computations have found a higher value and possibly a smaller associated error: $\rho_{loc}^{DM} = (0.39 \pm 0.03)$ GeV/cm^3 [102].

emission by hot gas in the intra cluster plasma, measurements of the velocity dispersion and strong gravitational lensing.
The theory of General Relativity predicts that light is "lensed" by mass. Hence, a gravitational lens is created when light coming from a distant bright source is bent by a massive object present in the trajectory between the source and the observer. Galaxies clusters are studied with this technique, and it can be concluded that DM is required to explain their masses [104, 105].

The bullet cluster [89] is claimed to be the most direct observational evidence for collisionless DM: two clusters have experienced a collision which caused a separation of DM and baryonic matter. The hot baryonic gas was shocked and decelerated, whereas the DM halos of the two clusters passed through each other without slowing down. Hence, much of the mass of the system resides outside of the central region of baryonic gas. This shows that DM self-interacts only very weakly.

Evidences on the cosmological scale The currently most accurate determination of the DM content in the universe comes from precise measurements of the Cosmic Microwave Background (CMB) fluctuations made by Planck [106] and WMAP satellites [107], and by the Atacama Cosmology Telescope (ACT) [108] and the South Pole Telescope [109]. According to these, the mean energy density in the universe is approximately equal to the critical density $\rho_c \sim 10^{-29}$ g cm^{-3}. Nevertheless, among the content of the universe, only 4.9% is made up of baryons. Of the unseen content, about the $\sim$ 26.8% is in the form of DM [88], and the remaining $\sim$ 68.3% is *dark energy* which is the origin of the recent accelerated expansion of the universe.
The CMB data provide indeed the most powerful measurements of the cosmological parameters [88, 110–112]. The anisotropies in the CMB spectrum are the acoustic oscillations that the photons underwent just before decoupling from baryons in the early universe. Angular fluctuations in the spectrum of this remnant radiation, give information about the geometry of the universe and its energy content. These measurements are remarkably consistent with the predictions of the standard cosmological model. This model is based upon a spatially-flat, expanding universe whose dynamics are governed by General Relativity and whose constituents are DM, dark energy (the cosmological constant Λ) and baryons. The curvature of the universe for instance, is inferred by the angular scale of the first peak of the temperature power spectrum: the universe is consistent with a flat geometry [79, 88]. The height of the second peak determines the baryon density, whereas using the third peak it is possible to get information about the DM density. The matter/DM/dark energy contents of the Universe are usually described by the parameter $\Omega_x = \rho_x/\rho_c$. The current values of the cosmological densities (of baryons, DM, matter and dark energy) are [79]:

$$\begin{aligned} \Omega_b h^2 &= 0.02205 \pm 0.00028, \\ \Omega_{DM} h^2 &= 0.1199 \pm 0.0027, \\ \Omega_m &= 0.315 \pm 0.017, \\ \Omega_\Lambda &= 0.685 \pm 0.017, \end{aligned} \tag{10}$$

where $h = 0.67$ is the scale factor for the Hubble expansion rate. The acoustic oscillations in the early Universe left their imprint also in the visible matter through the generation of

Baryon Acoustic Oscillations. The results are in agreement with those from CMB [113,114].

In addition to CMB observations, predictions from *Big Bang nucleosynthesis* (BBN) are in good agreement [4] with the observed abundance of the chemical elements as far as ordinary matter is only $\sim 4\%$ of the content of the Universe.

A further kind of indirect observation comes from type Ia supernovae, which can be used to infer evidence of dark energy (Ω_Λ) in the Universe. They appear feebler than expected and this can be explained by an accelerating universe. From Ω_Λ and Ω_{tot} the DM content is indirectly constrained too [115].

Dark matter candidates

In the literature, there is a plethora of DM candidates [116]. Although the first candidates that had been introduced were dark baryonic objects, nowadays it is well known that these are cosmologically insignificant. Indeed historically the first class of DM candidates which became popular were hidden heavy baryonic objects, stellar remnants or feeble stars such as black holes, dwarfs and neutron stars, called *MAssive Compact Halo Objects* (MACHOs) [117, 118]. They could also be formed of mirror matter [119]. The mass of these faint objects is inferred through microlensing effects. Nevertheless, because of many constraints, it has been shown that they are not numerous enough to explain DM [120–122]. Indeed, the need for non-baryonic forms of DM is supported by the fact that baryonic models find it difficult to explain the growth of structures from small initial conditions as it is suggested by cosmological observations. For instance, if the DM was entirely made of baryons the CMB anisotropies would look radically different. A further constraint on the baryon density of the universe can be inferred from the abundance of light elements (BBN). Hence, DM must be *non-baryonic*.
Candidates for non-baryonic DM can be found in particle physics, in the form of elementary particles produced in the early universe. Possible particle candidates for non-baryonic DM must satisfy several conditions:

- be electromagnetically neutral or interact very weakly with the electromagnetic radiation [123–125]. If this was not the case, features of the cosmic microwave background would be changed as well as the matter power spectrum, because of the interactions between the DM and the photons before recombination.
- be stable on cosmological time scales, otherwise they would have decayed.
- have the right cosmological abundance.
- fulfill the constraints on its self-interactions and the interactions with the SM particles.

[4] Actually, there is a mismatch with the stellar Li/H measurements. However, it is still unknown whether this inconsistency comes from systematic errors in the observed abundances, and/or uncertainties in stellar astrophysics or nuclear inputs, or it is due to new physics [73].

Hot, warm and cold dark matter A major classification of non-baryonic DM is based on its velocity at the time of galaxy formation. DM candidates can be separated into three main groups: *cold, warm* and *hot* DM (CDM, WDM and HDM). This classification deals with the *free-streaming length* of DM particles, i.e. how far the particles could move in the early universe. This length is related to the structure formation scale. Cosmological observations imply that DM should have had non-relativistic velocities at the time when structures start to form in the early universe, meaning that *cold* DM [126] is the preferred type [88, 127–129]. However, as we will discuss below, also the WDM scenario is a viable option, predicting differences with respect to the CDM model on small scales.

- **HDM** is highly relativistic at the time of galaxy formation: it can escape and wash out density perturbations on large scales in the early Universe. It is then strongly constrained by structure formation analysis. Indeed, in this scenario, structures do not form hierarchically (bottom-up), but they are created by breakup of the largest superclusters forming first (top-down cosmological scenario) [130]. Deep-field observations have excluded this scenario.
  Hot DM particles have a cosmological number density which is roughly the same as the microwave background photons. This leads to an upper bound on the mass of HDM particles of a few eV. The most widely studied candidate of HDM is the *neutrino* [131]. The upper bound on the light neutrino content of the Universe is currently [79]:

$$\Omega_\nu h^2 \sim \frac{\sum_\nu m_\nu}{93eV} \leq 0.00247 \quad 95\ \%\text{C.L.} \tag{11}$$

- **WDM** has properties intermediate between those of HDM and CDM. If WDM particles are thermally produced (see next paragraph), they decouple later in the early Universe than HDM and their number density is smaller. The WDM scenario gives roughly the same predictions as the CDM scenario on large scales, but on small-scale foretells less density perturbations [132–134]. This has a consequence in the expected number of dwarf galaxies. A further difference is related to the density distribution of DM inside the halos. WDM predicts a lower density in the central regions of large galaxies. The halos that form near the cutoff scale in the power spectrum as it is in the case of WDM, may be less concentrated and less cuspy than CDM halos. This may actually lead to a better fit with observations. Assuming a pure WDM cosmology, Lyman-α analysis provides a lower bound on the DM particle mass of ~ 1 keV [128]. Indeed, the formation of small DM halos is inhibited at high redshift and also star formation should be affected, thus leaving an imprint in the Lyman-α forest (the sum of absorption lines arising from the Ly-α transition of the neutral hydrogen in the spectra of distant galaxies and quasars).
  The CDM scenario shows some inconsistencies with some observations, for example the excess of the number of galactic satellites and their luminosities and the cuspiness of the central cores of galactic halos. WDM has been proposed to alleviate some of these apparent problems of CDM models, related to the matter power spectrum on scales $\lesssim$ few Mpc. However, from the latest Ly-α analysis [135], it seems that there is

little room for a contribution of the free-streaming of WDM to the solution of these problems, under the assumption of a thermal production of WDM. Examples of WDM candidates are light gravitinos and light sterile neutrinos.

- **CDM** particles have streaming velocities which are negligible for most astrophysical considerations. They are non relativistic at the time of decoupling from the primordial plasma. According to the CDM paradigm [126], structures grow hierarchically, in a *bottom-up* way: small objects collapse under their self-gravity and form first; larger objects are created later by merging. The CDM scenario is the most favoured one, as of today, because it is the one that best explains current cosmological observations (CMB, rotational curves, clusters and so on). However, despite its great success in explaining cosmic structure over many ranges of redshift, the CDM cosmological model has encountered a few challenges from observations, namely concerning the innermost regions of DM halos and the properties of the Milky Way's dwarf galaxy satellites [136–139]. Numerical simulations show that the central density profiles of DM halos exhibit a cuspy behaviour, whereas the observed galaxy rotation curves (in particular dwarf galaxies) give hints for constant density core. This is usually referred to as the *cusp/core problem* [137]. The second problem is known as the *missing satellite problem*: simulated DM halos possess a host of substructure formed by earlier collapses on smaller scales, predicting many more subhalos than those expected for the observed satellites of the Milky Way. A solution may lie in baryonic physics: the combination of a high gas density threshold for star formation and efficient supernova feedback, can lead to a less concentrated DM halo successfully reproducing the observed stellar and DM fractions of galaxies ([140] and references therein). A different solution might instead come from particle physics. Making DM warm, because its free-streaming velocity in the early universe is large, it can erase primordial fluctuations on sub-galactic scales.

Production mechanism of dark matter Another important classification of particle DM hinges upon its production mechanism. Particles that were in thermal equilibrium in the early universe are called thermal relics. These particles would have decoupled from the primordial plasma at *freeze-out*, when the annihilation rate became smaller than the expansion rate of the universe. They would then remain floating around in the universe as relics which can contribute to the average DM density, totally or just in part depending on their actual number density and mass.
Particles which were produced by a non-thermal mechanism are called non-thermal relics. For example, they could have been produced gravitationally at the end of inflation or through phase transitions. Axions may be non-thermally produced.

Among the possible non-baryonic candidates, the most widely studied are the Weakly Interacting Massive Particles (WIMPs), then there are axions, non-standard neutrinos such as sterile neutrinos [141], WIMPzillas [142] and many others. It is worth to remind that non-baryonic DM may naturally be multi-component. We will now shortly discuss WIMPs and axions.

Weakly Interacting Massive Particles WIMPs are the most studied class of CDM candidates, because they arise naturally in theoretical extensions of the SM of particle physics [143]. WIMP DM candidates are predicted by supersymmetry for example [144]. We will discuss this extension of the SM in Section 2.1.
This class of particles features interactions around the scale of weak interactions and masses near the weak scale. It is common to refer to the properties of this class of models as to the *WIMP "miracle"*. The origin of this coincidence lies in their natural virtue of achieving the correct relic abundance in the early universe. According to WIMP models, DM particles are kept in thermal and chemical equilibrium in the early universe with all other SM particles, via self-annihilation into particles of the SM and vice versa. As the universe expands and cools down, the WIMP number density decreases until they cannot self-annihilate anymore nor can they be created through the inverse process, because the average thermal energy of the lighter particles becomes insufficient to form a DM particle-antiparticle pair. Once the rate of these reactions of self-annihilation and of production of DM pairs becomes smaller than the Hubble expansion rate of the Universe, WIMPs *freeze-out* from equilibrium: they drop out of equilibrium with the thermal bath, meaning that their comoving number density remains fixed, unless decays are important. By solving the Boltzmann equations it can be inferred that their *relic density* is proportional to the inverse of the annihilation cross section [145]:

$$\Omega_\chi h^2 \propto \frac{3 \times 10^{-26} cm^3/sec}{\langle \sigma v \rangle_{ann}}, \tag{12}$$

for a WIMP of mass m_χ. Particles with a larger cross section would continue to annihilate for longer and lead to a smaller number density when the interactions cease.
From a dimensional analysis, it turns out that to get the correct relic density (see Eq. (10)), the annihilation cross section cannot be larger than the magnitude of cross sections for weak processes. When WIMPs freeze out, at temperature $T_F \sim m_\chi/20$, they are already non-relativistic behaving therefore as CDM.
WIMP candidates arise in many extension of the SM at the TeV scale. For instance, the lowest-mass eigenstate of the supersymmetric partners of SM particles, called the lightest supersymmetric particle (LSP), like the *neutralino*, is one of the most widely studied WIMP candidates. We will discuss some of these SUSY WIMPs in Section 2.2. Another widely studied non-supersymmetric WIMP candidate is the lightest Kaluza-Klein (KK) particle, usually the KK photon, which arises in theories with universal extra dimensions (UED) [146, 147].

Axions Axions emerge from the Peccei-Quinn solution to the strong-CP problem in the theory of strong interactions [148]. Indeed, in the Lagrangian of quantum chromodynamics (QCD), there exists a term which allows significant CP violation in QCD. When a small explicit symmetry breaking occurs, either in the Lagrangian or due to anomalies, the boson associated with the breaking acquires a mass and is called pseudo Nambu-Goldstone boson.

Axions are the pseudo Nambu-Goldstone bosons associated with the spontaneous breaking of a new global U(1) symmetry of Peccei-Quinn. Axions are predicted to be very light, but they could nevertheless constitute CDM, if they were produced non-thermally in the early Universe. See these references for more details on axions as DM candidates: [149–152].

2 Theoretical motivations for new physics beyond the Standard Model

Experimental observations that we have discussed in the previous Sections which are not explicable within the SM are not the only reason to look for new physics beyond it. Indeed, the SM suffers also from some theoretical problems, regarding for instance the origin of the flavor structure and the radiative corrections to the Higgs boson mass. These are some of the main open theoretical questions:

- The **apparent hierarchy of fermion family masses**: there seems to be a complete lack of universality in the origin of quark and lepton masses. The fermion spectrum suggests some form of family symmetry, but why masses span over 13 orders of magnitude in the interval from $\sim 10^{-2}$ eV for neutrinos to ~ 200 GeV for the top quark, is still not understood.
- **Charge quantization**, that is the equality of the magnitudes of the proton and electron electric charges, leading to the electrical neutrality of ordinary matter, has not been explained yet.
- **The Higgs hierarchy problem**
- **The unification of gauge couplings**
- The number of **free parameters**: SM has around 20 free parameters, between masses, mixing angles, couplings and so on.
- **Gravity:** the SM does not lead to a consistent theory of quantum gravity.

The idea of supersymmetry (SUSY) has been considered very appealing for several years because it can give an answer to many of the open issues in theoretical particle physics. Nevertheless, the discovery of the 125 GeV Higgs boson, and nothing else at LHC seems to put SUSY into trouble, at least in its minimal realization, because to raise the Higgs mass to the value measured by the ATLAS and CMS experiments, we need a quite large radiative correction. A solution would be to make the mass of the supersymmetric partner of the top quark heavy, thus meaning that the scale of SUSY breaking is much higher than what was expected just a few years ago. This implies that we are back also with the problem of fine-tuning, now that the idea of low-energy supersymmetry seems to be no longer valid. Anyhow, there are many non-minimal realizations of SUSY which are still valid.

2.1 Supersymmetry

SUSY was first proposed in the 1960s, in the perspective of looking for a symmetry to relate fermions and bosons and developed seriously during the next two decades [153–155]. SUSY was firstly introduced as the largest possible symmetry group, by describing the unification of internal symmetries (the $SU(3)_c \otimes SU(2)_L \otimes U(1)_Y$ gauge symmetry of the SM) with the spacetime symmetries of the Poincarè group (which consists of Lorentz transformations plus translations, i.e. the full symmetry group of spacetime, which is related to gravity).

However, the no-go theorem of Coleman and Mandula (1967, [156]) showed that this unification is impossible, because it would force the S-matrix to be trivial, unless supergroups and superalgebra are used.
In the 1970s, Wess and Zumino wrote down the first 4-dimensional quantum field theory which contained a supersymmetry [155] and Haag, Sohnius and Lopuszanski showed that SUSY is actually the only symmetry which is compatible with the Poincarè group [157].

Among the proposed theoretical extensions of the SM, SUSY is one of the most prominent, because it not only fixes most of the problems of the SM but it also has additional attracting features:

- it cancels many of the divergences that occur in quantum field theory;
- it provides a "natural" solution to the gauge hierarchy problem [5];
- it allows the gauge couplings to unify at the GUT scale (within a percent of precision);
- local SUSY leads naturally to quantum gravity.

Hereafter I will summarize in brief the main appealing features of SUSY.

A - Hierarchy problem This is maybe considered by many people one of the main motivations for the introduction of SUSY: a solution to the hierarchy problem, coming from the absence of quadratic divergencies. The hierarchy problem results from the fact that the mass of the Higgs boson is not protected by any symmetry in the SM. More generally, it concerns the fact that the weak scale is so much lighter than the Planck scale, which is usually assumed as the cutoff scale. The neutral part of the Higgs field, H, is a complex scalar field with potential:

$$V_H = m_H^2 H^2 + \lambda H^4. \tag{13}$$

The vacuum expectation value (VEV) v which occurs at the minimum of this potential must be non-vanishing in the SM. If $m_H^2 < 0$ and $\lambda > 0$ the vev is $v = \sqrt{\frac{-m_H^2}{2\lambda}}$ which corresponds to a continuum of minimum values in SU(2). It allows the spontaneous symmetry breaking of the SM. The value of the VEV is known experimentally to be $v \sim 246$ GeV. Being the Higgs boson a scalar particle, the Higgs mass-squared parameter m_H^2 tends to be close to the scale of the heaviest particle that it is coupled to, which may be up to the Planck scale [158]. Indeed, m_H^2 receives large loop corrections proportional to some cut-off scale Λ^2, with Λ normally assumed to be at the Planck scale $O(10^{19})$ GeV [6]. However, experiments have given indication that the Higgs mass is demanded to be of the order of the electroweak scale.

[5] At least historically this could be included among the attractive features of SUSY. Nevertheless, without any signal of SUSY at LHC at low energy, the hierarchy "problem" (if it actually is considered a problem) remains: a certain "little" amount of fine-tuning seems to be anyway necessary.

[6] Actually, the large quadratic contributions due to the superheavy fields can be entirely reabsorbed through the renormalization of the bare mass and therefore there is no dependence on the cut-off scale left in the physical Higgs mass.

Notably, from the recent results of the LHC collaborations ATLAS [159] and CMS [160] its mass should be around 125 GeV. The cancellation of the different loop contributions demands in the SM an extreme fine-tuning of parameters [161, 162]. This problem is solved in SUSY theories because each particle's contribution is canceled out by its superpartner, so that the Higgs mass remains small. This exact cancellation is related to the different statistics obeyed by fermions and bosons.
An example of this cancellation is shown in Fig. 1.1. Let's consider, as an example, the top quark and its superpartner, the *stop*.

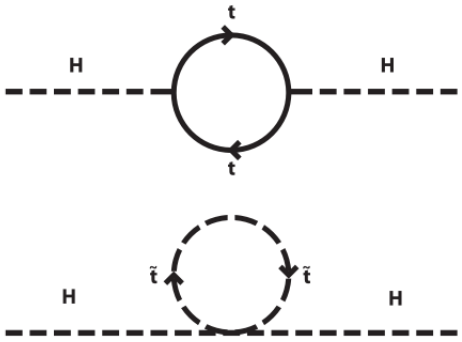

Figure 1.1: Feynman diagrams leading to top/stop 1-loop corrections to the Higgs boson mass.

They both contribute to the Higgs mass as shown in the figure. The contribution coming from the scalar particle, that is the stop, is:

$$\left(\Delta m_h^2\right)_{\tilde{t}} \sim \lambda_{\tilde{t}} \int \frac{d^4p}{(2\pi)^4} \frac{1}{p^2 - m_{\tilde{t}}^2} \tag{14}$$

and it is a quadratically divergent integral proportional to $m_{\tilde{t}}^2$. The contribution coming from the fermion, the top quark is instead:

$$\left(\Delta m_h^2\right)_t \propto |\lambda_t|^2 \int \frac{d^4p}{(2\pi)^4} \frac{1}{p^2 - m_t^2} + \log. \tag{15}$$

The log term stands for a logarithmic correction which is not dangerous for the renormalization. This contribution is proportional to m_t^2. In both cases, if m_t or $m_{\tilde{t}}$ are much larger than the tree-level mass of the Higgs, then also the corresponding correction will be much larger than the tree-level mass. However, if SUSY is unbroken

$$m_t^2 = m_{\tilde{t}}^2 \tag{16}$$

and

$$\lambda_{\tilde{t}} = -|\lambda_t|^2 \tag{17}$$

and the top and the stop contributions cancel exactly. This fact hints at the existence of an additional symmetry between fermions and boson, as SUSY is.
We still have to introduce the SUSY breaking, though. Indeed, experiments such as LEP and LHC have not found any evidence, by now, of SUSY particles with the same mass of the SM partners. This means that SUSY, if it exists, must be broken. If SUSY is "softly broken" (see later, Section 2.1), no new quadratic divergences are introduced, but only logarithmic divergences depending on the cut-off scale, like:

$$\int \frac{d^4p}{(2\pi)^4} \frac{1}{(p^2 - m^2_{\tilde{f}_i})(p^2 - m^2_{\tilde{f}_j})} \sim \int \frac{d^4p}{p^4} \tag{18}$$

which do not spoil the correct cancellation of the quadratic divergences. A logarithmic correction to the Higgs boson mass [163–167] remains, of the form

$$\Delta m_h^2 \propto \left(m^2_{\tilde{f}} - m^2_f\right) ln\left(\frac{\Lambda^2}{m^2_{\tilde{f}}}\right) \tag{19}$$

where Λ is the largest energy scale for which the standard model is valid, and $\tilde{f}$ is the superpartner of the fermion f. If the soft parameters have values close to the electroweak scale, this correction to the Higgs mass is under control and the Higgs boson mass itself remains naturally at the TeV scale. From the logarithmic correction to the Higgs mass, we can infer an upper bound on sfermion masses, requiring a maximum fine-tuning which can be constrained by naturalness arguments.

B - Gauge unification The coupling constants for the electromagnetism, the weak force and the strong force vary with the energy scale. This energy dependence is described by the renormalization group equations (RGE) [168]. We will discuss this in more detail in Chapter 3.
All these three forces are expected to unify at some very high energy scale which is called the GUT scale. In the SM this unification is not achieved, because the coupling nearly comes together in a single point but without coinciding. However, the extension of the particle content by supersymmetric partners influences the scale dependence of all gauge couplings. In SUSY the couplings run together at a single point almost exactly, a few orders of magnitude below the Planck scale, giving a further motivation for the existence of SUSY [169–173], as shown in Fig. 1.2. As a consequence, gauge coupling unification is sensitive to the superpartner mass scale, although the dependence is just logarithmic.

C - Dark matter Many supersymmetric models provide a DM candidate, the most studied is the neutralino which is a good WIMP DM candidate when it is the lightest supersymmetric particle (LSP). We will discuss SUSY DM in Section 2.2.

Before introducing the Minimal Supersymmetric Standard Model, we will present a short summary of the mathematical formalism needed in order to introduce a supersymmetric theory. For a nice review on SUSY formalism see for example [174, 175].

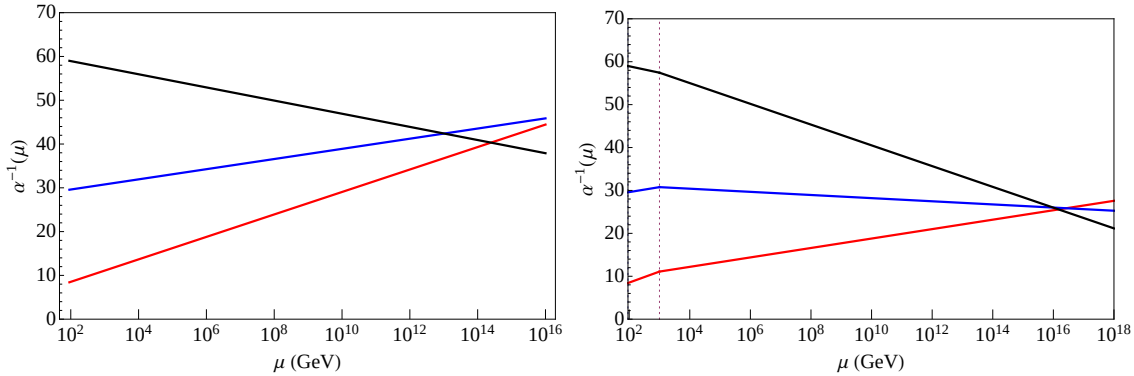

Figure 1.2: Unification of the gauge couplings (α_3 in red, α_2 in blue and α_1 in black) versus the energy scale μ, in the SM (left) and with SUSY (right). The soft SUSY-breaking scale is at 1 TeV and the running of the gauge coupling is at the one-loop level.

SUSY algebra SUSY is given by a set of generators Q_α which commute with the Hamiltonian. These operators are called *supercharges*. What makes this symmetry "super" is that the supercharges are fermionic (i.e. anti-commuting spinor operators), and they mix bosonic and fermionic states.

$$Q_\alpha|\text{Boson}\rangle = |\text{Fermion}\rangle \ , \qquad \text{Q}_\alpha|\text{Fermion}\rangle = |\text{Boson}\rangle \ . \tag{20}$$

It follows that in a SUSY theory each particle must have a superpartner with which it is exchanged under supersymmetry transformations and that differs by exactly one-half integer spin.
The simplest choice of SUSY generators is a 2-component (Weyl) spinor Q_α and its conjugate $\bar{Q}_{\dot{\alpha}}$. The SUSY generators, being fermionic, fulfill the commutator and anti-commutator relations

$$\{Q_\alpha, \bar{Q}_{\dot{\alpha}}\} = -2\sigma^\mu_{\alpha\dot{\alpha}} P^\mu \ , \quad \{Q_\alpha, Q_\beta\} = \{\bar{Q}_{\dot{\alpha}}, \bar{Q}_{\dot{\beta}}\} = 0 \ , \quad [Q_\alpha, P^\mu] = [\bar{Q}_{\dot{\alpha}}, P^\mu] = 0 \ , \tag{21}$$

with α, β (of Q) and $\dot{\alpha}, \dot{\beta}$ (of $\bar{\text{Q}}$) = 1,2, P^μ is the four dimensional operator of space-time translation and $\sigma^\mu = (1, \sigma_i)$, with σ_i being the Pauli matrices.
In order to characterize the irreducible representations of the super-group, one has to find the Casimir operators, that are those that commute with all the generators of the algebra. A representation will be labeled by the value that these invariant operators take when they act on them. The Casimir operator is defined as:

$$P^2 = P_\mu P^\mu \tag{22}$$

and the SUSY generators obey the vanishing commutator:

$$[Q_\alpha, P^2] = 0 \tag{23}$$

The irreducible representations of the SUSY algebra are called *supermultiplets* and include particles with the same mass, but different spins.

Superfield formalism The *superfield formalism* [176–182] is a compact way to describe supersymmetric theories and their properties, because in this framework the description of SUSY operators in superspace is similar to Poincare operators in Minkowski space. To easily build supersymmetric lagrangians, it is useful to introduce "fermionic coordinates". This means to extend the four space-time coordinates x_μ by four Grassmann coordinates Θ_α and $\bar{\Theta}_{\dot{\alpha}}$ which anti-commute and thus differ from the coordinates of Minkowski space which are instead "bosonic coordinates".
The Grassmann coordinates obey some rules, such as that the squared of a Grassmann coordinate is always zero and integration and differentiation with respect to Grassmann coordinates are identical operations.
This leads to the introduction of *superfields*, which are functions of Θ_α and $\bar{\Theta}_{\dot{\alpha}}$ and of the spacetime coordinates x_μ. The SUSY generators can be written explicitly as:

$$Q_\alpha = \frac{\partial}{\partial\Theta_\alpha} - i\sigma^\mu_{\alpha\dot{\alpha}}\bar{\Theta}^{\dot{\alpha}}\partial_\mu \ , \qquad \bar{Q}_{\dot{\alpha}} = -\frac{\partial}{\partial\bar{\Theta}_{\dot{\alpha}}} + i\Theta^\alpha\sigma^\mu_{\alpha\dot{\alpha}}\partial_\mu \ . \tag{24}$$

We can further define the covariant derivatives as

$$D_\alpha = \partial_\alpha + i\sigma^\mu_{\alpha\dot{\alpha}}\bar{\Theta}^{\dot{\alpha}}\partial_\mu, \qquad \bar{D}_{\dot{\alpha}} = -\partial_{\dot{\alpha}} - i\Theta^\beta\sigma^\mu_{\beta\dot{\alpha}}\partial_\mu. \tag{25}$$

These are valid for generic superfields Φ, which can be re-written in terms of *chiral* representations: $\Phi(x_\mu, \Theta_\alpha, \bar{\Theta}_{\dot{\alpha}}) = \Phi_L(x_\mu + i\Theta^\alpha\sigma^\mu_{\alpha\dot{\alpha}}\bar{\Theta}^{\dot{\alpha}}, \Theta_\alpha, \bar{\Theta}_{\dot{\alpha}}) + \Phi_R(x_\mu - i\Theta^\alpha\sigma^\mu_{\alpha\dot{\alpha}}\bar{\Theta}^{\dot{\alpha}}, \Theta_\alpha, \bar{\Theta}_{\dot{\alpha}})$.
In the "chiral" representation, Φ_L does not depend on $\bar{\Theta}_{\dot{\alpha}}$, whereas Φ_R does not depend on Θ_α.

Chiral superfields Nevertheless, to describe spin-0 bosons and spin-$1/2$ fermions we have to concentrate on special superfields, which are irreducible representations of the SUSY algebra. The chiral superfield (SUSY generator) obey the following relation:

$$\bar{D}_{\dot{\alpha}}\Phi_L = 0, \qquad D_\alpha\Phi_R = 0 \tag{26}$$

where the fields Φ fulfilling this relations are the chiral superfields which describe the left- or right-handed component of an SM fermion and the corresponding superpartners (the *sfermions*).
The explicit form for Φ_L is then:

$$\Phi_L = \phi(y) + \sqrt{2}\Theta\Psi(y) + \Theta^2 F(y) \ . \tag{27}$$

The fields ϕ and F are complex scalars, while Ψ is a Weyl spinor. F is an auxiliary field with an unusual mass dimension $+2$ and doesn't propagate. The expression for Φ_R is analogue.
Summarizing, chiral supermultiplets consist of the fermionic Weyl spinor fields Ψ, their complex scalar superpartners ϕ and complex auxiliary fields F, which are required to close the superalgebra off shell in perturbation theory.

Vector superfields To describe the spin-1 gauge bosons, we have to introduce the other irreducible representation of the SUSY algebra, which are vector superfields, and satisfy

$$V(x_\mu, \Theta_\alpha, \bar{\Theta}_{\dot{\alpha}}) = V^\dagger(x_\mu, \Theta_\alpha, \bar{\Theta}_{\dot{\alpha}}) \; . \tag{28}$$

This relation is invariant under supersymmetric translations. If we consider a left-chiral superfield $\chi(\Theta)$ with mass dimensions 0, we can expand V as

$$V = i\chi(\Theta) - i\chi^\dagger(\Theta) - \Theta\sigma^\mu\bar{\Theta}A_\mu + i\Theta^2\bar{\Theta}\bar{\lambda} - i\bar{\Theta}^2\Theta\lambda + \frac{1}{2}\Theta^2\bar{\Theta}^2 D \; . \tag{29}$$

D is again an auxiliary field, λ is the fermionic component of the vector superfield and A_μ is a gauge boson. Since V is massless, it can be shifted by a gauge transformation. The gauge in which the fields χ disappear is called Wess-Zumino gauge.
The gauge supermultiplet then consists of a massless spin 1 gauge boson A^a_μ , of its superpartner, a massless Weyl fermion λ^a and a real bosonic auxiliary field D^a, where a is the index running over the adjoint representation of the gauge group in consideration.

Superpotential The non-gauge interactions of a supersymmetric model are written using the *superpotential*. It is an holomorphic function of the chiral superfields Φ_j which includes the Yukawa couplings in the SUSY theory. Superfields Φ_j contain as components all the bosonic, fermionic, and auxiliary fields within the corresponding supermultiplet.
The most general form of the superpotential for a renormalizable model is

$$W = \frac{1}{2}\mu^{ij}\Phi_i\Phi_j + \frac{1}{3}Y^{ijk}\Phi_i\Phi_j\Phi_k \; . \tag{30}$$

where we have omitted linear terms in Φ_i which are not allowed in the MSSM, where none of the Φ_i is a gauge singlet.

Scalar potential It is useful to consider the scalar potential, since by Lorentz invariance only scalar fields can get a non-vanishing vacuum expectation value (vev). It is given by:

$$V(\phi, \phi^\dagger) = F^{\dagger i}F_i + \frac{1}{2}\sum_a D^a D^a = \sum_i \left(\frac{\partial W}{\partial \phi_i}\right)\left(\frac{\partial W}{\partial \phi_i}\right)^\dagger + \frac{1}{2}\sum_a g_a^2(\phi^{\dagger i}T_i^{aj}\phi_j)^2 \tag{31}$$

where T^a are the generators of the gauged Lie algebra. The F-terms are defined as $F_i = \left(\frac{\partial W}{\partial \phi_i}\right)^\dagger$ and they are fixed by Yukawa couplings and fermion mass terms. The D-terms are fixed by the gauge interactions and are defined as $D^a = -\sum_a g_a(\phi^{\dagger i}T_i^{aj}\phi_j)$.

Soft Lagrangian Since no supersymmetric particle has been discovered yet, notably any sparticle with the same mass as the "ordinary" SM particles, SUSY must be broken. This means that the theory should have a Lagrangian that is invariant under supersymmetry, but a vacuum state that is not, thus hiding SUSY at low energies. Nevertheless, the way how SUSY is broken is still unknown, and since it is not easy to break SUSY spontaneously, what is usually done is to introduce some *soft breaking terms*, with positive mass dimension, into

the Lagrangian to break SUSY by hand [183,184]. The name "soft" is related to the idea of preserving the main property of SUSY, which is the cancellation of quadratic divergencies. We list here the possible terms in the soft SUSY-breaking part of the Lagrangian:

$$-\mathcal{L}_{soft} = \left(\frac{1}{2}M_a\lambda^a\lambda^a + \frac{1}{2}B^{ij}\phi_i\phi_j + \frac{1}{6}A^{ijk}\phi_i\phi_j\phi_k\right) + h.c. + (m^2)^i_j\phi^\dagger_j\phi_i. \quad (32)$$

M_a are masses for the gaugino fields λ^a, B^{ij} and $(m^2)^i_j$ scalar squared-mass terms (implying that the scalars such as squarks, become usually heavier than the fermions of the same multiplet), A^{ijk} "trilinear" cubic-scalar couplings, which are related to Yukawa couplings. If ϕ_i was a gauge singlet, also a tadpole term $T^i\phi_i$ would be allowed, but this is not the case for the Minimal Supersymmetric Standard Model.
The terms in $\mathcal{L}_{soft}$ clearly break SUSY, because they involve only scalar and gaugino fields and not their respective superpartners.

2.2 The Minimal Supersymmetric Standard Model

The Minimal Supersymmetric Standard Model (MSSM) was born in the 80s with the intent of proposing a theory with softly broken supersymmetry that satisfies all phenomenological constraints [175, 177, 185–188]. The main motivation for introducing weak-scale supersymmetry is the absence of quadratic divergencies, as a technical solution to the hierarchy problem [189].
The idea of considering the minimal extension to the SM under which it becomes supersymmetric, leads to the MSSM as the smallest possible supersymmetric extensions of the SM without gauge anomalies. The MSSM contains an entire set of new superpartners of the SM particles. For minimality's sake, the MSSM has only one SUSY generator, but even this doubles the number of particles of the SM [7]. The scalar supersymmetric partners of the SM particles, are named by adding the prefix "s-" to the SM name, whereas the fermion superpartners are called by adding the sufix "-ino" to the name of the SM particle. The particle content of the MSSM is summarized in Tab. (1.2). The compact notation for the SUSY particles is the standard SM symbol with a tilde added. SM matter fermions and gauge bosons do reside in different representations of the SM gauge group and in the MSSM must be put in different superfields. In the MSSM there are five left-chiral superfields: Q and L, which contain respectively the quark/squark and lepton/slepton doublets of SU(2), U^c and D^c which contain the quark/squark singlets, and E^c which contains the lepton/slepton singlets. The left-chiral superfields transform under the fundamental representation, while the right-chiral ones transform in the conjugated representation. The vector bosons and gauginos transform under the adjoint representation. Moreover, apart from doubling the particle content of the SM, a new Higgs doublet has to be introduced. There are several arguments for the need for two Higgs doublets: - A model with a single Higgs doublet superfield has nonvanishing gauge anomalies associated with fermion triangle diagrams, due to the introduction of the higgsino, with respect to the SM; - It is not allowed to introduce

[7] Actually the number of particles in the MSSM is more than doubled with respect to the SM due to the presence of two Higgs doublets.

Left-chiral Superfields				
Name	Superfield	spin 0	spin $\frac{1}{2}$	$SU(3)_C \otimes SU(2)_L \otimes U(1)_Y$
squarks, quarks (3 families)	$\hat{Q}$	$(\tilde{u}_L \quad \tilde{d}_L)$	$(u_L \quad d_L)$	$(\mathbf{3}, \mathbf{2}, \frac{1}{6})$
	$\hat{U}^c$	$\tilde{u}_R^*$	u_R^c	$(\bar{\mathbf{3}}, \mathbf{1}, -\frac{2}{3})$
	$\hat{D}^c$	$\tilde{d}_R^*$	d_R^c	$(\bar{\mathbf{3}}, \mathbf{1}, \frac{1}{3})$
sleptons, leptons (3 families)	$\hat{L}$	$(\tilde{\nu} \quad \tilde{l}_L)$	$(\nu \quad l_L)$	$(\mathbf{1}, \mathbf{2}, -\frac{1}{2})$
	$\hat{E}^c$	$\tilde{l}_R^*$	l_R^c	$(\mathbf{1}, \mathbf{1}, 1)$
Higgs, Higgsinos	$\hat{H}_u$	$(H_u^+ \quad H_u^0)$	$(\tilde{H}_u^+ \quad \tilde{H}_u^0)$	$(\mathbf{1}, \mathbf{2}, \frac{1}{2})$
	$\hat{H}_d$	$(H_d^0 \quad H_d^-)$	$(\tilde{H}_d^0 \, \tilde{H}_d^-)$	$(\mathbf{1}, \mathbf{2}, -\frac{1}{2})$
Vector Superfields				
Name	Superfield	spin $\frac{1}{2}$	spin 1	$SU(3)_C \otimes SU(2)_L \otimes U(1)_Y$
gluino, gluon	$\hat{g}_\alpha$	$\tilde{g}_\alpha$	g_α	$(\mathbf{8}, \mathbf{1}, 0)$
winos, W bosons	$\hat{W}_i \quad i$=1,2,3	$\tilde{W}_i$	W_i	$(\mathbf{1}, \mathbf{3}, 0)$
bino, B boson	$\hat{B}$	$\tilde{B}^0$	B^0	$(\mathbf{1}, \mathbf{1}, 0)$

Table 1.2: Left-chiral and vector superfields of the MSSM and the quantum numbers with respect to the SM $SU(3)_C \otimes SU(2)_L \otimes U(1)_Y$ gauge group. Superfields are named with a hat and the hermitian conjugated is assigned by a c.

the hermitian conjugate of a Higgs superfield because the superpotential must not contain products of left-chiral and right-chiral superfields. Then, it turns out to be impossible to introduce $U(1)_Y$ invariant terms that give masses to both up- and down-type quarks if there is only one Higgs superfield. Indeed, we have to break the $SU(2) \otimes U(1)_Y$ invariance by SU(2) doublet scalars with hypercharge $\mid Y \mid = 1/2$. We therefore have to introduce dedicated Higgs superfields to break $SU(2) \otimes U(1)_Y$, H_d with hypercharge Y = -1/2, and H_u has Y = + 1/2, in order to obtain gauge invariant Yukawa couplings for both quark sectors.

Lagrangian and Superpotential of the MSSM

The MSSM superpotential defines the interactions between the superfields. The gauge interactions are determined by the choice of gauge group, which is the same as in the SM: $SU(3)_C \otimes SU(2)_L \otimes U(1)_Y$. A minimal realistic form of the MSSM superpotential is

$$W_{MSSM} = Y_e^{ab}\, \hat{L}_a^j\, \hat{E}_b\, \hat{H}_d^i\, \epsilon_{ij} + Y_d^{ab}\, \hat{Q}_a^{j\alpha}\, \hat{D}_{\alpha b}\, \hat{H}_d^i\, \epsilon_{ij} + Y_u^{ab} \hat{Q}_a^{i\alpha}\, \hat{U}_{\alpha b}\, \hat{H}_u^j\, \epsilon_{ij} + \mu\, \hat{H}_u^i\, \hat{H}_d^j \epsilon_{ij}\ , \quad (33)$$

where, i, j are $SU(2)_L$ indices, α is the $SU(3)_C$ color index and ϵ_{ij} is the totally antisymmetric Levi-Civita tensor in two dimensions. a, b are flavor indices. Y_e, Y_d and Y_u are three Yukawa couplings which are complex 3×3 matrices, while μ is a parameter with dimension of a mass.
We can either demand that W_{MSSM} respects lepton and baryon number, i.e. the "accidental" symmetries of the SM, or they could be broken explicitly in the MSSM.

We can then write the SUSY Lagrangian, as the sum of gauge interactions, matter interactions (W_{MSSM}) and kinetic terms, plus terms from the auxiliary fields (F and D). Moreover, terms arising from the choice of the gauge have to be added. See for example [190] for a complete description of the MSSM Lagrangian.
In the gauge and Yukawa sectors there is the same number of free parameters as in the SM, while regarding the Higgs sector the μ parameter is the supersymmetric version of the Higgs boson mass in the SM. Nevertheless, when we introduce SUSY breaking, a very large number of free parameters appear. The soft breaking lagrangian [191, 192] consists of mass terms for the scalars and for the gauginos as well as of scalar couplings of the same type as in the superpotential, with positive mass dimension

$$\begin{aligned} -\mathcal{L}_{soft}^{MSSM} = \quad & (m_Q^2)^{ij}\tilde{Q}_i^{a*}\tilde{Q}_j^a + (m_{u^c}^2)^{ij}\tilde{u}_i^c\tilde{u}_j^{c\,*} + (m_{d^c}^2)^{ij}\tilde{d}_i^c\tilde{d}_j^{c\,*} + (m_L^2)^{ij}\tilde{L}_i^{a*}\tilde{L}_j^a \\ & + (m_{e^c}^2)^{ij}\tilde{e}_i^c\tilde{e}_j^{c\,*} + m_{H_d}^2 H_d^{a*}H_d^a + m_{H_u}^2 H_u^{a*}H_u^a \\ & + \big[\frac{1}{2}M_1\tilde{B}^0\tilde{B}^0 + \frac{1}{2}M_2\tilde{W}^m\tilde{W}^m + \frac{1}{2}M_3\tilde{g}^n\tilde{g}^n + h.c.\big] \\ & + \epsilon_{ab}\big[T_u^{ij}\tilde{Q}_i^a\tilde{u}_j^c H_u^b + T_d^{ij}\tilde{Q}_i^b\tilde{d}_j^c H_d^a + T_e^{ij}\tilde{L}_i^b\tilde{e}_j^c H_d^a - B_\mu H_d^a H_u^b\big] \end{aligned} \tag{34}$$

where a and b are $SU(2)_L$ doublet indices, i, j are family indices, $m = 1, 2, 3$ and $n = 1, ...8$. T_α^{ij} are called *trilinear* parameters and sometimes they can be expanded as $A_\alpha^{ij}Y_\alpha^{ij}$ with $\alpha = u, d, e$. M_3, M_2, M_1 are the gluino, wino, and bino mass terms. The m_i^2 terms stand for the squark and slepton mass terms, whereas $m_{H_i}^2$ are the SUSY-breaking contributions to the Higgs potential. The $\mathcal{L}_{soft}^{MSSM}$ introduces many new parameters with respect to the ordinary SM, about 100 between masses, phases and mixing angles that cannot be absorbed by redefinitions.

The mechanism of spontaneous supersymmetry breaking and how the explicit breaking soft parameters are encoded in the soft part of the Lagrangian as the result of spontaneous supersymmetry breaking in a more fundamental theory, is still largely unknown. Many proposed theories introduced to explain SUSY breaking consist of at least two distinct sectors: a hidden sector consisting of particles that are completely neutral with respect to the SM, and a visible sector consisting of the particles of the MSSM. There may be no renormalizable tree-level interactions between particles of the two sectors, depending on the theory. Anyway, besides the origin of this hidden sector, one has to deal with the main question of how the breaking is communicated to the visible sector.
All proposed SUSY breaking schemes have to introduce some high energy scale, where soft terms are generated. This scale could be as high as the scale of Grand unification (GUT), or even the Planck scale in gravity mediated schemes [176, 193], or as low as a 100 TeV, for example in gauge mediated SUSY breaking (GMSB) [194].

Electroweak symmetry breaking in the MSSM

Let's introduce the Higgs sector of the MSSM, in order to describe the spontaneous breaking of the $SU(2) \otimes U(1)_Y$ symmetry. The SUSY Higgs potential contains three kinds of terms: 1) mass terms, arising from the *F - terms*; 2) quartic interactions, from SUSY *D - terms* and

3) additional mass and mixing terms from $\mathcal{L}_{SB}^{MSSM}$. Thus, the form of the scalar potential is:

$$\begin{aligned} V_H &= (|\mu|^2 + m_{H_u}^2)|H_u^0|^2 + (|\mu|^2 + m_{H_d}^2)|H_d^0|^2 - (B_\mu H_u^0 H_d^0 + \text{h.c.}) + \\ &\quad \frac{(g_1^2 + g_2^2)}{8}(|H_u^0|^2 - |H_d^0|^2)^2 \, . \end{aligned} \tag{35}$$

where g_1 and g_2 are respectively the $U(1)_Y$ and $SU(2)_L$ couplings. We can further define: $m_{1,2}^2 = m_{H_d,H_u}^2 + \mu^2$.

R-parity

In SUSY theories, lepton and baryon numbers are no longer conserved as in the SM by all the possible couplings present in the superpotential. There may be terms such as LLe^c, LH, Qd^cL or $u^cd^cd^c$ which break either lepton (L) or baryon (B) numbers. However, since currently there is no experimental evidence[8] (for example, no evidence of proton decay, which would break both L and B) of non-conservation of these two quantum numbers, these couplings need to be very small or there must exist some symmetry forbidding them.
R-parity is a $\mathbb{Z}_2$ symmetry which forbids these couplings and it is defined as:

$$R_p = (-1)^{3(B-L)-2s}, \tag{36}$$

where s stands for the particle spin. According to this definition all SM particles have $R_p = +1$ whereas the SUSY partners have $R_p = -1$.
R-parity can be motivated as a remnant of a larger symmetry, which is broken at higher energy scale: for example, left-right symmetric models (see Section 3.2) with a $U(1)_{B-L}$ symmetry, forbid terms which violate B or L. R-parity can occur naturally in SO(10) GUTs. This symmetry has some interesting phenomenological consequences. As to DM, while R-parity is conserved, the lightest supersymmetric particle (LSP) cannot decay and hence becomes a good DM candidate (if it fulfills also other requirements such as no electric/color charge). Regarding phenomenology at colliders instead, if R-parity is conserved, sparticles are always produced in pairs and when they decay, they decay to an odd number of LSPs, which can therefore be detected as missing energy.
Although the MSSM is assumed to be R-parity conserving, there are some classes of R-parity violating models which are weakly constrained by experiments [195]. On the other hand, these models have other interesting consequences, for instance the violation of L number supplies masses for the neutrinos.

SUSY Dark Matter

In a theory with R-parity conservation, the lightest supersymmetric particle can be a good DM candidate [87, 144]. The LSP is stable because of R-parity conservation, but in order to be suitable as DM candidate, it has to be also neutral and non-colored. Although the

[8] Although massive neutrinos may indicate L-number violation, if they are Majorana particles.

recent searches performed by the LHC challenge SUSY, they do not impose strong direct constraints on the DM nature. We are left then with basically three candidates among the superparticles: the sneutrino, the neutralino and the gravitino.

Neutralino DM The neutralinos are four Majorana fermionic mass–eigenstates defined as linear superpositions of the two supersymmetric partners of neutral SM gauge bosons (the gauginos $\tilde{B}$ and $\tilde{W}_3$) and of the two neutral Higgsinos ($\tilde{H}_u^0$ and $\tilde{H}_d^0$).

$$\chi = N_1\tilde{B} + N_2\tilde{W}_3 + N_3\tilde{H}_u^0 + N_4\tilde{H}_d^0. \tag{37}$$

They are labelled $\tilde{\chi}_1^0$, $\tilde{\chi}_2^0$, $\tilde{\chi}_3^0$ and $\tilde{\chi}_4^0$, in order of increasing mass. The lightest of these four eigenstates may play the role of the LSP, and it can inherit the correct thermal relic density in different regions of the parameter space. It is common to refer to the lightest neutralino as *the* neutralino. Neutralinos are Majorana fermions with weak interactions only, and they exhibit all the properties of WIMP DM.
In the basis $(\tilde{B}, \tilde{W}_3, \tilde{H}_1^0, \tilde{H}_2^0)$, the neutralino mass matrix can be written, in terms of the physical masses, as

$$\mathcal{M}_N = \begin{pmatrix} M_1 & 0 & -M_Z\cos\beta\sin\theta_W & M_Z\sin\beta\sin\theta_W \\ 0 & M_2 & M_Z\cos\beta\cos\theta_W & -M_Z\sin\beta\cos\theta_W \\ -M_Z\cos\beta\sin\theta_W & M_Z\cos\beta\cos\theta_W & 0 & -\mu \\ M_Z\sin\beta\sin\theta_W & -M_Z\sin\beta\cos\theta_W & -\mu & 0 \end{pmatrix}. \tag{38}$$

M_1 and M_2 are the bino and wino mass parameters, μ is the higgsino mass parameter, θ_W is the weak angle and $\tan\beta$ is the ratio of the vevs of the Higgs bosons. The neutralino mass matrix is diagonalized by a 4×4 rotation matrix N such that

$$M_N^{\text{diag}} = N^{-1\dagger} M_N N^{-1}, \tag{39}$$

to obtain the mass eigenstates. It is useful to define two parameters, the *gaugino fraction*, f_G, and the *higgsino fraction*, f_H, as

$$f_G = N_1^2 + N_2^2 \tag{40}$$

and

$$f_H = N_3^2 + N_4^2\ . \tag{41}$$

Neutralinos may be produced at LHC in cascade decays of heavier colored supersymmetric particles. The lack of a SUSY signal at the LHC with $\sqrt{s} = 7, 8$ TeV has raised the lower limit on the squark and gluino masses to $\gtrsim 1$ TeV. This leads to the conclusion that neutralino DM lighter than ten or so GeV are strongly constrained in generic MSSM scenarios with gaugino mass unification. Notably, a lower limit on the lightest neutralino mass of about 50 GeV can be derived for MSSM models with gaugino unification already from the LEP chargino mass limit [196], whereas in models with both gaugino and sfermion mass unification (constrained MSSM), this limit increases to above 100 GeV from the constraints set by the LHC data [73].
Limits from direct detection experiments (see Chap. 2) set quite stringent bounds on neutralino DM, however it remains a viable DM candidate.

Gravitino DM The gravitino $\tilde{G}$ is the supersymmetric partner of the graviton. This fermion of spin 3/2 arises in theories which combine supersymmetry and general relativity, like supergravity [197,198]. Once local SUSY is broken spontaneously, the gravitino acquires a mass, which can vary over a large range, from keV to TeV because of its strong dependence on the SUSY-breaking scheme. Nevertheless, the gravitino LSP model is subject to strict cosmological constraints. For instance, the relic abundance of thermally produced gravitinos is closely related to the reheating temperature after inflation [199, 200]. Moreover, there are constraints from Big Bang nucleosynthesis [201], regarding the observed abundances of the primordial light elements.

Sneutrino DM The neutralino as a DM candidate has been studied in literally hundreds of publications, but also sneutrinos as candidates for the cold dark matter have actually quite a long history [202–204]. However, ordinary left sneutrinos, i.e. the sneutrinos of the MSSM, have been ruled out [205] as the dominant component of the DM in the galaxy a long time ago due to their large direct detection cross section [206]. This leaves only "mixed" sneutrinos, i.e. sneutrinos which are partly singlets under the SM group, as good DM candidates. Motivated by neutrino oscillation data [77], we will study in Chapter 4 scalar neutrinos as DM candidates in models with a low-scale seesaw mechanism, either MSSM-like models with an inverse [207] or the linear seesaw [208, 209] or models based on an $U(1)_{B-L} \times U(1)_R$ extension of the MSSM group [210, 211].

2.3 SUSY searches at LHC

Direct searches for sparticle production at collider experiments such as the Large Hadron Collider (LHC) are the most important strategy for searching for SUSY. Nevertheless, recent SUSY searches at the LHC indicate that superparticles, especially squarks and gluinos, are not so light as previously expected. Direct searches are also supported by indirect searches of SUSY from different experiments such as the measurement of high-precision electroweak observables, or from astroparticle data. Although LHC searches are usually sensitive to heavier SUSY masses, they are in general model-dependent. Anyway, by now, all these kind of searches have imposed strong constraints on the allowed SUSY parameters space.

In this Section, we will focus on direct searches for new physics beyond the SM, namely we will shortly comment about the current status of SUSY searches at LHC. For the latest results we will refer to those presented on the webpages of the ATLAS [9] and CMS [10] experiments. The LHC at CERN has started proton-proton collisions at a center-of-mass energy of 7 TeV in 2010. It was then upgraded to 8 TeV in 2012. At the beginning of 2013 it went into a long shutdown for another upgrade to increase beam energy to 6.5 TeV per beam. Re-starting of the collisions is planned for early 2015. A broad program of SUSY particle searches has been underway at the LHC, since its opening: given that no sparticle has been observed yet, they have been translated into constraints on SUSY models.

[9] https://twiki.cern.ch/twiki/bin/view/AtlasPublic
[10] https://twiki.cern.ch/twiki/bin/view/CMSPublic/PhysicsResults

Current constraints on SUSY models

In the framework of the MSSM with R-parity conservation, SUSY particles are expected to be produced in pairs. At the LHC the most numerous produced SUSY particles are expected to be the SUSY partners of quarks, the squarks, and the partners of gluons, the gluinos. Indeed, one of the advantages of an hadronic collider with respect to a leptonic one (such as LEP) is that cross sections of QCD-mediated processes are larger, translating into higher sensitivity for colored SUSY particles like squarks and gluinos. The price to pay is the presence of large backgrounds of hadronic jets.
Colored sparticles at the LHC are mainly produced with squark-squark, squark-gluino and gluino-gluino interactions. SUSY signatures at LHC include high transverse momentum jets, which are produced in the decay chains of heavy colored sparticles (squarks and gluinos), along with a significant missing momentum originating from the LSP produced at the end of the decay chain.
In order to interpret the results of experimental searches, very accurate theoretical predictions for the cross sections are required. The observables that can be measured at LHC depend on the renormalisation scale, according to perturbation theory. Therefore a correct inclusion of higher order contributions is important for the prediction of the sparticles production rate.

The most stringent SUSY mass limits at the LHC are obtained by searches for gluino-gluino and squark-squark production. Assuming R-parity conservation, and depending on kinematics, squarks are expected to decay to a quark and a neutralino or chargino. Therefore, typical SUSY search signatures consist of a significant missing transverse momentum (when there is a neutral LSP), and high transverse momentum (p_T) jets produced in the decay chains starting from the heavy pair-produced squarks and gluinos, eventually accompanied by one or more isolated final states like photons or leptons (electrons, muons, taus, lepton pairs). These limits exhibit some model-dependence, for example on the neutralino mass. Indeed, limits on gluino masses are strongly affected by the assumption of this value; heavier neutralinos translate into less energetic jets and into less missing transverse momentum.
Best target regions for SUSY searches are those where the SM background is best evaluated. For instance, high-p_T cuts are good discriminators to search for SUSY signals and to reduce the QCD background of the SM.
Fig. 1.3 summarize the current status of SUSY searches by ATLAS at LHC. It contains data from the 7 TeV and 8 TeV data of 2011-2012. These limits, which are dominated by hadronic searches, have to be interpreted as lower bounds on the mass limits for SUSY particles within specific typical supersymmetric models. A similar analysis has been performed by CMS collaboration and is shown in Fig. 1.4.
By now, no evidence has been found for natural SUSY models with gluino masses below 1 TeV. Although none of the analyses has reported any significant excess above the SM background, there is still much expectation for the next LHC run at higher energy.

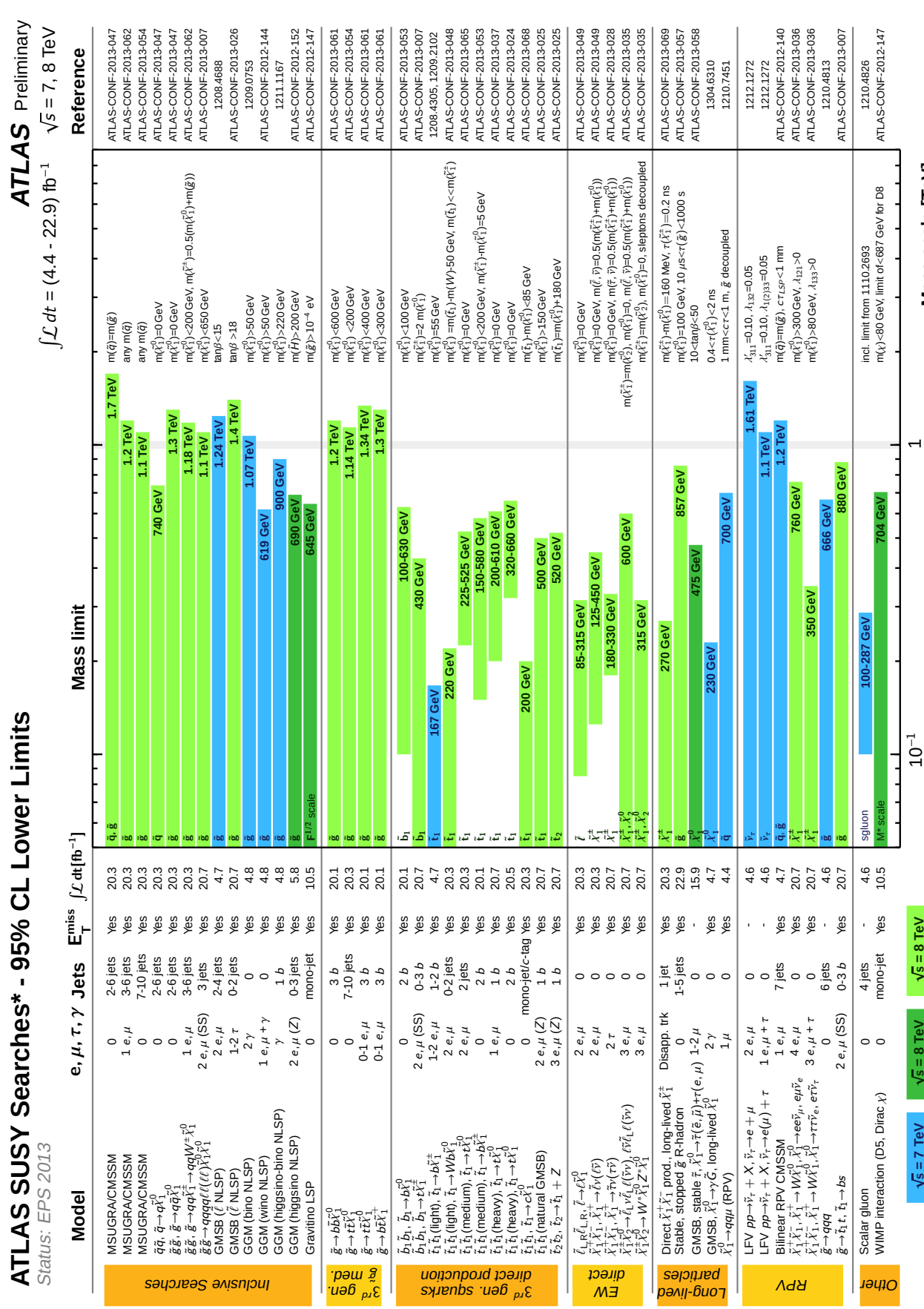

Figure 1.3: Mass reach of ATLAS searches for specific SUSY models (e.g. mSUGRA,GMSB). Status of figure: July 2013. Figure from https://twiki.cern.ch/twiki/bin/view/AtlasPublic.

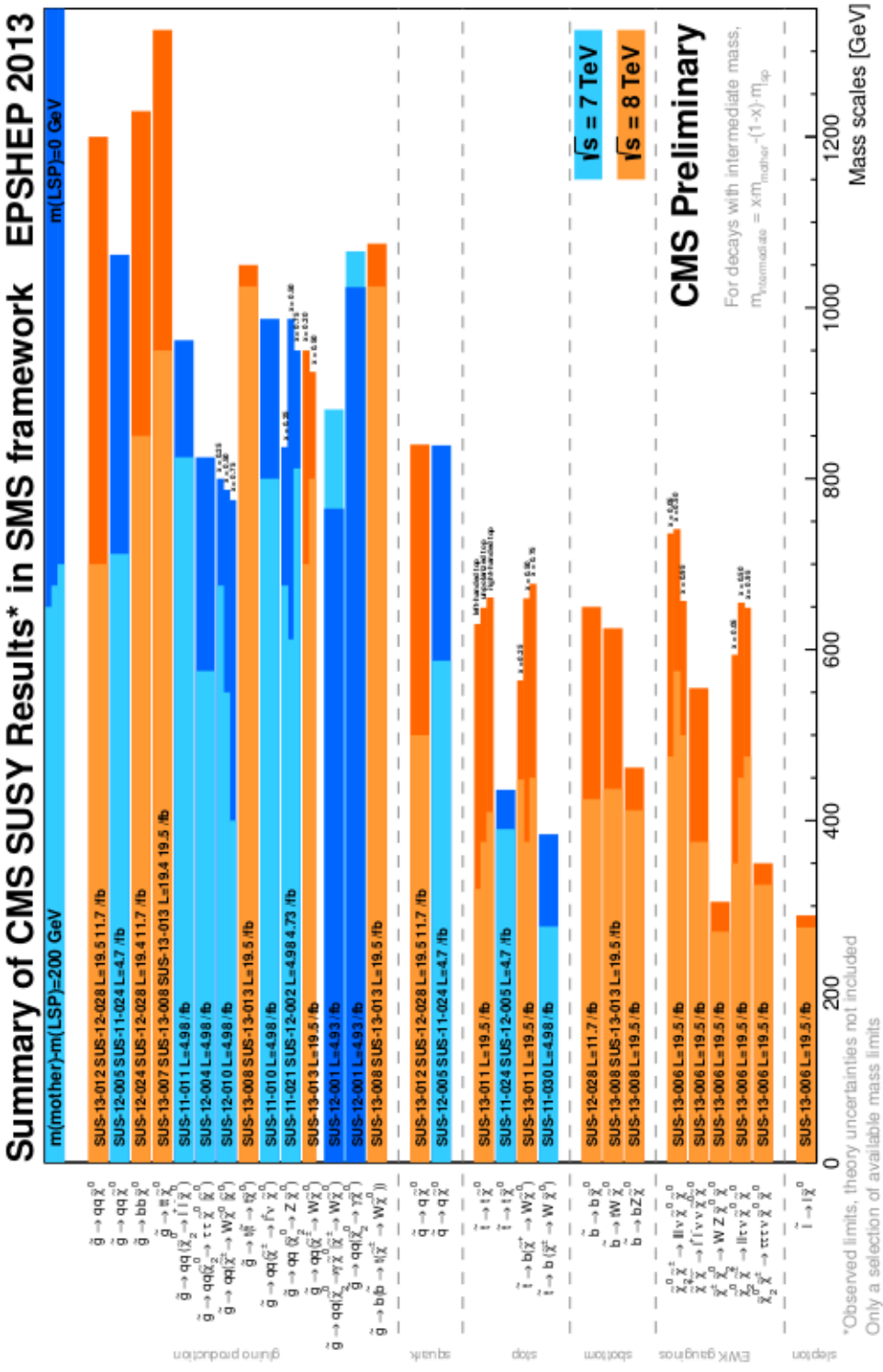

Figure 1.4: Mass reach of CMS searches for Supersymmetry. Best exclusion limits for the masses of the sparticles in various simplified model spectra, are shown, for R parity conserving scenarios, for m(LSP) = 0 GeV (dark shades) and m(mother) - m(LSP) = 200 GeV (light shades). Status of figure: July 2013. Figure from https://twiki.cern.ch/twiki/bin/view/CMSPublic.

3 Theoretical models: Grand Unified Theories (GUTs)

Despite the great success of the SM, its structure seems to be too complicated to be the ultimate theory of elementary particle physics. In this picture, the weak, electromagnetic and strong interactions are independent from each other, as can be seen by the group theory description of the SM. Its gauge group is indeed the direct product of three groups:

$$G_{SM} = SU(3)_C \times SU(2)_L \times U(1)_Y.$$

There are three independent gauge couplings, related to these three gauge groups in the SM. Due to higher-order corrections, each of these is actually a function of the energy scale. The *running* of the gauge couplings with the energy scale is described by the renormalization group equations (RGE) [212–214]. In many GUTs the three gauge couplings are predicted to meet at some high energy unification scale M_G, above which the three interactions are unified. In most of GUTs $M_G \sim 10^{16}$ GeV. Gauge coupling unification works very well within SUSY GUTs. The coupling constants of the SM, g_1, g_2 and g_3 unify exactly at the scale M_G with two loop renormalization group running and considering threshold corrections [215–218].

In Grand Unified Theories [169,219], the $SU(3)_C \times SU(2)_L \times U(1)_Y$ gauge group is embedded into a larger Lie group. The SM multiplets are accomodated into irreducible representations of such a larger group. Grand unification leads to important consequences, first of all gauge coupling unification, of course. But it also makes several predictions, like proton decay and Yukawa unification: a correlation among the various Yukawa couplings arising at the level of the low energy effective theory. Supersymmetric grand unified theories (SUSY GUTs) are an extension of non-SUSY GUTs. They differ at the level of the low scale effective theory, because in the former the low energy theory is assumed to satisfy a supersymmetry.

The smallest simple group into which the SM can be embedded is **SU(5)**. The first attempt to embed the three groups of the SM into this unified group was done in the Seventies by Georgi and Glashow [220]. In this theory the irreducible representations accommodating the matter fields of each SM family fit into two representations, $\mathbf{10} = (Q, u^c, e^c)$ and $\bar{\mathbf{5}} = (d^c, L)$. In this setting the quarks and leptons transform among each other under the gauge symmetry, and the baryon and lepton numbers are violated in the interactions of the matter particles with the gauge bosons. The presence of quark, leptons and their antiparticles in the same multiplet, leads to charge quantization. There are also new interactions that connect quarks with antileptons and with antiquarks and lead to new phenomena such as proton decay.
The experimental bounds on the proton lifetime [221] and accurate measurements of $sin^2\theta_W$ lead to the claim that the simplest non-SUSY SU(5) is ruled out, even with two-loop corrections.

The supersymmetric version of SU(5) [189] is meant to provide the correct matching of the running gauge couplings at the GUT scale and display all the other features of SUSY theories. In that version, the SU(5) multiplets become chiral superfields which contain also the sparticles. The particle spectrum includes all the SM states, plus their supersymmetric

partners and at least one pair of Higgs doublets: one to give mass to up-type quarks, and the other to down-type quarks and charged leptons. Minimal SUSY SU(5) is however excluded, by bounds on the proton decay width [222].

Other popular GUT schemes deal with larger Lie groups like SO(10) and E_6. We will comment here on SO(10) SUSY GUTs, which will be the topic of part of the thesis.

3.1 SO(10) SUSY GUTs

Being **SO(10)** a larger symmetry group, it fits the SM matter particles to a single representation, the spinor $\mathbf{16} = \mathbf{10} + \bar{\mathbf{5}} + \mathbf{1}$ (at the SU(5) level), thus leading to complete unification of both gauge couplings and SM multiplets [220, 223]. This multiplet allows for an extra particle, which has the quantum numbers of a right-handed neutrino, and becomes very attractive to accomodate "seesaw" models of neutrino masses (see Section 4.3). Moreover, since the number of multiplets accommodating the SM fermions is reduced with respect to the case of SU(5), the flavor problem of SM is addressed in a stronger way because of more constrained sum-rules for the effective Yukawa couplings. Therefore, the renormalizable minimal SUSY SO(10) model is worth of receiving a particular attention, being perhaps the most predictive renormalizable GUT model [224, 225].

The SM matter multiplets are fitted in the 16 rep of SO(10) in the following way:

$$\begin{aligned} \mathbf{16}_F &= (1,2,-1) \oplus (3,2,1/3) \oplus (1,1,0) \oplus (1,1,2) \oplus (\bar{3},1,-4/3) \oplus (\bar{3},1,2/3) \\ &= L_L \oplus Q_L \oplus \nu_L^c \oplus e_L^c \oplus u_L^c \oplus d_L^c. \end{aligned} \tag{42}$$

This setting allows for the presence of right-handed neutrinos in a natural way, since they are accomodated in the same representation as all the other matter fields of the SM. Moreover, correlations among the effective Yukawa couplings that have the same origin at high scale, are stronger than in the SU(5) case, thus reducing the number of free parameters. SO(10) has other interesting characteristics, for instance the absence of anomalies: chiral symmetry must be preserved, and SO(10) is the smallest group which is free from anomalies in a single multiplet.

The SO(10) symmetry must be broken to the $SU(3)_C \times SU(2)_L \times U(1)_Y$ gauge group of the MSSM. The flavour structure of the Yukawa couplings of the matter fermions with the MSSM Higgs doublets are dictated by the structure of the gauge symmetry. Hence, the dimensions of the Higgs representations are given by the properties of Lie groups [226, 227]:

$$\mathbf{16} \otimes \mathbf{16} = \mathbf{10} \oplus \mathbf{120} \oplus \mathbf{126}. \tag{43}$$

These are the three types of SO(10) Higgs multiplets that can give masses to the matter fermions. In the minimal SUSY SO(10) model, two Higgs multiplets, namely the vector $\mathbf{10}_H$ and the antisymmetric tensor $\mathbf{120}_H$, are used for the Yukawa couplings with matter supermultiplet $\mathbf{16}_i$ [228–230]. Indeed, any combination of Higgs representations can be used as effective operator.

SO(10) Breaking chains		
SO(10)	$SU(4)_C \times SU(2)_L \times SU(2)_R$ $SU(3)_C \times SU(2)_L \times SU(2)_R \times U(1)_{B-L}$ $SU(5)$ $SU(5) \times U(1)_X$	$SU(3)_C \times SU(2)_L \times U(1)_Y$

Table 1.3: Most common SO(10) breaking chains down to the SM (MSSM) gauge symmetry at low energies.

One of the great successes of the SM are its perturbative predictions, then it is interesting to consider GUTs which are renormalizable. Regarding the spontaneous symmetry breaking of the SO(10) group, scalar superpotentials exist that break the SO(10) symmetry to the $SU(3)_C \times SU(2)_L \times U(1)_Y$ gauge group of the MSSM. To break SO(10) in a proper way, along one of the possible breaking chains which are shown in Tab. (1.3), at each intermediate scale there must be the Higgs multiplets which are responsable for the symmetry breaking to the subsequent stage. Namely, they must have neutral components that are completely neutral with respect to the lower symmetry group, since they will be those which will acquire vacuum expectation values. Furthermore the mass terms in the scalar part of the superpotential which are related to the symmetry breaking, have to develop the correct negative signs. To break SO(10) down to the low energy scale at least two (three in the SUSY GUT) Higgs representations acquiring VEVs are required. The Higgs sector is however quite strongly constrained by the requirements of renormalizability and supersymmetry, and minimality: the peculiar choice of the Higgs sector leads to the strong predictivity of the model, thanks to the small number of free parameters.

The Yukawa coupling terms in the SUSY SO(10) superpotential are given by

$$W_Y = Y_{10}^{ij} \mathbf{16}_i \mathbf{10_H} \mathbf{16}_j + Y_{126}^{ij} \mathbf{16}_i \overline{\mathbf{126}}_\mathbf{H} \mathbf{16}_j \ , \tag{44}$$

where $\mathbf{16}_f$ is the SO(10) matter supermultiplet, $\overline{\mathbf{126}}_\mathbf{H}$ and $\mathbf{10_H}$ are the Higgs multiplets and Y are complex symmetric Yukawa coupling matrices. The 10-representation is the simplest one and the 126-dimensional representation is more essential than the $\mathbf{120}_H$, which would be anyhow a possible choice. The $\overline{\mathbf{126}}_\mathbf{H}$ plays a double role, contributing to the symmetry breaking and in the mechanism generating the masses of the SM matter fermions. Once decomposed into its components under the next step gauge symmetry, the component which gets a vev capable of breaking the left-right symmetry, being a $SU(2)_L$ singlet, can also generate a Majorana mass for the neutrino through the Yukawa coupling of the $\overline{\mathbf{126}}_\mathbf{H}$ with the matter multiplet $\mathbf{16}_f$.
However, the Higgs multiplet $\overline{\mathbf{126}}_\mathbf{H}$ alone is not sufficient to explain all the stages of the symmetry breaking chain nor to generate the correct CKM mixing in the quark sector, hence another Higgs multiplet is required. We have actually two other possibilities from Eq. (43): the vectorial $\mathbf{10_H}$ and the antisymmetric tensor $\mathbf{120}_H$ representations. Moreover, in the SUSY SO(10) model, also the conjugate representation $\mathbf{126_H}$ is necessary, in order to cancel an additional D-term which can drive SUSY breaking at a higher scale ($>$ TeV). Still an additional contribution, for example from the **120**-dimensional representation, is

necessary to break properly the SU(5) subgroup symmetry.
Therefore, regarding the Higgs sector, we need at least two distinct Higgs multiplets in a SUSY SO(10) model to break the symmetry properly, throughout all the breaking chain down to the $SU(3)_C \times U(1)_Q$: a usual choice may be the $\overline{\mathbf{126}}_\mathbf{H}$ and the $\mathbf{210}_\mathbf{H}$ representations, plus the $\mathbf{126}_\mathbf{H}$ required to preserve the D-flatness of the supersymmetric vacuum (i.e. by requiring $\langle D^a \rangle = 0$). In addition, to fit the flavor structure of the CKM matrix, a further multiplet must be added, for example the $\mathbf{10}_\mathbf{H}$ or the $\mathbf{120}_H$.

Supersymmetric SO(10) GUTs then provide a viable and testable extension of the Standard Model [228, 231–237]. Indeed, the few parameters of the mass matrices imply the strong predictability of the minimal SO(10) model for low energy experiments [238]. Moreover, another feature of the minimal SUSY SO(10) model is the automatic R-parity conservation along all the symmetry breaking chains, down to low energy. It can also be embedded into string theory models.

3.2 Pati-Salam and left-right symmetries.

The first unification assumption in the literature was made by Pati and Salam (PS) [239] who proposed that lepton number was the fourth color, thereby enlarging the color group from SU(3) to SU(4). This partial unification of quark-leptons entails that one family of quarks and leptons can reside in two irreducible representations of a left-right symmetric group $SU(4)_C \times SU(2)_L \times SU(2)_R$:

$$(\mathbf{4}, \mathbf{2}, \mathbf{1}) = \begin{pmatrix} u_r & u_b & u_g & \nu_e \\ d_r & d_b & d_g & e \end{pmatrix}_L \tag{45}$$

for the left-handed fermions of the first family, where *r,b,g* are the color charges of quarks and leptons are seen as the fourth color. Equivalently, the right-handed fermions are accomodated in the representation $(\bar{\mathbf{4}}, \mathbf{1}, \mathbf{2})$.
The weak hypercharge is

$$Y/2 = T_{3R} + 1/2(B - L) \tag{46}$$

therefore in PS electric charge is quantized.
After the introduction of the PS model, it was realized that the group SO(10) actually contain PS as a subgroup and it can unify quarks and leptons into one irreducible representation, thus leading to a more complete symmetry. In effect, the $\mathbf{16}_F$ representation of SO(10) can be decomposed into:

$$\mathbf{16}_F = (\mathbf{4}, \mathbf{2}, \mathbf{1}) \oplus (\bar{\mathbf{4}}, \mathbf{1}, \mathbf{2}) \tag{47}$$

at the PS stage and into

$$\mathbf{16}_F = \mathbf{10} \oplus \bar{\mathbf{5}} \oplus 1 \tag{48}$$

under SU(5).

Left-right symmetric models The origin of left-right (LR) symmetric models hails from the tentative explanation of the observed left-handedness of weak interactions by means of symmetry breaking [240, 241]. Indeed, the asymmetry between left and right is a reflection of the chiral structure of weak interactions, and it is still not understood.

We may think about restoring parity at high energies. The minimal model which implements this idea is based on the gauge group $U(1)_{B-L} \times SU(2)_L \times SU(2)_R$, thus introducing new gauge bosons, partners of the weak bosons of the SM [242, 243]. Both left-handed and right-handed fermions are assigned to $SU(2)_L$ and $SU(2)_R$ doublets, as if parity was an unbroken symmetry of the theory. The LR symmetry is then broken spontaneously, either at high energy scale (which fits well with GUTs and neutrino mass models) or at low energy ($\sim$ TeV), which turns to be more interesting because of possible experimental probes. The LR breaking results in new gauge bosons, $W_R^{\pm}, Z_R$, more massive than the standard $W_L^{\pm}$ and Z^0. Sure enough, the new W_R boson cannot be arbitrarily light, according to the chiral nature of the SM.

LR models can be easily embedded in a SO(10) GUT theory, since the LR symmetry can be part of the symmetry breaking chain as shown in Tab. (1.3). One possible breaking chain of SO(10) GUT models is

$$\begin{aligned} SO(10) &\to SU(3)_C \times SU(2)_L \times SU(2)_R \times U(1)_{B-L} \\ &\to SU(3)_C \times SU(2)_L \times U(1)_R \times U(1)_{B-L}. \end{aligned} \tag{49}$$

Among the many features of left-right symmetric models there is the capability to explain the mass of light neutrinos through the seesaw mechanism (see Section 4.3), which can be naturally embedded in these kind of models. Moreover, this setting shows another appealing feature, being capable of stretching the LR symmetry breaking down to the TeV scale, thus resulting of interest for searches at colliders. We will deal with this kind of models in more detail in Chapter 3.

4 Models for neutrino masses

In this Section we will comment briefly on the theoretical models accounting for neutrino masses. Detailed reviews on this subject can be found for instance in [244–248].

4.1 Dirac or Majorana?

A **Dirac mass term** for the neutrino in the SM would mirror the mass term for the electron, meaning that neutrino masses have the same origin as the other fermion masses. However this implies a naturalness problem, being the upper bound for the neutrino mass so small (~ 1 eV) and the masses of the other particles much heavier. Ignoring for the moment this problem, we can describe a Dirac neutrino by a 4-component Dirac spinor ν, which can be written as

$$\nu = \begin{pmatrix} \chi \\ \sigma_2 \phi^* \end{pmatrix} \tag{50}$$

where χ and ϕ are 2-component Weyl spinors and σ_2 is a Pauli matrix. According to their chirality properties, left-handed and right-handed neutrinos are definded as:

$$\nu_L = P_L\,\nu \qquad \nu_R = P_R\,\nu \tag{51}$$

where $P_{L,R} = \frac{1}{2}(1 \mp \gamma_5)$ are the chirality projectors. Therefore, in terms of Dirac spinors we obtain:

$$\nu_L = \begin{pmatrix} \chi \\ 0 \end{pmatrix} \qquad \nu_R = \begin{pmatrix} 0 \\ \sigma_2 \phi^* \end{pmatrix}. \tag{52}$$

If we further apply charge conjugation to ν

$$\nu^c = C\bar{\nu}^T = -\gamma^2\gamma^0\bar{\nu}^T = \begin{pmatrix} \phi \\ \sigma_2 \chi^* \end{pmatrix} \tag{53}$$

we see that the Weyl spinors χ and ϕ get exchanged. The consequence is that for Dirac neutrinos the antiparticle does not coincide with the neutrino: $\nu \neq \nu^c$.

The Lagrangian Dirac mass term for neutrinos would have the form:

$$-\mathcal{L}_D^{mass} = m_\nu^D \bar{\nu}_L \nu_R + h.c. = m_\nu^D \bar{\nu}\nu \tag{54}$$

if three families of right-handed neutrinos ν_R, singlets under the SM gauge group, are added to the SM particle spectrum, with their corresponding Yukawa couplings. The mass term $m_\nu^D = Y_\nu \langle H \rangle$ would come from the Lagrangian term after electroweak symmetry breaking:

$$-\mathcal{L}_Y = Y_\nu H L \nu^R + h.c, \tag{55}$$

Dirac	Majorana
$\nu \neq \bar{\nu}$	$\nu \equiv \bar{\nu}$
4 states: ν_L ν_R $\bar{\nu}_L$ $\bar{\nu}_R$	2 states: ν_L $\bar{\nu}_R$
$-\mathcal{L} = m_D\left(\bar{\nu}_L\nu_R + \bar{\nu}_R\nu_L\right)$	$-\mathcal{L} = \frac{1}{2}m_L\left(\bar{\nu}_L\nu_R^c + \bar{\nu^c}_R\nu_L\right) + \frac{1}{2}m_R\left(\bar{\nu^c}_L\nu_R + \bar{\nu}_R\nu_L^c\right)$

Table 1.4: Dirac neutrinos versus Majorana neutrino properties.

where Y_ν is a 3×3 matrix. Being the vev of the Higgs $\langle H \rangle \sim 100$ GeV and the absolute scale for neutrino masses below $\sim$ eV, the entries in Y_ν must be below 10^{-11}. This value of the Yukawa coupling for the right-handed neutrinos means that they couple very weakly to the rest of matter, thus leading to negligible contributions to other phenomenological processes. But, as we said at the beginning of the discussion, the right-handed neutrinos are not included in the SM because, so far, weak-interaction experiments have not detected them.

Since the neutrino has no electric charge, it is possible to write down another kind of mass term, the so called **Majorana mass term**, which for right-handed neutrinos would have the form:

$$M_R\bar{\nu}_R\nu_R^c. \tag{56}$$

It is indeed possible to build Lorentz invariant theories with spinors that only have two independent components, instead of four as for Dirac spinors. This is achieved by using the mathematical formalism of 2-component Weyl spinors. It is possible to describe Dirac fermions in terms of 2-component pieces, in order to understand the relationship between Dirac and Majorana fermions.
A 4-component spinor Ψ can be split as Eq. (50), where χ and ϕ are two 2-component spinors and it can be shown that one Dirac fermion is equivalent to two Majorana fermions with the same mass but opposite CP.
Majorana neutrinos have been introduced by Majorana [249] many years ago. The Majorana mass term annihilates a left-handed neutrino and creates a right-handed antineutrino, which means that it changes a particle to an antiparticle. In doing so, this term violates the lepton number L, changing it by two units. Indeed, Majorana fermions cannot have conserved U(1) charges. It is nonetheless a valid mass term because it changes the handedness in the right way to yield a nonzero mass, and it conserves electric charge because the neutrino has no electric charge. Nevertheless, as already said, it cannot be included in the SM because it violates the weak symmetry twice, changing the hypercharge by two units and not being invariant under the weak isospin symmetry. Indeed, left-handed neutrinos are part of a lepton doublet L, and the Higgs field also forms a weak doublet H, and the $SU(2) \times U(1)_Y$ gauge invariance forbids a Yukawa interaction of the kind HLL.

The properties of the two types of masses are summarized in Tab. (1.4). The nature of neutrinos also has phenomenological implications. For example, neutrinoless double beta

decay is possible only if neutrinos are Majorana type [250, 251].

We will comment here on one of the most popular mechanism to give masses to neutrinos beyond the SM: the *Seesaw mechanism* [72, 252–256]. There are many possible realizations of the seesaw mechanism. They all lead to the same pattern of neutrino masses but differ in many other respects. In the following we will discuss the three main realizations of the seesaw mechanism.

4.2 Weinberg operator

Generic new physics which may explain neutrino masses but is too heavy for being directly studied manifests at low energy as non renormalizable operators (NRO), suppressed by heavy scales Λ. An effective operator is a NRO that summarizes the essential ingredients of a model. Talking about Majorana neutrino masses, the essential operator violates the lepton number by two units. Such an effective operator must integrate out all high energy new physics, in full analogy with the non-renormalizable dimension-6 Fermi operator in the theory of weak interactions (where the W boson is integrated out at low energy scales).
Let's assume then that there is new physics at a high scale Λ. It will manifest itself by some non-renormalizable operator suppressed by powers of E/Λ at energies $\mathrm{E} \ll \Lambda$. A dimension five operator has been introduced by Weinberg in the 70s [257] of the form:

$$\mathcal{O}_W = \frac{1}{\Lambda} L_i L_j H H \tag{57}$$

where L_i and L_j are lepton doublets, and H is the SM Higgs doublet

$$H = \begin{pmatrix} \phi^+ \\ \phi^0 \end{pmatrix}$$

.
It is the only dimension-5 operator consistent with the gauge symmetry of the SM, and it generates a Majorana mass term for neutrinos after EWSB, through the nonzero vacuum expectation value (vev) of the Higgs:

$$\mathcal{O}_W^{\nu\nu} = \frac{1}{\Lambda} \nu_i \nu_j \phi^0 \phi^0 \tag{58}$$

thus leading to the dependence $m_\nu \propto \frac{\langle v \rangle^2}{\Lambda}$, which is quadratic in the Higgs vev, in contrary to the rest of fermions whose masses result to be linear in v.
The underlying nature of the Weinberg dimension five operator is still unknown. We don't know which realization of the seesaw mechanism is the one which gives birth to this low scale operator, nor the associated energy scale.

4.3 Seesaw mechanism

We can have high ($\Lambda \sim 10^{14} - 10^{15}$ TeV) and low-scale ($\Lambda \sim$ TeV) realizations of neutrino mass models, depending on the mass of the messengers associated with the Weinberg oper-

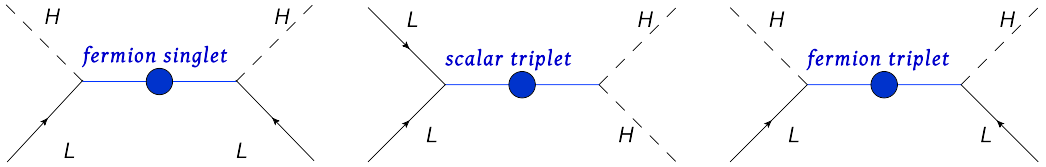

(a) Seesaw type I (b) Seesaw type II (c) Seesaw type III

Figure 1.5: Seesaw types

ator [258].

At tree-level, three different realizations of the Weinberg operator are possible:

- **Type I**: fermionic singlet [254, 259, 260]
- **Type II**: scalar triplet [72, 252, 253, 255, 261]
- **Type III**: fermionic triplet [256]

The one with the scalar singlet is not allowed, although doublets can be combined in singlets and triplets ($2 \otimes 2 = 1 \oplus 3$), because of symmetry reasons.

The most general approach to describe neutrinos is a combination of Dirac and Majorana mass terms.

Type I

A new fermion with no gauge interaction (a singlet) is added to the SM playing the role of the intermediate particle, a right-handed neutrino ν_R for instance, with mass M_{ν_R}. The Higgs and lepton doublets combine to form gauge singlets too. If Y_{ν_R} is the coupling $HL\nu_R$, we can write the mass term in the Lagrangian as:

$$\mathcal{L}_{\nu}^{mass} = -\frac{1}{2}\,(\bar{\nu}_L^c,\ \bar{\nu}_R)\, M \begin{pmatrix} \nu_L \\ \nu_R^c \end{pmatrix} + h.c. \tag{59}$$

being

$$M = \begin{pmatrix} 0 & m_{LR}^D \\ m_{RL}^D & M_{\nu_R}^M \end{pmatrix} \tag{60}$$

the mass matrix for the neutrino, where both Dirac mass terms m^D and Majorana mass terms m^M are present. The mass for the light left-handed neutrino is given by:

$$m_\nu = \frac{m_D^2}{M_{\nu_R}} = \frac{Y_{\nu_R}^2 v^2}{2M_{\nu_R}}. \tag{61}$$

The effective neutrino masses are much smaller than typical charged fermion masses.
In general, M_{ν_R} can be of any order, but there are two interesting extreme cases:

- *Pure Majorana neutrinos.* If $M_{\nu_R} >> Y_{\nu_R} v$ the diagonalization of the mass matrix gives three almost pure left-handed neutrinos with light Majorana masses $m_\nu = -m_D^T M_{\nu_R}^{-1} m_D$.

- *Pure Dirac neutrinos.* If $M_{\nu_R} = 0$ the mass matrix gives three Dirac neutrinos (pseudo-Dirac if $M_{\nu_R} << Y_{\nu_R} v$) with mass $m_\nu = Y_{\nu_R} v$. In this case the conservation of lepton number is restored. Nevertheless, to get the correct value of neutrino masses requires a Yukawa coupling of the order $Y_{\nu_R} \sim 10^{-12}$ much smaller than the other Yukawa couplings of the SM.

An alternative to the simplest type-I seesaw model, is obtained by extending the seesaw lepton content, by adding three extra SU(2) singlets S_i charged under $U(1)_L$. After electroweak symmetry breaking the mass matrix is:

$$M^\nu = \begin{pmatrix} 0 & m_D^T & M_L^T \\ m_D & 0 & M_R \\ M_L & M_R^T & \mu_S \end{pmatrix}. \tag{62}$$

in the basis ν, ν_R, S. When $M_L = 0$ and $\mu_S \neq 0$ it is called *inverse seesaw*, while when $M_L \neq 0$ and $\mu_S = 0$ we talk about *linear seesaw*. We will discuss these two kinds of seesaw mechanism in Chapter 4.

Type II

In this case a $SU(2)_L$ scalar triplet with hypercharge 1 is added to the SM, which we can call Δ. For instance, one can add one "Higgs" triplet Δ, composed by three components with charge $0, +1, +2$.
The Lagrangian mass term becomes:

$$\mathcal{L}^{mass} = -M_\Delta^2 |\Delta|^2 - \lambda_\Delta L \Delta L - \mu_h H \Delta H + h.c. \tag{63}$$

where we have omitted gauge and flavor indices for the sake of simplicity. Integrating out the heavy triplet generates the Majorana mass operator, $(LH)^2$ as in the previous case. The presence of both the terms $h_\Delta L \Delta L$ and $\mu_h H \Delta H$ breaks the lepton number by two units. When the Higgs field gets a vev v, as long as $M_\Delta >> v$ the light neutrino masses are generated:

$$m_\nu = \frac{\lambda_\Delta \mu_h v^2}{2 M_\Delta^2}. \tag{64}$$

The *seesaw mechanism* works also in this setting: the lightness of the left-handed neutrinos observed at low energies is again explained by the heaviness of another field, the triplet Δ.

Type III

Here, the H and L fields combine to form a fermion triplet and thus the intermediary particle must be a fermion triplet as well. The extra fermion Σ which is added to the SM is a $SU(2)_L$ triplet with zero hypercharge. The Lagrangian mass terms contain again flavor matrices:

$$\mathcal{L}^{mass} = -\frac{M_\Sigma}{2}\Sigma\Sigma - \lambda_\Sigma \Sigma L H + h.c. \tag{65}$$

The formal structure of this kind of seesaw is very similar to the structure of seesaw type-I. Indeed, everything works in the same way, and light neutrino masses are obtained:

$$m_\nu = \frac{\lambda_\Sigma^2 v^2}{2M_\Sigma}. \tag{66}$$

In conclusion, in this Chapter we have reviewed many interesting motivations for new physics beyond the SM and introduced some of the most promising theoretical extensions. We have also discussed possibile ways to experimentally test these scenarios, and commented about the present status of SUSY searches at the LHC. In the next Chapter, we will focus on WIMP DM searches.

CHAPTER

TWO

WIMP DARK MATTER SEARCHES

In Section 1.2 of the previous chapter we have introduced briefly some of the main DM candidates. In this thesis we will consider DM in the form of WIMPs. Therefore, for the sake of brevity, we will discuss here the search strategies for WIMP DM, and among them we will focus on the indirect detection. Indeed, indirect detection through γ-rays will be the topic of part II of this thesis.

WIMP DM particles are supposed to be bounded in the halo of our galaxy, which therefore represents a good place to look for relic WIMPs. The DM particles possess a matter density and velocity distributions which depend on the dynamics of the galaxy formation and evolution and which are subject to many uncertainties.
Experimental searches for DM relic particles depend on the particle physics properties of the DM particles, namely on their interactions with the SM particles. There are two approaches that take advantage of these interactions: (1) *direct detection:* the search for the interaction of DM particles with nuclei in underground detectors and (2) *indirect detection:* the search for the products of annihilations or decays of DM particles. Despite being very different, the two methods are complementary. Notably, a striking proof of the discovery of WIMP DM would be positive evidence seen with the two techniques.
Given a specific WIMP DM model, these observational channels can be related, as illustrated in Fig. 2.1. In addition, the figure relates these two techniques with the possible *direct production* of new particles in laboratory: usually at large colliders such as the LHC, or using specialized experiments (see Section 2.3 in Chapter 1). Nevertheless, the production of a new particle alone at accelerators is not sufficient to interpret it in terms of DM: only the interplay between the production at colliders and astrophysical observations could indeed lead to this interpretation.

1 Dark matter direct detection

WIMPs trapped inside our Galaxy can scatter off a nucleus in underground detectors, depositing about tens or hundreds of keV of kinetic energy, since their mean velocity relative to the galactic center is expected to be similar to that of galactic objects like stars, i.e.

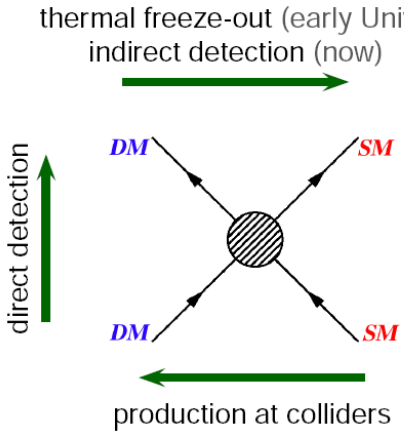

Figure 2.1: Basic scheme of different types of searches for DM, valid in absence of resonances and co-annihilations. The figure depicts the interaction of WIMP DM with SM particles. The cross sections for thermal production in the early Universe, for indirect detection and for direct detection are related to each other. Moreover, the production of new particles at colliders, which could be interpreted in terms of DM, is shown. Figure from (http://www.mpi-hd.mpg.de/).

$\sim 10^{-3}$c.
The direct detection rate of WIMPs depends on many parameters: on the particle physics side, the mass of the WIMP m_χ and its cross section on the target nuclei $\sigma_{\chi N}$, whereas on the astrophysics side, the local halo density ρ_0 and the velocity distribution of WIMPs in the galaxy $f(v)$. The differential rate is usually expressed in terms of counts/kg/day/keV [262]:

$$\frac{dR}{dE_R} = \frac{\rho_0}{m_N\, m_\chi} \int_{v_{min}}^{\infty} v f(v) \frac{d\sigma_{\chi N}}{dE_R}(v, E_R)\, dv\,, \tag{1}$$

where $\frac{d\sigma_{\chi N}}{dE_R}(v, E_R)$ is the differential cross-section for the WIMP-nucleus elastic scattering and v_{min} is the minimum WIMP velocity which can cause a recoil of energy E_R. For WIMPs which are gravitationally bound to the Milky Way the upper limit is actually the local escape velocity, that is the maximum speed in the galactic rest frame.
The WIMP-nucleus cross section is obtained starting from an effective lagrangian which describes the interactions of WIMPs with quarks and gluons:

$$\begin{aligned} \mathcal{L}_{AV} &= \chi\gamma^\mu\gamma_5\chi\; Q\gamma^\mu\gamma_5 Q \\ \mathcal{L}_{V} &= \chi\gamma^\mu\chi\; Q\gamma^\mu Q \\ \mathcal{L}_{S} &= \chi\chi QQ, \end{aligned} \tag{2}$$

where χ stands for the WIMP field and Q is the quark field. The former involves axial vector currents, while the other two involve scalar and vector (if the particle is not Majorana-type) WIMP and quark currents. The WIMP-nucleon cross section is then obtained through the use of the hadronic matrix elements, which although subject to large uncertainties, allow for the description of the nucleon content in terms of quarks and gluons. The WIMP-nucleon cross section can be separated in two contributions, one spin-independent and the other

spin-dependent. These two components are added through the inclusion of nuclear wave functions which finally give the total WIMP-nucleus cross section.
The axial-vector contribution in Eq. (2) gives a spin-dependent coupling, whereas the other two contribute to the spin-independent cross-section. The nucleus spin-dependent cross section depends on the nuclear spin factor **J**; the spin-independent cross section scales as $\sim A^2$ (for contact interactions and if the DM particle has the same coupling to protons and neutrons), the square of the mass of the nucleus.

Two experimental signatures are expected from WIMP signals in direct detection experiments: an annual modulation of the recoil rate due to the Earth speed variation, leading to a seasonal modulation and a daily forward/backward asymmetry of the nuclear recoil direction, due to the daily rotation of the Earth, namely the Earth's motion with respect to the Galactic rest frame [263].

Direct detection experiments can test a range of DM masses from a few GeV up to tens of TeV. Indeed, at low WIMP masses, the detector sensitivity drops because of the detector energy threshold. This leads to the need for low nuclear recoil energy threshold detectors. At high masses direct detection experiments actually tend to run out of sensitivity (with a linear decrease), due to the rate dependence on the inverse of the WIMP mass. Among many other parameters, the WIMP recoil rate depends on two factors: the total mass of the detector and the nuclear composition of the detector target. The best sensitivity is reached for WIMP masses close to the mass of the recoiling nucleus. Direct detection experiments usually make use of either Ge, Xe, Na, I, Si as target material.

In the last two decades the sensitivity of direct detection experiments has increased considerably, expecially in the low-mass range say below 100 GeV of mass. Nevertheless, DM has not been detected yet, although some intriguing signals have been reported, which might be attributed to DM (see later). There are nowadays many competing experiments all over the world: CDMS [264–267], CRESST [268], CoGeNT [269, 270], EDELWEISS [271], EURECA [272], DAMA [273], ZEPLIN-III [274], XENON [275, 276, 276, 277], COUPP [278], DRIFT [279], ArDM [280], WARP [281] and LUX [282].

The concept at the basis of direct detection experiments is to detect the recoil energy of nuclei hit by WIMPs which pass through the detector [206]. The scattering event will produce recoil energy which can be measured (through scintillation, ionization and heat depending on the target material and the detection technique) to extract information about WIMPs. However, the DM expected signal is much smaller than the background of muons, thus making this kind of experiments very challenging. The goal for these technologies is to shield the radioactive background, they are indeed installed underground to block cosmic muons, which would otherwise produce neutrons simulating the WIMP signals. Ideally these experiments can distinguish between the signal nuclear recoil and the background electron recoil. For a given deposited energy, the relative scintillation, ionization, or phonon signals (or a combination of them) are often different for electron and nuclear recoils and therefore allow for a discrimination. For instance, cryogenic detectors such as CDMS and CRESST operate at low temperatures ($\lesssim$ mK) and they can distinguish nuclear from electronic recoils using

different signals. In this kind of experiments the phonon response is used to determine the total recoil energy of an interaction, whereas a second detector response that is dependent on the type of recoil, such as scintillation (CRESST) or ionization (CDMS), provides information about the background.
Other experiments make use of noble liquid gas, such as XENON100, LUX, WARP, ArDM and Zeplin-III. The general principle behind this technique is that most of the noble gases, such as Xe, He and Ar scintillate from particle interaction. The scintillation light being not absorbed by the medium provides therefore a signal. Moreover, the outer layers of a large volume of liquid scintillator act as a self shielding, by absorbing external particles. This technology has also another variant which employs both a liquid and a gaseous phases (XENON100, LUX, WARP, ArDM). When a particle interacts with the liquid gas, it produces both a primary scintillation and electron-hole pairs; the electron then produce secondary ionization in the gaseous phase that leads to a secondary scintillation. Therefore, this technique utilizies both the scintillation and the ionization of the medium. Scintillation light signals are also produced in solid crystals proportionally to the amount of energy imparted to a recoiling electron. For instance, DAMA is an experiment that makes use of this technology.

We will now discuss some of the currently most important direct detection experiments, which are either currently running or have run in the last decade, and give very stringent constraints on WIMP cross sections. In particular, the most stringent constraints come from XENON100 and CDMS-II. Moreover we will comment about some experiments that have reported possible detection of signals, namely DAMA, CDMS-II, Cogent and CRESST.

CDMS The Cryogenic Dark Matter Search (CDMS) consists of a series of direct detection experiments started in 2002, located underground in the Soudan Mine in Minnesota [264, 265, 267]. The current experiment, CDMS-II, with its 5-kg Ge-Si target mass has set very sensitive limits on the interactions of WIMP DM with nuclei [265, 266].
CDMS belongs to the class of cryogenic detectors: it measures the ionization and phonons produced by every particle interaction in the germanium and silicon crystal substrates which it is made of. It can distinguish between WIMPs (or neutrons, which are nonetheless part of the background) and other charged particles because the ratio of ionization signal to phonon signal differs for particle interactions with atomic electrons and atomic nuclei. WIMPs are expected to produce these nuclear recoil. The two materials which compose the detector (Germanium and Silicon) can help with distinguishing between interactions from neutrons and those from WIMPs, since WIMPs are expected to have interaction rates depending on the mass of the nuclei. The low atomic mass of Silicium generally makes it a less sensitive target for spin-independent WIMP interactions: nevertheless, this material is advantageous in searches for WIMPs of relatively low mass.
The CDMS-II experiment gives a strong limit on the WIMP-nucleon cross-section above half the Z-boson mass, with the sensitive limit of $4 \times 10^{-44}\text{cm}^2$ for a WIMP mass of 60 GeV. It has been proposed to improve the CDMS series of experiments, with a larger detector called SuperCDMS [283, 284]. The sensitivity should increase by at least one order of magnitude.

XENON The XENON experiment [275–277, 285] makes use of a recent detector technology which contains liquid Xenon as the detector medium. It started in 2005 and it is placed at the Gran Sasso underground laboratory in Italy.
The principle behind this kind of dual-phase noble liquid detector, is that particle interactions inside noble gases such as Xenon produce scintillation and ionization. The scintillation light is then not absorbed by the medium, but can be extracted from large volumes of detector material. Moreover, if the volume of the liquid noble gas is very large, the inner part turns out to be almost entirely background-free, because the outer layers of the medium work as shields for the cosmic ray background. Apart from the scintillation light, the interaction of the WIMP with the noble gases creates electron-hole pairs. A strong electric field is then applied, to guide the electrons towards the part of the detector where the gaseous Xenon is held in equilibrium. There, the electrons produce ionization that leads to secondary scintillation. The secondary scintillation radiation is used to discriminate between electron (typical of gamma and beta radiation) and nuclear (typical of WIMPs and neutrons) recoils.
The first realization of the XENON experiment was called XENON10 and started in 2006 [275]. It did not find any WIMP signatures, but limits on WIMP-nucleon cross sections were set around 10^{-43}cm^2 for a 30 GeV WIMP mass. In 2008 the detector was updated to a larger version, XENON100 [276, 277]. Again, no DM signal was observed above the expected background, but the upper bound on the cross section has improved by one order of magnitude. Currently the project is getting improved to XENON1T [285], whose fiducial volume will contain 1 ton of liquid Xenon.

The LUX [282] detector is another example: it is a dual-phase 350 kg liquid xenon detector being commissioned in the Homestake mines, which aims to detect WIMPs with a spin independent cross section per nucleon of $\sim 10^{-46}\text{cm}^2$.

DAMA DAMA [286] is a direct detection experiment which uses radiopure scintillators (NaI, Xe) to search for WIMPs in the galactic halo. The first generation of detectors, DAMA/NaI [287, 288] operated from 1996 to 2002, whereas the 2nd generation DAMA/LIBRA has become operating in March 2003 [273, 289, 290].
DAMA/NaI was made up of almost 100 kg of low radioactive scintillating NaI(Tl) crystals. It was conceived to investigate the model independent annual modulation signature expected for DM. Indeed, due to its rotation around the Sun, the Earth should be exposed to a higher flux of DM particles in June 2 and to a smaller one in December. The experiment has been reporting since 1997 a positive model independent evidence of a cosine-like annual modulation signal which the collaboration claims to be compatible with the presence of DM particles in the galactic halo [286, 290–293].
The 2nd generation DAMA/LIBRA detector, has a larger target mass, $\sim$ 250 kg of highly radiopure NaI(Tl). This experiment, which is currently taking data, has further confirmed a peculiar annual modulation signal in the 2-6 keV energy region with all the characteristics typical of a DM-induced signal at 7.5 σ level. Including also the data from the first generation DAMA/NaI experiment the C.L. becomes 9.3 σ [286, 290].

We show in Fig. 2.2 the current upper limits on the spin independent cross section from

some direct detection experiments. Notably, we show the upper bounds from CDMS-II (Ge low threshold result) [265], CDMS-II (Silicon detectors upper limits) [267, 294], Edelweiss II [271], ZEPLIN-III [295], XENON100 [277] and the predictions for XENON 1T [285] and SuperCDMS [283]. We further show in the plot the regions of signal detections of CoGeNT [270] and DAMA/LIBRA [289]. Moreover, for the sake of illustration, we show in the plot the theoretical favoured regions for cMSSM and mSUGRA models [296, 297].

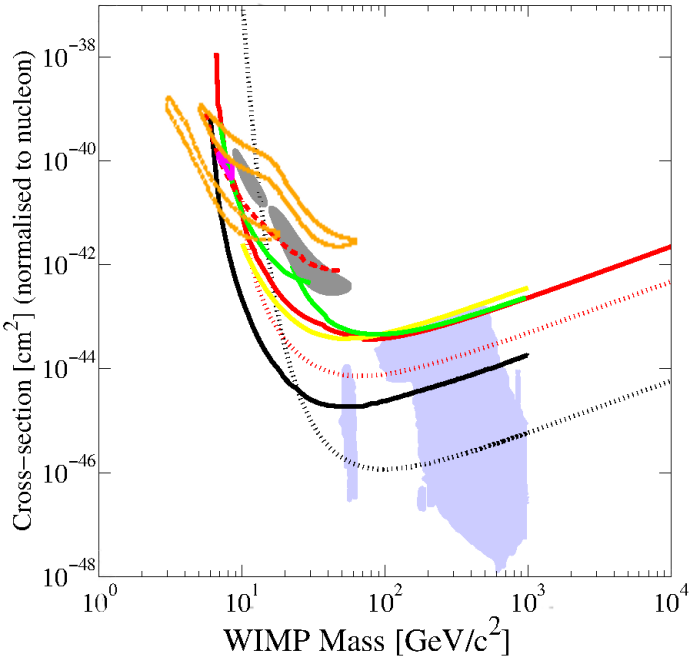

Figure 2.2: Plot showing results for direct detection experiments: summary of the latest results and future expectations for the bounds on spin independent cross section. In red (plain): CDMS-II (Ge low threshold result) [265]; red (dashed): CDMS-II (Silicon detectors upper limits) [267, 294]; magenta area: CoGeNT Annual Modulation Search [270]; orange regions: DAMA/LIBRA (with and without ion channeling) [289]; green (plain): Edelweiss II [271]; black (plain): XENON100 [277]; light blue area: frequentist analysis of the probable ranges for cMSSM and mSUGRA parameters [296, 297]; red (dotted): SuperCDMS (15 and 100 kg), proposal [283]; yellow (plain): ZEPLIN-III [295]; black (dotted): XENON 1T, predicted [285]. The cross section on the target nucleus has been renormalized to the equivalent cross section on a single nucleon in order to compare results from different direct search experiments. (Figure done with http://dmtools.brown.edu/)

There have already appeared intriguing signals that might be interpreted in terms of DM. We comment here briefly about these interesting although non definitive hints of DM particles.

1.1 Claims of possible detections of DM with direct detection experiments.

Some experiments, i.e. DAMA/LIBRA, CRESST, CDMS-II and CoGeNT, claimed anomalies in the data or even possible WIMP detection.
In the past decades many DM searches have been carried out focusing on WIMPs of mass in the range 100 GeV $< m_\chi <$ 1000 GeV. However some recent direct detection results have been pointing towards lighter particles, of mass $\sim$ 10 GeV, from observations of an excess of events over the expected background observed by CoGeNT, CRESST-II and CDMS-II, and the annual modulation signal seen by DAMA. Nevertheless, null observations by other leading experiments, such as XENON10, XENON100 and CDMS-Ge, set strong constraints thus leading to some tension with the previous results [277, 298–302].

The DAMA/LIBRA experiment [303], has reported a model independent positive evidence for the presence of particle DM in the galactic halo through the detection of a yearly modulation in the measured event rate. They observed an annual modulation signal with the maximum around June, as expected, in the 2 to 6 keV energy interval [286, 290]. The interpretation of this signal in terms of WIMP DM has raised many questions, concerning mainly the compatibility with other experiments. However, the DAMA collaboration claims that direct comparisons between experiments using different target materials is not straightforward, because it implies the consideration of scaling laws (to cross sections on nucleon for the different target nuclei). Moreover, other experiments like CDMS and XENON are not conceived for measuring the modulation signal. A further uncertainty which enters in the interpretation of these results is that one has to make assumptions in order to infer these constraints, for instance about the WIMP velocity distribution. In order to clarify the experimental situation, it would be necessary to follow a model independent approach. The issue of understanding the nature of the DAMA annual modulation has been widely studied in the literature [298, 299, 304]. Maybe the recent upgrade of the DAMA detector might help shedding light on this controversial situation.

The CoGeNT collaboration also reported an excess of low-energy events and annual modulation which could be explained in terms of a very light WIMP [269, 270]. The spectrum below 4 keV-electron equivalent exhibits an excess of events which is compatible with a light WIMP of mass $\sim$ 10 GeV. However, the CoGeNT collaboration has reported that there may be a possible instrumental inconsistency due to a higher estimate for the rate of non-rejected surface events near their energy threshold [300, 305].

The CRESST collaboration also claims an excess of events [268, 302], which is compatible with WIMPs of 10 and 30 GeV masses.

While no candidate events were found in the small data set from the first run of CDMS-II [294], a longer exposure of the CDMS-II Silicon detector [267] revealed three WIMP-candidate events with an expected total background of 0.7 events. Silicon detectors are a good choice to probe the light mass region of the parameter space because they have target nuclei with low mass number, and low energy threshold. The highest likelihood of this result

is found for a WIMP with mass ~ 8 GeV and a cross-section $\sim 10^{-41}\text{cm}^2$.

2 Dark matter indirect detection

Another DM detection technique consists in the search for the annihilation (decay) products of DM particles, such as photons, antimatter and neutrinos [87] as anomalous components in cosmic rays (CRs). The flux of such a radiation is proportional to the annihilation (decay) rate, which depends on the square of the DM density (or on the DM density in the case of DM decays). WIMPs are expected to annihilate very efficiently in regions of the surrounding universe where the DM density is high, like the galactic centre, dwarf spheroidal galaxies, and galaxy clusters, which therefore are good targets to look for indirect searches of DM.

Signatures of WIMP annihilation/decay are numerous, from neutrinos, to charged anti-particles (positrons, antiprotons and antideuterium) and photons (gamma rays, X-rays, synchrotron radiation). Any of the SM particles, quarks, leptons or gauge bosons can be the products of DM annihilation or decay. In annihilation processes the final state usually consists of a particle and its antiparticle. However, most of these particles decay rapidly, leaving as final products only stable particles.
Final states which consist of e^-, e^+ and μ^-, μ^+ can produce a hard $e^\pm$ spectrum and muons can also produce neutrinos. If WIMPs decay/annihilate into weak gauge bosons, gluons and quarks. The latter states hadronize, thus resulting in hadrons as final products, such as pions, protons and anti-protons, and eventually also deuterium and anti-deuterium nuclei. Neutral pions decay into γ-rays, whereas charged pions produce electrons, positrons and neutrinos. Taus can also decay hadronically to pions, thus leading to a γ-ray signal, or produce a $e^\pm$ spectrum and neutrinos. Final states with neutrinos only produce a neutrino spectrum, with a line feature if DM particles directly decay into neutrinos. If there is a photon in the final state the signal is a hard γ-ray spectrum either with a edge, or a line. Furthermore, any final state producing leptons can induce also secondary photon emissions through the Inverse Compton scattering (ICS) or as synchrotron radiation.

Obtaining convincing evidence for DM from astrophysical observations of annihilation (decay) products is quite a hard task, mainly because of the uncertainties that affect the astrophysical background. Likely, only a cross-correlation of multi-messenger signals could prove a DM detection, unless a *smoking gun* signal will come out (or will be confirmed, as for the claimed γ-ray line [306]). Concerning indirect detection, this for example could consist of mono-energetic photons from WIMP annihilation in space or high-energy neutrinos coming from the center of the Sun or Earth [87, 204].

2.1 Neutrino fluxes

Neutrinos can be an important product of WIMP annihilation. They have the advantage of propagating unabsorbed through the Galaxy and not being deviated by magnetic fields.

Moreover, they can cross dense objects with little interaction. They can be detected indirectly, through huge Ĉerenkov detectors located underground via the showers of secondary particles that they produce when interacting with the target material. The detector measures the Ĉerenkov light emitted by the charged particles (usually muons). The large muon background can be reduced by selecting only tracks which originate from neutrinos that come from the bottom, i.e. that have crossed the entire Earth. In this way experiments may detect neutrinos coming from DM annihilations in the Galactic halo or Galactic Center, or from satellite galaxies, although this kind of searches are usually less sensitive than other indirect detection channels. The non-observation of high-energy neutrino fluxes from the galactic center imposes constraints on the DM annihilation cross section.

Futhermore, neutrinos can originate from the center of the Sun or Earth. WIMPs may indeed slow down and be captured inside celestial bodies like the Earth or the Sun, thus enhancing their probability of annihilation [307]. WIMP annihilation processes include $\chi\chi \to t\bar{t}, b\bar{b}, c\bar{c}, ZZ, W^+W^-, \tau^+\tau^-$, which then decay into other particles among which are neutrinos with a mean energy $E_\nu \sim m_\chi/2 \div m_\chi/3$. Accumulation of the DM particles trapped by the gravitational potential well of the Sun for example, increases their number density, which can become large enough to produce detectable fluxes of neutrinos in neutrino telescopes like Super-Kamiokande [308,309], ANTARES [310], IceCube [311,312], MACRO [313], AMANDA [314]. Therefore, high-energy neutrinos ($\sim$ 1GeV $-$ 10 TeV) could be a signature of DM accumulated in the center of the Sun, since solar neutrinos produced in nuclear reactions have energies around MeV. The detection rate depends on many factors: the WIMP mass, the annihilation rate, and the density inside the celestial object. The differential neutrino flux is:

$$\frac{d\phi_\nu}{dE_\nu} = \frac{\Gamma}{4\pi d^2} \cdot \sum_i \frac{dN_i^\nu}{dE_\nu} B_i \,, \tag{3}$$

where d is the distance between the Sun and the Earth (or the Earth radius for neutrinos coming from the Earth), $\frac{dN_i^\nu}{dE_\nu}$ is the differential number of neutrino events for each channel, and B_i is the relative branching ratio and Γ is the annihilation rate which is related to the capture rate inside the Sun, assuming that the two rates reach, or nearly reach, the equilibrium inside the Sun. The capture rate is different for spin-dependent and spin-independent interactions.
Neutrinos are then observed by neutrino telescopes through their "muon tracks" produced in charged current interactions inside of or nearby the detector. For a neutrino flux $\frac{d\phi_\nu}{dE_\nu}$ the rate of muon tracks in a detector is [87]:

$$R_\nu = \int_{E_\mu^{thr}} dE_\nu \int_0^{1-E_\mu^{thr}/E_\nu} dy \; A(E_\mu) P_\mu(E_\nu, y; E_\mu^{thr}) \frac{d\phi_\nu}{dE_\nu} \tag{4}$$

where E_μ^{thr} is the muon threshold energy of the experiment, $A(E_\mu)$ is the effective area of the detector and $P_\mu(E_\nu, y; E_\mu^{thr})$ is the probability that a neutrino of energy E_ν interacts with a nucleon producing a muon of energy $E = (1-y)E_\nu$ above the detector threshold energy. This probability depends on the differential cross section for neutrino-nucleon charged-current scattering and on the "muon range", i.e. on the distance travelled by muons

before their energy drops below E_μ^{thr}.

These kind of searches, which look for DM captured in the Sun, are competitive with direct detection experiments for probing spin-dependent WIMP-proton scattering [315, 316]. Indeed, the non-observation of high-energy neutrino fluxes from the center of the Sun imposes constraints on the scattering cross section of DM particles with nuclei[1]. For instance, IceCube [316] has set recent upper limits on the DM annihilation rate, which then have been converted into limits on spin-dependent and spin-independent WIMP-proton cross-sections. Details about how neutrino limits are converted into bounds on spin-dependent and spin-independent cross sections, can be found in [317].

Other experiments like Super-Kamiokande [308,309] have set limits on WIMP DM, currently giving better results for lower WIMP masses than IceCube.
In the near future, the Precision IceCube Next Generation Upgrade (PINGU) will be able to cover the low-mass WIMP region and be competitive also in Galactic searches [318,319]. Moreover, low-threshold large water Cherenkov detectors, such as Hyper-Kamiokande [320], will improve the search in the low mass WIMP region due to a better sensitivity.

2.2 Light charged anti-matter in cosmic rays

Light charged anti-matter particles are more difficult to interpret as WIMP annihilation products, because being charged, they do not point directly back to the source where they originate, unlike neutrinos and gamma rays. Nonetheless, anti-matter particles can be an excellent signature of WIMP annihilation to look for, because they are much less abundant in the universe than the corresponding particles, and consequently the background is less important.

WIMPs bounded in the galactic halo may annihilate (or decay) into SM particles, which after decaying and through the processes of showering and hadronizing, give origin to fluxes of charged CRs. These charged particles, once produced in a given point of the galactic halo, propagate through the galactic magnetic field. The transport through the magnetic turbulences is described as a diffusion process. During their propagation to the Earth, these charged CRs may experience further energy losses due to synchrotron radiation, ICS, bremsstrahlung, Coulomb losses and nuclear spallations, depending on the particle species. While positrons are mostly affected by synchrotron radiation and ICS energy losses, for antiprotons the nuclear spallation is dominant. Therefore, the number density per unit energy dN_f/dE of the particle species f obeys a diffusion-loss equation [321] which contains terms accounting for the diffusion and the energy losses, as well as the source term accounting for DM annihilations (or decays). The latter, in case of DM annihilations, reads:

$$Q(E) = \eta \left(\frac{\rho}{m_\chi}\right)^2 \langle \sigma_{\rm ann} v \rangle \cdot \sum_i \frac{dN_f^i}{dE} B_i \,, \tag{5}$$

[1] Once an assumption is done between the relative balance between capture and annihilation (e.g. and typically, perfect equilibration between the two processes)

where m_χ is the mass of the DM particle, $\langle\sigma_{\rm ann}v\rangle$ is the WIMP annihilation cross section times the relative velocity, averaged over the DM velocity distribution. The sum runs over all primary channels i in which the CR species f is produced, B_i is the branching ratio into the final state f. Being E the energy of the secondary particle, $\frac{dN_f^i}{dE}$ is the energy distribution of the species f produced in a single annihilation. $\eta = \frac{1}{2}$ for a self-conjugate particle like a Majorana fermion or $\frac{1}{4}$ otherwise. ρ is the DM density distribution in the galactic halo. We will discuss about different DM density profiles in the introduction to Part II of this thesis. In case of decaying DM the injected spectrum of CR leptons per volume and time becomes:

$$Q(E) = \Gamma \left(\frac{\rho}{m_\chi}\right) \cdot \sum_i \frac{dN_f^i}{dE} B_i \,, \tag{6}$$

where Γ is the decay rate.

- **Positrons** An excess in the measured rate of the flux of cosmic positrons over the predicted rate could be due to the product of annihilations of DM. Hints of a rise in the positron fraction $\frac{e^+}{e^+ + e^-}$ at energies above ~ 10 GeV were present in the data of a spectrometer flown on a high-altitude balloon, the High Energy Antimatter Telescope (HEAT) [322] and also in the space-based spectrometer AMS-01 [323]. This behaviour was then confirmed by the precision measurements made firstly by the Payload for Antimatter Matter Exploration and Light-nuclei Astrophysics (PAMELA) [324] and then also by Fermi-LAT [325]. PAMELA's results generated great interest and speculations as to the origin of this positrons' excess.
  To explain the data in terms of DM, many ad-hoc candidates have been proposed [326–337]. If DM is the origin of this excess indeed, it must exhibit some characteristics in order to fit the data and not to be in contrast with other observations. Among these features, there is the need for very large boost factors (e.g., from Sommerfeld enhancement), in order to have a very large annihilation cross section to match the normalization of the positron ratio, ensuring that it still fits other cosmological constraints; moreover, either the DM is *leptophilic*, meaning it annihilates only into leptons or if DM particles annihilate also to weak gauge bosons and Higgs, or their mass must be heavier than TeV-scale. The latter requirement is due to anti-protons constraints: no excess in the $\bar{p}/p$ fraction has been measured by PAMELA [338], in the kinetic energy range between 60 MeV and 180 GeV. The result is in agreement with secondary production and propagation models. The constraints from antiproton data set very stringent limits both on annihilating and decaying DM [339–341].
  Concerning the theoretical candidates which could fit the positrons excess, new model building possibilities have been explored. Notably, regarding the possibility of getting a large annihilation cross section today ($\gtrsim 10^{-23}\mathrm{cm}^3\mathrm{s}^{-1}$), to fit the CR excesses, while keeping the smaller value of "natural" thermal cross section at the time of freeze-out, several possibilities of *boost factors* have been introduced. The enhancement of the production rate may indeed be achieved either via an *astrophysical* factor or via particle physics mechanisms. The astrophysical solution bears on the chance of achieving the enhancement through some overdensities in the DM density distribution, as

predicted by numerical simulations, although typical values are not large enough to explain the required boost factor. Another mechanism of enhancement is via a *resonant state*: if the resonance mass is just below twice the DM mass, the annihilation cross section becomes sensitive to the velocity of DM particles. Since the DM particles are moving much slower nowadays than at the epoch of thermal decoupling, the annihilation rate is enhanced because the resonant annihilation is more likely to occur [342–344]. Finally, maybe the most studied mechanism is the *Sommerfeld enhancement* [333,334,345–349]. This non-perturbative effect is well known in quantum mechanics since 1931, but it can occur also in DM annihilation when the DM particles annihilate with small relative velocity and exchanging a long-range interaction mediated by a particle of mass m_V. For the Sommerfeld enhancement to occur, there exists a relation between the mass of the DM, the mass of the force-mediator and the coupling constant: $\frac{m_{DM}}{m_V} \gtrsim \frac{1}{\alpha}$. The enhancement then depends on the kind of force and mediator (it has not necessarily to be a weak gauge boson, in which case the DM particle should be heavier than 10 TeV, but it can also be a new kind of force with light mediators). One of the features of the Sommerfeld enhancement is that it is inversely dependent on the velocity of DM particles and consequently it tends to saturate at large velocities. On the other hand, there are many significant modeling uncertainties in these DM scenarios, namely the propagation of charged particles through the Galaxy, the mass of WIMPs, and their interaction rates. However, besides DM annihilations, more standard astrophysical explanations of the positron fraction excess are possible. Notably, a proposal introduces nearby pulsars acting as accelerators and colliders that inject high energy positrons into the interstellar medium [350–354].
Very recently a much more precise measurement of the positron fraction at energies between 0.5 and 350 GeV has been made by the Alpha Magnetic Spectrometer (AMS-02) [355]. It confirms the excess of high-energy positrons in Earth-bound CRs: the positron fraction increases from 10 to 250 GeV. Positrons do not seem to show any preferred incoming direction nor a time variation. These results are in agreement with the DM-origin scenario. Nonetheless, the high precision of the AMS-02 experiment is not yet sufficient to discriminate between DM and pulsar origin of the rising positron fraction; more data are needed. Indeed, if the positrons have a DM origin, its number is expected to drop suddenly at some energy. This cut-off would be the "smoking gun" of DM and would indicate the mass of WIMPs because the positrons could not be created with more energy than the WIMPs' mass. Some recent works including the AMS-02 results, though, suggest that models in which the DM annihilates directly to leptons are no longer capable of producing the observed rise [354,356].

- **Antiprotons** Antiprotons may be produced by WIMP annihilation in the galactic halo. Indeed, when WIMPs annihilate into quarks or gauge bosons, $\bar{p}$ are produced in the hadronization process [2]. The background of antiprotons from galactic astrophysical sources is expected to be less important than the signal. Nevertheless, the estimate of the signal strength from antiprotons is affected by the uncertainty of the

[2]They can be produced even in leptophilic channels, taking into account electroweak corrections to the tree level production processes, if the DM mass is multi-TeV.

galactic propagation model, a process which involves both diffusion and energy losses, and of the solar wind modulation. Many works have been done on the topic, see for instance [340,357–360], and references therein. One among the most recent ones gives constraints from the current data from Pamela as well as explores the perspectives for AMS-02 [339].

- **Antideuterons** Antideuterons can also provide a useful indirect signature of DM annihilation [361]. The coalescence process of an antineutron and antiproton into an antideuteron is quite rare, however the secondary antideuteron background is even rarer, so antideuterons may constitute a clean signature for DM especially at low energies. A work about the status and the perspectives of this kind of searches has recently been published: near-future prospects of detection with AMS-02 and the General Antiparticle Spectrometer (GAPS) [362] are discussed in [363].

2.3 Gamma-rays from dark matter annihilations

In the last years, indirect γ-ray DM detection has evolved very rapidly, thanks to several experiments such as the Fermi-LAT space detector, and will keep on improving with new plans for a very large imaging air Cherenkov telescope array.

γ-rays can be produced by DM in different ways:

- **Prompt γ-rays**: are the direct product of DM annihilations.

  1. *γ-ray lines:* DM can directly annihilate in pairs into $\gamma\gamma$, γH, γZ, or into a photon and some new neutral state. This leads to monochromatic γ-rays with energy $E_\gamma = m_{DM}\left(1 - \frac{m_{Z,H}^2}{4m_{DM}^2}\right)$ or $E_\gamma = m_{DM}$ in the case of $\gamma\gamma$. This signal would give rise to a *line* as spectral feature, thus providing a striking evidence for DM, since astrophysical sources are unlikely to mimic this kind of signals. Unfortunatey, since the DM is neutral, this annihilation proceeds via loops of charged particles, or through some other mediators and consequently this annihilation channel is suppressed by $\mathcal{O}(\alpha_{em}^2)$. This makes the task of searching for this spectral feature quite hard because it is usually not actually visible against the continuous background, both of DM and astrophysical origin. However, this is not the only process giving rise to prompt γ-rays.
  2. *γ-ray continuum:* The hadronization and further decay of quarks as primary annihilation products leads to a continuum of γ-rays , essentially originating from the two-photon decays of neutral pions. The spectra for the different annihilation channels can be computed with event generators in a model independent way (see for example [364]). Secondary γ-rays show a featureless spectrum with a rather soft cutoff at the kinematical limit $E_\gamma = m_{DM}$.
  3. *Radiative emission* can be separeted into *Virtual internal bremsstrahlung (VIB)* and *Final state radiation (FSR).* Indeed γ-rays can arise also via bremsstrahlung from one of the internal particles in the annihilation diagram [365] (VIB), yielding

a sharp feature in the spectrum, that peaks at an energy corresponding to the DM mass. This emission is rather model-dependent. FSR photons are produced whenever the final products of WIMP annihilation are charged. It is dominated by collinear photons, thus most pronounced for light final state particles. This gives rise to a *continuum* of γ-rays which shows a peak at energies smaller than the mass of the DM and a sharp cut-off at $E_\gamma = m_{DM}$.

- **Secondary γ-rays**:

  1. *Inverse Compton Scattering*: the high-energy electrons and positrons, created in DM annihilations, can undergo ICS onto the low energy photons of the CMB, the galactic star-light and the infrared background. Photons are then upscattered at γ-ray energies. γ-rays from ICS also contribute to the continuum.
  2. *Bremsstrahlung*: the emission originates from the interactions of the electrons and positrons produced in DM annihilations with the electromagnetic fields of the atoms in the interstellar medium. The role of the bremsstrahlung in the computation of the overall DM γ-ray emission is particularly relevant for leptophilic DM candidates and for directions close to the Galactic plane, where the gas density is larger [366].

Most relevant targets for gamma-ray indirect detection Best targets to look at for γ-ray annihilation signals are DM dense objects and/or where the astrophysical background is low. However it is not easy to find such good targets which accomplish both the requirements at the same time. For instance: the Galactic Center (GC) is a higly dense target but unfortunately with a lot of background; therefore, it is usually preferred to look at small regions around it. Substructures (*subhalos*) of the galactic DM halo are predicted to exist by all CDM N-body simulations. If they exist, they are also dense targets. Dwarf spheroidal or other classes of satellite galaxies of the Milky Way, which are supposed to be DM dominated seem to be one of the preferred targets, because they have high DM density and small background. Wide regions of the galactic halo, from which a diffuse flux of γ-rays is expected, have a low density but they are affected by little background, especially if rings some tens of degrees wide in galactic coordinates are chosen to do the analysis [367]. Finally, large scale structures such as galaxy clusters can do a good job too, because they are quite dense objects and with little background, like dwarf galaxies. Another target to look at is the entire universe: γ-rays coming from all halos and subhalos do contribute to the so-called *extragalactic γ-ray background* which we will treat in detail in Part II.

- **Galactic center** Although the form of the density profile of DM in the central region of the halo is still unknown, the GC is perhaps the brightest source of γ-rays from DM annihilation (this is especially true assuming a cusped profile). The calculation of the γ-ray flux from DM annihilation in the GC implies the integration over a line of sight which necessarily crosses the galactic disk, which harbours high-energetic astrophysical processes which shade the DM contribution. The uncertainties related to the estimate of these processes makes the GC a challenging target to look at. Moreover, the DM distribution inside the galactic halo has many different parameterizations, which have

been obtained mainly by numerical simulations. They predict the same DM density value in location of the Solar system, but they differ most in the inner part of the galactic halo. We will discuss some of the well established DM density profiles in Part II.
Current limits on DM annihilation cross section have been inferred from observations of the GC [368–371] and these observations actually put the currently strongest limit for heavy WIMPs ($\sim$ 1 TeV): $\langle\sigma v\rangle \sim 10^{-25}\mathrm{cm}^3\mathrm{s}^{-1}$ [372].

- **Dwarf galaxies** Many of the uncertainties related to the GC can be avoided by looking at targets outside the galactic disk. Dwarf galaxies turn out to be an appealing target. They are satellite galaxies of the Milky Way, which are expected to be DM dominated, with poor astrophysical backgrounds (no active star formation nor hot gas) [373]. From measuring the velocity dispersion of stars in these satellites, the gravitational potential well is reconstructed and subsequently the DM density profile is inferred. This analysis allows to put stringent limits on the DM annihilation cross section [374, 375], which results to be bounded to values lower than the standard thermal cross section, for WIMPs of masses lower than few GeV. For heavier WIMPs, say of hundreds of GeV, the limits weaken.

- **Galaxy clusters** Galaxy clusters are the most massive virialized DM structures in the universe and are also good targets for indirect DM searches [376,377]. They may host a large population of DM substructures, as predicted by numerical simulations, which further enhance the detectability of DM in clusters through a boost factor. However little is known about the mass and spatial distributions of these subhalos, therefore limits obtained from galaxy clusters, although they can be very stringent because of the huge hierarchy of subhalos, are usually less robust than those obtained by dwarf galaxies. The most recent constraints obtained from this population are in principle stronger than those from dwarf galaxies, and they exclude the thermal cross section for WIMPs with masses up to 100 GeV ($b\bar{b}$ and $\tau^+\tau^-$ channels) [378], but they are affected by a large uncertainty in the modeling.

- **Galactic and extragalactic diffuse γ-ray emission** The diffuse γ-ray emission is supposed to consist of the truly diffuse galactic emission from the interstellar medium, the extragalactic background and the contribution from unresolved point sources. The former is the dominant component which has a wide distribution with most emission coming from the galactic disk.
The galactic diffuse non-thermal emission of γ-rays origins from the inelastic collisions of CRs with the interstellar gas. These collisions give birth to neutral pions, which then decay to γ-rays. Moreover, CR electrons and positrons produce γ-rays via processes like the bremsstrahlung with the interstellar gas and the ICS off the photons of the CMB.
Therefore, the diffuse galactic emission is closely connected to the production and propagation of CRs. The modelling of CR diffusion in the galaxy deals with the transport equation with a given source distribution and with boundary conditions for all CR species. Solving the transport equation requires the handling of the diffusion mechanism, the convection by the galactic wind, the treatment of energy losses, and

eventually, also accelerations. For a detailed study of the galactic diffuse γ-ray emission, we can refer to [379]. Uncertainties in the predictions of the hadronic contribution to the galactic diffuse emission have been addressed in [380].
The extragalactic diffuse γ-ray background emission (IGRB or EGB) is the component of the diffuse γ-ray emission which is most difficult to determine. It depends on the model adopted for the galactic diffuse background. Moreover, as we will discuss in Chapter 5, it contains an astrophysical contribution which is still unknown, but is believed to stem from unresolved point sources both galactic, such as pulsars and milli-second pulsars and extragalactic like blazars and star-forming galaxies.

Experimental searches in the γ-ray sky. Cosmic γ-rays can be viewed mainly from space, although above ~ 0.1 TeV their interactions with the atmosphere produce showers that can be detected by ground-based Ĉerenkov detectors through the light produced by the relativistic particles.
Concerning ground-based telescopes, Whipple was the first IACT (Imaging Air Ĉerenkov Telescope), then followed by four others which are arrays and can achieve larger effective areas, lower thresholds, and lower background: the High Energy Stereoscopic System (HESS), the Major Atmospheric Gamma Imaging Ĉerenkov telescope (MAGIC), and the Very Energetic Radiation Imaging Telescope Array System (VERITAS).
The HESS telescope [381] and VERITAS [382] are similar and complementary to each other, being situaded in opposite hemispheres. They are both made up of an array of IACTs. HESS is mainly sensitive to γ-rays in a range from tens of GeV to tens of TeV. The HESS collaboration has observed a strong γ-ray signal coming from the center of the galaxy, consistent with a point source [383]. It has then published many results about observations towards several different targets: the galactic center [383,384], the region coincident with the galactic plane of the Milky Way, called Galactic Ridge [385], the galactic center halo [372], dwarf galaxies [386, 387], globular clusters [388]. No statistically significant signal could be found in the HESS search for photon line-like signatures from DM annihilations [389], but only limits on the velocity-averaged DM annihilation cross section have been derived.
The VERITAS telescope also has observed the galactic center [390], some dwarf spheroidal galaxies [391, 392] and a galaxy cluster [393]. In the southern hemisphere there is also another telescope, the CANGAROO-III [394], whereas in the northen one the MAGIC telescope [395] in Canary island of La Palma, is currently taking data.
The IACTs have small fields of view, usually around 3-5 degrees. Therefore, they better point to known sources instead of scanning large regions of the sky. Space-based telescopes are better choices to look at more extended regions of the sky, although they have smaller effective areas. The Energetic Gamma Ray Experiment Telescope (EGRET) [396] was built in the Nineties to detect γ-rays in the low energy range (30 MeV to 30 GeV), in space. EGRET detected an anomalous signal in the diffuse galactic emission, notably an excess in GeV photons [397, 398] which was however not confirmed by later searches [399] and is thought to be due to instrumental problems.
In 2008 the NASA's Fermi Gamma-ray Space Telescope was launched [400]. Fermi includes the Large Area Telescope (LAT), a pair-conversion imaging γ-ray detector which detects photons with energy in the range 30 MeV to 300 GeV. It has a large field of view of 2.4 sr, which enables to look at a large portion of sky at once. The Fermi-LAT collaboration

has performed many interesting DM searches and published results about satellite galaxies [375, 401], the isotropic diffuse background [399], the galactic diffuse [402], clusters of galaxies [403] and γ-ray lines [404–406]. We will treat Fermi-LAT searches for DM in the isotropic diffuse background in better detail in Chapter 5.

From analysis of public Fermi-LAT data, many "claims" for DM have been made recently. Nevertheless, in all the cases the excesses or anomalies can be as well ascribed to astrophysical or instrumental origins. All of them can just be considered as tentative "hints", since most of the times these results are affected by uncertainties in the modeling of the astrophysical background or they are not confirmed by independent observations of the same signal in other regions or in other detection channels. For instance, an excess in the few GeV γ-ray energy region has been observed and eventually be associated to DM annihilation or to an astrophysical source (like Millisecond Pulsars), with origin in the Galactic Center [370, 407–410]. Moreover, a new extended source of GeV photons near the Galactic Center, above and below the galactic plane has been discovered [411]. It is labelled "Fermi Bubbles" and has a correspondence in the radio seen in WMAP data [412]. It consists of two defined regions, of several tens of degrees above and below the galactic plane, which seems to have origin by some process in the Galactic Center. However, the DM origin is not very favoured, while a CR origin is more probable [413].
A γ-ray excess from the Virgo cluster has also been measured [378]. Nonetheless, this result was considered highly uncertain from the beginning, because it depends on the estimate of the CR-induced photons, which, on the other hand, is not very accurate. A later analysis showed that accounting for some astrophysical point sources, previously not considered, the signal basically disappeared and it was instead possible to put quite strong constraints on the cross section for DM annihilation, which resulted to be even more stringent than those from dwarf galaxies [414].
In 2012 a quite strong claim was made, of an evidence of a (two) narrow line(s) in the γ-ray spectrum. The spectral feature observed is indeed compatible with what is expected for a narrow γ-ray line at 130 GeV (or corresponding to a DM mass of 150 GeV in the case of virtual internal bremsstrahlung). It has first been observed in the Galactic Center by using publicly available Fermi-LAT data by [306, 415]. The deduced annihilation rate is model-dependent, namely it depends on the DM density profile: it has been estimated $\sim 10^{-27}\mathrm{cm}^3\mathrm{s}^{-1}$. Later on, the literature on the topic has increased exponentially and similar claims have been made by other groups [416–419], with different significances. Even an evidence of two lines in galaxy clusters [420], at 111 and 130 GeV, was made. However, alternative explanations have been proposed [421–423], including a pulsar origin of the lines [424]. Furthermore, the Fermi-LAT collaboration did not find any globally significant lines in a bunch of regions selected to optimize sensitivity to different theoretically-motivated DM density distributions [406]. The effect has been intensely debated and it seems by now to be due to statistical fluctuation, although only the recollection of further data by the Fermi-LAT satellite will shed light on the "130 GeV line". If the DM origin should be confirmed, it would be natural to expect and then to observe also a γ-ray continuum at lower energies, due to the annihilation of DM particles into SM particles.

Summarizing, despite these "tentative" claims of DM evidence in the γ-ray sky, no signifi-

cant anomalous signals have been concretely observed by now. Concerning the near-future prospects of DM indirect detection through γ-rays, the next ten years will bring a plethora of new data. Indeed, present experiments, thanks to their increased sensitivity and accuracy, will allow to identify a signal or exclude many of the most common DM scenarios. Currently on-going experiments include Fermi-LAT, HESS-II, VERITAS and MAGIC. Planned telescopes like the ground-based Ĉerenkov telescope array (CTA) [425] and the space-based GAMMA-400 [426] will improve even more the DM searches, with their much better energy and angular resolution.

3 Further dark matter searches

3.1 Cosmological indirect searches

DM annihilations have an impact on some phases of the history of the universe, namely the Big Bang Nucleosynthesis (BBN) and the Cosmic Microwave Background (CMB), through the injection of energy and particles in the medium. Therefore, it is possible to infer quite strong constraint on DM annihilation cross section, very competitive with those from other indirect detection messengers.
Concerning BBN, the injection of electromagnetic radiation or high-energy hadrons in the medium by DM annihilations, can alter the formation of light nuclei [95, 427–429]. As a consequence, some of them may be destroyed or overproduced, thus leading to a different number of light elements which would be in contrast with observations. However the bounds set on the annihilation cross section by this kind of search, are not very stringent, being as weak as $\sim 10^{-23}\text{cm}^3\text{s}^{-1}$ for a TeV-scale DM.
CMB does a better job, setting more stringent constraints. The effect of energy injection at the recombination epoch would show up in the analysis of CMB anisotropies: the ionization of the gas would produce an increased amount of free electrons, which survive to later times and would affect the CMB anisotropies. The bounds depend on the annihilation channel, being the annihilation into e^+e^- the most effective in producing a sizable effect on the CMB. However, these constraints result to be very strong, even pushing the annihilation cross section much below the "standard" thermal value for light WIMPs [430–435].

3.2 Dark matter searches at colliders

In this paragraph we will discuss the possible production of a new particle at colliders, neutral and weakly interacting, which *might* be interpret as DM *only* if sustained also by astrophysical observations. Indeed, from this kind of accelerator measurements, we can just infer that the particles live long enough to escape the detector (a nanosecond). It is not possible to prove whether they are long-living enough to be the DM, that is to say stable also over cosmological timescales. Moreover it is not easy to infer information regarding their relic density, neither to prove that these particles form the DM which we observe in galactic halos, without an interplay with direct and indirect detection experiments.
A new particle which could be the DM may be discovered at colliders, notably at the LHC, as missing energy in an event. Indeed, they will not be observed directly once created because of their nature (they are comparable to neutrinos, being neutral and weakly interacting).

They are expected to be produced in decay chains of heavier particles. In the case of SUSY for example, they may come from the decay chain of some colored superparticles. However, it is possible to infer their existence from the missing energy when trying to reconstruct the decay chain. Another signature of new particles that could be candidates of DM can arise as events with a large amount of missing energy and a single jet or a single photon. Photons (or jets from a gluon) can indeed be radiated from quarks, giving monophoton (or monojet) plus missing transverse energy. This kind of searches at LHC as well as at Tevatron, has been translated into bounds on the production cross section of DM. In the framework of an effective field theory description of the interaction between DM and quarks and gluons, the bounds obtained at LHC have been shown to be competitive with those from direct searches, especially at low masses and for spin-dependent cross sections [436–441].
However, as of today no signal of new physics beyond the SM has been discovered at the LHC [436,438,442,443], which at present has been run at 8 TeV as the centre-of-mass energy. There is hope that this will not remain to be the case also in the future, when the energy should reach 14 TeV.

Part I

Phenomenology of SUSY GUT models

CHAPTER

THREE

SOFT MASSES IN SUSY SO(10) GUTS WITH LOW INTERMEDIATE SCALE

In this Chapter, based on [1], we will study the leading-log renormalization group equations (RGEs) evolution of the soft SUSY breaking parameters for four SO(10) GUT models with mSugra boundary conditions.
This work is motivated by the fact that the masses of SUSY particles like squarks and sleptons encode valuable information about the dynamics of the SUSY breaking, typically occurring at high energies. Moreover, further imprints in the soft SUSY spectra are left by new physics associated with some possible intermediate scale between the electro-weak (TeV) and the GUT scales. This may lead to interesting constraints about the new dynamics at the intermediate scales.

SUSY particle masses at TeV scale have to be calculated from the fundamental parameters of the models using RGEs. Although those fundamental parameters are a priori unknown, at least in minimal schemes there exist certain sum rules for SUSY particle masses, which allow to test the different SUSY-breaking mechanisms, as has been shown for the example of minimal Supergravity (mSugra) already some time ago [444]. Based on the detailed studies of the capabilities of the LHC and ILC experiments to measure SUSY particle masses [445–447], the accuracy with which different SUSY-breaking schemes can be tested has since then been calculated by a number of authors, for a few examples see [448–452].
However, most of these studies concentrated on models in which the particle spectrum between the electro-weak and the SUSY-breaking scale was exactly that of the Minimal Supersymmetric extension of the Standard Model (MSSM). Evolution under RGEs is, however, sensitive to the particle content of the theory. Thus, in principle, any superfield beyond the MSSM (with mass below the SUSY-breaking scale) will leave its imprint on the soft parameters. The specific shape of the squark, slepton and gaugino mass spectra, if measured with sufficient precision, can therefore provide invaluable information not only about the dynamics underpinning their origin, but also about physics at intermediate scales. In this Chapter, we study soft SUSY-breaking masses within certain classes of SUSY $SO(10)$ theories with different intermediate symmetries below the GUT scale $M_{\rm G}$. Our main motivation to study these models comes from the observed neutrino masses [21, 49, 453] and the possibility that

supersymmetry might be discovered soon at the LHC.
In the MSSM, if SUSY particles have TeV-scale masses[1], the gauge couplings unify (nearly) perfectly at around $M_G \sim 2 \times 10^{16}$ GeV. Adding new particles beyond the MSSM spectrum can easily spoil this attractive feature and, thus, the requirement of gauge coupling unification (GCU) imposes a severe constraint on SUSY model building. However, neutrino oscillation experiments [21, 49, 453, 456] have shown that at least two neutrino masses are non-zero [457,458] and at least one neutrino must have a mass $m_{\rm Atm} \geq 0.05$ eV. If neutrinos are Majorana particles, this value indicates that the scale of lepton number violation (LNV), $\Lambda_{\rm LNV}$, can not be larger (but could potentially be much smaller, see below) than roughly $\Lambda_{\rm LNV} \sim 10^{15}$ GeV. This value is significantly below M_G.
In the minimal SUSY $SU(5)$ model neutrinos are massless, just as in the MSSM and for the same reasons. However, it is fairly straightforward to extend minimal $SU(5)$ to include a seesaw mechanism which allows to explain the observed smallness of the neutrino masses. It is well known that, at the renormalizable level, there are exactly three ways [258] to do so: (i) Add (at least two) gauge singlet superfields, i.e. "right-handed neutrinos", this is now usually called type-I seesaw [259, 459, 460]; (ii) add a scalar triplet with $Y = 2$ (type-II seesaw) [72,253]; or (iii) add (two or more) *fermionic* triplets with $Y = 0$ (type-III seesaw) [256]. For the latter two cases, the successful unification of the MSSM can only be maintained if these heavy fields enter in complete $SU(5)$ multiplets. Thus, within SUSY models, GCU requires the type-II seesaw to be realized by adding a pair of Higgs 15-plets, while a type-III seesaw can be generated with (at least two) copies of 24-plets in the matter sector [258].
If we require Yukawas to be perturbative anywhere between the seesaw scale (i.e., $\Lambda_{\rm LNV}$) and the GUT scale M_G, all three types of seesaw require $\Lambda_{\rm LNV}$ to be below 10^{15} GeV. If we ask in addition that all gauge couplings remain perturbative, lower limits on SUSY type-II seesaw of the order of $\Lambda_{\rm LNV} \gtrsim 10^7$ GeV at 1-loop (or $\Lambda_{\rm LNV} \gtrsim 10^9$ GeV at 2-loop) [461] result. For type-III seesaw, perturbativity puts lower bounds on the seesaw scale of the order of $\Lambda_{\rm LNV} \gtrsim 10^{13}$ GeV for three copies of **24** of $SU(5)$ and around $\Lambda_{\rm LNV} \gtrsim 10^9$ GeV for two[2] copies of **24**. Since type-I seesaw adds only Standard Model (SM) singlets, there is no *lower* limit on its scale from perturbativity.
Models based on $SO(10)$ [223] are different from $SU(5)$ in that they automatically contain the necessary ingredients to generate non-zero neutrino masses: (i) The spinorial **16** of $SO(10)$ contains a complete SM family plus a gauge singlet, i.e. a right-handed neutrino. In addition, (ii) $U(1)_{B-L}$ is a subgroup of $SO(10)$. If the $U(1)_{B-L}$ is broken by $SU(2)_R$ triplets with $B - L = 2$, a seesaw mechanism of either type-I and/or type-II results automatically [460]. Alternatively, breaking $U(1)_{B-L}$ by $SU(2)_R$ doublets can give different realizations of the so-called inverse [207] and linear [208] seesaw schemes. The $SO(10)$ gauge symmetry can be broken to the SM gauge group in a variety of ways [463]. Since our main motivation is neutrino masses, all breaking chains of interest to us contain a left-right symmetry (LR) at some stage. SUSY LR models which use triplets to break $SU(2)_R$, whether using only

[1]Strictly speaking, within SUSY unification requires only gauginos to be light [454, 455], but not necessarily sfermions. We will not entertain this possibility.

[2]With only one copy of **24**, the seesaw scale could be lowered as far as the electro-weak scale. However, with only one **24**, neutrino data can not be explained unless non-renormalizable operators are added to the model [462].

$B-L=2$ triplets [464, 465] or both $B-L=2$ and $B-L=0$ triplets [466, 467], all require that the scale of $SU(2)_R$ breaking (v_R) is close to the GUT scale, typically $v_R \geq 10^{15}$ GeV from GCU. However, also in non-minimal versions of triplet-based models, one can not lower v_R arbitrarily, since one encounters either problems with proton decay or with perturbativity [468]. Allowing for either (a) sizeable GUT scale threshold corrections, (b) non-renormalizable operators or (c) adding some carefully chosen particles the authors of [469] find a lower limit on v_R of the order of $v_R \sim 10^9$ GeV.
However, the situation is different in models with doublets. It was shown in [470] that if one breaks $SU(2)_R \times U(1)_{B-L}$ by means of an $B-L=0$ triplet to $U(1)_R \times U(1)_{B-L}$ and, subsequently, the $U(1)_R \times U(1)_{B-L}$ symmetry gets broken down to $U(1)_Y$ by the Y-neutral components of $SU(2)_R$ doublets, it is possible to construct models in which the scale of $U(1)_R \times U(1)_{B-L}$ breaking, v_{BL}, can be as low as TeV. In [469] it was demonstrated that even the full $SU(2)_R$ can be brought down to the electro-weak scale, if only doublets are used in the symmetry breaking and if some additional particles are also light. An especially simple variant for a low v_R scale was discussed in [471]. Here, GCU is maintained for a TeV scale $SU(2)_R$ with only two requirements: (a) The numbers of light left and right doublets have to be different and (b) a (pair of) light coloured $SU(2)_L$ singlets needs to be added to the spectrum.
Obviously, all models with additional gauge groups lead to a potentially very rich phenomenology at the LHC. Current limits on new Z' (and W_R) gauge bosons are very roughly of the order of $m_{Z'} \gtrsim (5-6) * g$ TeV ($m_{W_R} \gtrsim 1$ TeV) [3] [473, 474], with exact numbers depending on the couplings, so there is ample room for discovery. One expects that for $\sqrt{s}=14$ TeV at the LHC limits for Z' bosons will improve to at least 3 TeV [475]. A W_R should be discovered at the LHC up to masses of the order of $4-4.6$ TeV [476,477], depending on luminosity. However, even if the new gauge bosons predicted in the models [469–471] are out of reach for the LHC, sparticle mass spectra will contain indirect hints for these new scales due to changes in the RGEs, as discussed above. This observation is in fact the main motivation for the calculations presented in this chapter.
Within the mSugra framework, one can define certain combinations of soft parameters, which are independent of the high scale input parameters at leading order. We will call such combinations "RGE invariants". In [478] it was pointed out that these invariants show a characteristic deviation from their mSugra expectations, if either a type-II or a type-III seesaw mediators are added to the MSSM spectrum. Here, we will study these invariants in different $SO(10)$ based models. We will construct variants of the models proposed in [470, 471] and will also consider a completely new model, in which v_R can be brought down to the electro-weak scale with the help of an intermediate Pati-Salam scale [239]. We will show how the RGE invariants calculated within these models depart from their mSugra values, how they differ from model to model and, importantly, also differ from the expectations for the minimal type-II and type-III seesaws. The invariants are therefore good indicators to distinguish between different GUT-based SUSY models.
Two comments might be in order at this point. First, our calculations rely on the assumption of strict mSugra boundary conditions. In principle, invariants can be calculated also in more complicated SUSY-breaking schemes, if the SUSY-breaking scale is larger than the

[3] These values were valid at the time of publication of this work. Current limits are: 2.86 TeV for a SM-like Z' and $m_{W_R} \gtrsim 1.8$ TeV [472].

mass scale of the new states. However, with a total of only four invariants (per generation) only SUSY-breaking schemes with very few additional parameters will lead to non-trivial consistency tests. Furthermore, while the invariants are certainly useful model discriminators, it has been shown that quantitatively important 2-loop corrections exist for both, the type-II [479] and the type-III seesaw [461]. A quantitative determination of the new intermediate scales will therefore most likely rely on a detailed numerical χ^2-analysis of measured SUSY spectra [480], using invariants only as guidance for which models might be interesting for further scrutiny.
The rest of the chapter is organized as follows. In the next Section, we shall specify four basic $SO(10)$ models of interest paying particular attention to their potential compatibility with the SM flavour structure. In Section III, we briefly comment on the evolution of the soft masses in mSugra models and, for completeness, recall the definitions of the RGE invariants, following essentially the discussion in [479]. The results of a simple analysis of their sensitivity to the intermediate scales in the four scenarios considered here are given in Section IV. Finally we close with a short discussion and outlook. Some technical details of the RGEs in models with more than a single abelian gauge factors are deferred to Section 5.

1 Specific SUSY SO(10) GUT models

Let us begin with a detailed specification of the four basic SUSY $SO(10)$ GUTs which shall be studied in Section 1.1. Though all of them, by construction, accommodate the low-energy measured values of the gauge couplings, they will in general yield vastly different MSSM soft spectra whose shapes would strongly depend on the character of the intermediate symmetries and the scales of their spontaneous breakdown.

1.1 General remarks

In all cases, we demand that the models should be realistic in several basic aspects and potentially interesting for our scope, namely:

- Requirement 1: SUSY $SO(10)$ unification with a sliding intermediate scale by which we mean that the position of a certain intermediate scale can be moved over a large energy range whilst the full compatibility with the electroweak constraints is maintained. This is a basic practical stipulation in order to be able to study the scale-dependence of the soft leading-log RGE invariants in such GUTs over a large range.

- Requirement 2: Renormalizable SUSY $SO(10) \to$ MSSM gauge symmetry breaking - this is namely to have in principle calculable thresholds.

- Requirement 3: Potentially realistic fermionic spectra - we demand that the effective Yukawa structure is rich enough to be able, at least in principle, to accommodate the low-energy matter-fermionic spectra and mixing. The sliding nature of the $SU(2)_R \times U(1)_{B-L}$ scale, however, typically calls for a non-canonical seesaw, such as inverse [207] or linear [208] seesaw. We will discuss these two types of seesaw mechanism in detail in Chapter 4.

- Requirement 4: MSSM Higgs doublet structure suitable for the implementation of the standard radiative symmetry breaking and also as a means to get unrelated Yukawa couplings for quarks and charged leptons.

As to the Requirement 1 above, we shall be namely interested in SUSY $SO(10)$ models with a sliding $SU(2)_R$ breaking scale which would be assumed to range from as low as several TeV up to essentially the GUT scale. From the gauge unification perspective, there are two basic strategies to devise such Models. In practice:

- One can attempt to compensate for the departure of the b-coefficients in the RGEs from their "canonical" MSSM values (due to the presence of $W_R^{\pm}$ and the $SU(2)_R$-breaking Higgs multiplets in the desert) by other multiplets brought down to the $SU(2)_R$-breaking scale, which would inflict further shifts to the b-coefficients (namely g_3) in order to compensate for the genuine low-scale $SU(2)_R$ effects. The main advantage of this approach is that $SU(2)_R \times U(1)_{B-L}$ becomes the only intermediate scale at play, so the $SO(10)$ gauge symmetry is broken down to the $SU(3)_c \times SU(2)_L \times U(1)_Y$ of the MSSM in just two steps. The slight complication here is the fact that the gauge-coupling unification in such a case is not exact, which brings an extra theoretical uncertainty into the game. [4]

- Alternatively, rather than compensating for the departure of the b-coefficients from their MSSM values due to the $W_R^{\pm}$ (and the associated Higgs multiplets) in the desert, one can take advantage of this and invoke an extra intermediate scale such as for instance $SU(4)_C \times SU(2)_L \times SU(2)_R$ of Pati and Salam and let it conspire with the $SU(2)_R \times U(1)_{B-L}$ so that the gauge unification is maintained. Though this can be somewhat more elaborate in practice, the clear advantage of such a scenario is that one can always devise an exact gauge coupling unification by a proper adjustment of the Pati-Salam scale.

In both cases, because we have quite a lot of beyond-MSSM dynamics in the desert, we expect significant effects of the relevant intermediate scale(s) on the shape of the MSSM squark and slepton spectra.
The first strategy above, especially in combination with the other requirements, is rather restrictive. Indeed, it imposes strict conditions on the b-coefficients in specific models which should essentially match those of the MSSM up to a uniform shift. Nevertheless, a variety of potentially realistic models can still be devised and, in particular, the behaviour of the RGE invariants in this class of theories can be strongly model-specific. We shall demonstrate this on a couple of scenarios of this kind derived from [471], c.f., Model I and Model II in section 1.2.
The sensitivity to the intermediate-scales dynamics should be even more pronounced in the latter class of scenarios with more than a single such scale at play. This is namely due to the fact that the extra fields in the desert associated to a higher intermediate symmetry (e.g., Pati-Salam) tend to affect the soft spectra stronger than in the former case with an intermediate $SU(3)_c \times SU(2)_L \times SU(2)_R \times U(1)_R$ only. This feature is going to be clearly visible in the specific model of this kind, c.f., Model III in section 1.2.

[4] This feature is already present at the MSSM level.

Field	Multiplicity	$3_c 2_L 2_R 1_{B-L}$	$SO(10)$ origin
Q	3	$(3,2,1,+\frac{1}{3})$	**16**
Q^c	3	$(\bar{3},1,2,-\frac{1}{3})$	**16**
L	3	$(1,2,1,-1)$	**16**
L^c	3	$(1,1,2,+1)$	**16**
S	3	$(1,1,1,0)$	1
δ_d, $\bar{\delta}_d$	1	$(3,1,1,-\frac{2}{3})$, $(\bar{3},1,1,+\frac{2}{3})$	**10**
Φ	1	$(1,2,2,0)$	**10**, **120**
χ, $\overline{\chi}$	1	$(1,2,1,\pm 1)$	$\overline{\mathbf{16}}$, **16**
χ^c, $\overline{\chi}^c$	3	$(1,1,2,\mp 1)$	$\overline{\mathbf{16}}$, **16**

Table 3.1: The relevant part of the field content of Model I with a sliding $SU(2)_R$-breaking scale discussed in Section 1.2. In the third column the relevant fields are characterized by their $SU(3)_c \times SU(2)_L \times SU(2)_R \times U(1)_{B-L}$ quantum numbers while their $SO(10)$ origin is specified in the fourth column.

However, a strong dependence of the invariants on the sliding scale should not be viewed as a generic feature of the SUSY $SO(10)$ GUTs. Indeed, there are simple scenarios in which the sliding intermediate scale does leave almost no imprints in the soft spectrum. We shall demonstrate this in a specific model with a sliding intermediate $U(1)_{B-L}$ scale (and a fixed $SU(2)_R$ scale at around 10^{14} GeV ensuring a proper gauge unification) of the kind given in [470], c.f., Model IV in the section 1.2. Here, the GUT-scale pattern of the RGE invariants is (almost) not changed by the running, leaving no good handle on the intermediate scale in the SUSY spectrum.

1.2 SUSY $SO(10)$ models with a sliding $SU(2)_R$ scale

Models I and II: single sliding intermediate scale

First, we shall introduce two variants of the model advocated in [471] which supply the original setting with a few extra ingredients in order to make it potentially realistic, c.f., Sect. 1.1.

Model I: The field content relevant to the running in this model is specified in Tab. (3.1). The original $SO(10)$ gauge symmetry is broken down to the MSSM in two steps via an intermediate $SU(3)_c \times SU(2)_L \times SU(2)_R \times U(1)_{B-L}$ symmetry stage. The first step, i.e., the $SO(10) \to SU(3)_c \times SU(2)_L \times SU(2)_R \times U(1)_{B-L}$ breaking, is triggered by an interplay between the VEVs of **45** and **210** of $SO(10)$. Subsequently, the $SU(2)_R \times U(1)_{B-L}$ gauge symmetry is broken down to the $U(1)_Y$ of hypercharge by the VEVs of the $\chi^c \oplus \overline{\chi}^c$ pair which can emerge for instance from its cubic interaction with a full singlet ρ[5]. Note that, at the one-loop level, such a neutral ρ field can be put essentially anywhere between M_{GUT} and

[5]It is perhaps worth mentioning that, for a very low scale of the $SU(2)_R \times U(1)_{B-L}$ breaking, the relevant VEV can be devised even without an extra singlet because, then, the interplay between a "RH μ-term" for $\chi^c \oplus \overline{\chi}^c$ and the relevant soft mass should be sufficient, in complete analogy with the $SU(2)_L$-doublet sector in the MSSM.

M_{SUSY} without any impact on the gauge unification. The b_i-coefficients at the $SU(3)_c \times SU(2)_L \times SU(2)_R \times U(1)_{B-L}$ level read $b_3 = -2$, $b_L = 2$, $b_R = 4$ and $b^{\rm c}_{B-L} = 13$ where the last number corresponds to the canonically normalized $B-L$ charge, which is obtained from the "physical" one (based on $B^{\rm p}_Q = +\frac{1}{3}$ and $L^{\rm p}_L = +1$) by means of the formula $(B-L)^{\rm c} = \sqrt{\frac{3}{8}}\,(B-L)^{\rm p}$. Note that these coefficients happen to be entirely identical to the setting advocated in [471] and, thus, the leading-log evolution of the soft SUSY-breaking parameters in that model is covered by our analysis of Model I, see Section 3.1. The scale of the $SU(2)_R \times U(1)_{B-L}$ breaking is not determined because it drops from the formula for the unification scale (owing namely to the hypercharge-matching condition $\alpha_Y^{-1} = \frac{3}{5}\alpha_R^{-1} + \frac{2}{5}\alpha_{B-L}^{-1}$) and affects only the value of the GUT-scale gauge coupling α_G which, however, is subject to much weaker constraints. More precisely, consider the RGE master equation:

$$\alpha_i^{-1}(\mathrm{t_a}) = \alpha_{\rm i}^{-1}(\mathrm{t_b}) + \frac{\mathrm{b_i^{a-b}}}{2\pi}(\mathrm{t_b} - \mathrm{t_a}), \tag{1}$$

where i = Y, R, B-L, 3, t_X stands for $\ln(\mathrm{v_X})$ being $\mathrm{v_X}$ the energy scale, b_i^{a-b} are the b-coefficients in the regime $[\mathrm{t_a}, \mathrm{t_b}]$ and $\mathrm{t_a} < \mathrm{t_b}$. The values of the coupling constants at the m_Z scale are known [473]. Let us use a matrix notation to specify the gauge couplings C_X. At the GUT scale for instance, $C_0 = \mathrm{diag}(\alpha_{\rm GUT}^{-1}, \alpha_{\rm GUT}^{-1}, \alpha_{\rm GUT}^{-1}, \alpha_{\rm GUT}^{-1})$. Define also $\gamma_R = \mathrm{diag}(\mathrm{b^R_{B-L}}, \mathrm{b^R_L}, \mathrm{b^R_3}, \mathrm{b^R_R})$ in the first regime $[\mathrm{v_R}, \mathrm{v_{GUT}}]$ and $\gamma_{MSSM} = \mathrm{diag}(\mathrm{b_L^{MSSM}}, \mathrm{b_3^{MSSM}}, \mathrm{b_Y^{MSSM}})$ in the second regime $[\mathrm{v_{SUSY}}, \mathrm{v_R}]$. Finally, the $\mathrm{v_R}$ matching condition is contained in

$$p = \begin{pmatrix} 1 & 0 & 0 & 0 \\ 0 & 1 & 0 & 0 \\ 0 & 0 & \sqrt{3/5} & \sqrt{2/5} \end{pmatrix}. \tag{2}$$

Then, in the three regimes $[\mathrm{m_Z}, \mathrm{v_{SUSY}}]$, $[\mathrm{v_{SUSY}}, \mathrm{v_R}]$, $[\mathrm{v_R}, \mathrm{v_{GUT}}]$, the one-loop gauge coupling running is described by:

$$\begin{aligned} C_R &= C_0 + \gamma_R(\mathrm{t_{GUT}} - \mathrm{t_R})/(2\pi); \\ C_{MSSM} &= p.C_R.p^T + \gamma_{MSSM}(\mathrm{t_R} - \mathrm{t_{SUSY}})/(2\pi); \\ \alpha_i(\mathrm{t_{SUSY}}) &= \alpha_i(\mathrm{m_Z}) - \mathrm{b_i^{SM}}(\mathrm{t_{SUSY}} - \mathrm{m_Z})/(2\pi). \end{aligned} \tag{3}$$

Equate $\alpha_2^{-1}(t_{GUT}) = \alpha_R^{-1}(t_{GUT})$ expressed in terms of the known values at the Z scale to get the value of the GUT scale:

$$\begin{aligned} t_{GUT} &= 1/(3b_R^R - 5b_L^R + 2b_{B-L}^R) \;\; ((10\pi)(\alpha_{B-L}(m_Z) - \alpha_L(m_Z))] \\ &+ \mathrm{t_R}\ (2\mathrm{b^R_{B-L}} - 5\mathrm{b^R_L} + 3\mathrm{b^R_R} + 5\mathrm{b_L^{MSSM}} - 5\mathrm{b_{B-L}^{MSSM}}) \\ &+ 5\mathrm{t_{SUSY}}\ (\mathrm{b_L^{SM}} - \mathrm{b_Y^{SM}} - \mathrm{b_L^{MSSM}} + \mathrm{b_Y^{MSSM}}) \\ &+ 5\mathrm{t_Z}\ (\mathrm{b_Y^{SM}} - \mathrm{b_L^{SM}})). \end{aligned} \tag{4}$$

It can be easily checked that the coefficient in front of $\mathrm{t_R}$ is zero.
This, on one hand, makes the gauge coupling unification in Model I qualitatively similar to the MSSM case, see Fig. 3.1. On the other hand, it is well known that in the MSSM the one-loop gauge unification is incompatible with the latest determinations of α_s unless the soft SUSY-breaking scale is pushed well below 1 TeV. This few percent mismatch is

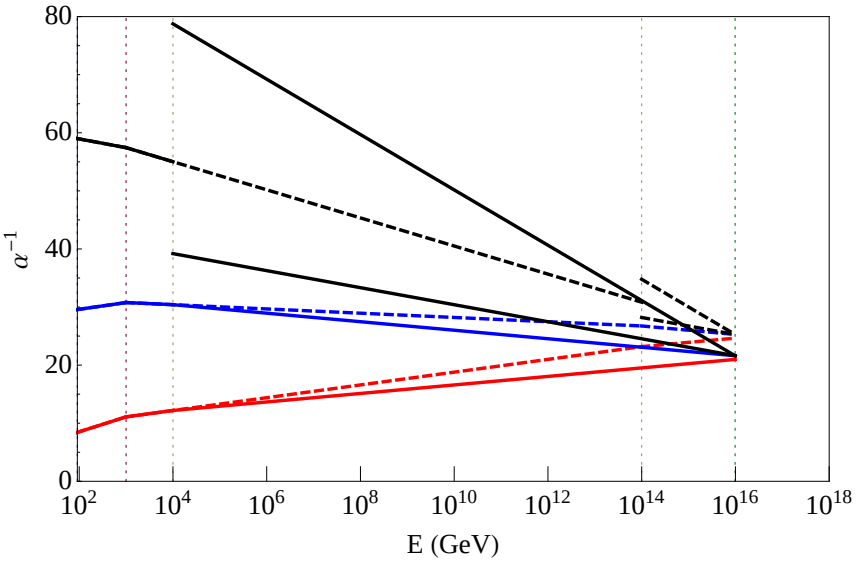

Figure 3.1: Gauge coupling unification in Model I in two limits corresponding to different positions of the sliding $SU(2)_R \times U(1)_{B-L}$ breaking scale V_R. In solid lines, we depict the RGE behaviour of the gauge couplings for V_R in the vicinity of the electroweak scale $V_R \sim 10^4$GeV while the dashed lines correspond to $V_R \sim 10^{14}$GeV. The position of the intersection region shifts slightly up with rising V_R but the corresponding scale remains intact.

expected to be accounted for by GUT-scale threshold corrections whose detailed analysis is, however, beyond the scope of this work. Thus, in what follows, we shall simply parameterize our ignorance of the shape of the GUT spectrum by considering unification regions from where the $SU(3)_c \times SU(2)_L \times SU(2)_R \times U(1)_{B-L}$ gauge couplings can emanate rather than unique unification points, c.f., Fig. 3.6 and discussion in Section 3.1. Though this approach is oversimplified in several aspects, it allows to estimate the magnitude of the theoretical error associated to the lack of exact gauge-coupling unification in this model.

Concerning the effective flavour structure of the model, there are two aspects worth some discussion here, namely, the structure of the effective MSSM Higgs doublet pair Φ and the possibility to accommodate the SM quark and lepton masses and mixing (requirements 3 and 4 formulated at the beginning of this Section). First, the effective L-R bidoublet $(1,2,2,0)$ corresponds to a massless combination of the $(1,2,2)$ and $(15,2,2)$ Pati-Salam components of **10** and **120** of $SO(10)$, respectively, which can mix at the GUT-level due to the PS-breaking VEV in an $SO(10)$-breaking multiplet such as **45** and/or **210**. Usually, the role of the extra Higgs such as **120** and/or **126** in the Yukawa sector is namely to provide Clebsch-Gordan coefficients that would break the degeneracy of the effective Yukawa couplings among up and down quarks and charged leptons. However, an extra **120** alone is still not enough as it does not yield enough freedom to accommodate the SM data [481]. Actually, the issue becomes even worse if the MSSM-level mass matrices for the two hypercharge components of Φ are virtually identical, as one can expect for a single bidoublet at play in the low-scale $SU(2)_R$-breaking regime. Both issues are potentially resolved due to the extra vector-like down-type quark pair $\delta_d \oplus \overline{\delta}_d$ and an additional $SU(2)_L$-doublet Higgs pair $\chi \oplus \overline{\chi}$ (which,

Field	Multiplicity	$3_c 2_L 2_R 1_{B-L}$	$SO(10)$ origin
Q	3	$(3,2,1,+\frac{1}{3})$	**16**
Q^c	3	$(\bar{3},1,2,-\frac{1}{3})$	**16**
L	3	$(1,2,1,-1)$	**16**
L^c	3	$(1,1,2,+1)$	**16**
S	3	$(1,1,1,0)$	1
δ_u, $\bar{\delta}_u$	1	$(3,1,1,+\frac{4}{3})$, $(\bar{3},1,1,-\frac{4}{3})$	**45**
Φ	1	$(1,2,2,0)$	**10**, **120**
χ, $\overline{\chi}$	1	$(1,2,1,\pm 1)$	$\overline{\mathbf{16}}$, **16**
χ^c, $\overline{\chi}^c$	2	$(1,1,2,\mp 1)$	$\overline{\mathbf{16}}$, **16**

Table 3.2: The same as in Tab. (3.1) for Model II defined in Section 1.2. The main variation with respect to Model I is the $B-L$ charge of the vector-like colour triplet pair owing to its different $SO(10)$ origin. The extra δ_u and $\bar{\delta}_u$ fields can mix with the up-type quarks at the MSSM level which leads to a potentially realistic effective flavour structure. In order to maintain the MSSM-like unification pattern, the number of the $SU(2)_R$ doublets has been reduced, thus making the setting slightly more compact than in Model I.

simultaneously, ensure the right b-coefficients for the running), c.f., Tab. (3.1). In this case, the down-type quark mass matrix is extended[6] to 4×4 which, together with the extra freedom in the MSSM doublet sector, should be enough to avoid the Grimus-Kuhbock-Lavoura (GKL) no-go theorem [481]. Let us also mention that the VEV of χ_L gives rise to the LS entry in the neutrino mass matrix generating the linear seesaw mechanism and, unlike in [470], it is not naturally suppressed in this case because $\chi \oplus \overline{\chi}$ resides well below the GUT scale. Thus, one has to assume a small $LS\chi$ Yukawa coupling.

Model II: The relevant b_i-coefficients at the $SU(3)_c \times SU(2)_L \times SU(2)_R \times U(1)_{B-L}$ level read $b_3 = -2$, $b_L = 2$, $b_R = 3$ and $b^{\rm can}_{B-L} = 29/2$. Indeed, these numbers differ from Model I only in the $SU(2)_R \times U(1)_{B-L}$ sector and the variations in the relevant b-coefficients obey $\Delta b_R + \frac{2}{3}\Delta b_{B-L} = 0$ so the b-coefficient associated to the "effective" MSSM hypercharge is the same as in Model I. Therefore, apart from the difference in the specific slopes of the $SU(2)_R \times U(1)_{B-L}$ curves the qualitative picture of the gauge coupling unification in Model II, c.f. Fig. 3.2, is very similar to that observed in Model I. Nevertheless, as we shall see in Section 3.1, even such a slight change in the gauge-coupling behaviour at the $SU(3)_c \times SU(2)_L \times SU(2)_R \times U(1)_{B-L}$ level is enough to generate a significant difference between the Model-I and Model-II soft invariants, especially if the $SU(3)_c \times SU(2)_L \times SU(2)_R \times U(1)_{B-L}$ running is long. However, if the $SU(2)_R \times U(1)_{B-L}$ gauge symmetry happens to be broken close to the GUT scale, the two models will be indistinguishable from the soft-sector point of view.

Concerning the flavour structure of Model II, it is indeed very similar to that of Model I, with the main difference that here the GKL no-go [481] is overcome by a 4×4 extension of the up-type quark mass matrix. Moreover, since it is the VEV of $\overline{\chi}$ rather than that of χ that enters the extended up-type quark mass matrix, $\langle\chi\rangle$ can be made much smaller than

[6] For an explicit $SO(10)$ realisation of this mechanism see e.g. [482] and references therein.

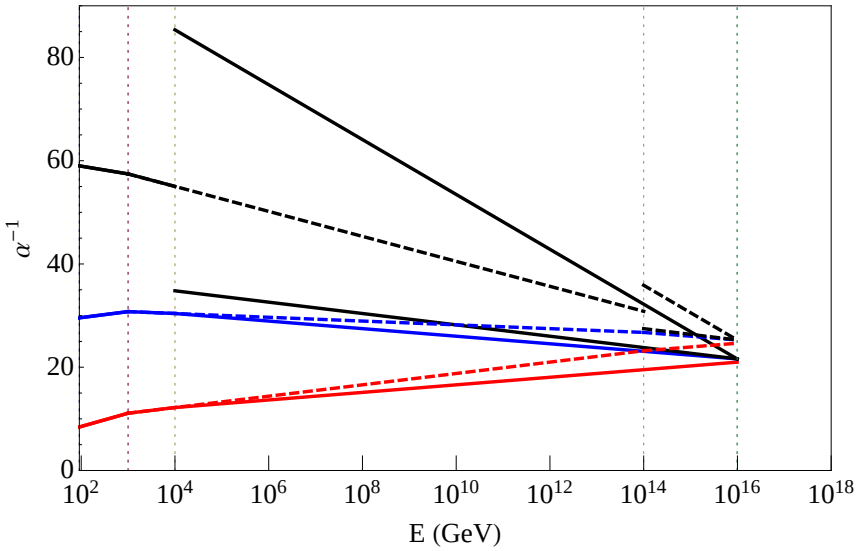

Figure 3.2: Gauge coupling unification in Model II in two limits corresponding to different positions of the sliding $SU(2)_R \times U(1)_{B-L}$ breaking scale V_R. In solid lines, we depict the RGE behaviour of the gauge couplings for V_R in the vicinity of the electroweak scale $V_R \sim 10^4$GeV while the dashed lines correspond to $V_R \sim 10^{14}$GeV. The position of the intersection region shifts slightly up with rising V_R but the corresponding scale remains intact.

$\langle\overline{\chi}\rangle$ which also relieves the need for the small $LS\chi$ Yukawa in the neutrino sector. Given also the reduced number of the $SU(2)_R$ doublets, Model II constitutes a somewhat more compact alternative to Model I.

Model III: sliding $SU(2)_R$ and Pati-Salam scales

The third model of our interest belongs to the second category of the simple classification given in Section 1.1. In particular, the sliding nature of the $SU(2)_R \times U(1)_{B-L}$ scale is achieved via an interplay with another intermediate scale, namely, the Pati-Salam $SU(4)_C \times SU(2)_L \times SU(2)_R$, rather than a delicate adjustment à la Model I or Model II owing to very specific field contents. Thus, the initial $SO(10)$ gauge symmetry is broken down to the MSSM in three steps. The field content relevant to the two intermediate-symmetry stages is given in Tab. (3.3). In more detail, the initial $SO(10) \to SU(4)_C \times SU(2)_L \times SU(2)_R$ breaking is triggered by the GUT-scale VEV of 54 of $SO(10)$. The subsequent $SU(4)_C \times SU(2)_L \times SU(2)_R \to SU(3)_c \times SU(2)_L \times SU(2)_R \times U(1)_{B-L}$ breaking is due to the VEV of the Ψ emerging again from its interplay with an extra singlet. Finally, the $SU(2)_R \times U(1)_{B-L}$ symmetry is broken down to the MSSM by means of the VEVs of $\chi^c \oplus \overline{\chi}^c$ which are connected by the $B-L$-neutral $SU(2)_R$-triplet Ω. At the Pati-Salam stage, the b_i-coefficients read $b_4 = 3$, $b_L = 6$, $b_R = 14$ while at the $SU(3)_c \times SU(2)_L \times SU(2)_R \times U(1)_{B-L}$ level they are $b_3 = -2$, $b_L = 3$, $b_R = 11$ and $b^{\rm can}_{B-L} = 10$.
In this model, both the position of the GUT scale as well as the value of α_G depend on both intermediate scales. However, unlike in Models I and II, here the gauge unification can always be made exact, c.f., Fig. 3.3, even at the one-loop level, and, thus, there is no

Field	Mult.	$3_c 2_L 2_R 1_{B-L}$	Pati-Salam	$SO(10)$
Q	3	$(3,2,1,+\frac{1}{3})$	$(4,2,1)$	**16**
Q^c	3	$(\bar{3},1,2,-\frac{1}{3})$	$(\bar{4},1,2)$	**16**
L	3	$(1,2,1,-1)$	$(4,2,1)$	**16**
L^c	3	$(1,1,2,+1)$	$(\bar{4},1,2)$	**16**
Σ^c	3	$(1,1,3,0)$	$(1,1,3)$	**45**
δ_d, $\bar{\delta}_d$	1	$(3,1,1,\mp\frac{2}{3})$	$(6,1,1)$	**10**
Φ	2	$(1,2,2,0)$	$(1,2,2)$	**10**
Ω	1	$(1,1,3,0)$	$(1,1,3)$	**45**
χ, $\overline{\chi}$	1	$(1,2,1,\pm 1)$	$(\bar{4},2,1)$,$(4,2,1)$	$\overline{\mathbf{16}}$, **16**
χ^c, $\overline{\chi}^c$	1	$(1,1,2,\mp 1)$	$(4,1,2)$,$(\bar{4},1,2)$	$\overline{\mathbf{16}}$, **16**
Ψ	1	absent	$(15,1,1)$	**45**

Table 3.3: The effective field contents of Model III in the two intermediate symmetry stages.

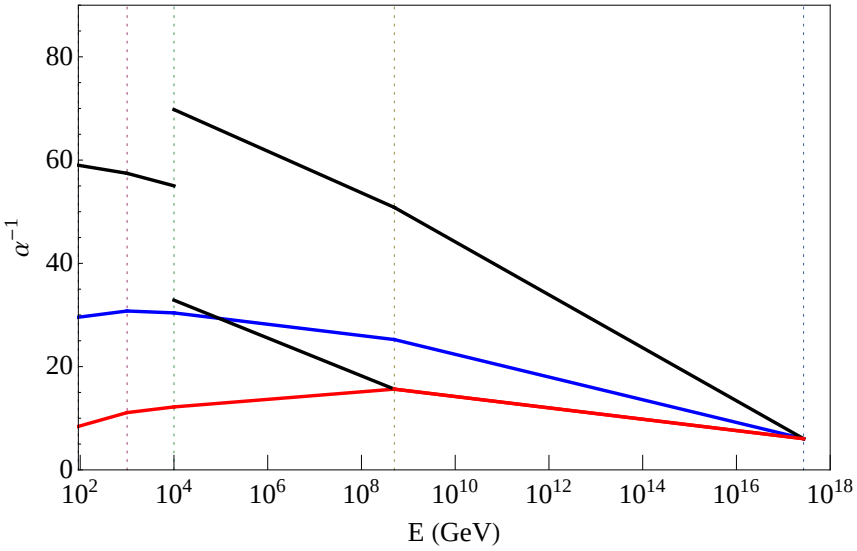

Figure 3.3: Running in the Model III variant of the low-LR scale SUSY SO(10). Here the SO(10) gauge symmetry is broken first into a Pati-Salam intermediate stage stretching from the unification point down to the relevant energy scale V_{PS} (in the middle) and, subsequently, to the L-R symmetry stage. The value of V_{PS} is correlated to the position of the L-R breaking scale V_R which can again slide from as low as few TeV up to roughly 10^{14}GeV, c.f., Fig. 3.9.

extra theoretical uncertainty other than the error in the electroweak-scale α_s to be taken into account.

The flavour structure of this model relies on the presence of three extra copies of $SU(2)_R$ triplet Σ^c which in the neutrino sector play a role similar to that of S in Models I and II. In particular, they expand the 6×6 neutrino mass matrix to 9×9 where, e.g., the $L^c\Sigma^c$ sector comes from the contraction with the VEV of χ^c, but without any entry generated at the $L\Sigma^c$ "linear seesaw" position. Thus, there is no need for an extra fine-tuning in the seesaw

formula in Model III. Moreover, the charged components of Σ^c can mix with the charged leptons and, hence, provide the welcome departure from the down-type quarks even if the MSSM doublets span over 10's of $SO(10)$ only. Indeed, the relevant 6×6 charged-lepton mass matrix looks schematically like

$$M_\ell \propto \begin{pmatrix} Y v_d^{10} & 0 \\ \langle \overline{\chi}^c \rangle & \mu_{\Sigma^c} + \langle \Omega \rangle \end{pmatrix} , \tag{5}$$

where the row and column bases are $\{L, \Sigma^{c-}\}$ and $\{L^c, \Sigma^{c+}\}$, respectively, and μ_{Σ^c} is the associated singlet mass parameter. Note also that the VEV of Ω is antisymmetric in the generation space and, thus, does not contribute to the neutrino Majorana mass matrix. Finally, the two MSSM Higgs doublets are different because the underlying bi-doublets are contracted through Ω and, therefore, the effective up-type quark Yukawa coupling differs from the down-type one even without the need to resort to the mixing with the vector-like $\delta_d \oplus \bar{\delta}_d$ pair.

1.3 SUSY $SO(10)$ models with a sliding $U(1)_R$ scale

All the models discussed so far featured an intermediate $SU(2)_R \times U(1)_{B-L}$ symmetry which, at a certain scale, was broken directly down to the $U(1)_Y$ of the MSSM hypercharge. The full $SU(2)_R$, however, is not the minimal option to realize a gauge symmetry acting in the RH sector of the matter spectrum in a way compatible with the MSSM quantum numbers. Indeed, the hypercharge sum-rule $Y = T_R^3 + (B-L)/2$ trivially holds even if one sticks to the $U(1)_R$ subgroup of the original $SU(2)_R$ generated by T_R^3 alone.
On the other hand, within $SO(10)$ broken down to an intermediate $SU(3)_c \times SU(2)_L \times U(1)_R \times U(1)_{B-L}$ stage, only Z' and the associated $U(1)_R \times U(1)_{B-L} \to U(1)_Y$-breaking Higgs fields remain light (at least in minimally fine-tuned scenarios) and, thus, the intermediate-scale dynamics is generally much simpler than in the models based on the full $SU(2)_R \times U(1)_{B-L}$. In view of that, one can expect that also the intermediate-scale dependence of the soft RGE invariants will be much milder than in the former case. Moreover, with more than a single abelian gauge factor at play, there is a new class of effects associated with the so called kinetic mixing between the associated gauge fields. Both these aspects make this class of models worth further scrutiny.

General remarks

Remarkably, the simplicity of the minimally fine-tuned $U(1)_R \times U(1)_{B-L} \to U(1)_Y$ scenarios automatically implies the scale of this spontaneous symmetry breakdown is a sliding one. Indeed, minimal fine-tuning implies that the spectrum of the Model in the unbroken phase consists of that of the MSSM plus Z' plus an MSSM-neutral Higgs responsible for the relevant symmetry breaking. Since the gauge field associated to the hypercharge (B_Y) does not feel any effect of either Z' nor the hypercharge-neutral Higgs[7] the "effective" hypercharge gauge coupling (corresponding to a relevant combination of g_Y and g_R) in this picture runs as if it were in the MSSM, at least at the one-loop level. Thus, the specific position of the

[7] To put this statement on a firm ground the effects of the kinetic mixing must be considered, see, e.g., [483].

Field	Mult.	$3_c2_L1_R1_{B-L}$	$3_c2_L2_R1_{B-L}$	$SO(10)$
Q	3	$(3,2,0,+\frac{1}{3})$	$(3,2,1,+\frac{1}{3})$	**16**
Q^c	3	$(\bar{3},1,\pm\frac{1}{2},-\frac{1}{3})$	$(\bar{3},1,2,-\frac{1}{3})$	**16**
L	3	$(1,2,0,-1)$	$(1,2,1,-1)$	**16**
L^c	3	$(1,1,\pm\frac{1}{2},+1)$	$(1,1,2,+1)$	**16**
S	3	$(1,1,0,0)$	$(1,1,1,0)$	1
Φ	2	$(1,2,\pm\frac{1}{2},0)$	$(1,2,2,0)$	**10**
Ω	1	absent	$(1,1,3,0)$	**45**
χ, $\overline{\chi}$	1	absent	$(1,2,1,\pm1)$	$\overline{\mathbf{16}}$, **16**
χ^c, $\overline{\chi}^c$	1	$(1,1,\pm\frac{1}{2},\mp1)$	$(1,1,2,\mp1)$	$\overline{\mathbf{16}}$, **16**

Table 3.4: The effective field contents of Model IV relevant to the two intermediate symmetry stages.

$U(1)_R \times U(1)_{B-L} \to U(1)_Y$ breaking scale is, in this case, irrelevant for the one-loop gauge running.
This, however, is not the case for the leading-log soft RGE invariants of our interest. In particular, unlike B_Y, both the $U(1)_R \times U(1)_{B-L}$ gauge bosons enter the renormalized propagators of squarks and sleptons, shown in Fig. 3.4, and one can expect a residual

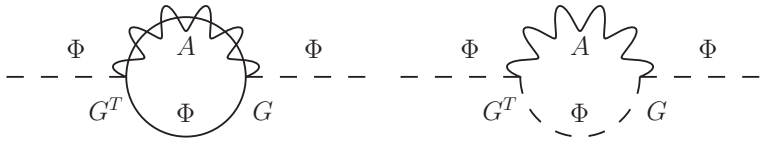

Figure 3.4: Renormalized propagators of squarks and sleptons.

dependence of the invariants on the $U(1)_R \times U(1)_{B-L}$-breaking scale. In Fig. 3.4 the U(1) gaugino field and the quark (lepton) field enter the first loop, while the U(1) gauge boson and the squark (slepton) field enter the second one. Nevertheless, as we shall demonstrate in a particular realization of this simple scheme, such effects should be much milder than those in the scenarios with the full gauged $SU(2)_R$ symmetry.

Model IV: $U(1)_R \times U(1)_{B-L} \to U(1)_Y$ breaking

Here we consider a variant of the basic SUSY $SO(10)$ model advocated in [470] in which an extended intermediate $U(1)_R \times U(1)_{B-L}$ stage follows a short $SU(2)_R \times U(1)_{B-L}$ phase. The field content relevant to the RG running in the first two parts of the symmetry-breaking chain is given in Tab. (3.4).
In more detail, after the initial $SO(10) \to SU(3)_c \times SU(2)_L \times SU(2)_R \times U(1)_{B-L}$ breaking triggered by essentially the same mechanism as in Models I and II, the subsequent $SU(2)_R \times U(1)_{B-L} \to U(1)_R \times U(1)_{B-L}$ requires a VEV of the Ω field which, at the level of an effective theory, can again emerge from its interplay with a LR singlet. The last symmetry-breaking step is then achieved in a similar manner by the VEVs of the MSSM-neutral components of the $\chi^c \oplus \overline{\chi}^c$ fields.

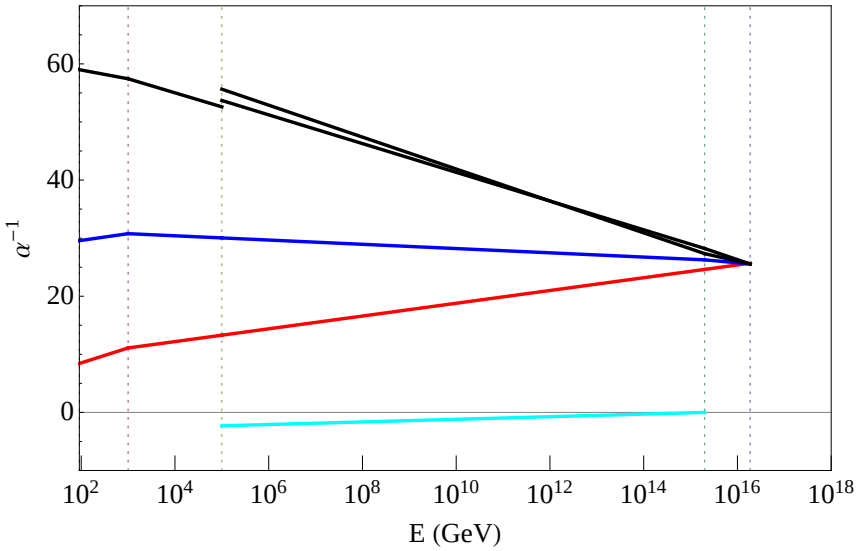

Figure 3.5: Running in Model IV with a low $B-L$ scale. Note the effects of the U(1) mixing in the running & matching; the lowest curve corresponds to the off-diagonals of the $(GG^T/4\pi)^{-1}$ matrix.

The relevant b_i-coefficients at the $SU(3)_c \times SU(2)_L \times SU(2)_R \times U(1)_{B-L}$ level read $b_3 = -3$, $b_L = 2$, $b_R = 5$ and $b^{\rm can}_{B-L} = 15/2$. In the $SU(3)_c \times SU(2)_L \times U(1)_R \times U(1)_{B-L}$ stage, however, the effects of the $U(1)$ mixing must be taken into account and, thus, the b-coefficients in the $U(1)_R \times U(1)_{B-L}$ sector constitute a matrix of anomalous dimensions γ. One has $b_3 = -3$, $b_L = 1$ and

$$\gamma^{\rm phys} = \begin{pmatrix} 15/2 & -1 \\ -1 & 18 \end{pmatrix} , \tag{6}$$

which should be brought into the canonical basis by means of a normalization matrix $N = {\rm diag}(1, \sqrt{3/8})$, $\gamma^{\rm can} = N\gamma^{\rm phys}N$. The details of the one-loop RGE evolution of gauge couplings and soft masses in theories with more than a single abelian gauge factor are summarized in Section 5. The qualitative features of the gauge-coupling running in this setting can be seen in Fig. 3.5.

Concerning the flavour structure of the model, the situation is essentially identical to that described in the original work [470]. The only exception is a second LR bi-doublet retained until the $U(1)_R \times U(1)_{B-L}$ breaking scale which might be necessary in order to get a potentially realistic pattern of the effective Yukawa couplings. Nevertheless, the salient features of the Model in the soft sector should not depend much on the detailed realization of the effective Yukawa pattern.

2 Leading-log RGE invariants

In this Section we focus on the calculation of the invariants using mSugra boundary conditions. mSugra is defined at the GUT-scale, $M_{\rm G}$, by a common gaugino mass $M_{1/2}$, a common scalar mass m_0 and the trilinear coupling A_0, which gets multiplied by the corresponding

Yukawa couplings to obtain the trilinear couplings in the soft SUSY breaking Lagrangian [8]. In addition, at the electro-weak scale, $\tan\beta = v_u/v_d$ is fixed. Here, as usual, v_d and v_u are the vacuum expectation values (vevs) of the neutral components of H_d and H_u, respectively. Finally, the sign of the μ parameter has to be chosen.
Renormalization group equations for general supersymmetric models are known up to 2-loop order [485]. The only case not covered in the otherwise general equations given in [485] are supersymmetric models with more than one $U(1)$ group. With more than a single abelian gauge factor, there appears a new class of effects associated with the so called kinetic mixing between the associated gauge fields. RGEs for this case have been derived very recently in [483].
Barring for the moment the effects of $U(1)$ mixing present in Model IV, at the 1-loop level, one can devise a simple set of analytic equations for the soft terms. Gaugino masses scale as gauge couplings do and so the requirement of GCU fixes the gaugino masses at the low scale

$$M_i(m_{SUSY}) = \frac{\alpha_i(m_{SUSY})}{\alpha(M_G)} M_{1/2}. \tag{7}$$

Eq. (7) implies that the relationship of the M_i to $M_{1/2}$ is changed in Models I to III, since $\alpha(M_G)$ is shifted.
Neglecting the Yukawa couplings for the soft mass parameters of the first two generations of sfermions one can write

$$m_{\tilde{f}}^2 \;=\; m_0^2 + \frac{M_{1/2}}{\alpha(M_{\rm G})^2} \sum_{R_j} \sum_{i=1}^{N} \tilde{f}_i^R \alpha_i(v_{R_j})^2 \,. \tag{8}$$

Here, the sum over "R_j" runs over the different regimes in the models under consideration, while the sum over i runs over all gauge groups in a given regime. $\alpha_i(v_{R_j})$ is to be understood as the gauge coupling of group i evaluated at the upper end of regime R_j. In the MSSM one would have only to consider one regime, namely from the SUSY scale to the GUT scale. In Models I and II we have two different regimes, while in Models III and IV there are a total of three regimes to consider.
The different $\tilde{f}_i^R$ can be written in a compact form as:

$$\tilde{f}_i^R \;=\; \frac{c_i^{f,R}}{b_i} \left[1 - \left(\frac{\alpha_i(v_x)}{\alpha_i(v_y)} \right)^2 \right] , \tag{9}$$

where v_x and v_y indicate the value of the relevant α at the lower and higher boundaries of the regime under consideration, respectively. The $c_i^{f,R}$ coefficients given in Tab. (3.5) are proportional to the values of the quadratic Casimir of representation R_f hosting the matter field f with respect to the group G in the regime R

$$c_i^{f,R} = 2C_G(R_f) \,. \tag{10}$$

[8] It is sometimes argued that this setup should better be called CMSSM, since there are even simpler models of supergravity type breaking in which A_0 is not a free parameter, as for example in Polonyi type supergravity [174, 484]. Since we will be concerned with only the first two sfermion generations this distinction is irrelevant for us.

They are readily evaluated from the basic formula

$$C_G(R)d(R) = T_2(R)d(G)\,, \tag{11}$$

where $d(G)$ is the dimension of the group G, $T_2(R)$ the Dynkin index of the representation R and $d(R)$ is its dimension. Note that the coefficients $c_i^{f,R}$ are different for the different fermions, which leads to a different coefficient in front of $M_{1/2}$ in Eq. (8). The b_i in Eq. (9) are the one-loop b-coefficients for the different models defined in the previous Section. For completeness, the well-known one-loop beta-coefficients for the MSSM are (in the traditional $SU(5)$ normalization): $b = (b_1, b_2, b_3)^{MSSM} = (\frac{33}{5}, 1, -3)$.
Eq. (8) is valid neglecting $U(1)$-mixing effects. The extra effects due to the kinetic $U(1)$ mixing relevant in Model IV are summarized in the Section 5; for a more detailed discussion including higher-loop effects, see [483].

$\tilde{f}$	$\tilde{E}$	$\tilde{L}$	$\tilde{D}$	$\tilde{U}$	$\tilde{Q}$
MSSM					
$c_1^{f,MSSM}$	$\frac{6}{5}$	$\frac{3}{10}$	$\frac{2}{15}$	$\frac{8}{15}$	$\frac{1}{30}$
$c_2^{f,MSSM}$	0	$\frac{3}{2}$	0	0	$\frac{3}{2}$
$c_3^{f,MSSM}$	0	0	$\frac{8}{3}$	$\frac{8}{3}$	$\frac{8}{3}$
$U(1)_R \times U(1)_{B-L}$					
$c_{BL}^{f,BL}$	$\frac{3}{4}$	$\frac{3}{4}$	$\frac{1}{12}$	$\frac{1}{12}$	$\frac{1}{12}$
$c_L^{f,BL}$	0	$\frac{3}{2}$	0	0	$\frac{3}{2}$
$c_R^{f,BL}$	$\frac{1}{2}$	0	$\frac{1}{2}$	$\frac{1}{2}$	0
$c_3^{f,BL}$	0	0	$\frac{8}{3}$	$\frac{8}{3}$	$\frac{8}{3}$
LR					
$c_{BL}^{f,LR}$	$\frac{3}{4}$	$\frac{3}{4}$	$\frac{1}{12}$	$\frac{1}{12}$	$\frac{1}{12}$
$c_L^{f,LR}$	0	$\frac{3}{2}$	0	0	$\frac{3}{2}$
$c_R^{f,LR}$	$\frac{3}{2}$	0	$\frac{3}{2}$	$\frac{3}{2}$	0
$c_3^{f,LR}$	0	0	$\frac{8}{3}$	$\frac{8}{3}$	$\frac{8}{3}$
Pati-Salam					
$c_L^{f,PS}$	0	$\frac{3}{2}$	0	0	$\frac{3}{2}$
$c_R^{f,PS}$	$\frac{3}{2}$	0	$\frac{3}{2}$	$\frac{3}{2}$	0
$c_4^{f,PS}$	$\frac{15}{4}$	$\frac{15}{4}$	$\frac{15}{4}$	$\frac{15}{4}$	$\frac{15}{4}$

Table 3.5: Coefficients $c_i^{\tilde{f}}$ for Eq. (8) for different symmetry stages. The MSSM and the LR parts are relevant to all four models under consideration; the $U(1)_R \times U(1)_{B-L}$ and the Pati-Salam parts are used solely for Model IV and Model III, respectively.

Individual SUSY masses depend strongly on the initial values for m_0 and $M_{1/2}$. However, one can form four different combinations, which we choose to be

$$\begin{aligned} LE &\equiv (m_{\tilde{L}}^2 - m_{\tilde{E}}^2)/M_1^2, \\ QE &\equiv (m_{\tilde{Q}}^2 - m_{\tilde{E}}^2)/M_1^2, \\ DL &\equiv (m_{\tilde{D}}^2 - m_{\tilde{L}}^2)/M_1^2, \\ QU &\equiv (m_{\tilde{Q}}^2 - m_{\tilde{U}}^2)/M_1^2. \end{aligned} \tag{12}$$

It is easy to see that, at the leading-log level, m_0 and $M_{1/2}$ drop out of the equations for the invariants. Note, that one could have equally well normalized to any of the other two gaugino masses. The choice of M_1 is only motivated by the expectation that it will be the gaugino parameter measured with the smallest error, at least in standard (mSUGRA,GMSB) SUSY models.

3 Sliding scale imprints in the leading-log RGE Invariants

3.1 Models I and II with a sliding $SU(2)_R$ scale

The method: As we have already mentioned in Section 1, in Models I and II the sliding nature of the $SU(2)_R$ scale makes it impossible to get an exact unification, in full analogy with the MSSM. Since, however, this is just about a 2% effect, we shall not attempt to improve on this by either looking for a suitable set of threshold corrections or by going beyond the one-loop approximation[9]. Rather than that, we shall just parameterize our ignorance of the "true values" of the unification scale position and the unified gauge coupling in terms of a pair of small "offset" parameters scanning over the area of the relevant "non-unification triangle" shown in Fig. 3.6. In what follows, we shall use the error on $\alpha_S(M_Z)$ given in [486], $\Delta(\alpha_S(M_Z)) = 0.002$, which does not take into account the latest QCD lattice calculations results.

The results: In FIGs. 3.7 and 3.8 we display the v_R-dependence of the RGE invariants in Models I and II due to the running effects subsumed by Eq. (8). The bands correspond to the error in the gauge-coupling unification inherent to these settings which, at the leading-log level, can be taken into account by scanning over the area of the relevant non-unification triangle, c.f., Fig. 3.6. The upper (yellow) band refers to the combination QE, the (blue) band which at low v_R partially overlaps with QE represents DL, whereas the third (brown) band is QU and, finally, the lowest (green) band refers to the LE combination. Note that, for practical reasons, the invariants QE and DL have been scaled down by a factor of ten. The same colour-code is adopted in the other figures in this Section.
Several comments are in order here: In general, the invariants exhibit a logarithmic dependence on v_R. For v_R close to the MSSM scale (on the left), the QU and LE invariants overlap. This is attributed to the enhanced gauge symmetry throughout the whole $m_{\rm SUSY}$-$M_{\rm G}$ range which makes $m^2_{\tilde{Q}}$ and $m^2_{\tilde{U}}$ as well as $m^2_{\tilde{L}}$ and $m^2_{\tilde{E}}$ behave the same, see the LR-stage $c_i^{\tilde{f}}$-coefficients in Tab. (3.5). In the $v_R \to M_{\rm G}$ limit, the mSugra values of the invariants (modulo the MSSM non-unification) are reproduced. Concerning QE and DL, the first thing to notice is that these invariants tend to increase with v_R departing from $M_{\rm G}$, thus leading to a pattern characteristic to this class of models. Moreover, they are more sensitive to the initial condition because the colour-effects in their evolution do not cancel, thus leading to larger bands.

[9] Indeed, this would be inconsistent as we are concerned only with the leading-log approximation for the softs.

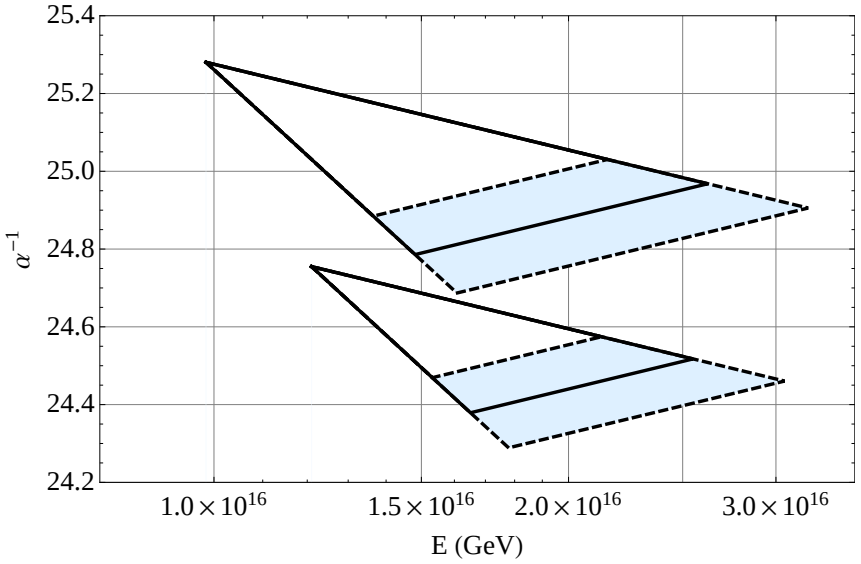

Figure 3.6: The MSSM-like non-unification triangle in Models I and II with $v_R = 10^{14}$ GeV for two different values of the unknown soft-SUSY breaking scale ($m_{\rm SUSY} = 1$ TeV for the upper one and $m_{\rm SUSY} = 500$ GeV for the lower). The upper sides of the triangles corresponds to α_L^{-1} while the lower-left sides depict the "effective" α_Y^{-1} defined as $\frac{3}{5}\alpha_R^{-1} + \frac{2}{5}\alpha_{B-L}^{-1}$. The light blue area surrounding the α_S^{-1} line represents the 1σ uncertainty in $\alpha_s(M_Z)$ as given in [486]. Both triangles move down for lower values of v_R, see Figs. 3.1 and 3.2.

Naturally, the main difference between Fig. 3.8 and Fig. 3.7 is expected in the low-v_R regime where the effects due to the slight difference in the Model-I and Model-II spectra are most pronounced and the QU and LE invariants run faster due to a larger ratio of the coupling constants in the relevant Eq. (9).

3.2 Model III with sliding $SU(2)_R$ and PS scales

The method: In Model III, the LR and PS intermediate scales can be always adjusted so that one gets an exact one-loop unification for v_R stretching up to about 10^{14} GeV, c.f., Fig. 3.9. This is technically achieved by relating the value of the PS scale to the value of the LR scale as

$$\begin{aligned} t_{PS} &= \frac{1}{2}t_{LR} - \frac{1}{12}\Big(14t_{SUSY} + 20t_Z \\ &+ \pi(18\alpha_S(t_Z)^{-1} - 33\alpha_L(t_Z)^{-1} + 15\alpha_Y(t_Z)^{-1})\Big) \end{aligned} \tag{13}$$

Here, the t_x stand for $ln(m_X)$ as usual. Thus, the main uncertainty at this level comes from the experimental error in $\alpha_S(M_Z)$. In what follows, we shall vary v_R and v_{PS} along the constant $\alpha_S(M_Z)$-error trajectories, namely, within $\pm1\sigma$, corresponding to the boundaries between the yellow and white areas within the parameter area depicted in Fig. 3.9.

The results: In this case, the intermediate-scale dependence of the leading-log RGE invariants is yet more pronounced than in Models I and II, c.f., Fig. 3.10. As before, the

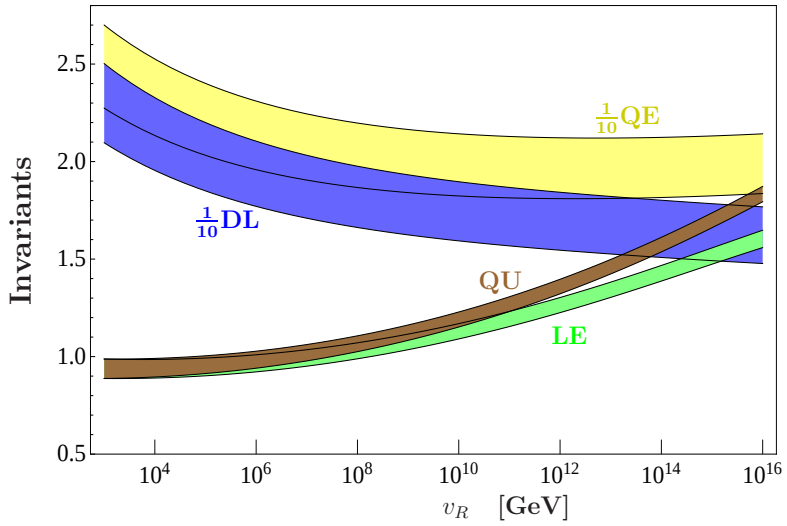

Figure 3.7: The v_R-dependence of the leading-log invariants in Model I, c.f., Section 1.2. The bands represent the error due to the non-exact gauge-coupling unification depicted in Fig. 3.6. For practical reasons, the numerical values of the invariants QE and DL have been scaled down by a factor of ten.

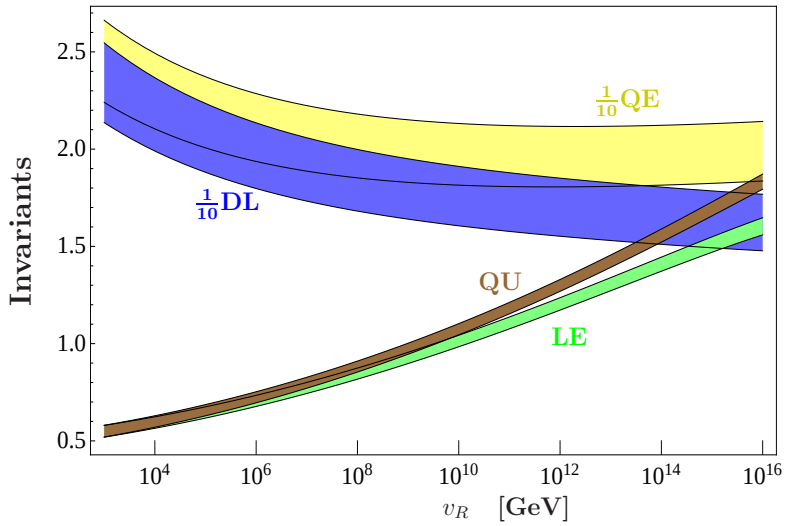

Figure 3.8: The same as in Fig. 3.7 but for Model II of Section 1.2. The QU and LE behaviour differs from that in Fig. 3.7 mainly in the low-v_R regime.

numerical values of the invariants QE and DL have been conveniently scaled down by a factor of ten. For each of the four invariants, the solid curve Fig. 3.10 corresponds to $\alpha_S(M_Z)$ fixed at its central value and the dashed and dotted lines refer to the -1σ and $+1\sigma$ trajectories, respectively. On the high-v_R tail, the different curves stop at different energies due to the need to respect the natural $v_R < v_{PS}$ hierarchy reflected by the "diagonal" cut to the parametric space in Fig. 3.9.

For all four invariants under consideration, we observe a stronger v_R-dependence than in

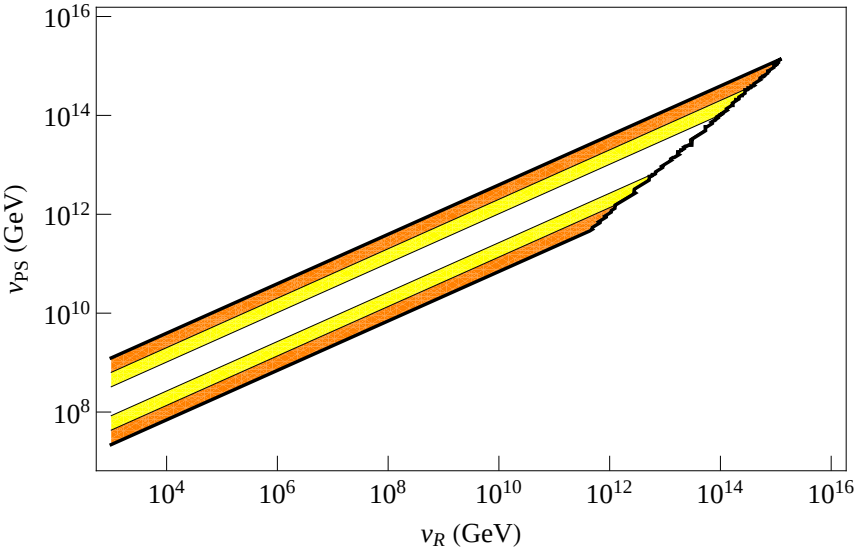

Figure 3.9: The correlation of the intermediate symmetry-breaking scales in Model III (allowed region coloured). The contours correspond to the quality of the fit of $\alpha_S(M_Z)$ for each choice of the Pati-Salam breaking scale v_{PS} and the LR breaking scale v_R, within 1σ (white area within the coloured band), 2σ (yellow) and 3σ (orange) of the range quoted in [486].

Models I and II. This is namely due to the extended Pati-Salam running which contributes with larger $c_i^{\tilde{f}}$-coefficients than the LR stage, c.f., Tab. (3.5). Moreover, unlike in Figs. 3.7 and 3.8, three out of four invariants grow with lowering v_R while the fourth one even becomes negative for v_R close to the MSSM scale, thus, again, leading to a very characteristic pattern.

3.3 Model IV with a sliding $U(1)_R \times U(1)_{B-L}$ scale

The method: Finally, in Model IV, c.f. Section 1.3, the unification is exact for any value of the sliding scale v_{BL} below a (constant) v_R in the ballpark of roughly 3×10^{15} GeV, c.f., Fig. 3.11. Thus, as before, the main uncertainty at this level comes from the experimental error in $\alpha_S(M_Z)$ which translates into small shifts in v_R. In what follows, we shall again vary v_{BL} along the constant $\alpha_S(M_Z)$-error trajectories, namely, within $\pm 1\sigma$, corresponding to the boundaries between the yellow and white areas within the parametric region depicted in Fig. 3.11.

The results: In the two panels of Fig. 3.12, the four invariants of our interest are depicted as functions of v_{BL}. As in the case of Model III, for each of them the solid line corresponds to the central-value trajectory in the parametric space of Fig. 3.11, whereas the dashed and dotted curves refer to the -1σ and $+1\sigma$-trajectories, respectively.
Due to the very special nature of the sliding scale in this setting, all four invariants exhibit only a very mild v_{BL} dependence, with the strongest effect of the order of few per cent observed in the LE case. This is because the v_{BL} scale enters into the soft masses only

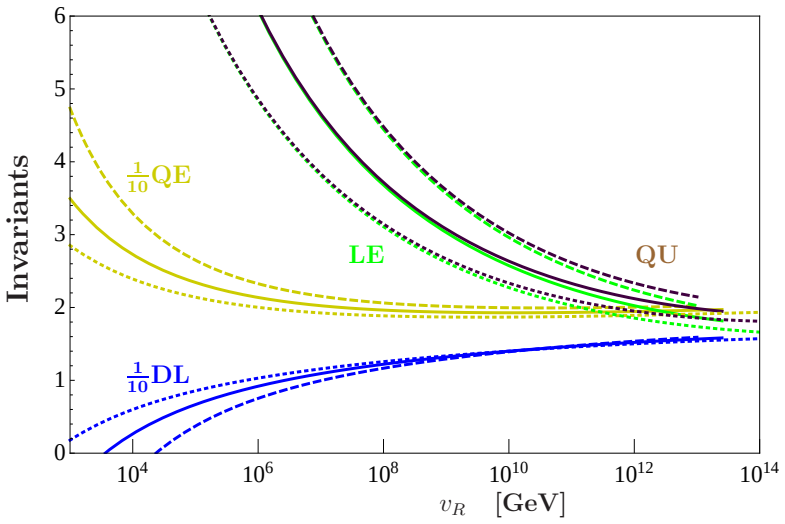

Figure 3.10: Intermediate-scale dependence of the RGE invariants Model III, see Section 1.2. For each of the four invariants, the solid curve corresponds to $\alpha_S(M_Z)$ fixed at its central value and the dashed and dotted lines refer to the -1σ and $+1\sigma$ trajectories, respectively; c.f. Fig. 3.9.

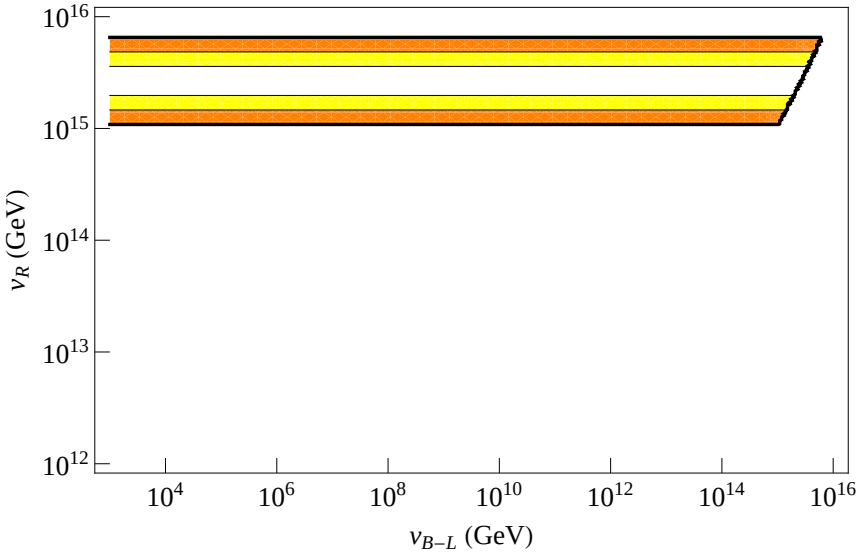

Figure 3.11: The parameter space of Model IV of Section 1.3. The contours correspond to the different quality of the $\alpha_S(M_Z)$ fit for different choice of the L-R breaking scale v_R, namely, to 1σ (white), 2σ (yellow) and 3σ (orange) values for the range quoted in [486].

through the slight changes in the abelian gauge couplings, which, however, are overwhelmed by the colour effects in all the other invariants. This, however, will make it rather difficult to distinguish this model from the MSSM, namely because such a discrimination is efficient only if more than a single invariant differs significantly from the mSugra value so that the intermediate scale can be independently constrained from more than a single quantity.
Finally, let us comment in brief on the case where the $U(1)_R \times U(1)_{B-L} \to U(1)_Y$ breakdown

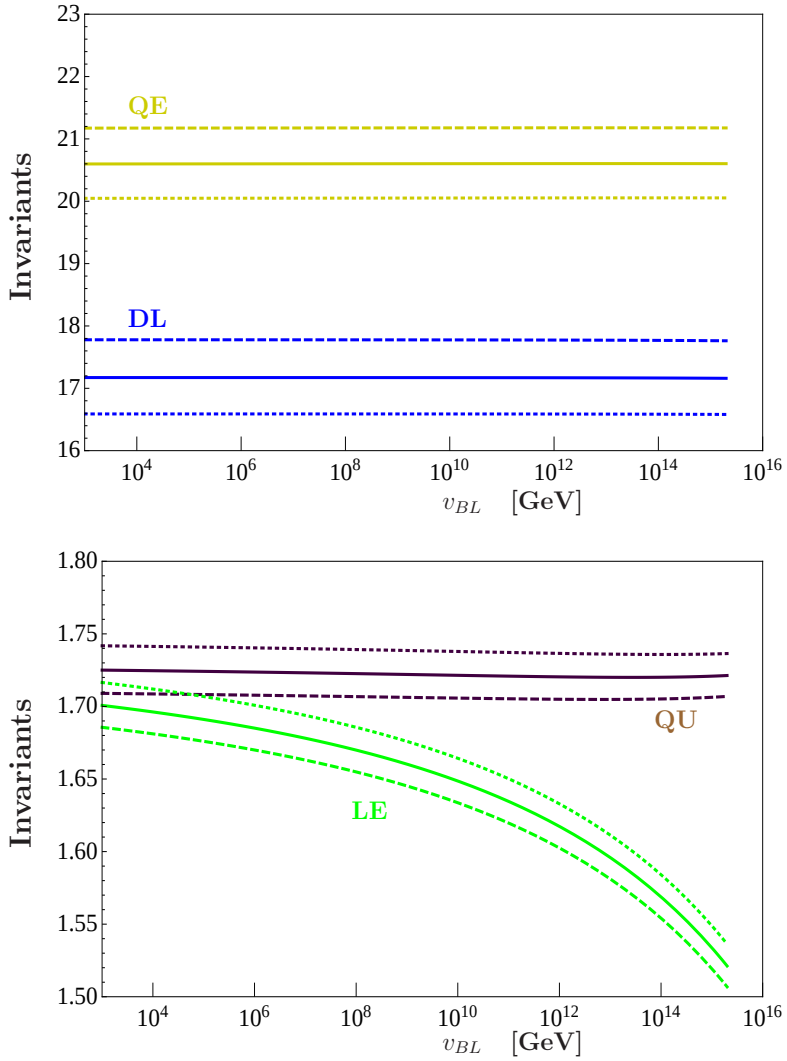

Figure 3.12: The v_{BL}-scale dependence of the RGE invariants in Model IV. For practical purposes the figure has been split into two panels. For each of the four invariants, the solid curves correspond to $\alpha_S(M_Z)$ fixed at its central value while the dashed and dotted lines refer to the -1σ and $+1\sigma$ trajectories corresponding to roughly $v_R \sim 2 \times 10^{15}$ GeV and $v_R \sim 4 \times 10^{15}$ GeV, respectively; c.f. Fig. 3.11.

is not triggered by $SU(2)_R$ doublets like above but by, e.g., $SU(2)_R$ triplets. We expect that for such models the effects on the invariants would be similar to those expected in Model IV, and certainly smaller than those observed in Models I-III.

3.4 Squark and slepton spectra.

In Fig. 3.13 we plot the shapes of the MSSM squark and slepton spectra obtained in mSugra and in Models I, II and III calculated for the SPS3 benchmark point, i.e. for $m_0 = 90$ GeV and $M_{1/2} = 400$ GeV. This figure is to be understood only as an illustrative example of the

different spectra generated in our different models. For each of the cases, the horizontal lines (bottom to top) correspond to $m_{\tilde{e}^c}$ (light blue), $m_{\tilde{l}}$ (blue), $m_{\tilde{u}^c}$ (orange), $m_{\tilde{d}^c}$ (light orange) and $m_{\tilde{q}}$ (purple). In order to pronounce the differences, the v_R scale has been in all cases chosen very low, namely, $v_R \sim 10^3$ GeV, and consequently v_{PS} in Model III is fixed to $v_{PS} \sim 10^7$ GeV by gauge unification. The masses of the $\tilde{d}^c$ and of the $\tilde{u}^c$ almost coincide in all the Models. Models I and II differ from the mSugra case namely by the smaller splittings observable in the squark as well as in the slepton masses, which is more pronounced for the latter model. However, the spectrum of Model III is strongly compressed due to an extended Pati-Salam stage which makes it rather outstanding.
We decided not to overpopulate the figure by displaying the gaugino masses which, indeed, are obtained by a simple rescaling (7); the SUSY-to-GUT-scale ratios of the relevant α's can be inferred from the evolution of the gauge couplings, c.f. FIGs 3.1, FIGs 3.2, FIGs 3.3 and FIGs 3.5.

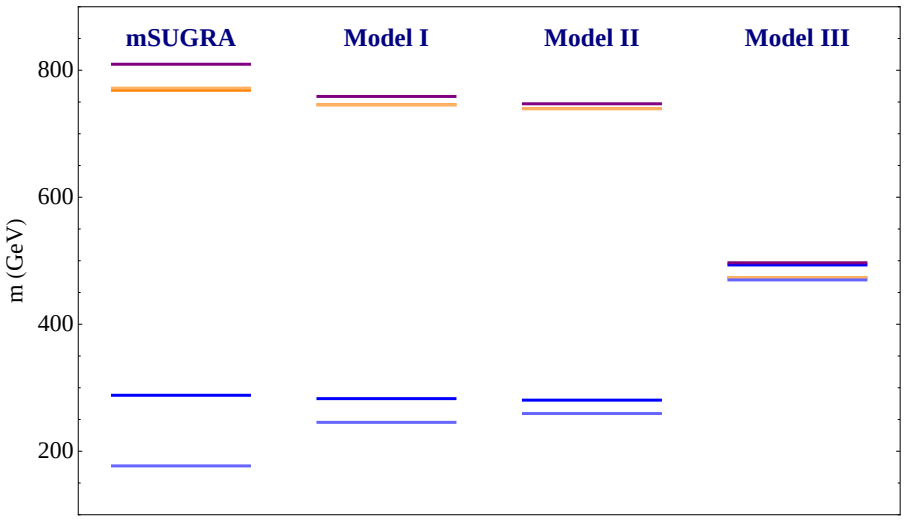

Figure 3.13: The MSSM squark and slepton spectra mSugra and Models I, II and III calculated for the SPS3 benchmark point, i.e. for $m_0 = 90$ GeV and $M_{1/2} = 400$ GeV. In all cases, $v_R = 10^3$ GeV and $v_{PS} \sim 10^7$ GeV in Model III . From botton to top the horizontal lines correspond to: $m_{\tilde{e}^c}$ (light blue), $m_{\tilde{l}}$ (blue), $m_{\tilde{u}^c}$ (orange), $m_{\tilde{d}^c}$ (light orange) and $m_{\tilde{q}}$ (purple). We do not show the results for model IV in this figure, since they are very similar to the mSugra case.

4 Discussion and outlook

We have studied the leading-log RGE evolution of the MSSM soft SUSY breaking parameters for four different GUT models with mSugra boundary conditions. Although all the settings are based on the unified $SO(10)$ gauge group, they differ at the level of intermediate scale symmetry groups and/or particle content below the GUT scale. Two of the models discussed (Models I and II of Sects. 1.2 and 1.2), which differ only in their beyond-MSSM field contents, feature an intermediate left-right symmetry which, at the level of precision

used in this calculation, can be broken to $SU(3)_c \times SU(2)_L \times U(1)_Y$ of the MSSM almost anywhere between $M_{\rm G}$ and the soft SUSY-breaking scale. In Model III (c.f., Section 1.2) the sliding nature of the $SU(2)_R$-breaking scale relies on an additional intermediate Pati-Salam symmetry. Finally, in Model IV (see Section 1.3), the left-right symmetry is broken at a relatively high scale, but there is instead a sliding scale corresponding to the breaking of its $U(1)_R \times U(1)_{B-L}$ remnant. All models we consider are able to accommodate the neutrino data by either inverse or linear seesaw.

The extra gauge groups and/or beyond MSSM fields change the evolution of the soft parameters with respect to the basic mSugra expectation. The invariant mass combinations we considered are especially suited to uncover the effects of beyond-mSugra physics on the SUSY spectra. Remarkably, while invariants contain only a logarithmic dependence on the new physics scales, their behavior is *qualitatively* different in different models.

In our Models I and II, the invariants LE and QU (c.f., Section 2) are always lower than the mSugra limit, while DL and QE are always larger. The former is a direct consequence of the LR symmetry, while the latter reflects mainly the shift in $\alpha(M_{\rm G})$ the models exhibit with respect to the MSSM expectation. Moreover, in spite of only a mild difference in the particle content, the invariants differ quantitatively between Model I and Model II.

In contrast to that, in the Pati-Salam based Model III, LE and QU are always larger than in mSugra, with a rather strong dependence on the v_R scale, namely due to the higher dimensionality of the relevant multiplets at the Pati-Salam stage. At the same time, in Model III, DL is always below the mSugra limit, while QE hardly varies at all as a function of v_R. Finally, Model IV is an example of how a new scale can be effectively "hidden" from the RGE invariants in special constructions: Despite containing a new scale potentially as low as $\mathcal{O}(1)$ TeV, all invariants are always very close to the mSugra limit in this model. Technically, this is achieved by maintaining the beta coefficients for the $SU(2)_L$ and $SU(3)_c$ factors as in the MSSM all the way up to a scale close to $M_{\rm G}$, while the sliding feature of the $U(1)_R \times U(1)_{B-L}$ breaking scale "shields" all invariants from the effects of the new group, with the exception of LE, which, however, changes only very weakly.

It is especially interesting to compare our results with those obtained for minimal seesaw models within mSugra. Invariants for seesaw have been studied previously in [461, 478, 479]. Type-I seesaw adds only singlets to the MSSM and thus, just like our Model IV, can not be distinguished from the pure mSugra case by means of the invariants only. Type-II and type-III seesaw, on the other hand, change the b-coefficients with respect to the MSSM, but do not extend the gauge group. As a result, for minimal seesaws all four invariants are larger than their mSugra limit if the seesaw scale is below the GUT scale, as indicated by neutrino data. Thus, the invariants should allow to distinguish our $SO(10)$-based Models I to III from type-II and type-III seesaw.

The RGE invariants are, therefore, good model discriminators, at least in principle. However, any attempt to quantitatively determine the scale of a new physics within a particular scenario must inevitably address the accuracy of their calculation. Different types of errors need to be considered here. First, there are the errors from uncertainties in the values of the input parameters. The largest error currently stems from the completely unknown m_{SUSY}, see Fig. 3.6 and Eq. (7). Once SUSY masses, indeed, have been measured, this will become irrelevant and the largest error will, most likely, be $\Delta(\alpha_S)$.

Next, the RGE invariants considered here are calculated to the leading-log precision only.

However, in some cases, important higher order effects such as genuine 2-loop corrections and 1-loop thresholds can emerge; for the seesaw, this was studied recently in [461, 479]. Both, 2-loop running and 1-loop SUSY thresholds can, of course, be taken into account, but the calculation of the invariants at this level can not be done analytically. Instead, it requires numerical tools such as, e.g., SPheno [487, 488] and SARAH [489–491].

Probably more important than the above theoretical considerations, eventually, will be the fact that the invariants are not directly measurable quantities. Conversion of the invariants into the measured sparticle masses (or extraction of relevant soft parameters from sparticle measurements) requires additional *experimental* input. In case of the first two generations of sfermions this requires at least a reliable measurement of $\tan\beta$ for the determination of the D-terms. In addition, at variance with the situation in the minimal seeesaw models, the breaking of the extra gauge symmetries can potentially produce new D-terms not present in the $SU(3)_C \times SU(2)_L \times U(1)_Y$ case. Usually it is assumed that any beyond-SM gauge group is broken in a "D-flat" manner in order to avoid problems with tachyonic sfermions. However, since we wish to extract information from sfermion masses themselves, it will certainly be prudent to do a combined fit on the new parameters instead of simply *assuming* D-flatness.

The prospects of measuring sparticle masses at the LHC and, possibly, at the future ILC have been studied by many authors, for a detailed review see, for example [446]. In general, one expects that slepton and gaugino masses, if within the kinematical reach of the ILC, can be measured at the per mille level or even better. Coloured sparticles, however, might be too heavy to be produced at the ILC. At the LHC, the precision with which sparticle masses can be measured depends strongly not only on the absolute scale of the SUSY masses, but also decisively on the mass ordering of the sparticles. If long decay chains such as $\tilde{q} \to \chi_2^0 q$ with $\chi_2^0 \to \tilde{l}l \to l^\pm l^\mp \chi_1^0$ were available, many SUSY masses could be measured with accuracies down to (few) percent. From the detailed studies of [446], the authors of [480] concluded that the precision of ILC+LHC combined would make it possible to see indications for a seesaw of either type II or type III for nearly all relevant seesaw scales. In an LHC-only analysis, the seesaw scale must be below 10^{14} GeV even in favourable circumstances [480] or might not leave a trace in the LHC data at all.

Comparing roughly the changes in spectra induced in the seesaw models studied in [480] with the changes expected in our $SO(10)$ models, we expect that a detailed, numerical calculation should be able to probe most, if not all the interesting parameter space of our models, if SUSY is found at the LHC and precise mass measurements are done with the help of an ILC.

Nevertheless, direct searches for low energy SUSY have given null results up to now. This work has been published before the LHC had completed its $\sqrt{s} = 8$ TeV run, in which both the ATLAS and CMS collaborations collected approximately 20 fb^{-1} of data. Recent analyses by the two experiments at 8 TeV have excluded $m_{\tilde{g}} \lesssim 1000$ GeV in the mSUGRA model (see the discussion about LHC searches in Chapter 1 Section 2.3). However, there remains interesting prospects for the detection of SUSY particles and therefore the measurement of the SUSY spectra with the next LHC run at higher center-of-mass energy [492–494].

Finally, we would like to mention that the models we have studied in this chapter have potentially also a rich phenomenology beyond the MSSM apart from the invariants. There are the new gauge bosons, additional Higgses, additional gauginos/higgsinos, large lepton flavour violation and many other effects worth studying.

5 One-loop running with U(1) mixing

In this Section we give some technical details of the one-loop evolution of gauge couplings and soft-SUSY-breaking terms in Model IV of Sect. 1.3 in which extra kinetic mixing effects, generally present in theories with multiple $U(1)$ gauge factors, emerge. This, in the approach advocated in, e.g., [483], amounts to extending the notion of the individual gauge couplings and gaugino masses associated to different $U(1)$ gauge factors to matrix forms, which, subsequently, complicates the relevant generalized evolution equations.

Gauge couplings

To deal with the effects of the kinetic mixing in cases with more than a single abelian gauge factor like in Model IV of Sect. 1.3 it is convenient to work with a matrix of gauge couplings rather than with each of them individually, which would require an extra RGE for the kinetic mixing parameters, c.f., [483]. In the $U(1)_R \times U(1)_{B-L}$ case this amounts to defining

$$G = \begin{pmatrix} g_{RR} & g_{RX} \\ g_{XR} & g_{XX} \end{pmatrix} . \tag{14}$$

where X is a shorthand notation for the canonically normalized $B-L$. The evolution equation can be then written as

$$\frac{\mathrm{d}}{\mathrm{d}t} A^{-1} = -\gamma \,, \tag{15}$$

where $A^{-1} \equiv 4\pi (GG^T)^{-1}$ and $t = \frac{1}{2\pi}\log(\mu/\mu_0)$. Here we have defined the relevant matrix of anomalous dimensions by

$$\gamma \equiv \sum_f Q_f Q_f^T \,, \tag{16}$$

where the summation is taken over all the chiral superfields f in the model and Q_f denotes a column vector of $U(1)_R$ and $U(1)_{B-L}$ charges of each f.
The matching condition between such high-energy gauge couplings (corresponding to $U(1)_R \otimes U(1)_{B-L}$ in the case of our interest) and the effective-theory one (i.e., $U(1)_Y$ of the MSSM) at scale t_0 then reads

$$\alpha_Y^{-1}(t_0) = p_Y^T \, A^{-1}(t_0) p_Y \,, \tag{17}$$

where $p_Y^T = (\sqrt{\frac{3}{5}}, \sqrt{\frac{2}{5}})$ are the coefficients of the hypercharge Y in the space of the R- and $B-L$-charges, namely, $Y = \sqrt{\frac{3}{5}} T_R^3 + \sqrt{\frac{2}{5}} X$. Thus, one has

$$\begin{aligned} g_Y^{-2} \;=\; & (g_{RR} g_{XX} - g_{RX} g_{XR})^{-2} \left[\frac{3}{5} \left(g_{XX}^2 + g_{XR}^2 \right) \right. \\ & \left. + \frac{2}{5} \left(g_{RR}^2 + g_{RX}^2 \right) - \frac{2}{5}\sqrt{6} \left(g_{RR} g_{XR} + g_{RX} g_{XX} \right) \right] . \end{aligned} \tag{18}$$

Soft SUSY-breaking terms

Neglecting for simplicity the Yukawa couplings and also the "Trace-terms" (denoted by $\mathcal{S}$ in [485]), which in mSugra yield only sub-leading correction to the leading-log approximation used in this work, one can write the generalized evolution equation including the effects of the $U(1)$ mixing [483] as

$$\frac{\mathrm{d}}{\mathrm{d}t}\tilde{m}_f^2 = -\frac{1}{\pi} Q_f^T G M M^\dagger G^T Q_f \,, \tag{19}$$

where G is the matrix of gauge couplings, M is the gaugino mass matrix and $t = \frac{1}{2\pi}\log \mu/\mu_0$. This is to be solved together with the gauge coupling (15) and gaugino evolution equations. The latter reads at one loop

$$\frac{\mathrm{d}}{\mathrm{d}t} M = \frac{1}{8\pi}\left(M G^T \gamma G + G^T \gamma G M\right) \,. \tag{20}$$

The simplicity of the system (15), (19) and (20) and, in particular, the flavour-diagonal mSugra initial condition, admits to write the general solution in a closed and compact form

$$A^{-1}(t) = A^{-1}(t_0) - \gamma (t - t_0) \,, \tag{21}$$

$$(G^{-1T} M G^{-1})(t) = \frac{1}{4\pi}\alpha_G^{-1} M_{1/2} \,, \tag{22}$$

and, in particular,

$$\tilde{m}_f^2(t) - \tilde{m}_f^2(t_0) = 2 M_{1/2}^2 \alpha_G^{-2} \times Q_f^T A_0^{-1}\left[\gamma^{-1} - A^{-1} A_0 \gamma^{-1} A_0 A^{-1}\right] A_0^{-1} Q_f \,, \tag{23}$$

where $A_0 \equiv A(t_0)$ and $A \equiv A(t)$.

CHAPTER

FOUR

SNEUTRINO DARK MATTER IN LOW-SCALE SCENARIOS

1 Introduction

The neutralino as a DM candidate has been studied in literally hundreds of publications, but also sneutrinos as candidates for the CDM have actually quite a long history [202–204]. However, ordinary left sneutrinos, i.e. the sneutrinos of the MSSM, have been ruled out [205] as the dominant component of the DM in the galaxy a long time ago due to their large direct detection cross section [206]. This leaves only "mixed" sneutrinos, i.e. sneutrinos which are partly singlets under the SM group, as good DM candidates. Motivated by neutrino oscillation data [77], in this Chapter we study sneutrinos as DM candidates in models with a low-scale seesaw mechanism, either MSSM-like models with an inverse [207] or the linear seesaw [208, 209] or models based on an $U(1)_{B-L} \times U(1)_R$ extension of the MSSM group [210, 211].
Singlet sneutrinos as DM have been studied in the literature before. Neutrino masses require that pure "Dirac"[1] sneutrino must have tiny Yukawa couplings. Unless the trilinear parameters are huge, Dirac (right) sneutrinos are therefore never in thermal equilibrium in the early universe [495, 496]. [2] However, they could still be non-thermal DM produced in the decay of the NLSP ("next-to-lightest supersymmetric particle") [498]. Also, trilinear terms are usually thought to be proportional to the associated Yukawa couplings, $T_\nu \propto Y_\nu A \sim \mathcal{O}(1)$ eV. Treating T_ν as a free parameter of the order of $\mathcal{O}(100)$ GeV, Dirac sneutrinos can be made good thermal DM candidates, as has been discussed in [499–501]. Very light mixed sneutrinos of this type have been studied in [502]. The LHC phenomenology of mixed Dirac sneutrino DM was studied in [503]. Alternatively to a large A-term, Dirac sneutrinos could also be made thermal DM in models with an extended gauge group [504, 505]. A model with sneutrino DM where the observed neutrino masses and mixings can arise entirely as a consequence of supersymmetry breaking effects in the sneutrino sector is considered in [506]. In [507] the right-handed sneutrino as DM candidate is studied in the supersymmetric F_D-term model of hybrid inflation.

[1] That conserve L number

[2] Unless Dirac neutrino masses are due to a tiny vev of a non-standard Higgs field [497]. In this case, Dirac sneutrinos could be the DM and even explain the much discussed claim for a tentative 130 GeV γ line in the FERMI data [306, 415].

In the classical seesaw picture [72, 254, 259, 459] lepton number is broken at a very large energy scale, possibly close to the unification scale. In such a setup also the right sneutrinos are very heavy and decouple; the sneutrinos remaining in the light spectrum are then very MSSM-like. One could, of course, simply put the scale of the seesaw low, say around the TeV scale. Yukawa couplings of the order of $\mathcal{O}(10^{-6})$ could fit neutrino data and the right sneutrinos are thermalized. In such an electro-weak scale seesaw right sneutrinos are overabundant unless (i) (again) a large trilinear parameter is assumed [508]; (ii) a new $U(1)$ group is introduced [509]; or (iii) sneutrinos have a large coupling to the NMSSM ("next-to-minimal Supersymmetric Standard Model") singlet [510, 511].
However, the situation is different in extended seesaw schemes like the inverse [207] or the linear seesaw [208, 209]. Here, additional singlets need to be introduced, but the neutrino Dirac Yukawa couplings can take essentially any value and it is the smallness of the inverse or linear seesaw terms which "explains" the smallness of the observed neutrino masses. In these setups the sneutrinos are highly mixed states. Inverse seesaw sneutrino DM has been studied previously in [512–514]. Our work differs in several aspects from these earlier papers. [512] calculated all masses at tree-level and did not carry out a detailed fit to neutrino data, while we use full 2-loop RGEs for the parameters, one-loop corrected mass matrices and pay special attention to constraints from neutrino masses. Also the paper [513] has some overlap with our work, but concentrates more on collider phenomenology of the inverse seesaw with sneutrino DM.
There are also some recent paper studying extended gauge groups. [515] studies inverse seesaw in an $SU(2)_R$ extension of the MSSM. Also two papers based on sneutrinos in $U_{B-L}(1) \times U_Y(1)$ have been published recently. In [516] an inverse seesaw is implemented in $U_{B-L}(1) \times U_Y(1)$. In [517] sneutrino DM within the $U_{B-L}(1) \times U_Y(1)$ group was studied assuming a standard seesaw. However, none of the above papers has studied linear seesaw variants. Finally, we mention that part of the results discussed in this Chapter have been presented also at conferences [518].
All our numerical calculations have been done using `SPheno` [487, 488], for which the necessary subroutines were generated using the package `SARAH` [489–491]. We have written the `SARAH` input files for the inverse and the linear seesaw, while for the $U(1)_{B-L} \times U(1)_R$ model we used the `SARAH` input files from [211]. The calculation of the relic density of the LSP is then done with `MicrOmegas` [519] version `2.4.5` based on the `CalcHep` [520] output of `SARAH`. To perform the scans we used a Mathematica package (`SSP`) [521].
The rest of this Chapter is organized as follows. In the next Section we first recall the main features of the supersymmetric inverse and linear seesaws, before discussing briefly the minimal $U(1)_{B-L} \times U(1)_R$ extension of the standard model. In Section 3 we discuss phenomenological constraints on the parameter space of the different setups. In Section 4 we then calculate the relic density and direct detection cross section. We conclude in Section 5.

2 Setup: Low scale seesaws and extended gauge groups

In this Section we briefly discuss the different setups, which we will use in the numerical sections of the Chapter. We first discuss supersymmetric inverse and linear seesaw, before

recalling the main features of the minimal $U(1)_{B-L} \times U(1)_R$ extension of the MSSM. The latter can be realized with either inverse or linear seesaw, but has some interesting additional features which are not covered by either the inverse or linear seesaw extensions of the MSSM.

2.1 Inverse and linear seesaw

In both, the inverse and the linear seesaws the particle content of the MSSM is extended by two types of singlet superfields, $\hat{\nu}^c$ and $\hat{S}$. The former is assigned a $L = +1$, while the latter has formally $L = -1$. The total superpotential can be written as

$$W = W_{\rm MSSM} + W_{\nu^c} + W_{\rm ISS} + W_{\rm LSS} \tag{1}$$

Here, $W_{\rm MSSM}$ is the usual MSSM superpotential

$$W_{\rm MSSM} = Y_u\, \hat{u}\, \hat{q}\, \hat{H}_u \, - Y_d\, \hat{d}\, \hat{q}\, \hat{H}_d \, - Y_e\, \hat{e}^c\, \hat{l}\, \hat{H}_d \, + \mu\, \hat{H}_u\, \hat{H}_d \; . \tag{2}$$

Lepton number conserving terms for the new singlet fields $\hat{\nu}^c$ ("right-handed neutrino") and $\hat{S}$ can be written as

$$W_{\nu^c} = Y_\nu\, \hat{\nu}^c\, \hat{l}\, \hat{H}_u \, + M_R\, \hat{\nu}^c\, \hat{S} \; . \tag{3}$$

The first term generates Dirac neutrino masses, once the H_u acquires a vacuum expectation value, while the second term is a mass term for the new singlet fields. In the inverse seesaw lepton number is violated by the term

$$W_{\rm ISS} = \frac{1}{2} \mu_S\, \hat{S}\, \hat{S} \; , \tag{4}$$

while in the linear seesaw case one writes lepton number violation as:

$$W_{\rm LSS} = Y_{SL}\, \hat{S}\, \hat{l}\, \hat{H}_u \; . \tag{5}$$

In both cases, it is usually assumed that the lepton number violating terms are small [207–209], see also the discussion in Section 3. The neutrino mass matrix and the resulting constraints on the model parameters are discussed in Section 3.1.

In supersymmetric models with lepton number violation, also the scalar neutrinos must have a lepton number violating mass term [522]. This term, $\tilde{m}_M^2$, is given by the difference between the eigenvalues of the real and imaginary components of the scalar neutrinos. It is therefore convenient to separate the sneutrino mass matrix into CP-even and CP-odd blocks [523]: [3]

$$\mathcal{M}^2 = \begin{pmatrix} \mathcal{M}_+^2 & \mathbf{0} \\ \mathbf{0} & \mathcal{M}_-^2 \end{pmatrix} . \tag{6}$$

Mass matrices for the scalar neutrinos are different in the inverse and linear seesaws. At the tree-level, in the inverse seesaw the $\mathcal{M}_\pm^2$ are given by: [4]

$$\mathcal{M}^2_{\pm,ISS} = \begin{pmatrix} m_L^2 + D^2 + (m_D^T m_D) & A_{LR}^T & m_D^T M_R \\ A_{LR} & m_{\nu^c}^2 + (M_R M_R^T) + (m_D m_D^T) & \pm M_R \mu_S + B_{M_R} \\ M_R^T m_D & \pm \mu_S M_R^T + B_{M_R}^T & m_S^2 + \mu_S^2 + M_R^T M_R \pm B_{\mu_S} \end{pmatrix} \tag{7}$$

[3] Separation into CP-even and CP-odd blocks requires CP-conservation, i.e. all parameters in the mass matrices below have to be real.

[4] We correct some misprints in [512, 524]

in the CP eigenstates basis: $\Phi^T = (\tilde{\nu}_+, \tilde{\nu}^c_+, S_+, \tilde{\nu}_-, \tilde{\nu}^c_-, S_-)$. Here, $D^2 = \frac{1}{2}m_Z^2 \cos 2\beta$ are the MSSM D-terms, $m_D = \frac{1}{\sqrt{2}} v_u Y_\nu$, $A_{LR} = T_{Y_\nu} v_u - \mu m_D \mathrm{cotg}\beta$, B_{M_R} is the soft bilinear term, T_{Y_ν} is the soft trilinear and m_L^2, $m_{\nu^c}^2$ and m_S^2 are the scalar soft masses for the doublet and the singlets respectively. Only μ_S and the corresponding bilinear soft term B_{μ_S} violate lepton number and only these two come with different signs in the CP-even and CP-odd mass matrices.
The symmetric sneutrino mass matrix in Eq. (7) can be diagonalized by a 9×9 matrix as follows

$$U_{\tilde{\nu}}^{ISS}\ \mathcal{M}^2_{\tilde{\nu}}\ U_{\tilde{\nu}}^{T\ ISS} = \mathrm{diag}(m^2_{\tilde{\nu}_1}, \ldots, m^2_{\tilde{\nu}_9})\ , \tag{8}$$

with $m^2_{\tilde{\nu}_1} < \cdots < m^2_{\tilde{\nu}_9}$. We can also introduce the parameter $f_{\tilde{\nu}mix}$, which measures the *leftness* of the sneutrino :

$$f_{\tilde{\nu}mix} = \sqrt{\Sigma_{i=1}^3 U^2_{\tilde{\nu}\ 1i}}. \tag{9}$$

For the linear seesaw one finds

$$\mathcal{M}^2_{\pm,LSS} \tag{10}$$
$$= \begin{pmatrix} m_L^2 + D^2 + (m_D^T m_D) + (M_L^T M_L) & A_{LR}^T \pm M_L^T M_R^T & m_D^T M_R \pm A_{LS}^T \\ A_{LR} \pm M_R M_L & m_{\nu^c}^2 + (M_R M_R^T) + (m_D m_D^T) & \pm m_D M_L^T + B_{M_R} \\ M_R^T m_D \pm A_{LS} & \pm M_L m_D^T + B_{M_R}^T & m_S^2 + M_L M_L^T + M_R^T M_R \end{pmatrix}$$

with all definitions as in Eq. (7) and $M_L = \frac{1}{\sqrt{2}} v_u Y_{SL}$ and $A_{LS} = T_{Y_{SL}} v_u - \mu M_L \mathrm{cotg}\beta$.
The diagonalizing 9×9 matrix is

$$U_{\tilde{\nu}}^{LSS}\ \mathcal{M}^2_{\tilde{\nu}}\ U_{\tilde{\nu}}^{T\ LSS} = \mathrm{diag}(m^2_{\tilde{\nu}_1}, \ldots, m^2_{\tilde{\nu}_9})\ , \tag{11}$$

in complete analogy with Eq. (8).
In these simple setups all other mass matrices are as in the MSSM and, therefore, not discussed here.

2.2 Minimal $SU(3)_c \times SU(2)_L \times U(1)_{B-L} \times U(1)_R$ extension of the MSSM

In order to explain why neutrinos are so much lighter than all other matter particles, we have considered in the previous Section two variants of the seesaw which can, in principle, be implemented at virtually any mass scale. Such seesaw schemes are actually most easily realized in a particular class of extensions of the MSSM with an extended gauge group [1, 470, 471] based on the $SO(10)$ breaking chains

$$SO(10) \ \rightarrow\ SU(3)_c \times SU(2)_L \times SU(2)_R \times U(1)_{B-L} \rightarrow SU(3)_c \times SU(2)_L \times U(1)_Y \tag{12}$$
$$SO(10) \ \rightarrow\ SU(3)_c \times SU(2)_L \times SU(2)_R \times U(1)_{B-L} \tag{13}$$
$$\rightarrow\ SU(3)_c \times SU(2)_L \times U(1)_R \times U(1)_{B-L} \rightarrow SU(3)_c \times SU(2)_L \times U(1)_Y$$

A MSSM-like gauge unification is in this case perfectly viable, and compatible with a $U(1)_R \times U(1)_{B-L}$ stage stretching down to TeV. We will follow Eq. (13), since this variant

	Superfield	$SU(3)_c \times SU(2)_L \times U(1)_R \times U(1)_{B-L}$	Generations
	$\hat{Q}$	$(\mathbf{3}, \mathbf{2}, 0, +\frac{1}{6})$	3
	$\hat{d^c}$	$(\overline{\mathbf{3}}, \mathbf{1}, +\frac{1}{2}, -\frac{1}{6})$	3
	$\hat{u^c}$	$(\overline{\mathbf{3}}, \mathbf{1}, -\frac{1}{2}, -\frac{1}{6})$	3
	$\hat{L}$	$(\mathbf{1}, \mathbf{2}, 0, -\frac{1}{2})$	3
	$\hat{e^c}$	$(\mathbf{1}, \mathbf{1}, +\frac{1}{2}, +\frac{1}{2})$	3
	$\hat{\nu^c}$	$(\mathbf{1}, \mathbf{1}, -\frac{1}{2}, +\frac{1}{2})$	3
	$\hat{S}$	$(\mathbf{1}, \mathbf{1}, 0, 0)$	3
	$\hat{H}_u$	$(\mathbf{1}, \mathbf{2}, +\frac{1}{2}, 0)$	1
	$\hat{H}_d$	$(\mathbf{1}, \mathbf{2}, -\frac{1}{2}, 0)$	1
	$\hat{\chi}_R$	$(\mathbf{1}, \mathbf{1}, +\frac{1}{2}, -\frac{1}{2})$	1
	$\hat{\bar{\chi}}_R$	$(\mathbf{1}, \mathbf{1}, -\frac{1}{2}, +\frac{1}{2})$	1

Table 4.1: The Matter and Higgs sector field content of the $U(1)_R \times U(1)_{B-L}$ model. Generation indices have been suppressed. The $\hat{S}$ superfields are included to generate neutrino masses via the inverse seesaw mechanism. Under matter parity, the matter fields are odd while the Higgses are even.

can be realized with the minimal number of additional superfields with respect to the MSSM particle content. This model [1, 470], which we will call the minimal $U(1)_{B-L} \times U(1)_R$ extension (mBLR, for short) has been studied in two recent papers [210, 211]. We will follow the notation of [211] quite closely.

The particle content of the mBLR model is given in table (4.1). In this setup, the presence of $\hat{\nu}^c$ is required for anomaly cancellation. Breaking the $SU(2)_L \times U(1)_{B-L} \times U(1)_R$ to $U(1)_Q$ requires additional Higgs fields. The vev of the fields χ_R and $\bar{\chi}_R$ break $U(1)_{B-L} \times U(1)_R$, while the vevs of H_u and H_d break $SU(2)_L$ and $U(1)_Y$. Note that since H_u and H_d are charged also under $U(1)_R$, in the mBLR new D-terms are generated in the mass matrix for the scalars. These additional contributions with respect to the MSSM allow to have a larger mass for the lightest MSSM-like CP-even mass eigenstates and makes it possible to have a $m_{h^0} \simeq 125$ GeV without constraints on the supersymmetric particle spectrum [210, 211].

Assuming matter parity [211], apart from the MSSM superpotential the model also has the terms

$$W_S = Y_\nu \hat{\nu^c} \hat{L} \hat{H}_u + Y_s \hat{\nu^c} \hat{\chi}_R \hat{S} - \mu_R \hat{\bar{\chi}}_R \hat{\chi}_R + \mu_S \hat{S} \hat{S}. \tag{14}$$

The 2nd term generates $M_R = \frac{1}{\sqrt{2}} Y_s v_{\chi_R}$ while the last term generates the inverse seesaw discussed above. The model can, in principle, also be written with a linear seesaw included [470]. Note, that the model assigns lepton number necessarily in a different way then discussed in the last subsection, since here $B - L$ is gauged. Thus, $B - L$ is broken by the vevs of χ_R and $\bar{\chi}_R$. However, neutrino masses are generated in exactly the same way as in the simpler inverse seesaw model, discussed in the previous subsection.

It is useful to reparametrize the vevs in a notation similar to the MSSM, i.e.:

$$\begin{aligned} v_R^2 &= v_{\chi_R}^2 + v_{\bar{\chi}_R}^2 \,, \quad v^2 = v_d^2 + v_u^2 \\ \tan\beta_R &= \frac{v_{\chi_R}}{v_{\bar{\chi}_R}} \,, \quad \tan\beta = \frac{v_u}{v_d}. \end{aligned} \tag{15}$$

The mass of the new Z'-boson is approximately (at tree level) given by [211]

$$m_{Z'}^2 = \frac{g_R^4 v^2}{4(g_{BL}^2 + g_R^2)} + \frac{1}{4}(g_{BL}^2 + g_R^2) v_R^2 \,. \tag{16}$$

Thus, v_R must be larger than approximately $v_R \gtrsim 5$ TeV, see also next Section.
Mass matrices for all sfermions for this model can be found in [211]. For us the sneutrino mass matrix is most important. In the mBLR model it is given by the expression for the inverse seesaw, with exception of $M_R = \frac{1}{\sqrt{2}} Y_s v_{\chi_R}$ and new D-term contributions:

$$\begin{aligned} D_{LL}^2 = \;& \tfrac{1}{8} \left((g_{BL}^2 + g_{BLR}^2 - g_{BL} g_{RBL}) v_R^2 \cos(2\beta_R) + (g_L^2 + g_R^2 + g_{BL} g_{RBL}) v^2 \cos 2\beta \right) \\ D_{RR}^2 = \;& \tfrac{1}{8} \Big((g_{BL}^2 + g_R^2 + g_{BLR}^2 + g_{RBL}^2 - 2 g_{BL} g_{RBL} - 2 g_R g_{BLR}) v_R^2 \cos(2\beta_R) \\ & + (g_R^2 + g_{RBL}^2 - g_{BL} g_{RBL} - g_R g_{BLR}) v^2 \cos 2\beta \Big) \end{aligned} \tag{17}$$

Here, D_{LL}^2 replaces D^2 of the simpler models, while D_{RR}^2 are the new D-terms in the $(\tilde{\nu}^c, \tilde{\nu}^c)$ part of the mass matrix. Due to the lower limit for the Z' mass, see Eq. (16), and since the new D-terms in Eq. (17) can have either sign, the free parameter $\tan\beta_R$ is constrained to be close to $\tan\beta_R \simeq 1$, otherwise one of the sneutrinos (or one of the charged sleptons) becomes tachyonic.

3 Phenomenological constraints

In this Section we discuss phenomenological constraints on the parameter space of the different models. Below, we concentrate on neutrino masses and lepton flavour violation. Other constraints on the model space come from SUSY searches at colliders, from Z^0 physics (LEP) and from the Higgs results of the LHC collaborations ATLAS [525] and CMS [526]. "Heavy" singlet neutrinos with mass below the Z^0 boson are excluded by LEP experiments [527–529], which set limits on $|U_{ij}^\nu|^2$ of the order of 10^{-3} to 10^{-5} for the neutrino mass range from 3 GeV up to 80 GeV. L3 has searched also for heavy iso-singlet neutrinos decaying via $N \to lW$ and set limits which range from $|U_{ij}^\nu|^2 \lesssim 2 \times 10^{-3}$ for masses of 80 GeV to $|U_{ij}^\nu|^2 \lesssim 10^{-1}$ for masses of 200 GeV [530]. Most importantly, the invisible width of the Z^0 boson [73] puts an upper limit on the 3×3 sub-block U_{ij}^ν, $i, j \leq 3$, of the neutrino mixing matrix: $\left| 1 - \sum_{ij=1, i \leq j}^3 \left| \sum_{k=1}^3 U_{ik}^\nu U_{jk}^{\nu,*} \right|^2 \right| < 0.009$ at the 3-σ level even when the new mostly singlet neutrinos are heavier than the Z^0 boson [211]. Finally, the Z^0 width rules out pure left sneutrinos lighter than approximately half of the Z^0 mass, but sneutrinos with suppressed coupling to the Z^0 below roughly $0.02 - 0.1$ with respect to the MSSM coupling and masses below $m_{\tilde{\nu}} \lesssim 40$ GeV are allowed.
In inverse seesaw models the Higgs can decay to heavy plus light neutrino, if the heavy neutrino has a mass below the Higgs mass [211, 531]. This limits the Yukawa couplings

to roughly below $|Y_\nu| \lesssim 0.02$ for $M_R \lesssim 120$ GeV from measured data on the channel $h \to WW^* \to ll\nu\nu$ [531]. For larger M_R current Higgs searches provide essentially no constraint yet, unless the lightest sneutrino is lighter than $m_{h^0}/2$. In this case, the upper limit on the branching ratio of the Higgs into invisible final states [532] provides roughly an upper limit on $|Y_\nu|$ of the order of $|Y_\nu| \lesssim 0.2(0.05)$, for $A_0 = 0(2)$ TeV, $M_{1/2} = 1$ TeV and $tan\beta = 10$. The same experimental constraint leads to an upper bound also on the parameter $f_{\tilde{\nu}mix}$ (see Eq. (9)): $f_{\tilde{\nu}mix} \lesssim 0.03(0.06)$.
For the model with the extended gauge group searches for a new Z' boson at the LHC provide important constraints. Both, CMS [533] and ATLAS [534] have searched for, but not observed any hints for, Z''s within the context of different models. For the $U(1)_{B-L} \times U(1)_R$ model the limits are of the order of (roughly) $m_{Z'} \gtrsim (1.7 - 1.8)$ TeV [5].
SUSY searches at ATLAS [535] and CMS [536] provide lower limits on squark and gluino masses. For example, in mSUGRA/CMSSM models with $\tan\beta = 10$, $A_0 = 0$ and $\mu > 0$, squarks and gluinos of equal mass are excluded for masses below 1500 GeV [535]. This limit essentially rules out any value of $M_{1/2}$ below approximately $(600 - 700)$ GeV for $m_0 \lesssim 1000$ GeV and $M_{1/2}$ below $(350-400)$ GeV in the limit of large m_0 for pure CMSSM. Of course, the observation of a new resonance with a mass around $125 - 126$ GeV [525, 526], if interpreted as the lightest Higgs boson, provides important constraints on SUSY parameters as well. However, these constraints are different for the different models we study in this Chapter. We will discuss them therefore when we discuss numerical scans in Section 4.

3.1 Neutrino masses

Inverse seesaw

In the inverse seesaw the neutrino mass matrix can be written at tree-level as

$$M^\nu = \begin{pmatrix} 0 & m_D^T & 0 \\ m_D & 0 & M_R \\ 0 & M_R^T & \mu_S \end{pmatrix}. \tag{18}$$

The smallness of the observed neutrino masses is then usually explained as the hierarchy $\mu_S \ll m_D < M_R$.
Following the notation of [537], we can count the number of physical parameters of the model as $N_{\rm phys} = N_Y - N_G + N_{G'}$. Here, N_Y is the number of parameters in the Yukawa matrices (or mass matrices), N_G the number of generators of the original symmetry group G which is broken into G' by the presence of the Yukawas (or mass terms). In table 4.2 the counting for the inverse seesaw is summarized.
After absorbing all unphysical parameters by field rotations, we find a total of 30 real parameters, 21 moduli (12 masses and 9 mixing angles) plus 9 phases. It is common practice to choose a basis in which the charged lepton mass matrix (Yukawa: Y_e) is diagonal, which fixes 3 parameters. The remaining parameters could be fixed by going to a basis where M_R is real and diagonal. In this case Y_ν and μ_S are completely general, arbitrary matrices,

[5] These values were valid at the time of publication of this work. Current limits are: $m_{Z'} \gtrsim 2.86$ TeV for a SM-like Z' and $m_{W_R} \gtrsim 1.8$ TeV [472].

	Parameters	Moduli	Phases
N_Y	Y_e, Y_ν, M_R Dirac type	$3 \times n^2$	$3 \times n^2$
N_Y	μ_S Majorana type	$\frac{n(n+1)}{2}$	$\frac{n(n+1)}{2}$
N_G	$U(n)_L \bigotimes U(n)_{\nu^c} \bigotimes U(n)_{e^c} \bigotimes U(n)_S$	$4 \times \frac{n(n-1)}{2}$	$4 \times \frac{n(n+1)}{2}$
$N_{G'}$	no LF conservation		
N_{phys}		21	9

Table 4.2: Parameter counting for MSSM with an inverse seesaw for three generations.

containing the remaining 24 free parameters. For fitting the neutrino data, however, it is more useful to first rewrite the neutrino Yukawa couplings using a generalization of the Casas-Ibarra parametrization [538].
Consider first the effective mass matrix of the light neutrinos for the inverse seesaw. It is given by

$$m_\nu^{eff} = m_D^T M_R^{T^{-1}} \mu_S M_R^{-1} m_D. \tag{19}$$

We can rewrite m_D as [539]

$$m_D = M_R^T V_\mu^T (\sqrt{\hat{\mu}_S})^{-1} R \mathrm{Diag}(\sqrt{m_{\nu_i}}) U_\nu. \tag{20}$$

Here U_ν is the mixing matrix determined by the oscillation experiments, in the basis where the charged lepton mass matrix is diagonal, m_{ν_i} are the three light neutrino masses, R is an arbitrary real orthogonal 3×3 matrix and $\hat{\mu}_S$ are the eigenvalues of the matrix μ_S with V_μ the matrix which diagonalizes μ_S.
Eqs (19) and (20) allow to fit neutrino data in a straightforward way, if the tree-level contribution dominates, see below. Since one can always choose a basis where M_R is diagonal, the flavour violation necessary to fit oscillation data resides in m_D and in μ_S. Particularly simple solutions are found, assuming either μ_S or m_D are diagonal too. For diagonal μ_S, for example, one finds

$$m_D = \mathrm{Diag}(\sqrt{\frac{m_{\nu_i}}{\mu_{S_i}}} M_{R_i}) U_\nu. \tag{21}$$

Oscillation experiments have determined the mass squared differences and mixing angles of the active neutrinos with high precision, see for example [77]. Recently also the last of the mixing angles in the left-handed neutrino sector has been measured in two reactor neutrino experiments, DAYA-BAY [57] and RENO [58]. With all these data, the situation can be summarized as follows: The atmospheric neutrino mass squared difference and angles are $\Delta(m^2_{\mathrm{Atm}}) = (2.31 - 2.74) \times 10^{-3}$ eV^2 (normal hierarchy) and $\sin^2\theta_{\mathrm{Atm}} = 0.36 - 0.68$, the solar parameters are $\Delta(m^2_\odot) = (7.12 - 8.20) \times 10^{-5}$ eV^2 and $\sin^2\theta_\odot = 0.27 - 0.37$ and finally $\sin^2\theta_{13} = 0.017 - 0.033$, all at 3 σ c.l. [77]. Apart from the data on the reactor

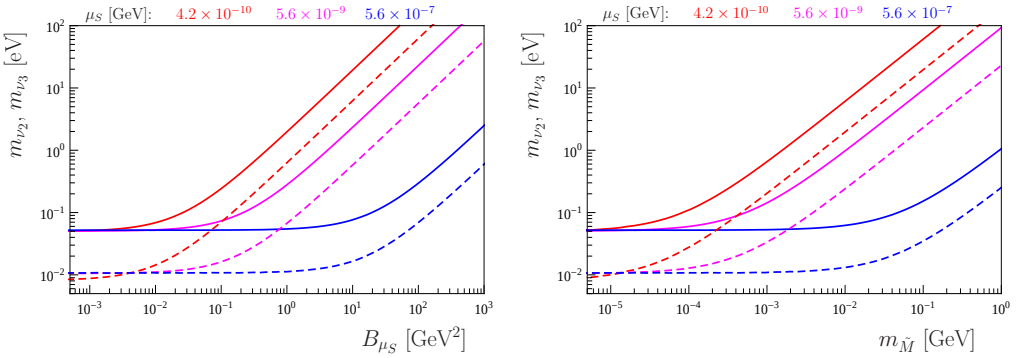

Figure 4.1: Neutrino masses versus B_{μ_S} (left) and versus $m_{\tilde{M}}$ (right) for one particular but arbitrary parameter point (see text), for three different values of μ_S.

angle, neutrino angles are still well-fitted by the tribimaximal mixing ansatz [540], which has $\sin^2\theta_{\rm Atm} = 1/2$ and $\sin^2\theta_\odot = 1/3$.

The large atmospheric and solar angles require large off-diagonals in at least one of the two matrices Y_ν or μ_S. For the case of strict normal hierarchy ($m_{\nu_1} \equiv 0$) and diagonal μ_S, oscillation data can be well fitted to leading order in the small parameter $\sin\theta_{13}$ by

$$Y_\nu = |Y_\nu| \begin{pmatrix} 0 & 0 & 0 \\ a & a(1-\frac{\sin\theta_{13}}{\sqrt{2}}) & -a(1+\frac{\sin\theta_{13}}{\sqrt{2}}) \\ \sqrt{2}\sin\theta_{13} & 1 & 1 \end{pmatrix} , \tag{22}$$

with

$$a = \left(\Delta m^2_\odot / \Delta m^2_{\rm Atm}\right)^{\frac{1}{4}} \sim 0.4 , \tag{23}$$

where $|Y_\nu|$ can be easily calculated from μ_S and M_R.

The above discussion is valid at tree-level. In the inverse seesaw neutrino masses also receive important corrections at the 1-loop level, once B_{μ_S} becomes sizeable [524]. An example is shown in Fig. 4.1. Here, we have chosen as an example $m_0 = 100$, $M_{1/2} = 1000$, $A_0 = 0$ (all in GeV) $\tan\beta = 10$, $\mathrm{sgn}(\mu) > 0$ and $M_R = 250$ GeV. For this plot we assume μ_S and $B_{M_R} = 3\times 10^4$ GeV^2 to be diagonal and degenerate. Y_ν is then fitted by Eq. (20). A smaller value of μ_S implies then a larger value for the entries in Y_ν.

In the left of Fig. 4.1 we show m_{ν_2} and m_{ν_3} as function of B_{μ_S}, while the plot on the right shows the same neutrino masses as a function of $m^2_{\tilde{M}}$, the mass squared difference between the CP-even and CP-odd sneutrinos. This splitting is proportional to B_{μ_S}, while loop neutrino masses are proportional to $Y_\nu^2 B_{\mu_S}$. To restrict the neutrino mass to be smaller than the atmospheric scale than results in an upper limit on $Y_\nu^2 B_{\mu_S}$. For $|\mu_S| \sim 5\times 10^{-7}$ GeV, corresponding to the largest entries in Y_ν to be of order $\mathcal{O}(10^{-2})$, the splitting can be as large as $\mathcal{O}(10^{-1})$ GeV. Note, however, that with typical mSugra-like boundary conditions one expects naively that $B_{\mu_S} \simeq \mu_S m_0 \sim 10^{-4} - 10^{-7}$ GeV^2. In this case splitting between the sneutrinos becomes negligible.

Linear seesaw

For the linear seesaw the neutrino mass matrix is given by

$$M^\nu = \begin{pmatrix} 0 & m_D^T & M_L^T \\ m_D & 0 & M_R \\ M_L & M_R^T & 0 \end{pmatrix}, \tag{24}$$

with the effective neutrino mass matrix for the light neutrinos given as

$$m_\nu = m_D^T M_R^{T^{-1}} M_L + M_L^T M_R^{-1} m_D. \tag{25}$$

For the linear seesaw one finds for the CI parametrization [539]

$$m_D = -M_R (M_L^T)^{-1} U_\nu^T \sqrt{m_{\nu_i}} A \sqrt{m_{\nu_i}} U_\nu \tag{26}$$

where A has the following general form:

$$\begin{pmatrix} \frac{1}{2} & a & b \\ -a & \frac{1}{2} & c \\ -b & -c & \frac{1}{2} \end{pmatrix}, \tag{27}$$

with a, b, c real, but arbitrary numbers. The parameter counting for the linear seesaw is given in table (4.3). We have in total 36 real parameters, 24 moduli (12 masses and 12 mixing angles) plus 12 phases. Fits to neutrino data can be easily done using Eqs. (25) and (26).
For example, for strict normal hierarchy, degenerate M_R and diagonal and degenerate Y_{SL} one finds to leading order in θ_{13}

$$\begin{aligned} Y_\nu = |Y_\nu| \{ \; &- \frac{m_{\text{Atm}}}{2} \begin{pmatrix} 0 & \frac{\sin\theta_{13}}{\sqrt{2}} & \frac{\sin\theta_{13}}{\sqrt{2}} \\ \frac{\sin\theta_{13}}{\sqrt{2}} & \frac{1}{2} & \frac{1}{2} \\ \frac{\sin\theta_{13}}{\sqrt{2}} & \frac{1}{2} & \frac{1}{2} \end{pmatrix} \\ &+ \frac{m_\odot}{3} \times \Big(\begin{pmatrix} -1 & -1 & 1 \\ -1 & -1 & 1 \\ 1 & 1 & -1 \end{pmatrix} + \sqrt{2} \sin\theta_{13} \times \begin{pmatrix} 0 & \frac{1}{2} & \frac{1}{2} \\ \frac{1}{2} & 1 & 0 \\ \frac{1}{2} & 0 & -1 \end{pmatrix} \Big) \}, \end{aligned} \tag{28}$$

where again, the prefactor $|Y_\nu|$ can be calculated from $|Y_{SL}|$ and M_R. Note that the flavour structure of Eq. (28) differs significantly from Eq. (22) for the same choice of angles, see the discussion about lepton flavour violation in the next subsection.
In case of the linear seesaw, loop contributions to the neutrino masses from the splitting in the sneutrino sector is always negligible for neutrino masses in the sub-eV range, assuming the trilinears to be proportional to $T_x \propto Y_x A_0$. This can be understood as follows: The difference in the eigenvalues of the CP-even and CP-odd sector is entirely due to the different signs in the off-diagonals in Eq. (10). As can be easily shown, the maximum difference in the eigenvalues is reached for $Y_{SL} \simeq Y_\nu$. However, Eq. (25) shows that the product $Y_{SL} Y_\nu$ is required to be small, due to the observed smallness of neutrino masses. Thus, the splitting in the sneutrino sector in case of linear seesaw is maximally of the order of $m_\nu m_{SUSY}$, i.e. $\mathcal{O}(10^{-9})$ GeV^2.

	Parameters	Moduli	Phases
N_Y	Y_e, Y_ν, Y_{SL}, M_R Dirac type	$4 \times n^2$	$4 \times n^2$
N_G	$U(n)_L \bigotimes U(n)_{\nu^c} \bigotimes U(n)_{e^c} \bigotimes U(n)_S$	$-4 \times \frac{n(n-1)}{2}$	$-4 \times \frac{n(n+1)}{2}$
$N_{G'}$	no LF conservation		
N_{phys}		24	12

Table 4.3: Parameter counting for the linear seesaw model for three generations.

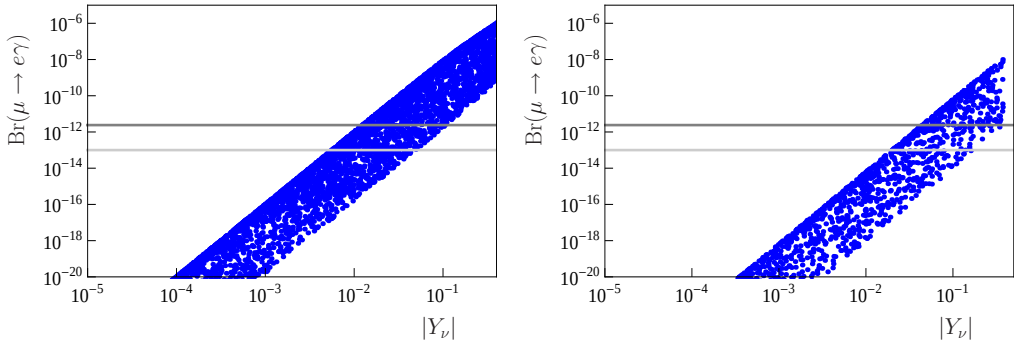

Figure 4.2: Br($\mu \to e\gamma$) calculated in the inverse (left) and linear (right) seesaw. Here, all flavour has been put into the Yukawa Y_ν, while neutrino angles have been fitted to their best fit point values [77]. A random scan over m_0 and M_R in the interval [100,1000] GeV and $B_{M_R} = [10^3, 10^6]$ GeV^2 has been performed for these points. Note that the axes are the same for inverse and linear seesaw for an easier comparison. Linear seesaw leads to smaller LFV than inverse seesaw for equal choice of neutrino angles.

3.2 Lepton flavour violation

In any supersymmetric model, limits on lepton flavour violating decays such as $\mu \to e\gamma$ provide an important constraint on the parameter space [541]. In models with a low scale seesaw especially important constraints come from $l_i \to 3l_j$ [542] and from $\mu - e$ conversion in nuclei [543].

The fit to neutrino data requires non-trivial flavour violating entries in at least one of the Yukawa or mass matrices: Y_ν or Y_{SL} for linear and Y_ν or μ_S for inverse seesaw. If we assume that the LFV resides in Y_ν, limits on the Yukawa result as shown in Fig. 4.2. In this figure we have chosen μ_S (left) or Y_{SL} (right) diagonal and neutrino angles have been fitted to their best fit point values [77] using Y_ν. A random scan over m_0 and M_R in the interval [100,1000] GeV and $B_{M_R} = [10^3, 10^6]$ GeV^2 has been performed for these points, fixing $\tan\beta = 10$ and $M_{1/2} = 2.5$ TeV. Upper limits of the order of (few) 10^{-2} (10^{-1}) result for inverse (linear) seesaw, despite the heavy SUSY spectrum (due to the large value of $M_{1/2}$). Much stronger limits result for lighter spectra. Note that $l_i \to 3l_j$ [542] and $\mu - e$ conversion in nuclei [543] can lead to even stronger limits. We will not repeat this exercise here.

Note also, as discussed in the next Section, that the constraints from relic density of sneutrinos lead to an approximate lower bound on the absolute size of the Yukawa coupling

$|Y_\nu|$.

4 Sneutrino Dark Matter

In this Section we discuss the relic abundance (RA) and the direct detection cross section (DD) of sneutrinos in the different models. We will first discuss the simpler case of the inverse/linear seesaw and then turn to the mBLR model.

In order to reduce the number of free parameters in our numerical scans, we calculate all spectra with CMSSM-like boundary conditions, i.e. we choose $(m_0, M_{1/2}, A_0, \tan\beta, \mathrm{sgn}(\mu))$, from which all soft parameters at the electro-weak scale are calculated using full 2-loop RGEs. Unless noted otherwise, we always assume that the trilinear soft parameters are related to the superpotential parameters in a "mSugra"-like way: $T_\alpha \propto Y_\alpha A_0$ at m_{GUT}.

In addition to the MSSM parameters, we have the neutrino Yukawa couplings Y_ν and several model specific parameters. These are M_R and B_{M_R} and, in case of the inverse (linear) seesaw μ_S and B_{μ_S} (Y_{SL}). While, in principle, all of these are matrices we use Eq. (20) and (26) to fit neutrino data and usually assume all matrices are diagonal except one.

For the mBLR model we have the free parameters Y_s, v_R, $\tan\beta_R$, μ_R and m_{A_R}. Recall, $M_R = Y_s v_R/\sqrt{2}$ and m_{A_R} is the CP-odd scalar Higgs mass in the χ_R sector. Due to the constraints from LFV discussed above, we usually put all LFV into either μ_S (inverse seesaw) or Y_{SL} (linear seesaw). This way we only have to check for the constraints from Z^0 and Higgs physics and lower limits on squarks and gluinos discussed in Section 3.

4.1 Inverse/Linear seesaw

Sneutrinos can be made the LSP, practically independent from the actual choice of the CMSSM parameters. This can be easily understood from Eqs. (7) and (9) and is demonstrated by two simple examples in Fig. 4.3.

In Fig. 4.3 we show two examples of tree-level sneutrino masses calculated as function of B_{M_R} for two particular but arbitrary choices of parameters: $m_0 = 100$, $M_{1/2} = 1000$, $A_0 = 0$ and $\mu = 800$ all in GeV and $|Y_\nu| = 0.1$ and $\tan\beta = 10$. In addition, $M_R = 200$ GeV (left) and $M_R = 500$ GeV (right). This calculation was made in a one generation toy model and serves only for illustration. The general behaviour is easily understood. First, recall that within CMSSM roughly $m_{\chi_1^0} \sim m_{\tilde{B}} \sim 0.4 M_{1/2}$. Entries on the diagonals of the sneutrino mass matrix are of the order $m^2_{LL} \simeq m_0^2 + 0.5 M_{1/2}^2$, $m^2_{\nu^c\nu^c} \simeq m_0^2 + M_R^2$ and $m^2_{SS} \simeq m_0^2 + M_R^2$. If $\sqrt{m_0^2 + M_R^2} \lesssim 0.4 M_{1/2}$ (one of the pair of) right sneutrinos is the LSP, see left plot. On the other hand, for larger values of m_0 and or M_R, right sneutrinos still can be the LSP if $B_{M_R} \gtrsim \sqrt{m_0^2 + M_R^2}$, since in this case a large off-diagonal in the sneutrino mass matrix leads to a large splitting between the two lightest eigenstates, with the lighter one becoming very light, see right plot. Since B_{M_R} is naively expected to be of order m^2_{SUSY}, sizeable splitting between the right sneutrinos is expected and in a random scan over parameters such sneutrinos emerge as LSP quite often. Note, that a light eigenvalue in the sneutrino sector can also be made by a large off-diagonal in the sneutrino mass matrix in the LR and LS entries of the mass matrix.

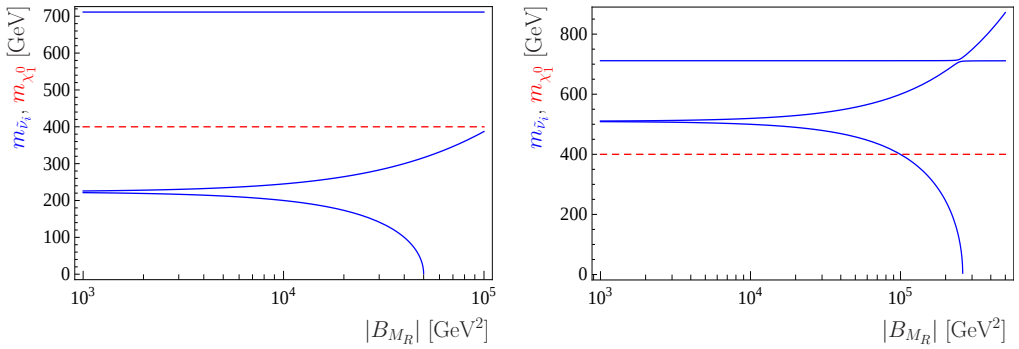

Figure 4.3: Two examples of tree-level sneutrino masses calculated as function of B_{M_R} for two particular but arbitrary choices of parameters: $m_0 = 100$, $M_{1/2} = 1000$, $A_0 = 0$ and $\mu = 800$ all in GeV and $|Y_\nu| = 0.1$ and $\tan\beta = 10$. In addition $M_R = 200$ GeV (left) and $M_R = 500$ GeV (right). For comparison also the lightest neutralino mass is shown.

In the early universe sneutrinos can annihilate into SM particles through various types of interactions. The most important Feynman diagrams are shown in Figs 4.4 and 4.5. Fig. 4.4 shows the quartic interaction between two sneutrinos and two Higgses and s-channel Higgs exchange. The former is very efficient for $m_{\tilde{\nu}_{LSP}} \geq m_{h^0}$, while the latter is important near $m_{\tilde{\nu}_{LSP}} \simeq m_{h^0}/2$. Fig. 4.5 shows the quartic interaction with W- and Z-bosons and t-channel neutralino exchange. The importance of the latter depends on the SUSY spectrum.

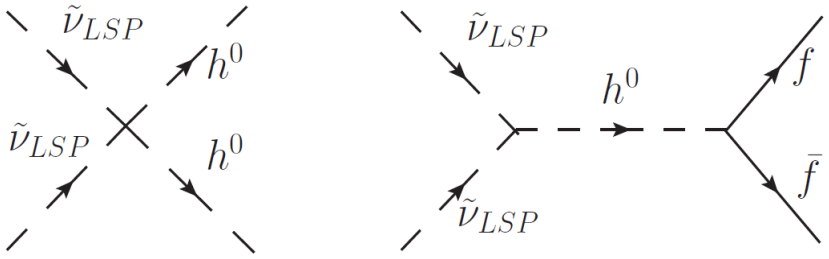

Figure 4.4: Examples of Feynman diagrams contributing to the $\tilde{\nu}_{LSP}\tilde{\nu}_{LSP}$ annihilation: To the left quartic interaction; to the right s-channel Higgs exchange.

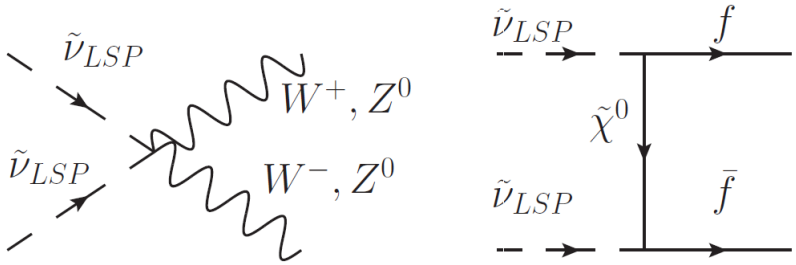

Figure 4.5: Examples of Feynman diagrams contributing to the $\tilde{\nu}_{LSP}\tilde{\nu}_{LSP}$ annihilation: To the left quartic interaction with gauge bosons; to the right t-channel neutralino exchange.

The relative importance of different diagrams is strongly dependent on the kinematical regime. A typical example of final state branching ratios versus the lightest sneutrino mass is shown in fig (4.6). In this scan we have fixed $m_0 = 120$, $M_{1/2} = 600$, $A_0 = 0$ all in GeV and $|Y_\nu| = 0.4$ and $\tan\beta = 10$. In addition $\mu_S = [10^{-11}, 10^{-9}]$ GeV.

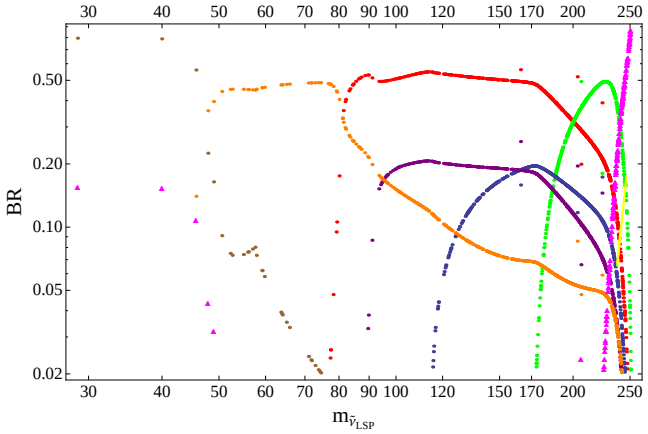

Figure 4.6: Examples of final state branching ratios for the annihilation cross section of sneutrinos to SM final states versus the lightest sneutrino mass (in GeV). For the parameter choices of this scan, see text. Calculation uses the inverse seesaw model. Different kinematical regimes are visible, see discussion.

From left to right we see that the most important channels are $\tilde{\nu}_{LSP}\tilde{\nu}_{LSP} \longrightarrow \tau\overline{\tau}$ (magenta with triangles), $\tilde{\nu}_{LSP}\tilde{\nu}_{LSP} \longrightarrow b\bar{b}$ (brown), $\tilde{\nu}_{LSP}\tilde{\nu}_{LSP} \longrightarrow \nu\nu^c$ (orange), $\tilde{\nu}_{LSP}\tilde{\nu}_{LSP} \longrightarrow W^+W^-$ (red), $\tilde{\nu}_{LSP}\tilde{\nu}_{LSP} \longrightarrow Z^0Z^0$ (purple), $\tilde{\nu}_{LSP}\tilde{\nu}_{LSP} \longrightarrow HH$ (blue), $\tilde{\nu}_{LSP}\tilde{\nu}_{LSP} \longrightarrow t\bar{t}$ (green); finally, to the right of the figure, the contributions coming from the coannihilations are shown: $\tilde{e}\tilde{e} \longrightarrow \tau\tau$ (magenta with triangles), and $\tilde{e}\overline{\tilde{e}} \longrightarrow \gamma\gamma$ (in yellow).
For low sneutrino masses the determination of the relic abundance is dominated by Higgs exchange, see Fig. 4.4 right. Since the Higgs couplings are proportional to SM fermion masses, $b\bar{b}$ is most important in the low mass regime, followed by $\tau\overline{\tau}$. For sneutrino masses above approximately $m_{\tilde{\nu}_{LSP}} \sim 45$ GeV the final state $\nu\nu$ becomes dominant in this example. This is because with these parameter choices the lightest of the "singlet" neutrinos has a mass of about 45 GeV and the Higgs couples always to $\nu_L\nu^c$, i.e. one light and one heavy neutrino.
Single Z^0 exchange is less important than Higgs exchange, since scalar-scalar-vector couplings are momentum suppressed. For $m_{\tilde{\nu}_{LSP}} \gtrsim 80$ GeV, however, two gauge boson final states become dominant, the channel W^+W^- being more important than Z^0Z^0. For masses above $m_{\tilde{\nu}_{LSP}} \gtrsim 120$ GeV also two Higgs final states are sizable. All these final states are due to quartic interactions, see Fig. 4.4 left and Fig. 4.5. Due to the large top Yukawa coupling, the two top final state, once kinematically possible, becomes very important. And, finally, for $m_{\tilde{\nu}_{LSP}}$ approaching the NLSP mass, in this example the lightest scalar tau, coannihilation into taus becomes dominant.
Next, we have performed a general scan over the parameter space of the model choosing randomly $(m_0, M_{1/2}, A_0, \tan\beta, \mathrm{sgn}(\mu))$ in the interval $m_0 = [100, 3000]$, $M_{1/2} = [200, 3000]$, $A_0 = 0$, $\tan\beta = 10$ and $\mathrm{sgn}(\mu) > 0$ and $|Y_\nu| = 0.3$, $M_R = [0, 1000]$. B_{M_R} is calculated

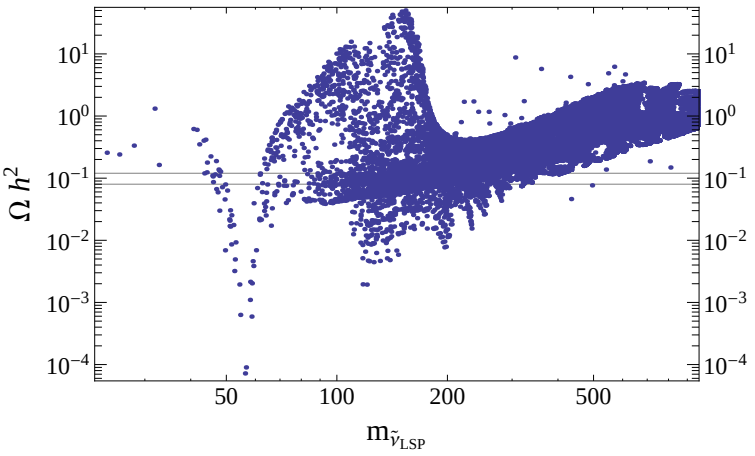

Figure 4.7: General scan for the inverse seesaw model. The plot shows Ωh^2 versus the mass of the lightest sneutrino (in GeV) for points in which the sneutrino is the LSP.

accordingly to enhance the percentage of sneutrino LSP points. We post-select data points with sneutrino LSPs and cut on all points not fulfilling the lower bounds on squark and gluinos masses from the LHC [535]. Results are shown in Fig. 4.7 for the case of the inverse seesaw. Shown is the calculated RA (Ωh^2) versus the mass of the lightest sneutrino for points in which the sneutrino is the LSP. The band, which is the allowed range from WMAP [544], shows that one can easily get points with the correct relic abundance over a wide range of parameters. The figure is for the inverse seesaw, linear seesaw is qualitatively very similar.

The plot shows several distinct features. First, for masses of sneutrinos around $m_{\tilde{\nu}_{LSP}} \simeq 60$ GeV a strong reduction of the RA occurs, due to the s-channel Higgs exchange. As can be seen, this diagram is very effective in reducing the RA whenever $m_{\tilde{\nu}_{LSP}}$ is within a few GeV of the mass of the Higgs, but less important elsewhere. In the region above $m_{\tilde{\nu}_{LSP}} = 80$ GeV, quartic interactions with the gauge bosons are effective and above $m_{\tilde{\nu}_{LSP}} = 175$ GeV two-top final states become dominant. For very large $m_{\tilde{\nu}_{LSP}}$ one sees an overall trend that the RA rises with rising sneutrino mass, apart from a few scattered points. Low RA, i.e. $\Omega h^2 \simeq 0.1$, in this high mass regime can practically only be made via co-annihilation or s-channel heavy Higgs exchange. Note that the fact that there are only a few points with $m_{\tilde{\nu}_{LSP}}$ below 50 GeV is just an artifact of the scanning procedure. However, the general trend is that for very light sneutrinos the calculated RA is larger than $\Omega h^2 \sim 0.1$. These light sneutrinos would require $|Y_\nu| \gtrsim 0.2$, which is incompatible with the constraints coming from the invisible Higgs decay into sneutrinos, as commented in Section 3.

We will come back to a more detailed discussion of light sneutrinos in the next Section.

In Fig. 4.7 we have fixed the neutrino Yukawa couplings to a constant value. However, sneutrinos which are purely singlets do not couple to gauge bosons and thus their relic abundance is usually too large. For mixed sneutrinos the RA depends strongly on the choice of $|Y_\nu|$. An example is shown in Fig. 4.8. The figure shows on the left (right) results for the inverse (linear) seesaw. In both cases we have fitted neutrino data, using Eqs. (20) and (26), and scanned over the parameters: m_0 and M_R in the interval [100,1000] GeV and $B_{M_R} = [10^3, 10^6]$ GeV^2. Here, $M_{1/2}$ was fixed to $M_{1/2} = 2.5$ TeV and $\tan\beta = 10$ and $A_0 = 0$.

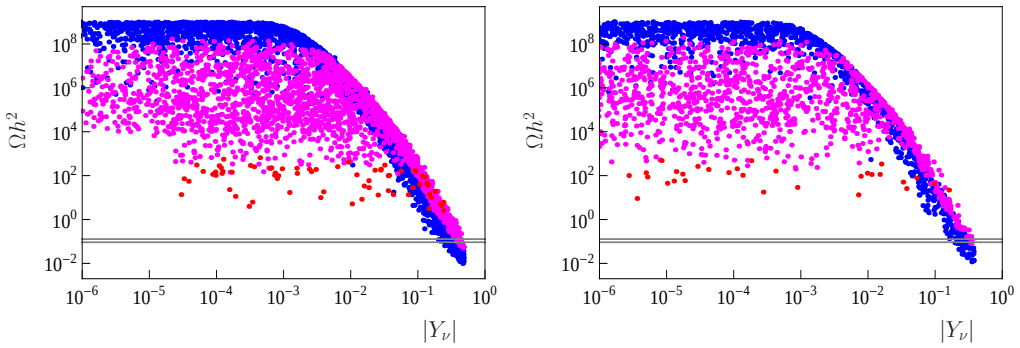

Figure 4.8: Scan for the inverse (left) and linear (right) seesaw model. The plot shows Ωh^2 versus $|Y_\nu|$ in a scan over the remaining parameters, see text. The color coding of the points shows the mass difference between the lightest sneutrino mass and the NLSP (next-to-LSP) mass, in this scan practically always the lightest of the charged sleptons. Red: $m_{NLSP} - m_{LSP} < 100$ GeV, violet: $100 < m_{NLSP} - m_{LSP} < 500$ GeV, blue: $m_{NLSP} - m_{LSP} > 500$ GeV. For a discussion see text.

The choice of such a large $M_{1/2}$ guarantees that all points have a lightest Higgs mass in the vicinity of 125 GeV. It also makes all SUSY particles, except the sneutrino, relatively heavy. The points in Fig. 4.8 are color coded by the mass difference between the lightest sneutrino mass and the NLSP (next-to-LSP) mass, in this scan practically always the lightest of the charged sleptons. Red: $m_{NLSP} - m_{LSP} < 100$ GeV, violet: $100 < m_{NLSP} - m_{LSP} < 500$ GeV, blue: $m_{NLSP} - m_{LSP} > 500$ GeV. For large $|Y_\nu|$ the RA goes down as $\Omega h^2 \propto |Y_\nu|^{-4}$, for small values of Y_ν the points show practically no dependence on $|Y_\nu|$. This is because the determination of the RA is then dominated by coannihilation processes with the lightest stau. These can be very efficient, if $\Delta m^2 = m_{\tilde{l}}{}^2 - m_{\tilde{\nu}_{LSP}}{}^2 \simeq$ few GeV, less so for larger mass differences. Thus, to reduce the relic density of the sneutrino to acceptably small values, one needs either a special kinematic configuration, such as co-annihilation or s-channel resonance, or $|Y_\nu|$ has to be larger than roughly $|Y_\nu| \gtrsim 0.1$.

Direct Detection

Direct detection of the sneutrinos consists in detecting the recoil energy coming from the elastic scattering of sneutrinos with nuclei inside a detector. The interaction, which occurs in the non relativistic limit, since the velocity of DM particles in the Galactic halo is small, comes from basically two diagrams contributing at tree level: the t-channel exchange of a neutral Higgs or of the Z boson (see fig(4.9)). Which of the two diagrams is the more important one depends on the actual value of $|Y_\nu|$.
The Z–boson exchange cross section is [508]:

$$\sigma^Z_{\tilde{\nu}_{LSP}\,\mathcal{N}} = \frac{G_F^2}{2\pi} \frac{m^2_{\tilde{\nu}_{LSP}} m^2_{\mathcal{N}}}{(m_{\tilde{\nu}_{LSP}} + m_{\mathcal{N}})^2}\, \mathrm{f}^4_{\tilde{\nu}\mathrm{mix}}\, \left[\mathrm{A}_{\mathcal{N}} + 2(2\sin^2\theta_\mathrm{W} - 1)\mathrm{Z}_{\mathcal{N}}\right]^2 \tag{29}$$

where $m_{\mathcal{N}}$ is the nucleus mass, $A_{\mathcal{N}}$ and $Z_{\mathcal{N}}$ are the mass number and proton number of the nucleus, $f_{\tilde{\nu}mix}$ is the factor which takes into account the mixing between the sneutrino states, see Eq. (9), and G_F is the Fermi constant.

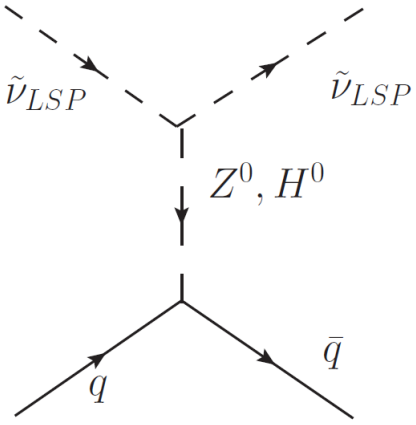

Figure 4.9: Diagrams contributing to the direct detection cross section: elastic scattering of $\tilde{\nu}_{LSP}$ over quarks.

The Higgs–bosons exchange scattering cross section is [508]:

$$\sigma^{Higgs}_{\tilde{\nu}_{LSP}\,\mathcal{N}} = \frac{m_p^2}{4\pi(m_{\tilde{\nu}_{LSP}} + m_{\mathcal{N}})^2}\left[f_p Z_{\mathcal{N}} + f_n\left(A_{\mathcal{N}} - Z_{\mathcal{N}}\right)\right]^2 \tag{30}$$

where $\mathcal{N}$ denotes the nucleus, and the quantities $A_{\mathcal{N}}$ and $Z_{\mathcal{N}}$ are the mass number and proton number of the nucleus, f_p and f_n are hadronic matrix elements which parametrize the quark composition of the proton and the neutron, and which represent the effective coupling of the $\tilde{\nu}_{LSP}$ to the nucleus, but are subject to considerable uncertainties [508, 545].

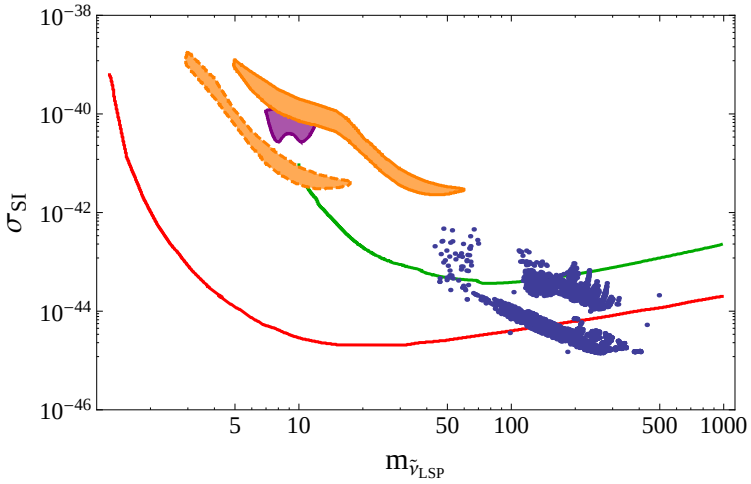

Figure 4.10: Direct detection cross section (in $[cm^2]$) for sneutrino LSPs (masses in GeV), for the inverse seesaw model. The points are those from Fig. 4.7 compatible with the upper bound on the relic abundance. Also the current limits from XENON-100 [546] (red line), CDMS [265] (green line), DAMA (with and without channeling, orange regions) [289], and Cogent [269] (purple region) are shown for comparison.

In figure (4.10) we depict the direct detection cross section versus the LSP sneutrino mass (blue points). The points are the same as shown in Fig. 4.7, but after a cut on the relic abundance. In the same plot, the current limits from XENON-100 [546] (red line), CDMS [265] (green line), DAMA (with and without channeling, orange regions) [289], and Cogent [269] (purple region) are shown. The major bound nowadays comes from the XENON-100 experiment [546], whose best sensitivity is around 10^{-44}cm^2 for a DM candidate of 50 GeV. The sneutrinos show a SI cross section $\sigma_{SI} \lesssim 10^{-42}\text{cm}^2$, and for masses $m_{\tilde{\nu}_{LSP}} \gtrsim 100$ GeV they are compatible with current limits by XENON-100. However, XENON-1T, whose sensibility should improve up to 10^{-46}cm^2, will test those cross sections.
We have not been able to find low sneutrino masses of the order of $\mathcal{O}(5-10)$ GeV, which have the correct relic density and fulfill at the same time the constraints from the direct detection experiment XENON-100 [546]. However, this calculation has been done with $B_{\mu_S} \propto m_0\mu_S$ and lepton number violation in the sneutrino mass matrix leads to the mass splitting between the real and the imaginary part of the lightest sneutrino, and the scattering via Z boson exchange occurs inelastically, through a transition from the real to the imaginary or viceversa. Points shown in Fig. 4.10 have all very small splitting in the sneutrino sector, but if the mass splitting is greater than some keV, scattering is strongly suppressed at direct detection experiments. Indeed, the maximum kinetic energy that the sneutrino LSP can transfer to the detector depends on the velocity it moves relative to the nucleus v ($\simeq 10^{-3}$ in the galactic halo),the nucleus mass M and the angle θ of scattering:

$$E = \frac{A^2v^2}{M}(1 - cos(\theta)) \tag{31}$$

where $A = \frac{m_{\tilde{\nu}_{LSP}}M}{m_{\tilde{\nu}_{LSP}}+M}$, which would give, in the case of a Xenon detector for instance, and $m_{\tilde{\nu}_{LSP}} = 100$ GeV, E = 25 keV (if $\cos(\theta) = 0$). For heavier sneutrinos with a mass of the order of TeV, for a splitting larger than some hundred keV the direct detection cross section goes to zero. Such "large" splitting is currently not excluded in the inverse seesaw, compare to Fig. 4.1. Thus, in principle inverse seesaw can evade the constraints from direct detection, when the Z-boson exchange diagram is the dominant contribution to the direct detection cross section, while linear seesaw can not, see the discussion in Section 3.1.

4.2 mBLR model

In this subsection we discuss the DM phenomenology of the supersymmetric $U(1)_R \times U(1)_{B-L}$ extension of the standard model. The main difference to the simpler models discussed previously are the presence of the extra gauge boson Z' and the possibility to have an additional light, mostly singlet Higgs boson, which lead to some important changes in the phenomenology.
First, recall that the $U(1)_R \times U(1)_{B-L}$ gauge symmetry of this model is spontaneously broken to the hypercharge group $U(1)_Y$ by the vevs v_{χ_R} and $v_{\bar{\chi}_R}$ of the scalar components of the $\hat{\chi}_R$ and $\hat{\bar{\chi}}_R$ superfields whereas the $SU(2)_L \otimes U(1)_Y \to U(1)_Q$ breaking is driven by the vevs v_d and v_u of the neutral scalar components of the $SU(2)_L$ Higgs doublets H_d and H_u up to gauge kinetic mixing effects. The tadpole equations for the different vevs can

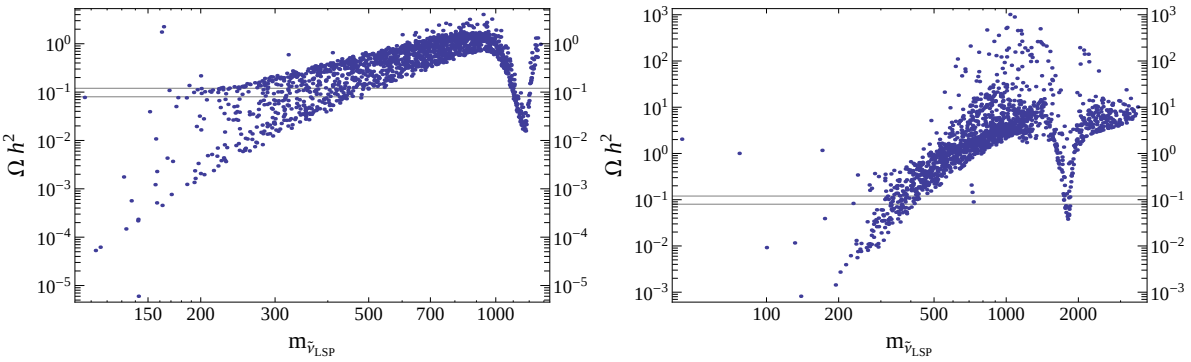

Figure 4.11: Scan for the CmBLR version of the extended gauge model. Parameters are varied as follows: $m_0 = [0, 6000]$ GeV, $M_{1/2} = [3000, 8000]$ GeV, $\tan\beta_R = [1.0,1.3]$. The other parameters are set to the values $\tan\beta$=10, $A_0 = -4500$ GeV, $Y_S = \mathrm{diag}(0.3)$; v_R has been chosen different in the two plots, $v_R = 6$ TeV and $v_R = 10$ TeV, respectively. Masses of the $\tilde{\nu}_{LSP}$ are in GeV.

be solved analytically for either (i) ($\mu, B_\mu, \mu_R, B_{\mu_R}$) or (ii) ($\mu, B_\mu, m^2_{\chi_R}, m^2_{\bar{\chi}_R}$) or (iii) ($m^2_{H_d}$, $m^2_{H_u}$, $m^2_{\chi_R}$, $m^2_{\bar{\chi}_R}$) [211].

We address the minimal version option (i) as CmBLR (constrained mBLR), since it allows to define boundary conditions for all scalar soft masses at m_{GUT}, reducing the number of free parameters by four, although leading to some constraints on the parameter space, such as a lower bound on $\tan\beta_R$ ($\tan\beta_R > 1$) [211]. The second option (ii) is instead more flexible, and we have made use of it in some of our scans, too. We will refer to this option as χ_RmBLR version (non-universal χ_R masses mBLR). We have not used the last option, which we only mentioned for the sake of completeness.

The result of Ωh^2 for two general scans is shown in Fig. 4.11. Parameters have been scanned as described in the figure caption. Note that there are two fixed but different choices of v_R in the left and right plots, leading to two different values of the Z' mass. In both plots in Fig. 4.11 the main feature clearly visible is the Z' pole. Indeed, the annihilation of the $\tilde{\nu}_{LSP}$ LSPs into SM particles via the Z' becomes efficient when the mass of the $\tilde{\nu}_{LSP}$ is close to half the mass of the Z'. The mass of the Z' can be calculated analytically [211] and mainly depends on the value of v_R, see Eq. (16). The ATLAS searches for a Z' set a lower limit on its mass which is 1.8 TeV, and this translates into a lower limit on $v_R \gtrsim 5$ TeV, see the plot on the left. The plot on the right shows that choosing a higher value of v_R we can get very heavy $\tilde{\nu}_{LSP}$ DM with the correct RA, up to masses of several TeV.

The main annihilation channels for sneutrino DM for the points of Fig. 4.11 are shown in Fig. 4.12. Far from the Z'-pole resonance these are $\tilde{\nu}_{LSP}\tilde{\nu}_{LSP} \longrightarrow \tau\overline{\tau}$ (magenta), $\tilde{\nu}_{LSP}\tilde{\nu}_{LSP} \longrightarrow b\bar{b}$ (brown), $\tilde{\nu}_{LSP}\tilde{\nu}_{LSP} \longrightarrow \nu\nu^c$ (orange), $\tilde{\nu}_{LSP}\tilde{\nu}_{LSP} \longrightarrow W^+W^-$ (red), $\tilde{\nu}_{LSP}\tilde{\nu}_{LSP} \longrightarrow Z^0Z^0/Z_RZ_R$ (purple), $\tilde{\nu}_{LSP}\tilde{\nu}_{LSP} \longrightarrow HH$ (blue), $\tilde{\nu}_{LSP}\tilde{\nu}_{LSP} \longrightarrow t\bar{t}$ (green). The quartic coupling with two Higgses (h^0, h^0_{BLR} and A^0, depending on whether they are kinematically allowed, depending on the $\tilde{\nu}_{LSP}$ mass) is one of the most efficients, as before. For lower masses the annihilation via the MSSM Higgs is the most efficient, as can be noticed by the small relic density for lower masses, especially in the first plot, where on the left end side we are approaching the region where the quartic Higgs coupling is important

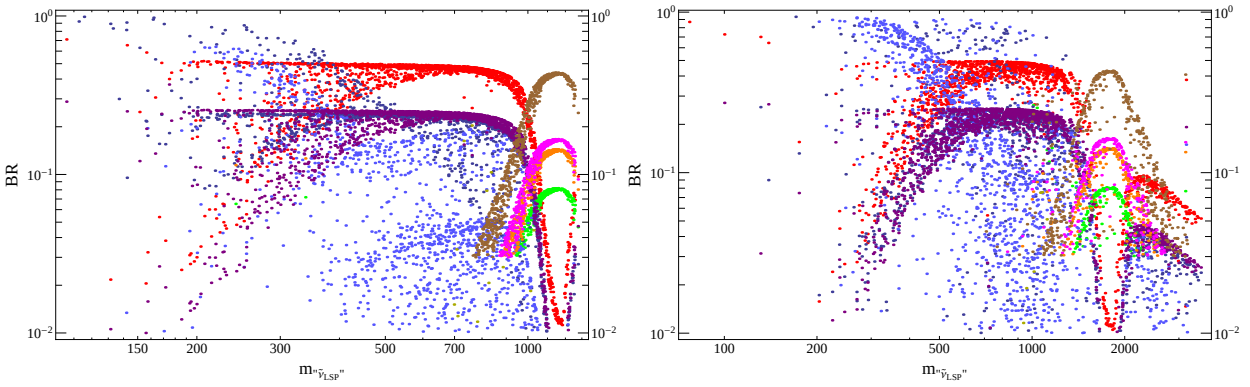

Figure 4.12: Final state branching ratios for the annihilation cross section of sneutrinos to SM final states versus the lightest sneutrino mass (in GeV). For the parameter choices of these scans see Fig. 4.11. For a discussion of the different kinematical regimes which are visible, see text.

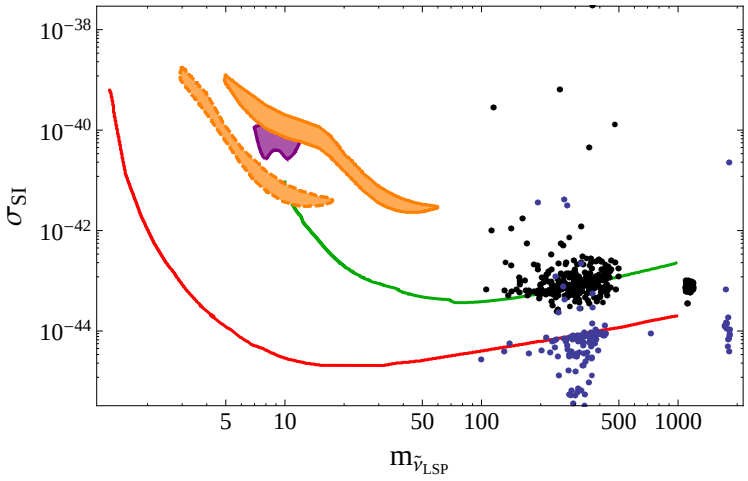

Figure 4.13: Direct detection cross section (in cm^2) for sneutrino LSPs in the BLR model. Masses are in GeV. Black points refer to the scan described in Fig. 4.11 left with $v_R = 6$ TeV. Blue points stand for the scan of Fig. 4.11 right with $v_R = 10$ TeV. All points shown fulfill the RA constraints. Higher v_R leads in general to lower DD cross section.

(for $m_{\tilde{\nu}_{LSP}} \simeq 120$ GeV).

Recall that in this model the Higgs sector is more complicated due to the extended gauge structure. The $U(1)_{B-L} \times U(1)_R$ breaking results in one additional light Higgs, h^0_{BLR} [210]. The mixing between the MSSM Higgs h^0 and the h^0_{BLR} enhances the mass of the mostly MSSM Higgs, leading to a MSSM-like Higgs in agreement with the most recent ATLAS and CMS preferred regions, without much constraints on the SUSY spectrum. However, this enhancement of the MSSM Higgs mass occurs usually in the model if the h^0_{BLR} has a mass of the order of the MSSM-like state or less, i.e. the presence of a light singlet Higgs is preferred unless the SUSY spectrum is rather heavy (in which case the CMSSM limit is reached).

We have also checked for constraints coming from direct detection in the limit of negligible sneutrino splitting. Examples for direct detection cross section are shown in Fig. 4.13. As before, see Fig. 4.10, different experimental constraints are also shown. All points shown fulfill the constraints from relic abundance. We have calculated two scans, one with $v_R = 6$ TeV (black) and one with $v_R = 10$ TeV (blue). As can be seen, practically all of the points with $v_R = 6$ TeV in this scan are excluded by the limit from XENON-100, while most of the $v_R = 10$ TeV are allowed. Thus XENON-100 puts currently a lower bound on v_R (and thus the Z' mass) of the order of $v_R \simeq 10$ TeV for sneutrino LSPs as DM.
The origin of this surprisingly strong constraints lies in the $Z^0 - Z'$ mixing. The mixing angle between these two states is roughly of the order $\theta_{Z^0 Z'} \sim (g_L v^2)/(g_R v_R^2)$. Thus the right sneutrinos, which couple mostly to the Z', couple via this mixing also to the Z^0. The Z^0 has an experimentally fixed mass. Thus, the only possibility to suppress the DD cross section [6] is to increase v_R.

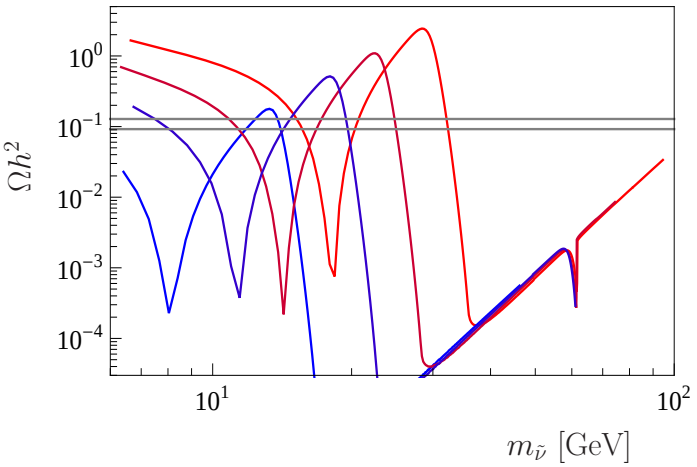

Figure 4.14: Scan into the low sneutrino mass region using the mBLR model. For the parameter choices see text. The figure demonstrates that the mBLR mode can give the correct RA for low mass sneutrinos in those parts of the parameter space where a light, singlet Higgs is present.

Finally, Fig. 4.14 shows a dedicated scan for low mass sneutrinos in the mBLR model. The different curves are slight variations of the parameters near the study point BLRSP1. The original parameters of BLRSP1 were: $m_0 = 470$, $M_{1/2} = 700$, $\tan\beta = 20$, $A_0 = 0$, $v_R = 4700$, $\tan\beta_R = 1.05$, $\mu_R = -1650$ and $M_{A_R} = 4800$ GeV. To obtain very light sneutrinos, m_0 has been lowered to $m_0 = 440$ GeV, while the different curves are for $M_{1/2} = 650, 660, 675$ and 700 GeV and the scanning runs m_{A_R} from $3000 - 4000$ GeV. The resulting scan produces sneutrinos with masses in the interval $[5, 100]$ GeV, while the lightest Higgs mass, in this case a mostly singlet Higgs, has a mass eigenvalues of $m_{h_1} \simeq 1 - 50$ GeV. The figure shows a pole around $m_{\tilde{\nu}_{LSP}} \simeq 62$ GeV, due to a mass for the MSSM-like Higgs of around $124 - 125$ GeV in all cases. There appear additional dips in the RA for smaller sneutrino masses, whenever

[6] Apart from a large sneutrino splitting.

$m_{\tilde{\nu}_{LSP}} \simeq m_{h_1}/2$. This demonstrates that in the extended gauge model it is possible to have the correct RA even for very low sneutrino masses.
However, note that, while the model can in principle give DD cross section large enough to explain the DAMA [289], and Cogent [269] hints, such points will always be inconsistent with the constraints from XENON-100 [546], also for the case of inelastic dark matter [547].

5 Conclusions

We have studied low scale seesaw models with a sneutrino LSP. We considered two possibilities: Models with the MSSM gauge group and either a linear or inverse seesaw and a model with the gauge group $SU(3)_c \times SU(2)_L \times U(1)_{B-L} \times U(1)_R$ and an inverse seesaw. Sneutrinos can be the DM in both cases, fulfilling all known experimental bounds.
However, while inverse and linear seesaw lead to different results for LFV, in general, they give similar DM results. There are some differences in detail, though: In the inverse seesaw it is possible to avoid all direct detection constraints using a large enough splitting in the sneutrino sector, which leads to "inelastic" dark matter. This is not possible in the linear seesaw, due to constraints from neutrino physics.
In the extended gauge model there is more freedom than in the simpler MSSM-group based models. Especially very light ($\mathcal{O}(1)$ GeV) or very heavy ($\mathcal{O}$(several) TeV) sneutrinos can give the correct relic density, due to the existence of a mostly singlet Higgs in the former case and due to the Z' in the latter. Very light sneutrinos could explain the hints from DAMA [289] or Cogent [269], but are inconsistent then with XENON-100 [546, 547]. It is interesting to note that in the limit of small sneutrino mass splitting the DD limit from XENON-100 [546] leads to a lower limit on v_R of the order of $\mathcal{O}(10)$ TeV for sneutrino LSPs as the dominant component of the galactic DM.
To distinguish different models of sneutrino DM from DM phenomenology alone will not be possible. However, the inverse/linear sneutrino setups which we have considered rely on the presence of more generations of right-handed (sterile) neutrinos with presumably large Yukawa couplings, i.e. sizeable mixing with the ordinary light neutrinos. Such states can be searched for in the LHC and limits have been published recently by both, the CMS [548] and ATLAS [549] collaborations. LHC phenomemology of the model with extended gauge group has recently been discussed in [211].

Part II

Indirect detection of Dark Matter through γ-rays

Among all possible messengers for DM indirect searches, γ-rays play an important role. Indeed, they can propagate essentially unperturbed through the galaxy thus directly pointing to their sources and therefore carrying spatial information. We already discussed this in Chapter 2.
Indirect γ-ray DM detection is evolving very rapidly, thanks to some high precision experiments, such as Fermi-LAT. This powerful role of γ-rays in indirect searches for DM provides our motivation for part of the research done in this thesis and notably to this Chapter.

The expected DM-induced γ-ray flux from a direction ψ in the sky, is given by the product of two factors:

$$\frac{d\phi_\gamma}{dE_\gamma}(E_\gamma, \psi) = J(\psi) \times \Phi^{PP}(E_\gamma), \tag{32}$$

where $J(\psi)$ is the *astrophysical factor* and $\phi(E)$ is the *particle physics factor* (PP).

Before entering the details of the work, we have to start with some technical introduction concerning how γ-ray fluxes are calculated and the uncertainties related to this computation.

The astrophysical term The astrophysical factor describes the integration performed along the line of sight (l.o.s.). For annihilating DM, the factor reads:

$$J(\psi) = \int_{\Delta\psi} \frac{d\Omega}{\Delta\psi} \int_{\text{l.o.s}} \rho^2(\mathbf{r}) d\ell, \tag{33}$$

where ρ is the density of DM particles, and the integration is in the direction ψ along the line ℓ. Moreover, the flux has been averaged over the opening angle $\Delta\psi$ of the detector. In case of DM decays, the integration is over density instead of density squared.

The particle physics term The PP factor only depends on the properties of the DM particle. It can usually be pulled outside the integral of Eq. (33) for WIMPs with typically very small velocities, such that it does not depend on the velocity distribution. However, this is not valid in case of velocity-dependent cross section, like in the case of Sommerfeld enhancement.

1. **Annihilating dark matter**
   In this case the PP term can be expressed as

$$\frac{\mathrm{d}\Phi_\gamma^{PP}}{\mathrm{d}E_\gamma}(E_\gamma) \equiv \eta \frac{1}{4\pi} \frac{\langle\sigma v\rangle_{\text{ann}}}{m_\chi^2} \cdot \sum_i \frac{dN_\gamma^i}{dE_\gamma} B_i \,, \tag{34}$$

   where m_χ is the mass of the DM particle, $\langle\sigma v\rangle_{\text{ann}}$ is the annihilation cross section times the relative velocity, averaged over the DM velocity distribution, B_i is

the branching ratio into the final state i and $\frac{dN_\gamma^i(E_\gamma)}{dE_\gamma}$ is the photon spectrum per annihilation (which is dependent on the annihilation channels). The sum is done over all annihilation channels. The usual value for $\langle\sigma v\rangle_{\rm ann}$ is the "thermal cross section" $\langle\sigma v\rangle \sim 3\cdot 10^{-26}{\rm cm}^3{\rm s}^{-1}$, which is the annihilation rate expected for thermally produced WIMPs in absence of resonances and co-annihilations. $\eta = \frac{1}{2}$ for a self-conjugate particle like a Majorana fermion or $\frac{1}{4}$ otherwise.

2. **Decaying dark matter**
For γ-rays produced from the decay of DM, the flux is formally the same as Eq. (32), but the particle physics term changes in the following way:

$$\frac{{\rm d}\Phi_\gamma^{PP}}{{\rm d}E_\gamma}(E_\gamma) \equiv \frac{1}{4\pi}\frac{1}{m_\chi \tau}\cdot\sum_i \frac{dN_\gamma^i}{dE_\gamma}B_i\,, \tag{35}$$

where the decay lifetime τ enters, instead of the annihilation cross section.

The photon spectrum depends on the annihilation channels. We focus on a generic WIMP candidate, instead of restricting ourselves to a specific particle physics model, which is depicted through the values of the mass of the DM particle, m_χ, the annihilation cross section $\langle\sigma_{\rm ann}v\rangle$ or the decay lifetime τ and the γ-ray photon spectrum (yield). The latter receives three contributions: i) γ-rays produced by DM particles annihilating directly into two photons, Z^0H or $Z^0\gamma$, giving rise to monochromatic lines, ii) γ-rays from decay of neutral pions produced by hadronization of final states of DM annihilation, which produce a γ-ray continuum, iii) γ-rays from radiative emissions, if charged particles are produced, which also contribute to the continuum. Internal bremsstrahlung may also contribute inducing harder spectra and the possibility of bumps near the energy cut-off set by the DM mass.

The required ingredients to calculate the expected γ-ray flux from DM annihilation or decay through Eq. (32) are always model dependent.

Concerning the astrophysical factor, the modelling of the DM density distribution is the main task. We will now shortly review the main halo profiles.

Dark matter halo density profiles

The CDM paradigm predicts the formation of DM structures called *halos* and substructrures called *subhalos* or *clumps*. From numerical simulations, we know how these structures evolve [7]. Computer simulations indeed, allow to follow the non-linear evolution of DM perturbations, starting from realistic and well constrained cosmological initial conditions. The final structures are the DM halos that are expected to embed galaxies and galaxy clusters.

[7] Although with some caveats: most of DM simulations do not include baryons, which lead to a different phenomenology. See Chapter 6.

Numerical simulations Numerical simulations have experienced a solid algorithmic and hardware development that led to the improvement of the mass and spatial resolution by orders of magnitude. Indeed, today it is possible to simulate individual galaxies, in a full cosmological context with up to billions of particles and a spatial resolution of ~ 1 kpc. Current simulations like Via Lactea-II [550], GHALO [551] and Aquarius [552] are among the best resolved ones. Allowing for some differences caused by the use of different cosmological parameters, the main results of Via Lactea-II and Aquarius are very similar. This means that current cosmological N-body simulations may be considered as good approximations to CDM halos on a large mass and spatial range. Furthermore, N-body simulations demonstrate how hierarchical merging gives rise to substructures, both gravitationally bound (subhalos) and unbound (streams). Concerning how much of the DM is in the form of substructures, it is useful to consider the cumulative mass function of subhalos, which can be approximated by a power-law of the form $M^{-\alpha}$ with $\alpha = 1.9 - 2.0$. The steep slope means that a significant fraction of the mass is inside small subhalos, which are still unresolved in current numerical simulations.
Nevertheless, a realistic description of the DM distribution requires also the treatment of the baryons and their dynamical interactions with the DM. Baryonic matter dominates the gravitational potential in the central region of the galactic halo, thus it could have a great impact on the DM distribution with respect to the pure DM simulations. Hence, the DM density profiles can steepen through the adiabatic contraction due to the introduction of dissipating baryons in the simulations [553–556]. On the contrary, if feedback from star formation and supernovae dominates over cooling and infall processes, the presence of baryons could produce the opposite effect of leading to cored profiles rather than cusped ones [557–559]. The magnitude of this effect depends on the baryonic fraction that slowly dissipates via radiative cooling. However, it is not yet very clear how strongly the presence of baryons changes the inner distribution of DM in galaxies.

General DM density profile A useful general parametrization of DM halos, which can describe a large number of commonly used profiles is

$$\rho_\chi^{\alpha\beta\gamma}(r) = \rho_\odot \left[\frac{r}{r_\odot}\right]^{-\gamma} \left[\frac{1+(r_\odot/r_s)^\alpha}{1+(r/r_s)^\alpha}\right]^{\frac{\beta-\gamma}{\alpha}} , \tag{36}$$

where r is the distance from the halo center, $r_\odot \simeq 8.33$ kpc is the position of the Sun and $\rho_\odot \simeq 0.4$ GeV cm^{-3} the local DM density [97–100, 102].

The most used DM profiles are described hereafter.

NFW In the literature, halo density profiles seemed initially to be well-fit by a single functional form. Pure-DM simulations showed that most of CDM halos can be described by a universal profile, the NFW profile [560]:

$$\rho(r)^{NFW} = \frac{\rho_s}{(r/r_s)(1+r/r_s)^2}. \tag{37}$$

It can be obtained from Eq. (36) with $(\alpha, \beta, \gamma) = (1, 3, 1)$. The scale radius r_s is related to the peak circular velocity scale and it is used to define the halo concentration $c_{\rm vir} = r_{\rm vir}/r_s$, where $r_{\rm vir}$ is the "virial" radius. The logarithmic slope of the profile at r_s is $d{\rm ln}\rho/d{\rm lnr} = -2$. This scale seems to mark the division between two regions in the distribution of the halo, the central part of the profile which goes as $\rho(r) \propto r^{-1}$ and an outer region with a steeper profile going as $\rho(r) \propto r^{-3}$.
Nevertheless, as larger simulations started to resolve smaller scales, it has been observed that good fits are obtained by letting the inner slope γ of the NFW function (Eq. (37)) become a free parameter, instead of forcing $\gamma = 1$.

Moore Some halos follow the NFW profile quite well, but others are better approximated with a steeper profile as suggested by [561]:

$$\rho(r)^{Moore} = \frac{\rho_s}{(r/r_s)^{1.16}(1 + r/r_s)^{1.84}}. \tag{38}$$

Einasto Another option is to use the Einasto profile [562–564]

$$\rho(r)^{Ein} = \rho_s e^{-\frac{2}{\alpha}[(r/r_s)^{\alpha}-1]} , \tag{39}$$

where α is the additional free parameter. It describes the shape of the density profile. Larger values of α result in steeper inner profiles and shallower outer profiles. The quantity $-\frac{2}{\alpha}$ is such that ρ_s is the density at the effective radius r_s, which encloses the volume containing half of the total mass.

Isothermal Cored profiles, such as the truncated isothermal profile [565, 566] might be more motivated by the observations of galactic rotation curves:

$$\rho(r)^{iso} = \frac{\rho_s}{\left(1 + (r/r_s)^2\right)} , \tag{40}$$

where r_s is the core radius and ρ_s the central density. The cored isothermal profile follows from Eq. (36) when setting $(\alpha, \beta, \gamma) = (2, 2, 0)$. A feature of this kind of profile is that the radial velocity dispersion is constant, on the contrary to NFW profiles which show a strong dependence of the radial velocity dispersion upon the radius.

Burkert Another cored profile is the Burkert profile [567] which appears to best-fit the observed rotation curves of dwarf galaxies, which are known to be dominated by DM. It is an empirical law that resembles a pseudo-isothermal halo:

$$\rho(r)^{bur} = \frac{\rho_s}{(1 + r/r_s)\left(1 + (r/r_s)^2\right)} . \tag{41}$$

Moore and Stadel A new two parameter fitting function of the density profile has been proposed [551] to fit a series of simulations of a Galactic mass DM halo at different mass resolutions:

$$\rho(r)^{MS} = \rho_0 e^{-\lambda[\ln(1+r/R_\lambda)]^2}. \tag{42}$$

This function has a linearly varying logarithmic density gradient. It has a constant logarithmic slope down to a scale R_λ, below which it approaches the central maximum density ρ_0 as $r \to 0$.
All the proposed profiles differ most in the inner part of the galactic halo, while they are quite similar above a few kiloparsecs, and notably in the location of the Solar system. Apart from very extreme scenarios, which can be excluded by microlensing and stellar rotation curve observations, the difference in the expected DM annihilation flux from the innermost region of the galactic halo, between the most cored profiles and the most cusped ones, can be as large as five orders of magnitude.

CHAPTER

FIVE

DARK MATTER CONSTRAINTS FROM THE FERMI-LAT EXTRAGALACTIC γ-RAY BACKGROUND

1 Introduction

The indirect search for DM through its annihilation products in rare charged CRs and in multi-wavelength channels requires very accurate measurements and an unambiguous estimation of all the possible backgrounds to the DM signal. In the last years, dedicated experiments have provided unprecedented results by extending the energy ranges of the measured cosmic species as well as the precision of the data [568–574]. Further data are expected by the Fermi-LAT and Pamela on-going missions, and by the AMS-02 experiment on board the International Space Station. From the theoretical side, many efforts have been addressed to a better and increasingly detailed modelling of the astrophysical processes which shape, at different levels, the observed fluxes. Data from cosmic antiprotons [572, 573] have been shown to be compatible with the standard production from CRs impinging on the interstellar gas [341]. The anomalous increasing positron fraction measured by Pamela [568, 569] and confirmed by Fermi-LAT [575] may be explained by emission from near pulsars overimposed to a standard CR population [576, 577]. Alternatively, a DM component with very high cross section or sources concentration has been invoked [333, 578–580]. Unprecedented γ-ray measurements by Fermi-LAT have boosted interpretation of diffused and point sources emission in terms of exotic components from DM annihilation in the halo of the Milky Way, in extragalactic near objects or in cosmological structures [574, 581–583]. The very signature would be the monochromatic line, which nevertheless provides tiny signal on a remarkable background [584].

The high latitude γ-ray emission measured by Fermi-LAT [574], given its reduced contamination by galactic sources, can be a powerful tool to set limits on the contribution of DM to the measured flux. The data are indeed the result of a non trivial subtraction procedure and show a high isotropic feature.

The aim of the present research is to set *conservative* upper limits on the galactic weakly interacting massive particle (WIMP) DM annihilation cross section into γ-rays. Several upper limits have been obtained through different and complementary indirect research means [341,372,401,431,583,585–589]. However, it is usually not straightforward to compare

these results, given the model dependence, the different assumptions on the astrophysical backgrounds, and the theoretical uncertainties. We will confront the γ-rays coming both from the DM halo and high-redshift protohalos with the background observed by Fermi-LAT at high latitudes. The conservative approach is achieved - in addition to prudent assumptions on the particle physics model and DM distribution in the Galaxy - through the comparison of the putative DM signal with a high latitude diffuse emission spectrum (i.e. IGRB) obtained with minimal subtractions of known unresolved sources.
This chapter proceeds as follows. In Section 2 we discuss the possible contributions to the high latitude γ-ray emission from unresolved point sources and truly diffuse processes. We subtract the non-negligible fluxes to the Fermi-LAT data and draw two possible scenarios for the high latitude emission. In Section 3 we derive conservative upper limits to the DM annihilation cross section by identifying the residual γ-ray flux with γ-rays from DM annihilation in the galactic halo and in primordial DM small halos at high redshift. In the latter case, we study models in which the DM annihilation cross section has an explicit dependence on the inverse of the velocity. We discuss also a possible Sommerfeld enhancement of the annihilation cross section and derive limits on its amplitude. In Section 4 we draw our conclusions.

2 The extragalactic γ-ray background

A diffuse γ-ray emission has been measured by the Fermi-LAT detector at high latitudes ($|b| > 10^o$) [574]. The spectrum has been obtained after the subtraction from the data of the sources resolved by the telescope, the (indeed model dependent) diffuse galactic emission, the CR background in the detector and the solar γ-ray emission. The resulting flux decreases with a power law of the photon energy with spectral index 2.41 ± 0.05. It shows a highly isotropic sky distribution and is generically classified as isotropic diffuse γ-ray background (IGRB) or extragalactic γ-ray background (EGB).
The 1451 sources listed in the First Fermi-LAT catalog (1FGL) [590] represent the best-resolved survey of the sky in the 100 MeV to 100 GeV energy range. For each low–flux source there may be a large number of *unresolved* point sources which have not been detected because of selection effects, or too low emission. Most of the unassociated high latitude sources are blazars, a class of Active Galactic Nuclei (AGNs), and their pile to the IGRB with the largest flux [591]. Galactic resolved pulsars and Milli-Second Pulsars (MSPs) represent the second largest population in the Fermi-LAT catalog [590,592] and they are expected to contribute significantly to the putative IGRB. A non-negligible γ-ray flux seems to be guaranteed by unresolved normal star-forming galaxies [593]. Ultra-high energy CRs (UHECRs) may induce secondary electromagnetic cascades, originating neutrinos and γ-rays at Fermi-LAT energies [594]. Contributions from unresolved blazars and MSPs are believed to contribute at least few percent to the Fermi-LAT IGRB, while predictions for star-forming galaxies and UHECRs are highly model dependent.
Other astrophysical sources may emit in the high latitude γ-ray sky: i) radio-quiet AGN [595,596], and Fanaroff and Riley radio galaxies of type I and II [597–599] whose contribution is strongly model dependent and likely bound to few percent of the IGRB; ii) γ-ray bursts (GRBs), estimated less than 1% of the diffuse extragalactic γ-ray background [600]; iii)

star-burst and luminous infrared galaxies. The relevant flux may cover a significant fraction of the IGRB ($\leq 20\%$) [601], but the model dependence is such to prevent firm statements on the relevance of this extragalactic source; iv) nearby clusters of galaxies, which could yield about $1\% - 10\%$ of the EGRET IGRB [602–604]; v) gravitational induced shock waves, produced during cluster mergers and large-scale structure formation, whose fluxes are quite model dependent and may reach few percent [605, 606]. All these γ-ray sources have been shown to contribute to less than 1% of the Fermi-LAT IGRB or to be too highly model dependent. In the latter case, a very high uncertainty band would be associated with the γ-ray source, whose lower limit likely gives a negligible contribution to the Fermi-LAT IGRB. They will therefore be neglected in the rest of this chapter.
In the following, we describe a few classes of γ-ray emitters whose unresolved flux is firmly estimated in a non-negligible Fermi-LAT IGRB percentage. In a conservative scenario (Model I), we will subtract AGN and MSPs to the Fermi-LAT IGRB as derived in Ref. [574]. A more relaxed model (Model II) will be drawn by the further subtraction of a minimal flux from star-forming galaxies and CRs at the highest energies.

2.1 BL Lacs and FSRQs

An AGN is a compact region at the center of a galaxy, probably originated by galactic matter accretion onto a super-massive black hole. The released large amount of gravitational energy flows away through powerful jets of relativistic particles which in turn produce X and γ radiation. Blazars are those AGNs for which the jets are close to our l.o.s. The blazar classification includes BL Lacs (BL Lacertae), which present a complete or nearly complete lack of emission lines, and FSRQs (flat-spectrum radio quasars). Blazars constitute the class of γ-ray emitters with the largest number of identified members. Therefore, unresolved blazars are expected to have a sizable contribution to the IGRB, [607]. The largest uncertainties in determining the blazars contribution are their unknown spectral energy distribution and luminosity function [596, 608]. In addition to phenomenological predictions, an analysis of the observed source count distribution through Monte Carlo simulations has been performed in Ref. [591]. The reliability of the algorithm relies on a good agreement with the real data, from the comparison of reconstructed γ-ray fluxes and spectral properties of the sources. The energy spectrum is well described by a power-law for both FSRQs (softer) and BL Lacs one (harder), being the intersection between the two fluxes at about 400 MeV. Following our conservative approach - which is meant to consider the minimum unavoidable contribution to the IGRB from unresolved astrophysical sources - we will adopt blazar contributions from the curves delimiting the lower uncertainty bands displayed in Fig. 20 of Ref. [591]. The ensuing flux is displayed in our Fig. 5.1 as dotted (dot-dashed) line for BL Lacs (FSRQs) contribution.

2.2 Pulsars and MSPs

As a result of their short periods, typical MSPs may be brighter in the γ-rays and much older than ordinary pulsars [609]. The ages of MSPs generally exceed the oscillation time across the galactic disk by a large factor so that MSPs are expected to be more prevalent at high latitudes. On the contrary young, energetic ordinary pulsars are more concentrated close to

the Galactic plane, where they were born. In the first year of Fermi-LAT observations [590], 63 pulsars have been identified. Among them: (i) 16 pulsars at $|b| > 10^{o}$, of which 11 are MSPs; (ii) 5 MSPs at $|b| > 40^{o}$ and (iii) 1 MSP at $|b| > 60^{o}$. We estimate a minimal but not negligible contribution of the unresolved MSPs population to the γ-ray flux at high latitudes. We adopt an empirical prescription outlined in Ref. [610], which is based on the spectra of the eight MSPs detected by Fermi in the first 9 months [611] of operation. The differential energy spectra of the Fermi-detected MSPs are well described by a truncated power law:

$$\frac{dN}{dE} = KE^{-\Gamma}e^{-E/E_{cut}}. \tag{1}$$

Γ and E_{cut} are assumed to be $\langle\Gamma\rangle = 1.5$ and $\langle E_{cut}\rangle = 1.9$ GeV, while K has been obtained for $|b| \geq 40^{o}$.
In order to evaluate Eq. (1) for different observational regions - namely changing the normalization K - we follow the prescriptions given in Ref. [609]. Assuming a disk-like latitude profile, the ratio of the average intensities at different latitudes is given by:

$$\frac{I_{MSP}(|b| \geq b_1)}{I_{MSP}(|b| \geq b_2)} = \frac{\ln[(\sin|\mathrm{b_1}|)^{-1}]}{\ln[(\sin|\mathrm{b_2}|)^{-1}]}, \tag{2}$$

where $I_{MSP}(|b| \geq b_i)$, $i = 1, 2$, is the average MSP intensity over a solid angle $\Omega = 4\pi(1 - \sin|b_i|)$ defined by the integration from the minimal latitude b_i up to 90^{o}, written as:

$$I_{MSP} \equiv \frac{S_{tot}}{\Omega} = \frac{S_{min}}{\Omega} \cdot \left(\frac{\delta - 1}{\delta - 2}\right) \cdot \left(\frac{S_{min}}{S_{th}}\right)^{1-\delta} \cdot N(S > S_{th}). \tag{3}$$

S_{min} refers to the assumed Euclidean logN-logS flux distribution of the galactic MSP population, which is parameterized by a power-law with spectral index $\delta = 2.5$ for $S \geq S_{min}$. According to [609], we set $S_{min} = 10^{-10}$ ph s^{-1} cm^{-2}. $N(> S_{th})$ is the number of resolved sources above a given flux threshold S_{th}. We update the estimation for I_{MSP} in Ref. [609] with the more recent observations for $|b| \geq 10^{o}$ reported in Ref. [611], where 8 MSPs have been found above $S_{th} = 2 \cdot 10^{-8}$ ph s^{-1} cm^{-2} (lowest detected MSP flux). We find:

$$I_{MSP}(|b| \geq 10^{o}, E > 100 \text{ MeV}) = 6.54 \cdot 10^{-7}\mathrm{cm^{-2}s^{-1}sr^{-1}}. \tag{4}$$

K is then derived from:

$$I_{MSP} = \int_{E_{min}}^{E_{max}} \frac{dN}{dE} dE \ , \tag{5}$$

where $\frac{dN}{dE}$ refers to Eq. (1). Cross-checking the average MSP intensities obtained with the prescription outlined above, and the results in Ref. [610] for $|b| \geq 40^{o}$, we find a relative difference of about 30%, due to the theoretical uncertainties on the assumed logN-logS and the latitude profile. We consider such a discrepancy as an empirical theoretical uncertainty on the determination of K, and fix the unresolved MSPs contribution subtracting a 30% uncertainty from the estimated average intensity. The MSP contribution is shown in Fig. 5.1 as a double dot-dashed line.

2.3 Star-forming Galaxies

Unresolved normal star-forming galaxies are expected to give a guaranteed contribution to the high latitude isotropic diffuse γ-ray background. Fermi-LAT has identified the source of the diffuse emission from our Galaxy due to the collisions of CRs with interstellar gas, leading to γ-rays from π^0 decay in flight. This observation provides a ground to estimate the γ-ray luminosity of star-forming galaxies, by scaling the CR flux with the massive star formation rate and fixing the amount of the gas in the external galaxy. Theoretical predictions are greatly affected by uncertainties in the determination of the star formation rate of the galaxies and their gas content [593,608,612]. Given the uncertainty surrounding key elements of the determination of this contribution, in our strictly conservative approach we do not take into account this component. In a more relaxed perspective, we consider the lowest predicted contribution from star-forming galaxies [593]. It is derived assuming an increase in the number of star forming galaxies with the redshift. The adopted emission corresponds to the long dashed curve in Fig. 5.2.

2.4 UHECRs

UHECRs accelerated in astrophysical objects produce secondary electromagnetic cascades during their propagation in the cosmic microwave and infrared backgrounds. Ref. [594] shows that if the primary CRs are dominated by protons, such cascades can contribute between 1% and 50% of the GeV-TeV diffuse photon flux measured by the EGRET experiment. In Ref. [613], the EGB spectrum from UHECRs (normalized to the HiRes data) has been obtained through a Monte Carlo simulation of the cascade development and compared with the measurement of the IGRB by Fermi-LAT. In our more relaxed, nevertheless conservative scenario, we will subtract the ankle model contribution to the Fermi-LAT IGRB [613], which we show in Fig. 5.2. This γ-ray component has the peculiar behaviour to slightly increase with increasing energy, and at 100 GeV may account 8% of the Fermi-LAT measured IGRB.

3 Models for the IGRB

As a result of the previous analysis, we now proceed by subtracting from the Fermi-LAT IGRB [574] additional contributions from unresolved sources at latitudes $|b| > 10^{\circ}$. The contributions to the IGRB that we will remove from the Fermi-LAT spectrum are minimal. In fact, as extensively explained in the previous sections, the predictions that we will take into account for the relevant unresolved sources are the lowest ones according to the literature. In addition, for MSPs we have lowered existing calculations by updating them to the Fermi-LAT observations.

In what we label Model I, we subtract from the Fermi-LAT IGRB [574] the unresolved contributions for both BL Lacs and FSRQs as outlined in Section 2.1, and the unresolved MSPs flux obtained according to the prescription Section 2.2. The results are shown in Fig. 5.1, where the Fermi-LAT IGRB data [574] are shown along with our power–law fit. The contributions from BL Lacs, FSRQs and MSPs are identified by dotted, dot-dashed and double dotted-dashed curves, respectively. The fluxes from the blazar populations follow power–laws, with softer (harder) spectrum for the FSRQs (BL Lacs). The crossing point

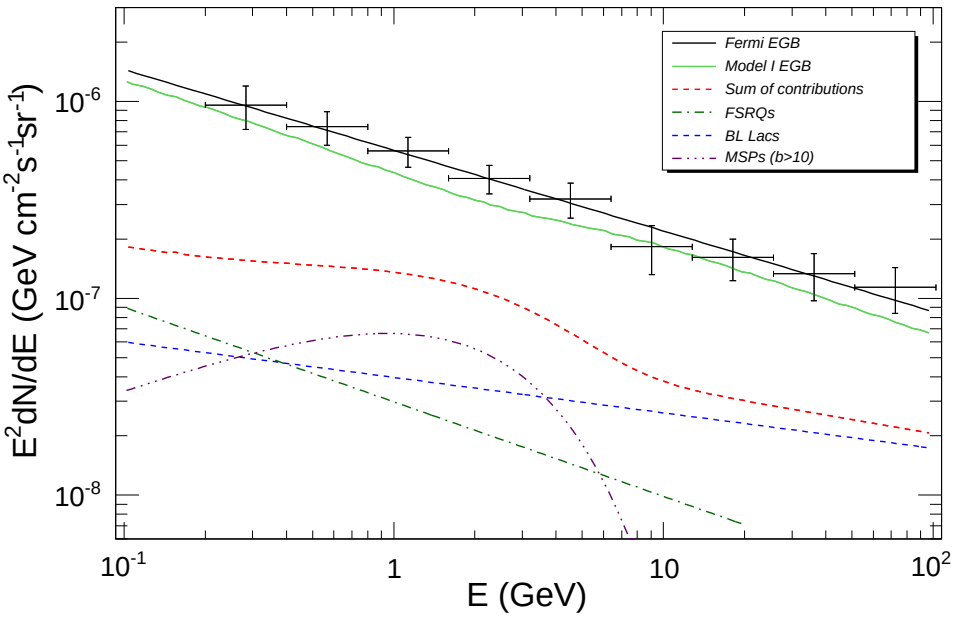

Figure 5.1: γ-ray spectrum for $|b| > 10^o$ latitudes. Fermi-LAT data points are displayed along with their power–law fit (solid black curve) [574]. The dotted (blue), dot-dashed (green) and double dot-dashed (purple) curves correspond to BL Lacs, FSRQs and MSPs contribution, respectively. The dashed (red) curve is the sum of the previous three fluxes. The solid (lower, green) curve is derived by subtracting the three contributions to the Fermi-LAT result (Model I).

for the two curves is around 300 MeV: above this energy BL Lacs flux dominates over the FSRQs one. The γ-rays from unresolved MSPs show a peculiar spectrum peaked at about 1 GeV and dominate over the blazar spectra from 300 MeV up to 3-4 GeV. The sum of the three contributions reflects the MSPs flux shape with a mild bump. At about 100 MeV the three sources explain 10% of the Fermi-LAT IGRB and 30% above 1 GeV. The residual flux Model I, obtained by subtracting the sum of the three contributions (dashed curve) to the Fermi-LAT best fit flux is identified by the lower solid curve. It is not a net power law due to the dip in the GeV region introduced by the MSPs flux.
Fig. 5.2 refers to the scenario where the additional contributions from star-forming galaxies (long dashed line) and UHECRs (solid points) as outlined in Section 2.3 and Section 2.4 add to explaining the Fermi-LAT IGRB. These two further contributions add with the previous ones (blazars and MSPs of Model I) and the total sum is displayed by the dashed red line. The solid (green) curve derives from the subtraction of all these contributions from the Fermi-LAT IGRB (solid black line fitting the data points) and is labelled Model II hereafter. Notably, the contribution from star-forming galaxies turns out to be relevant for $E \leq 1$ GeV, whereas the γ-rays from UHECRs give non-negligible fluxes only at the high-end of the energy spectrum. We notice that at 100 MeV Model II explains about 70% of the Fermi-LAT IGRB, while above 1-2 GeV they count about 50% of the total. To consider

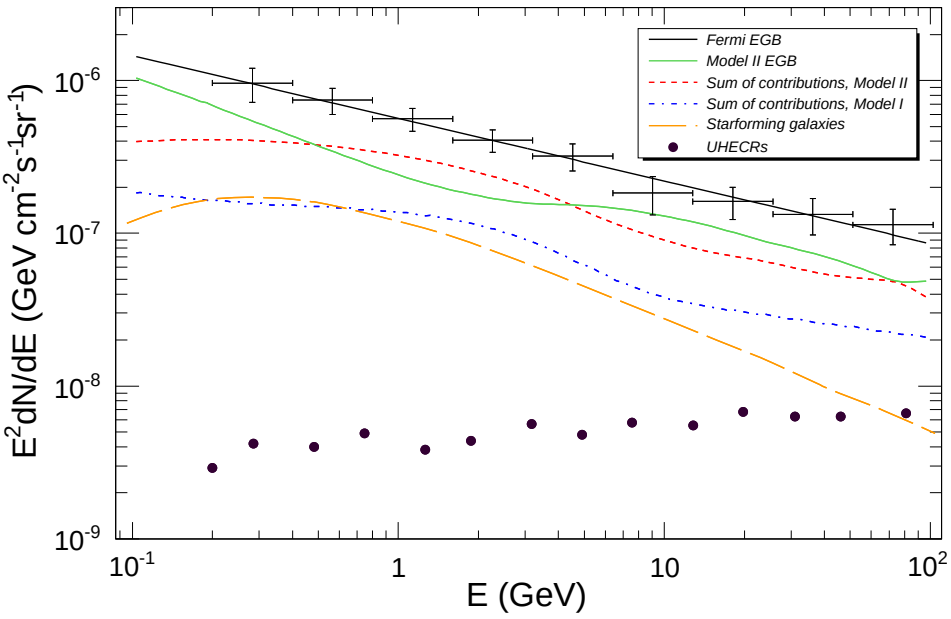

Figure 5.2: γ-ray spectrum for $|b| > 10^{o}$ latitudes. Fermi-LAT data points are displayed along with their power–law fit (solid black curve) [574]. Black dots and long dashed-curve (orange) correspond to the UHECRs and star-forming galaxies γ-ray fluxes, respectively. The dot-dashed (blue) curve corresponds to the sum of BL Lacs, FSRQs and MSPs contribution (see Fig. 5.1), the short-dashed (red) to the sum of the previous components with the star-forming galaxies and UHECRs ones. The solid (lower, green) curve is derived by subtracting all the contributions to the Fermi-LAT result (Model II).

additional astrophysical components to the IGRB further decreases the residual flux (lower solid line) with respect to the Fermi-LAT IGRB (upper solid line) and shrinks the room left to potential exotic sources, like DM annihilations.

4 Upper bounds on DM annihilation cross section

In this Section we derive conservative upper limits on the WIMP annihilation cross section. We make the hypothesis that the residual fluxes we have derived in Section 3 are entirely provided by the γ-rays produced by thermalized WIMP DM in the halo of the Milky Way.

4.1 γ-rays from DM annihilation

The flux of γ-rays $\Phi_\gamma(E_\gamma, \psi)$ originated from WIMP pair annihilation in the galactic halo [614–616] and coming from the angular direction ψ is given by Eq. (32)
The photon spectrum in the continuum originates from the production of fermions, gauge bosons, Higgs bosons, and gluons from the annihilation of WIMP pairs. The spectra dN_γ/dE_γ from DM final states into $b\bar{b}$, $\mu^+\mu^-$ and $\tau^+\tau^-$ have been taken from Refs. [364,617].

Halo profile	Isothermal a = 3.5 kpc	NFW [560] a = 25 kpc $r_c = 0.01$ kpc	Einasto [619] $\alpha = 0.142$ $r_{-2} = 26.4$ kpc $\rho_{-2} = 0.05$ GeV cm^{-3}
$\|b\| > 10^o$	2.389	2.400	2.833
$10^o < \|b\| < 20^o$	4.020	4.166	5.752
$\|b\| > 60^o$	1.226	1.283	1.232

Table 5.1: Values for $I_{\Delta\Omega}$ in units of GeV^{2}cm^{-6}kpc. For all these profiles $\rho_l = 0.4$ GeV cm^{-3} , $R_{Sun} = 8.2$ kpc.

The extrapolation down to m$_\chi$=10 GeV seems guaranteed within 10% of uncertainty for all the annihilation channels [618] (a more careful derivation being beyond the scope of this work).
The quantity $I(\psi)$ is the integral performed along the l.o.s. of the squared DM density distribution:

$$I(\psi) = \int_{l.o.s.} \rho^2(r(\lambda,\psi))d\lambda\,. \tag{6}$$

with ψ being the angle between the l.o.s. and the direction pointing toward the galactic center (GC) and defined in function of the galactic coordinates so that $\cos\psi = \cos b\cos l$. When comparing with experimental data, Eq. (6) must be averaged over the telescope observing solid angle, $\Delta\Omega$:

$$I_{\Delta\Omega} = \frac{1}{\Delta\Omega}\int_{\Delta\Omega} I(\psi(b,l))d\Omega\,. \tag{7}$$

The integral of the squared DM density over the line-of-sight depends on the choice on $\rho(r)$. When including the galactic center in the integration (Eq. (6)), different DM distributions may lead to very different results for $I(\psi)$. However, since our analysis is applied to high latitude regions, the various descriptions for $\rho(r)$ point to very similar values for $I(\psi)$. We neglect any clumpiness effects and assume a smooth distribution of DM in the galactic halo. The results for $I_{\Delta\Omega}$ for different DM density distributions and observational regions are reported in Table 5.1. All the DM profiles provide very similar results for latitudes well above the galactic plane. Hereafter, the results will be provided for the cored isothermal density profile.

4.2 Results on annihilation cross section

In this Section we derive upper bounds at 90% C.L. on the WIMP annihilation cross section from the γ-ray Fermi-LAT IGRB and the IGRB residual fluxes identified as Model I and II in Section 3.
For the Fermi-LAT IGRB [574], the upper bounds at 90% C.L. on $\langle\sigma v\rangle$ are obtained by requiring that the DM signal calculated according to Eq. (32) does not exceed the measured flux plus 1.6σ (one-sided upper limit on the $\langle\sigma v\rangle$ parameter). The corresponding constraints

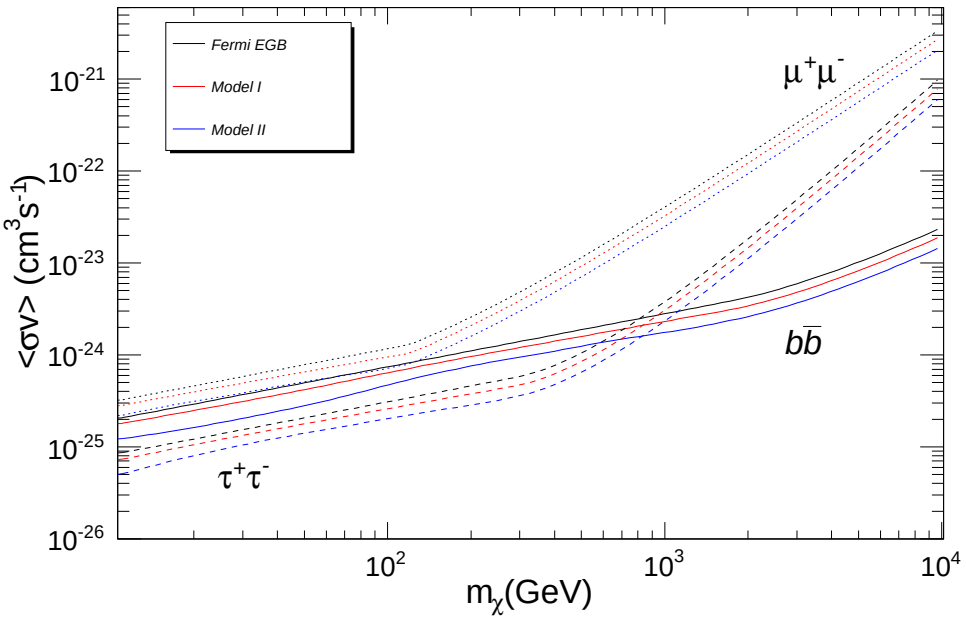

Figure 5.3: Upper bounds on $\langle\sigma v\rangle$ from γ-ray in the high latitude galactic halo, as a function of the DM mass. From top to bottom, solid lines refer to 90% C.L. limits from the comparison with Fermi-LAT IGRB (black lines), Model I (red lines), Model II (blue lines) (see text for details). Dotted, solid and dashed lines correspond to DM annihilation into $\mu^+\mu^-$, $b\bar{b}$, $\tau^+\tau^-$, respectively.

are plotted as black lines in Fig. 5.3. From the same data we have then subtracted the unresolved blazars and MSPs minimal contribution, as described at length in Section 3, and derived the upper bounds on $\langle\sigma v\rangle$ corresponding to Model I (red lines). Similarly, upper bounds for the Model II IGRB are obtained from the further subtraction of the minimal flux from star forming galaxies and UHECRs (blue lines). In Fig. 5.3 we display the conservative upper bounds on the thermal annihilation DM cross section at 90% C.L., derived within the previous assumptions. Dotted, solid and dashed lines correspond DM annihilation into $\mu^+\mu^-$, $b\bar{b}$, $\tau^+\tau^-$, respectively. Given the scaling of the DM flux $\propto m_\chi^{-2}$, constraints on $\langle\sigma v\rangle$ increase with the mass and span about two orders of magnitude in the considered mass interval. It is evident from Fig. 5.3 that the subtraction of the minimal amount of γ-rays from unresolved sources lowers the limits on $\langle\sigma v\rangle$ by at least 50%. The Fermi-LAT data for the IGRB are available also for latitudes $10^o < |b| < 20^o$ and $|b| > 60^o$ [574]. The flux in Eq. (32) changes for the mere normalization factors given in Table 5.1. However, given the intensity of the measured fluxes our upper limits do not change if derived for the other high latitude regions.

Given the theoretical uncertainties affecting the DM content and the astrophysical backgrounds, the results in Fig. 5.3 are of the same order of magnitude or lower than the bounds on $\langle\sigma v\rangle$ from cosmological DM [583], from the galactic center [372], or from inverse Compton processes evaluated from γ-rays in different portions of the sky [585]. Very recently

(during the review process of the present Chapter) the Fermi-LAT collaboration performed a combined analysis on ten Milky Way satellite galaxies [589], corroborated by the analysis in Ref. [374]. The absence of DM signals from these objects leads to upper limits on $\langle\sigma v\rangle$ which are close to 10^{-26} for masses about 10 GeV and 10^{-24} for m_χ=1 TeV. These bounds are close to the ones established in the present work for the high mass side, and stronger for the low mass range. The two results, given unavoidable modelling in the extraction of the upper bounds, strengthen each other in disfavouring a DM candidate with an annihilation cross section much higher than the electroweak reference value $3 \cdot 10^{-26}$ cm^3/s for very low WIMP masses. We make notice that the IGRB spectra we have obtained in Model I and II could be further reduced, whether by the subtraction of additional components or by increasing the predictions for each contribution, set at the minimum in the present work. A smaller γ-ray flux at high latitudes could therefore be as powerful as the measurements from the dwarf spheroidal galaxies.
We emphasize that our limits are almost model independent: little dependence on the DM distribution, being at high latitudes, and mild differences due to final states.
Our limits are *conservative*: it is very unlikely that a higher $\langle\sigma v\rangle$ be compatible with Fermi-LAT IGRB. Similarly, our upper limits could be lowered only with assumptions on non-homogeneous DM distributions or, of course, comparing to a smaller IGRB residual.

4.3 Bounds on the Sommerfeld enhancement for $\langle\sigma v\rangle$

Recent measuraments of the excess of CR positrons [568] have stimulated the interpretation of data in terms of annihilating DM with fairly large annihilation cross sections of the order of $10^{-23} - 10^{-22}$ cm^3/s. These numbers are at least three orders of magnitude larger than the value indicated by observations of the DM abundance due to thermal production. One way to boost the annihilation cross section is through the Sommerfeld effect [333, 345–349], generically due to an attractive force acting between two particles, *i.e.* a Yukawa or a gauge interaction. In the case of DM particles, the main effect of such an attractive force would be to enhance $\langle\sigma v\rangle$ by a factor proportional to $1/\beta = c/v$, where v is the velocity of the DM particle ($1/v$ enhancement). The net result on the annihilation cross section writes as $\langle\sigma v\rangle = \mathrm{S}\,\langle\sigma v\rangle_0$, where S sizes the Sommerfeld enhancement of the annihilation amplitude. We have evaluated the Sommerfeld enhancement S using the approximation of the Yukawa potential by the Hulthen potential, for which an analytic solution is possible [620, 621] (and checked that the solution coincides with the numerical one). The Sommerfeld enhancement factor behaves as $1/v$ and for very small velocities it saturates to constant values. Given α the coupling constant and m_ϕ the mass of the new force carrier, if the quantity $m_\phi/m_\chi \cdot \alpha$ is close to the values that make the Yukawa potential have zero-energy bound states, the enhancement is much larger; indeed, the enhanced cross section shows resonances at $m_\chi = \frac{4m_\phi n^2}{\alpha}$ (n $= 1, 2, 3...$), which grow as $1/v^2$, up to the point where they get cut off by finite width effects.
In Fig. 5.4 we show the Sommerfeld enhanced cross sections for $\alpha = \frac{1}{4\pi}$, $\beta = 10^{-8}$ and a force carrier of mass $m_\phi = 1$ GeV (upper curve) and $m_\phi = 90$ GeV (lower curve). We over-impose the upper bounds obtained in the previous Section from the residual IGRB Model I and Model II and already displayed in Fig. 5.3. Our results show that a Sommerfeld enhancement due to a force carrier of $m_\phi < 1$ GeV ($\alpha = \frac{1}{4\pi}$) is strongly excluded by Model

I and II for the Fermi-LAT IGRB data. For a massive force carrier (90 GeV) only the resonant peaks above the TeV mass are excluded. The result holds for $\beta = 10^{-8}$ up to $\beta = 10^{-3}$. Comparable constraints have been obtained in [430, 431] through the analysis of perturbations to the CMB angular power spectrum
Therefore, high latitude γ-ray observations interpreted as due to DM annihilation in the Milky Way halo bound the Sommerfeld enhancement of the annihilation cross section to a factor of 3-10-50-200 for m_χ=10-100-1000-5000 GeV, respectively. In case a Yukawa-like potential describes this non-relativistic quantum effect, a force carrier heavier than 1 GeV is definitely required.

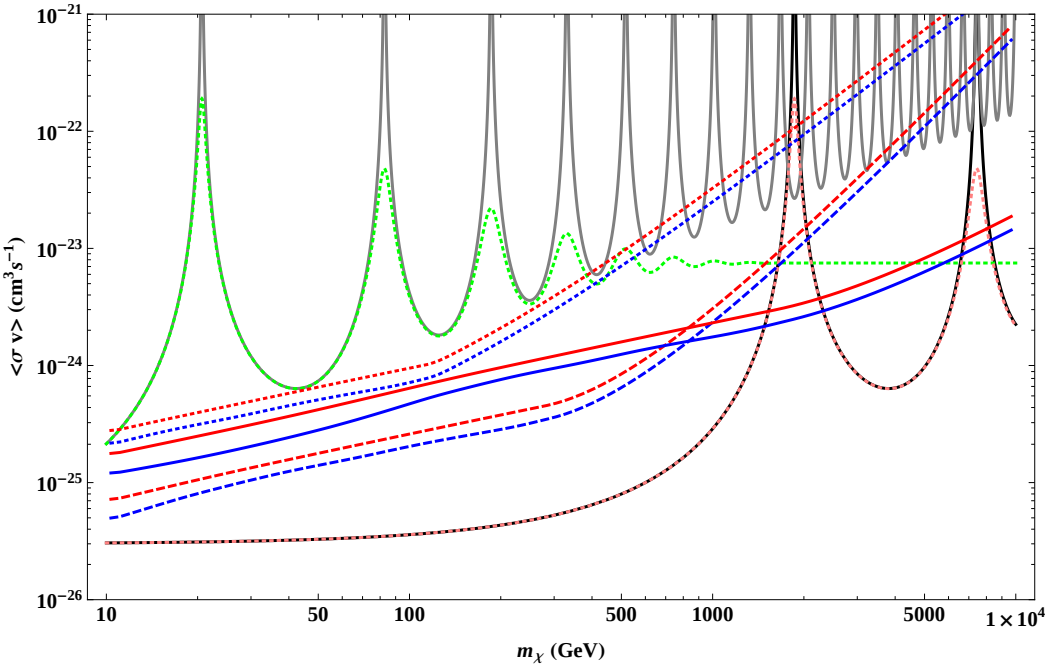

Figure 5.4: Sommerfeld enhancement of the annihilation cross section as a function of the DM mass, for $\alpha = \frac{1}{4\pi}$. Solid curves are for $\beta = 10^{-8}$, dotted ones for $\beta = 10^{-3}$. The upper (lower) resonant curve is obtained for a force carrier of mass $m_\phi = 1$ GeV (90 GeV). The upper (lower) dotted, solid and dashed curves correspond to the upper bounds for IGRB Model I (Model II) derived from WIMPs annihilating in the high latitude galactic halo in $\mu^+\mu^-$, $b\bar{b}$, $\tau^+\tau^-$, respectively (see Fig. 5.3.)

4.4 Bounds from the high-redshift protohalos

A possible way to boost the annihilation rate is to modify the particle theory and make the ansatz that the annihilation cross section depends on the inverse of the velocity [622]. A boosted production of γ-rays in models with $\langle\sigma v\rangle \propto 1/v$ has been proposed for the first bound objects formed in the early phases of the universe [623, 624]. After the matter-radiation equality is reached, DM perturbations start growing via gravitational instability and form the first bound protohalos at a redshift of about 140. The birth of these protohalos depends on the properties of the DM particles, since they are responsible of the primordial

inhomogeneities. The complete decoupling of DM particles from the thermal bath happens later with respect to the freeze-out temperature T_f, at a temperature of kinetic decoupling T_{kd}, because scattering events with SM particles keep the WIMPs close to thermal equilibrium. For $T \leq T_{kd}$, free-streaming and acoustic oscillations compete to damp the power spectrum of matter density fluctuations, which sets in turn the mass M_c of primordial DM structures [625–628]. For very small values of M_c, the details of the QCD phase transition could further slightly damp the actual cutoff mass [629]. In general, however, both the thermal and kinetic decouplings from the cosmic plasma are heavily linked to the WIMP nature and interactions with SM particles. The velocity dispersion of the first protohalos that collapse at redshift z_C is estimated to be very small ($\beta \sim 10^{-8}$) [624]. Therefore, models for $\langle\sigma v\rangle$ depending on the inverse of v predict a boosted flux of DM annihilation products. The photons arising from WIMP annihilations in very early halos can freely propagate with their energy red-shifting and reach the Earth in the range $\sim$ keV - TeV, while photons emitted out of this transparency window are absorbed by the intergalactic medium.
The $1/v$ enhancement of the annihilation cross section may be simply parameterized by writing [624]:

$$\langle\sigma v\rangle = \langle\sigma v\rangle_0 \frac{c}{v} \ \mathrm{cm}^3/\mathrm{s}. \tag{8}$$

The energy density in photons today from WIMP annihilation in the primordial halos can be theoretically predicted by:

$$\rho_\gamma = 5.28 \cdot 10^6 \left(\frac{M_c}{M_\oplus}\right)^{-1/3} \langle\sigma v\rangle_0 B_{2.6} \left(\frac{m_\chi}{\mathrm{TeV}}\right)^{-1} \mathrm{GeVcm}^{-3}, \tag{9}$$

where the cosmological boost factor B, normalized to 2.6 ($B_{2.6} = B/2.6$) takes into account that the DM is distributed according to a Navarro-Frenk-White (NFW) density profile with the lowest concentration parameter [624] and M_c is in units of terrestrial masses ($M_\oplus$). Eq. (9) can be compared with the experimental photon density inferred for the Fermi-LAT IGRB [574] and for our two IGRB models derived in Section 3, which is obtained by integrating the photon flux on the Fermi-LAT energy range (100 MeV - 100 GeV). We obtain:

$$\rho_\gamma \simeq 6.62 \cdot 10^{-16} \left(\frac{E_\gamma}{\mathrm{GeV}}\right)^{-0.41} \mathrm{GeV\ \ cm}^{-3}\ \ (\mathrm{Fermi-LAT}) \tag{10}$$

$$\rho_\gamma \simeq 5.65 \cdot 10^{-16} \left(\frac{E_\gamma}{\mathrm{GeV}}\right)^{-0.41} \mathrm{GeV\ \ cm}^{-3}\ \ (\mathrm{Model\ I}) \tag{11}$$

$$\rho_\gamma \simeq 4.5 \cdot 10^{-16} \left(\frac{E_\gamma}{\mathrm{GeV}}\right)^{-0.46} \mathrm{GeV\ \ cm}^{-3} (\mathrm{Model\ II}, \mathrm{E}_\gamma > 8\ \mathrm{GeV}) \tag{12}$$

We constrain $\langle\sigma v\rangle_0$ by comparison of Eq. (9) with the experimental γ-ray density. The results are displayed in Fig. 5.5 as a function of the WIMP mass. The three central lines

bound the $\langle\sigma v\rangle_0$ (Eq. (8)) parameter from Fermi-LAT photon density given in Eq. (10), Eq. (11) and Eq. (12) respectively, from top to bottom, when $M_c = M_\oplus$. The upper (dashed) and the lower (dotted) bounds are derived for Model II when $M_c = 10^2 M_\oplus$ (upper) and $10^{-2} M_\oplus$ (lower). The bounds on $\langle\sigma v\rangle_0$ are strong: for WIMP masses below 100 GeV it is forced to be $< 10^{-33}$ cm^3/s. Upper bounds grow to $< 10^{-32}$ cm^3/s for $m_\chi \simeq 1$ TeV and sets to $< 10^{-31}$ cm^3/s at 10 TeV. We make notice that they are more stringent than limits obtained from primordial light elements abundance and CMB anisotropies [630] and significantly improve the bounds of Ref. [624].

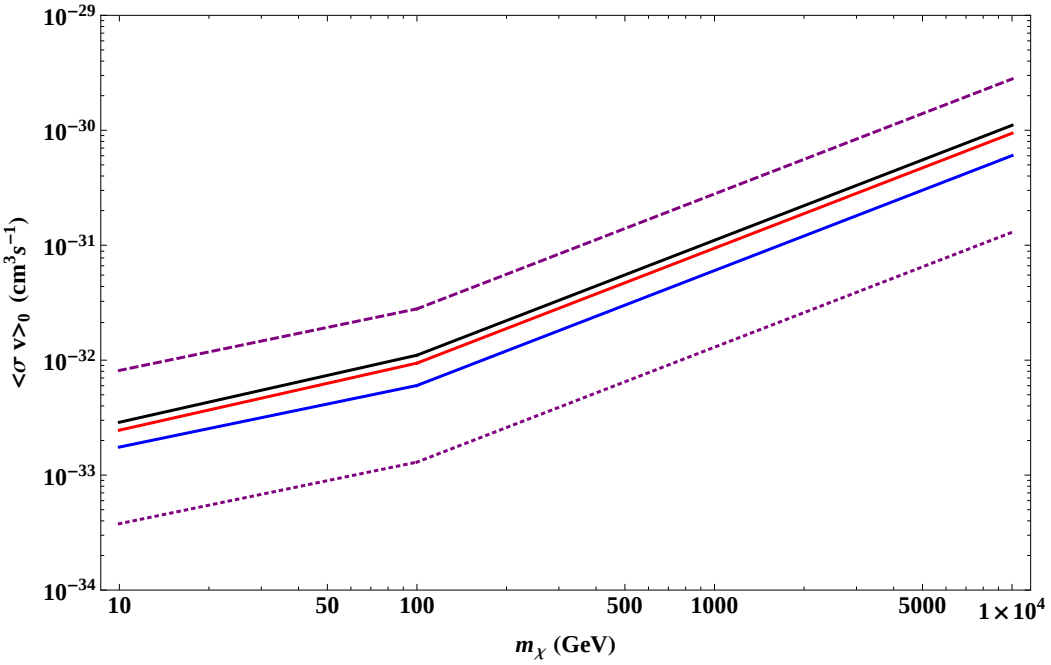

Figure 5.5: Bounds on $\langle\sigma v\rangle_0$ from Eq. (8), as a function of the DM mass. The central three bounds are obtained for $M_c = M_\oplus$, and from Eqs. (10) (black line), (11) (red line) and (12) (blue line) respectively, from top to bottom. The upper (lower) purple lines are derived from Eq. (12) for Model II IGRB and $M_c = 10^2 M_\oplus (10^{-2} M_\oplus)$.

The 1/v behaviour of the $\langle\sigma v\rangle$ may be identified with the Sommerfeld effect for velocities $\beta \gg (m_\phi/m_\chi)^{1/2}$ [346]. For lower velocities, as are the ones typical for protohalos, the series of resonances appears (see Section 4.3) and the Sommerfeld enhancement S behaves as $1/v^2$ close to the peaks. In this case, the upper bounds on the annihilation cross section may be obtained by rescaling $\langle\sigma v\rangle = \langle\sigma v\rangle_0 S$ with a factor $1/\beta \cdot m_\phi/m_\chi$. From Eqs. (9) - (12) it is straightforward to notice that the bounds on a Sommerfeld enhanced $\langle\sigma v\rangle$ derived from a overproduction of γ-rays in protohalos, are much stronger than the ones imposed by annihilation in the high-latitude galactic halo.

5 Conclusions

The γ-ray IGRB measured by Fermi-LAT [574] likely includes contributions from galactic and extragalactic *unresolved* sources. We have explored possible non-negligible diffuse con-

tributions from unresolved blazars, MSPs, star-forming galaxies and UHECRs. Lead by a conservative attitude, we have considered the minimal contribution for all sources, and neglected those objects whose high latitude flux is not excluded to be less than 1% of Fermi-LAT IGRB. Two residual IGRB fluxes have been derived by subtraction of the additional fluxes from the Fermi-LAT IGRB: Model I is obtained after the subtraction of unresolved BL Lacs, FSRQs and galactic MSPs, while Model II is the residual flux after the further subtraction of star-forming galaxies and UHECRs.
From our new residual IGRB fluxes, we have set upper limits on the DM annihilation cross section into γ-rays. A conservative upper bound on $\langle\sigma v\rangle$ is derived by assuming that the Model I and II IGRB are entirely due to WIMPs pair-annihilating in the halo of our Galaxy. Values for $\langle\sigma v\rangle \gtrsim 10^{-25}$ cm^3/s are strongly excluded for $m_\chi \simeq 10$ GeV, while for $m_\chi \simeq 100$ GeV (1 TeV) the annihilation rate is bounded to $3 \cdot 10^{-25}$ cm^3/s (10^{-24} cm^3/s). This results holds for DM annihilating into $b\bar{b}$. Stronger limits below m_χ= 1 TeV are derived for annihilation into the leptonic τ annihilating channel, while for the μ channel the limits are close to the $b\bar{b}$ below m_χ= 100 GeV, and weaker above this mass. Annihilation into leptons is therefore excluded at a level which strongly disfavours the interpretation of cosmic positron fraction data in terms of leptophilic DM with small cosmological boost factors. The latter boost factors are in turns strongly limited by antiproton data [341].
The bounds on $\langle\sigma v\rangle$ have been interpreted in terms of Sommerfeld enhancement of the annihilation cross section. A Sommerfeld enhancement due to a force carrier of $m_\phi < 1$ GeV ($\alpha = \frac{1}{4\pi}$) is strongly excluded by Model I and II for the Fermi-LAT IGRB data. For a massive force carrier (90 GeV) only the resonant peaks above the TeV mass are excluded. High latitude γ-ray observations interpreted as due to DM annihilation in the Milky Way halo bound the Sommerfeld enhancement of the annihilation cross section to a factor of 3-10-50-200 for m_χ=10-100-1000-5000 GeV, respectively, and in case an annihilation into light quarks occurs. For $m_\chi \lesssim$ 6-700 GeV these limits are reduced by a factor of few for the pure $\tau^+\tau^-$ annihilation channel. In case a Yukawa-like potential describes this non-relativistic quantum effect, a force carrier heavier than 1 GeV is definitely required.
Finally, we have explored the possibility that the residual γ-ray IGRB is entirely due to cosmological annihilation of DM in protohalos at high redshift. Within the hypothesis that $\langle\sigma v\rangle$ is inversely proportional to the WIMP velocity, very severe limits are derived for the velocity-independent part of the annihilation cross section, depending on the protohalo mass.

Recently, an updated calculation of the resulting upper bounds on the DM annihilation cross section from the contribution of annihilating galactic DM to the IGRB has been presented [631]. In that paper the authors take into account both prompt and inverse-Compton emission for DM-induced γ-rays and they include the astrophysical contribution from unresolved misaligned AGNs (MAGN).

CHAPTER

SIX

UNCERTAINTIES ON GAMMA-RAY ANISOTROPY FROM DM IN THE MILKY WAY

The energy spectrum of the isotropic γ-ray background has already been introduced and studied extensively in Chapter 5. We saw that current estimates of the astrophysical unresolved contribution to this emission suggest that there is still open room for exotic physics such as DM.
The energy spectrum of γ-rays due to annihilations of DM particles in the smooth galactic DM halo, in the galactic DM substructures (clumps, subhalos) and in extragalactic halos has been computed by several groups using analytical and numerical techniques. Constraints on DM models have been derived from the observed IGRB spectrum [3, 631].

Gamma-rays have the interesting property of almost not being deflected nor absorbed while propagating through the galaxy, therefore they carry spatial information about the distribution of sources. For this reason anisotropies imprinted in the IGRB can be used to discriminate populations of sources with different spatial distributions, in particular DM from standard astrophysical sources (see for instance [632–634]).
The good angular resolution of the Fermi-LAT instrument allows to study the angular power spectrum (APS) of the IGRB. The Fermi-LAT collaboration already reported the detection of some angular power above the noise level in the multipole range $l \sim 155 \div 504$ with a significance ranging from 7.2σ between 2 and 5 GeV to 2.7σ between 10 and 50 GeV [635]. Currently, the angular power spectrum on large angular scales, $l \lesssim 155$, is not used because of a potential contamination by the galactic foreground emission (such as pion decay). Predictions for the APS produced by various populations of unresolved sources, both of astrophysical [632–634] and of DM origin [636–648], have been made by several groups. A very exhaustive discussion of the energy spectrum and of the APS due to galactic and extragalactic DM sources has been provided [649]. In that work the authors used the results of the detailed cosmological structure formation N-body simulation Millennium-II [650] and of the Aquarius [552] simulation to compute both the energy spectrum and the APS in two benchmark particle DM scenarios. In contrast with previous works, these observables were computed in [649] by directly using the results of the numerical N-body simulations.

As discussed in [649], the extragalactic (EG) contribution to the energy spectra and anisotropies is affected by large uncertainties. The contribution from DM halos and subhalos that are not resolved by N-body simulations leads to a 2-order of magnitude uncertainty on the predicted level of the extragalactic energy spectrum. Depending on the particular assumptions made in the extrapolation of the unresolved (sub)halo distributions, the EG spectrum might be the dominant or the subdominant component of the total energy spectrum. In the same way, the intensity APS can receive a significant or a negligible contribution from extragalactic (sub)structures.

On the other hand, uncertainties in the galactic contribution were not thoroughly assessed in [649]. Besides the ones discussed in [649], at least two other sources of uncertainties must be taken into account. First of all, computing the power spectrum at $l \gtrsim 100$ requires to extrapolate the DM profile to very small scales at least for the main halo, much below the resolution of current numerical simulations. Furthermore, different spatial distributions of substructures can lead to different APS. For instance, substructures with large masses ($M \gtrsim 10^8$ $\mathrm{M}_\odot$) are expected to be only a few; hence the statistical fluctuations associated to their distribution can be large.

In this Chapter we will discuss these two sources of uncertainty in the APS of the γ-ray emission from DM annihilation in our galaxy. We will realize two separate analysis: 1) we will address the uncertainty related to the extrapolation of the DM profile using a pure DM simulated galaxy [140]. 2) Concerning the uncertainty pertaining to the spatial distribution of galactic substructures, we will realize a MonteCarlo simulation based on analytical fits to the distribution of substructures simulated by Aquarius [552, 651].

The Chapter is organized as follows: in Section 1 we will introduce the N-body simulation [140] and we will comment about different fits to the DM density distribution in the simulated galaxy. In Section 2 we will discuss the realization of the MonteCarlo simulation which we will use to study the uncertainties related to the spatial distribution of subhalos. In Section 3.1 we will show the impact of these uncertainties on the APS. Finally, in Section 4 we will comment about the results and future perspectives.

1 Uncertainty related to the extrapolation of the DM density profile

1.1 Gamma-rays from dark matter annihilation

As we discussed in the introduction to Part II, the γ-ray flux $\mathrm{d}\Phi_\gamma/\mathrm{d}E_\gamma$ from DM annihilating particles, defined as the number of photons collected by a detector per unit of time, area, energy and solid angle) is written as the product of two terms: a *particle physics* (PP) term and an *astrophysical* contribution (J).
The PP term encodes all the information about the particle physics nature of DM. A general WIMP candidate is for this purpose completely defined by its mass, m_χ, its annihilation cross section times the relative velocity $\langle\sigma v\rangle_{\mathrm{ann}}$ and its γ-ray photon yield. In our study we

just consider γ-ray continuum and we further neglect the contribution coming from inverse Compton scattering if electrons and positrons are produced in DM annihilation or decay processes. Indeed, these contributions are usually subdominant and, as for γ-ray lines, also model-dependent.
In the following, concerning the particle physics factor, we assume annihilation into $b\bar{b}$, a DM mass of 200 GeV and $\langle\sigma v\rangle \sim 3 \cdot 10^{-26}\mathrm{cm}^3\mathrm{s}^{-1}$.

The second term of Eq. (32), $J(\psi, \theta, \Delta\Omega)$, depends on how the DM is distributed in space, i.e. on the DM density distribution. This term is of direct relevance to our computations.

In our theoretical calculations, however, we will consider a very small observational solid angle, such that we will compute the following quantity

$$J(\Psi, \theta) = \frac{1}{\Delta\Omega} J(\Psi, \theta, \Delta\Omega) \simeq \int_{\mathrm{l.o.s}} \rho^2(s, \Psi, \theta) \ \mathrm{d}s \ . \tag{1}$$

As we will evaluate only the γ-ray flux and power spectrum for our own Galaxy, we will neglect absorption in the following.

1.2 DM distribution from a N-body numerical simulation

The spatial distribution of DM describes both the main smooth halo and the possible sub-halo population, and it rules the spectrum of anisotropies searched for in the γ-ray sky.

In the following we will refer to the DM halo and subhalos of the simulated N-body galaxy g15784 part of the Making Galaxies in a Cosmological Context (MaGICC) programme [140]. This galaxy has a mass of $1.48{\times}10^{12}\mathrm{M}_\odot$ and 27 subhalos with masses of the order of $10^8 - 10^9 M_\odot$.

Concerning the DM density profile, we fit the DM distribution of the main halo in [140] with three different profiles, namely NFW [560], Einasto [562] and Moore & Stadel (MS):

$$\rho(R) = \frac{\rho_s}{(R/R_s)(1+R/R_s)^2} \qquad \text{(NFW)} \tag{2}$$

$$\rho(R) = \rho_0 \exp\left(-\frac{2}{\alpha}\left[\left(\frac{R}{R_s}\right)^\alpha - 1\right]\right) \qquad \text{(Einasto)} \tag{3}$$

$$\rho(R) = \rho_0 \exp\left(-\lambda\left[\ln\left(1+\frac{R}{R_\lambda}\right)\right]^2\right) \qquad \text{(MS)} \ . \tag{4}$$

The resulting distributions are shown in Fig. 6.1. We remark that all these profiles provide statistically equivalent fits to the DM distribution obtained from the numerical simulation. They clearly overlap at scales probed in the simulation, that are used to perform the fit, but they display very different behaviours at smaller scales. In particular, the NFW profile is more peaked, while the MS one has a large core. At small scales, the difference between the DM distribution fitted with a peaked or a cored profile becomes very sizeable.

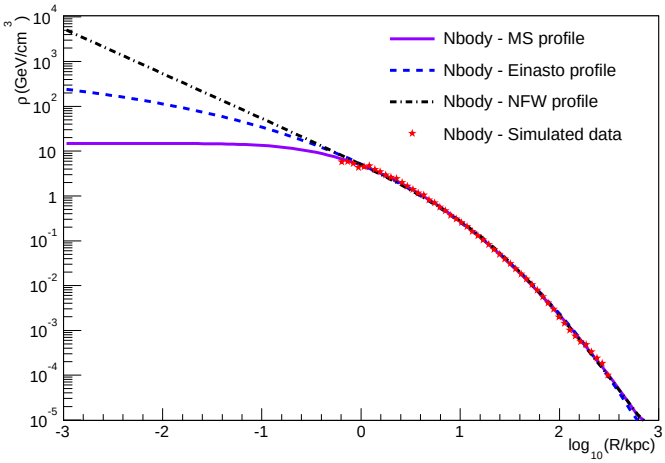

Figure 6.1: DM spatial profiles for the main halo in a typical N-body simulation. The same halo has been fitted using a MS (solid violet curve), an Einasto profile (dashed blue curve) and a NFW profile (dotted-dashed black curve). The red points correspond to simulated data points, according to the simulation g15784 of [140].

For what concerns the galactic substructures, we use the same three profiles to fit their DM distributions.

2 Uncertainty due to the clumps distribution

The second kind of analysis that we perform is the study of the uncertainty related to the clumps distribution.
In order to evaluate the statistical fluctuations of the APS associated to the spatial and mass distributions of galactic clumps we used the results from the Aquarius simulation [552] to sample the distribution of individual subhalos with mass 10^5 $\mathrm{M}_\odot < M < 10^{10}$ $\mathrm{M}_\odot$. This will allow to evaluate statistical fluctuations of the APS associated to their presence. We have checked that the spatial fluctuations due to smaller unresolved clumps are negligible.

2.1 Modeling the galactic DM distribution with the Aquarius simulation

In this section we describe the modelling of the components of the galactic halo, i.e. the smooth component and the subhalo population. Indeed, a correct description of the clumps distribution is required in order to highlight the chance of detecting DM subhalos through the gamma-ray induced signal. High resolution N-body simulations indicate that a large fraction of the MW halo mass is embedded in substructures. The CDM scenario predicts the formation of these virialized structures, with masses as small as $M_{min} \sim 10^{-6}\mathrm{M}_\odot$, depending on the particle physics nature of the DM candidate [625, 653]. M_{min} can indeed

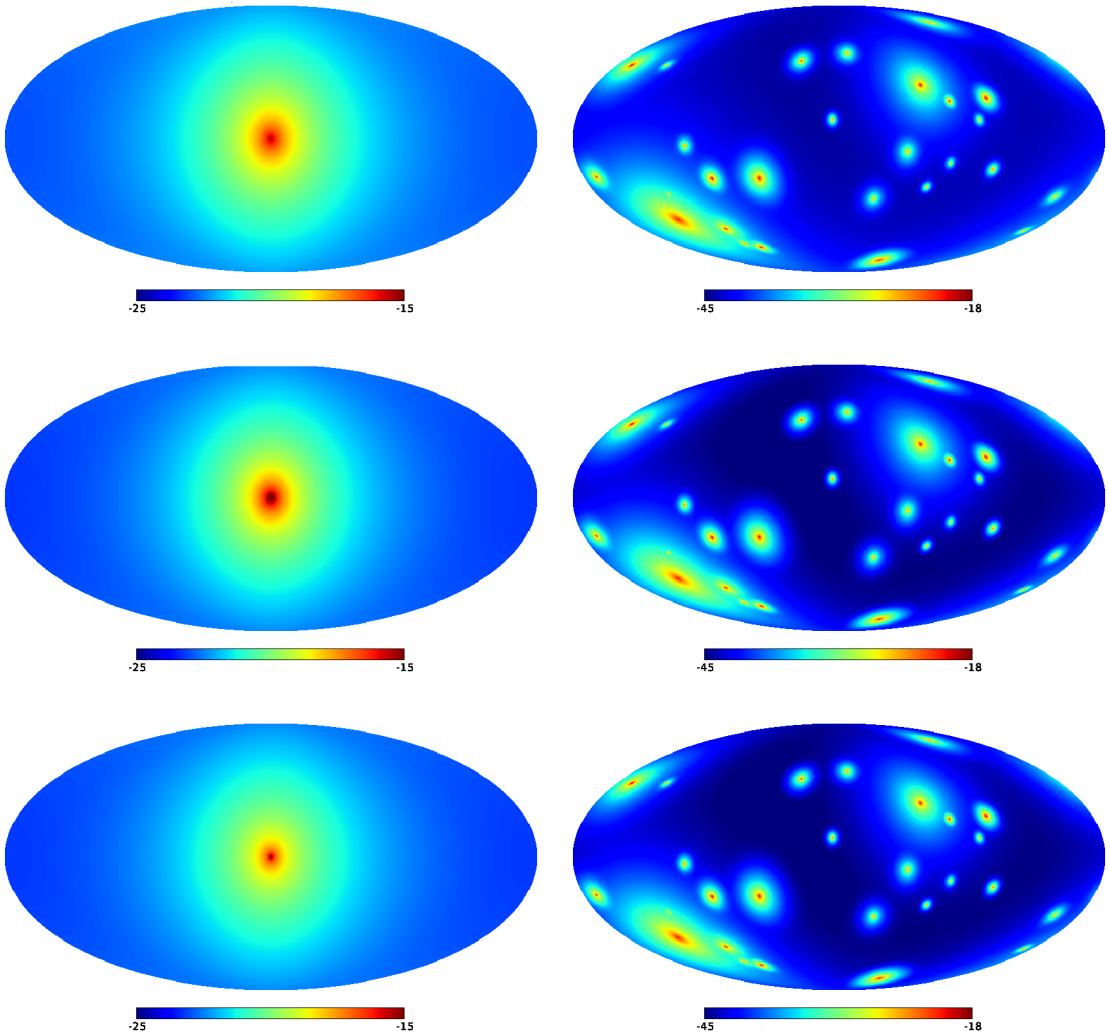

Figure 6.2: All-sky maps of the gamma-ray intensity (in units of log GeV^{-1} $\mathrm{cm}^{-2}\mathrm{s}^{-1}\mathrm{sr}^{-1}$) from DM annihilation in the simulated galaxy g15784 from [140]. The first column shows the smooth halo contibution, and the second one the substructures contribution. In the first row the halos (both the smooth and the clumps) are fitted with the MS profile; in the second row with the Einasto profile and in the last one with NFW. Maps are generated by using the HEALPix software [652]. See section 2.2.

vary between 10^{-3} and 10^{-12} $\mathrm{M}_{\odot}$ depending on the particle physics model. The particle nature of the DM determines the small-scale cutoff in the matter power spectrum of density fluctuations from which the minimum mass M_{min} is inferred. For instance, in a SUSY scenario with the neutralino as DM candidate, typical values of M_{min} are in the range $10^{-11}\mathrm{M}_{\odot}\mathrm{h}^{-1}, 10^{-3}\mathrm{M}_{\odot}\mathrm{h}^{-1}$ [654].
Nevertheless, the mass resolution of current numerical simulations is around $10^{5}\mathrm{M}_{\odot}$. We have checked that smaller unresolved clumps with masses between 10^{-6} and 10^{5} $\mathrm{M}_{\odot}$ give a negligible contribution to the APS.

We model the galactic substructure population as in [651], which is inspired by high resolution pure DM simulations of MW-sized galaxy halos. However, since the resolution of this kind of numerical experiments does not cover all the expected mass range for the substructures at z=0, the authors [651] have extrapolated the description down to smaller halos. We use a MonteCarlo algorithm to create several realizations of this galactic clumps distribution.
We always use R for the galactocentric radial coordinate, while we use r for the *clump-centric* radial coordinate. We always assume spherical symmetry. We reserve the subscript sm for the smooth component, while sh will be used for quantities related to substructures; cl will refer to the DM distribution *inside* each substructure. We call M_{MW} the mass of the Milky Way. We define the total DM density profile $\rho_{tot}(R) = \rho_{sm}(R) + \rho_{sh}(R)$. Notice that this sum is the quantity that usually is considered to have a "NFW or Einasto shape". The two addenda need not to have the same shape as their sum. In fact, the density profile of the smooth component is obtained by difference

$$\rho_{sm}(R) = \rho_{tot}(R) - \rho_{sh}(R) \ . \tag{5}$$

On the contrary, the DM density profile within a substructure, $\rho_{sub}(r)$, is assumed to be the same as the one of the total halo (but with different characteristics).
We define the subhalo mass density profile (subhalo density per unit subhalo mass) as

$$\frac{d\rho_{sh}(M_{sh}, R)}{dM_{sh}} = \rho_{sh}(R)\mathcal{F}(\mu, M_{sh}) \ , \tag{6}$$

with $\mathcal{F}(\mu, M_{sh}) = \mathcal{F}_0(M_{sh}/M_\odot)^{-\mu}$ the normalized mass function. The normalization is such that, quoting from [651], its integral is unity in the surveyed mass range. The fraction of the total mass found in substructures is called f_{tot}.

Concentration Let us define r_{200} the radius (measured from the center of the clump) which encloses an average DM density equal to 200 times the critical density of the Universe $\rho_{\rm cr} = 3{\rm H}^2/(8\pi{\rm G})$, and let us call r_s the scale radius of the DM distribution inside the substructure. Then we define the concentration parameter $c_{200} \equiv r_{200}/r_s$. The concentration depends in general on the clump mass and on the position in the halo. According to numerical simulations it can be parameterized as

$$c_{200}(M_{sub}, R) = \left(\frac{R}{R_{vir}}\right)^{-\alpha_R} \times \left[C_1 \left(\frac{M_{sub}}{M_\odot}\right)^{-\alpha_1} + C_2 \left(\frac{M_{sub}}{M_\odot}\right)^{-\alpha_2}\right] \tag{7}$$

Regarding the DM density profile,

$$\rho_{tot}(R) = \rho_s \exp\left\{-\frac{2}{\alpha}\left[\left(\frac{R}{r_s}\right)^{\alpha} - 1\right]\right\} \tag{8}$$

$$\rho_{\rm sh}(R) = \rho_a \exp\left\{-\frac{2}{\alpha_a}\left[\left(\frac{R}{r_a}\right)^{\alpha_a} - 1\right]\right\} \tag{9}$$

$$\rho_{cl}(r) = \rho_{s,cl} \exp\left\{-\frac{2}{\alpha}\left[\left(\frac{r}{r_{s,cl}}\right)^{\alpha} - 1\right]\right\} \ , \tag{10}$$

where the only parameter to be computed is ρ_a, which is set by f_{tot}, which in turn is set by imposing that the mass fraction in substructures matches the one found in the resolved sub halo mass range of the simulation. All the other parameters come from the original fits of simulation results performed by the Aquarius team. $\rho_{s,cl}$ is normalized over the volume of the subhalo to give its virialized mass.

Tidal effects The above discussion includes also an extrapolation of the substructures profiles in the galactic center region which is poorly explored by simulations due to poor resolution. Indeed, the actual distribution might be different from the extrapolated one, due to the presence of tidal effects that tend to disrupt substructures close to the galactic center. To account for this effect, the so called Roche criterion is often used: a substructure is destroyed when its scale radius r_s is larger than the tidal radius $r_{\rm tid}$

$$r_{\rm tid}(R) = \left(\frac{M_{\rm sh}}{3M_{\rm MW}}\right)^{1/3} R \tag{11}$$

The MonteCarlo algorithm gives the position and the mass of a substructure according to Eq. (6), within the Milky Way virial radius and until the total substructure mass is reached. Then, if the substructure survives tidal disruption, its concentration is computed and its scale radius is inferred. Finally, all the other relevant clumps parameters (its 3D position, its virial radius ...) are derived and stored in a `ROOT` [1] [655] TTree file. The numerical values of the parameters used in the procedure are shown in Tab. 6.1.

2.2 Sky-Maps Generation

The γ-ray intensity maps from DM annihilation in our own galaxy are generated by using the HEALPix [2] software [652]. The projection into a 2-dimensional map is done assuming resolution 9, i.e. `N_side`=512, corresponding to an angular area of approximately 4×10^{-6} sr for each pixel. We use HEALPix to compute the APS of the simulated maps.
The DM distribution, ρ, can be thought of as composed by two contributions, the main galactic halo and the substructures. Hence, the J factor reads

$$\begin{aligned} J &= \int_{\rm l.o.s.} \left(\rho_{\rm sm}(s) + \sum_i \rho_{{\rm cl},i}(s)\right)^2 ds \\ &= \int_{\rm l.o.s.} \left(\rho_{\rm sm}(s)^2 + \sum_i \rho_{{\rm cl},i}(s)^2 + 2\,\rho_{\rm sm}(s) \cdot \sum_i \rho_{{\rm cl},i}(s) + \sum_i \sum_{j\neq i} \rho_{{\rm cl},i}(s) \cdot \rho_{{\rm cl},j}(s)\right) ds \\ &= J_{\rm sm} + J_{\rm cl} + J_{\rm cl,sm} + J_{\rm cl,cl} \end{aligned}$$

[1] `http://root.cern.ch`
[2] `http://healpix.sourceforge.net`

Table 6.1: Numerical values of the parameters of the DM distribution modelled according to Aquarius simulation [552,651].

Ω_m	0.25
Ω_Λ	0.75
σ_8	0.9
n_s	1
H_0 (km/s/Mpc)	73
Minimum resolved mass ($M_\odot$)	$10^{4.5}$
ρ_s ($10^6 M_\odot$ kpc^{-3})	2.8
$R_{\rm vir}$ (kpc)	433
$M_{\rm MW}$ ($M_\odot$)	2.5×10^{12}
r_s (kpc)	20
α	0.17
$\mathcal{F}_0$ ($M_\odot^{-1}$)	3.6×10^{-6}
$N_{\rm sub}$	1.1×10^{15}
$M_{\rm sub}^{\rm tot}(< R_{\rm vir})$ ($M_\odot$)	4.2×10^{11}
$f_{\rm tot}(< R_{\rm vir})$	0.17
f	0.132
M_1 ($M_{\rm MW}$)	1.8×10^{-8}
M_2 ($M_{\rm MW}$)	10^{-2}
ρ_a ($M_\odot$ kpc^{-3})	2840.3
α_a	0.678
$R_a \equiv r_b$ (kpc)	199
μ	1.9
α_R	0.237
C_1	232.15
C_2	-181.74
α_1	0.0146
α_2	0.008

(12)

where

$$J_{\rm sm} = \int_{\rm l.\,o.\,s.} \rho_{\rm sm}(s)^2\, ds \tag{13}$$

$$J_{\rm cl} = \int_{\rm l.\,o.\,s.} \sum_i \rho_{{\rm cl},i}(s)^2\, ds \tag{14}$$

$$J_{\rm cl,sm} = 2 \int_{\rm l.\,o.\,s.} \sum_i \rho_{\rm sm}(s) \cdot \rho_{{\rm cl},i}(s)\, ds \tag{15}$$

$$J_{\rm cl,cl} = \int_{\rm l.\,o.\,s.} \sum_i \sum_{j\neq i} \rho_{{\rm cl},i}(s) \cdot \rho_{{\rm cl},j}(s)\, ds \tag{16}$$

The upper limit of the integration is:

$$s_{\rm max} = \sqrt{R_{\rm vir}^2 + R_\odot^2 - 2\, R_\odot\, R_{\rm vir}\, \cos({\rm b})\, \cos({\rm l})} \tag{17}$$

where $R_{\rm vir}$ is the virial radius of the galaxy and (b, l) the galactic coordinates of the l. o. s.. While the terms $J_{\rm sm}$ and $J_{\rm cl}$ need to be evaluated with full accuracy, the interference terms are subdominant but very time-consuming (in terms of computational time), therefore we compute them according to a simplified procedure. For $J_{\rm cl,sm}$ the integral is evaluated by taking into account the emission from the clump up to a radial distance from its center equal to N times the virial radius, with $N = 4$. We have tested the impact of varying N on both the intensity maps and the power spectrum, up to $N = 10$. The power spectra differ by less than few percent at low multipoles and are equivalent from $l = 5$ on.
Similarly, the interference term $J_{\rm cl,cl}$ is evaluated by considering non-zero the product $\rho_{{\rm cl},i}\rho_{{\rm cl},j}$ only if the following two conditions are met:

- the relative distance between the two clumps is less than ten times the sum of the two virial radii.
- the distance from the l. o. s. to the center of each clump is equal to 4 times its virial radius.

We checked that varying the two conditions impacts less than few percent on the power spectrum.

Unresolved substructures

The sub halo mass density profile has been derived from a fit to the current simulations results and it is strictly valid only down to the mass resolution limit of the simulations. Yet, substructures with smaller mass could be present and we need to evaluate their contribution. In order to extrapolate the distribution of substructures in a mass range below the simulation resolution, we assume that both mass and space probability distributions are the same as for the resolved substructures, and we compute the contribution of substructures

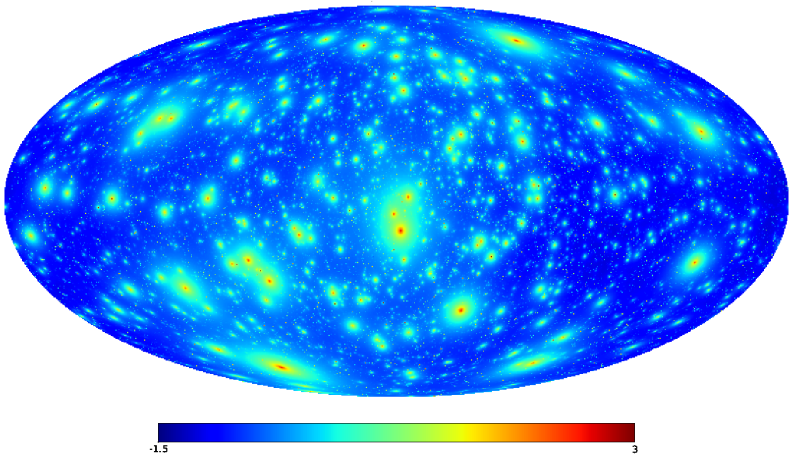

Figure 6.3: Map of the gamma-ray dimensionless intensity (divided by the mean intensity squared) from DM annihilation of the term of interference between the smooth halo and the resolved subhalos modelled as explained in section 2.1. The map is in a logarithmic scale and we subtracted the all-sky average intensity of the smooth-clumps interference component.

from $10^{-6}\ M_\odot$ up to $10^5\ M_\odot$ as follows.

The mass and spatial probability distribution functions are written as

$$\frac{dP_M}{dM} = \mathcal{F}(\mu, M_{sh}) \tag{18}$$

$$\frac{dP_R}{dV} = \frac{\rho_{sh}(R)}{f_{\rm tot}\, M_{\rm MW}}. \tag{19}$$

From the spatial and mass probability distribution functions we compute the average contribution from the unresolved clump distribution:

$$\langle J_{\rm cl}^{\rm unres} \rangle = N_{\rm tot} \int_{\rm l.o.s.} \frac{dP_{\rm R}}{dV}\, dl \int_{M_{\rm min}}^{M_{\rm max}} \mathcal{L}(M)\, \frac{dP_{\rm M}}{dM}\, dM \tag{20}$$

where $\mathcal{L}(M)$ is the luminosity of a single clump:

$$\mathcal{L}(M) = \int_{V_{\rm cl}} \rho_{\rm cl}(r)^2 dV = 4\,\pi \int_0^{R_{\rm vir,cl}} \rho_{\rm cl}(r)^2\, r^2\, dr\,. \tag{21}$$

and $M_{\rm min} = 10^{-6}$ and $M_{\rm max} = 10^5$.

As we have already commented before, unresolved clumps give a negligible contribution to the total APS.

3 Angular power spectrum of the DM-induced γ-ray emission

We consider the angular power spectrum (APS) C_ℓ of an intensity map $I(\Psi)$ where Ψ is the direction in the sky. The **intensity** angular power spectrum is given by the coefficients

$$C_\ell = \frac{1}{2\ell+1}\left(\sum_{|m|>\ell}\langle|a_{\ell m}|^2\rangle\right) \tag{22}$$

with the $a_{\ell m}$ determined by expanding the map in spherical harmonics, after subtracting the average value of the intensity over the region of the sky considered:

$$I(\Psi) = \frac{\mathrm{d}\Phi}{\mathrm{d}E}(\Psi) - \langle\frac{\mathrm{d}\Phi}{\mathrm{d}E}(\Psi)\rangle = \sum_{\ell=0}^{\infty}\sum_{m=-\ell}^{m=\ell} a_{\ell m}Y^*_{\ell m}(\Psi). \tag{23}$$

The intensity APS indicates the *dimensionful* size of intensity fluctuations and can be compared with predictions for astrophysical sources whose collective intensity is known or assumed ([634]). Moreover, the intensity APS is an additive quantity: the intensity APS of a sum of maps is equivalent to the sum of the intensity APS of each map, provided that the maps are uncorrelated (i.e. that the product $a_i a_j^* = 0$).
However, it is possible to define also another quantity, the so-called **fluctuation** angular power spectrum, by dividing the intensity angular power spectrum C_ℓ of a map by the mean sky intensity squared $\langle\mathrm{d}\Phi/\mathrm{d}E\rangle^2$. The fluctuation angular power spectrum characterizes the angular distribution of the emission independent of the intensity normalization and it is *dimensionless*. To obtain the fluctuation APS of a sum of maps, it is necessary to multiply each coefficient by the relative emission of each map with respect to the total, squared:

$$C_\ell^{fluct} = \sum_i f_i^2 C_{\ell,i}^{fluct}, \tag{24}$$

where $f_i = \frac{\langle\mathrm{d}\Phi^i/\mathrm{d}E\rangle}{\langle\mathrm{d}\Phi/\mathrm{d}E\rangle}$.
We also remind that it is usual convention to plot the APS multiplied by $\ell(\ell+1)/2\pi$.

3.1 Results

We have calculated the intensity APS for the all-sky γ-ray intensity maps from DM annihilation in our own galaxy, for both the smooth halo and the substructures of the simulated galaxy g15784 from the MAGICC project using the HEALPix [3] software [652]. In all cases, annihilation into $b\bar{b}$ is assumed, a DM mass of 200 GeV and $\langle\sigma v\rangle \sim 3\cdot 10^{-26}\mathrm{cm}^3\mathrm{s}^{-1}$. The γ-ray flux has been obtained at 4 GeV.

Computing the APS to increasing large multipoles requires exploring the DM distribution at smaller and smaller scales, possibly much smaller than the resolution of current numerical

[3] `http://healpix.sourceforge.net`

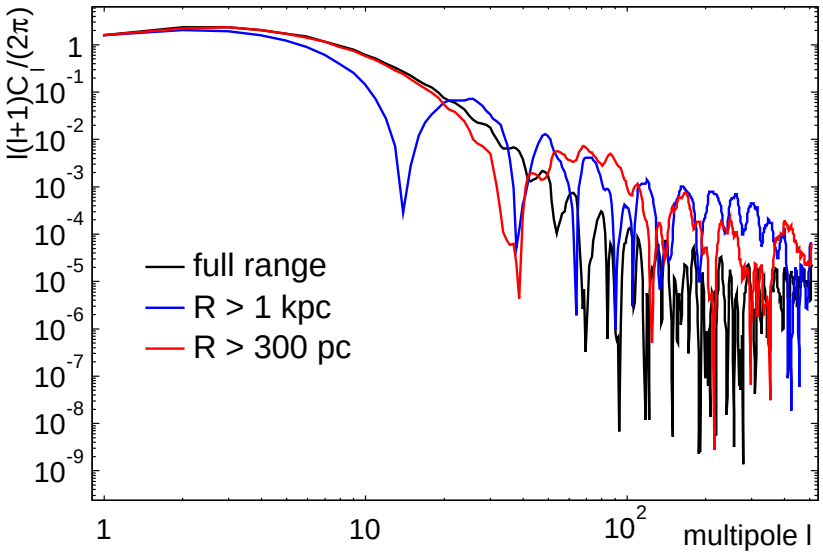

Figure 6.4: Fluctuation APS for the smooth halo of g15784 fitted with an Einasto profile. The black curve refers to the full range case, while the colored curves depict the APS obtained setting the DM density equal to zero when $R < 0.3$ kpc (red) or $R <$1 kpc (blue).

experiments. In order to quantify the uncertainties associated to the extrapolation of the different DM profiles, we show in Fig. 6.4 the APS computed for the smooth halo fitted with an Einasto profile, where we set $\rho = 0$ if $R < 0.3$ kpc (near-future expected spatial resolution of numerical simulations) or $R <$1 kpc (current spatial resolution of numerical simulations). The extrapolation clearly affects the APS at multipoles $l \gtrsim 10$ (corresponding to an angle of about 18°).
We showed in Fig. 6.1 a comparison of three different DM profiles used to fit the results of numerical experiments for the main halo. These profiles are very similar on large scales, because they fit the same distribution, but their behavior at small scales is very different: the MS profile displays a core, while the Einasto and NFW ones are more peaked. This difference is transferred to the APS, as we show in Fig. 6.4. The scope of this plot is to show how much the change of the density in the central region of the main halo affects the behaviour of the fluctuation APS already at small multipoles (i.e. large angles, where the differences should be milder).

In Fig. 6.5 we show the intensity APS computed for: i) the main halo described by the different, while equivalent parameterizations of Eqs. 3, 4 and 2; ii) the sub-structures resolved by the simulation. The gamma-ray intensity in a given direction is obtained by piling up the contributions from all subhalos encountered along the line of sight, up to a distance of 500 kpc.
We have further accounted for the contribution from unresolved subhalos using the procedure described in section 2.2 and checked that it is negligible.
The different behavior of the main halo profiles at small scales affects the APS up to seven

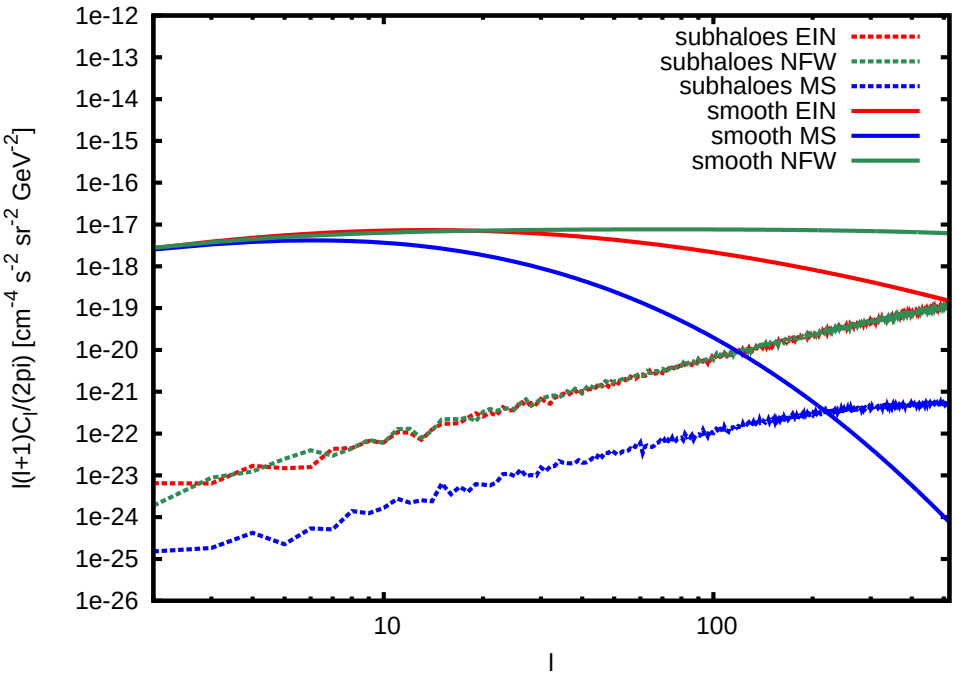

Figure 6.5: Intensity APS of the set of all-sky gamma-ray maps at 4 GeV from DM annihilation (see 2.2 for details about the maps generation). In all cases, annihilation into $b\bar{b}$ is assumed, a DM mass of 200 GeV and $\langle\sigma v\rangle \sim 3 \cdot 10^{-26}\mathrm{cm}^3\mathrm{s}^{-1}$. Solid (dashed) lines indicate the smooth (clumps) contribution. Green lines stand for halos whose density distribution is fitted with a NFW profile; red lines refer to the Einasto profile whereas blue lines to the MS profile. The intensity APS gives a measure of the relative anisotropies of the smooth halo and subhalos components.

orders of magnitude at large multipoles ($l \sim 500$). Remarkably, at $l \gtrsim 100$ the power spectra differ by several orders of magnitude. This makes reliable observations of the shape of the power spectrum at large multipoles a very useful tool to have a glimpse of the DM distribution on scales smaller than the resolution of numerical simulations. In particular, the peaked NFW profile yields more power at small scales, while the APS of the cored MS profile dies out already above $\ell \simeq 50$. Concerning the subhalo contribution, there is no difference between the APS for halos fitted with an Einasto or a NFW profile, whereas the APS is much milder in the case of the cored MS profile. When considering both the smooth and subhalos contributions, the APS signal is dominated by the smooth halo component in the case of NFW and Einasto profiles, but this is not true any more if the DM density profile inside halos is described by the cored profile of MS. In the latter case indeed, the APS for the subhalos becomes dominant at $l \sim 200$.
Therefore, this kind of analysis might help in the debate about the real shape of the DM distribution in the centers of the galaxies, and in particular of the Milky Way. Indeed, such a strong dependence of the power spectrum on the behavior of the DM profile at small scales could yield a significant contribution for the resolution of the peak vs cored debate. Future observations of the shape of the power spectrum that can be attributed to DM, will allow us

to explore the distribution of galactic DM at scales smaller than the resolution of N-body simulations.

Furthermore, we evaluate the uncertainty due to the presence of substructures by performing several realizations of their distributions, used the MonteCarlo method described in Section 2. We performed 500 realizations in the mass band $10^5 < \mathrm{M}/\,\mathrm{M}_\odot < 10^{10}$.

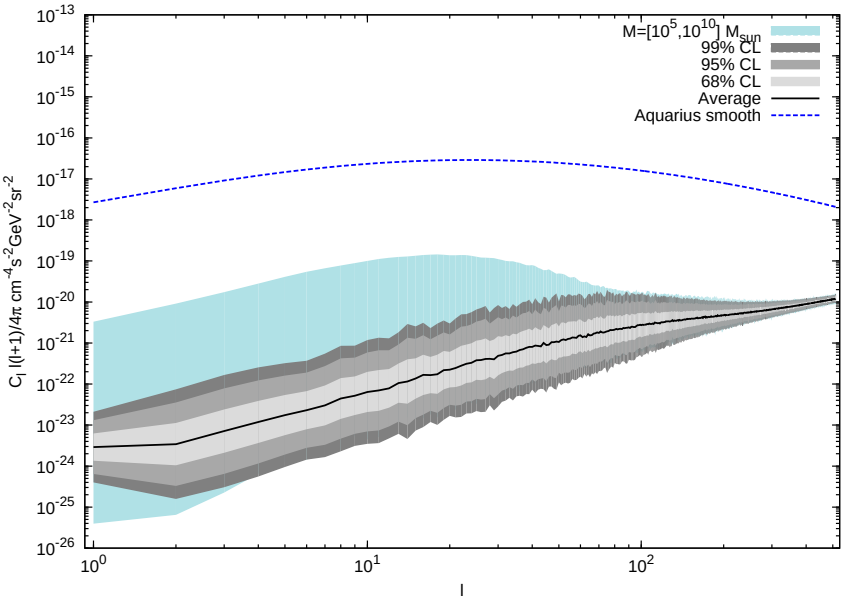

Figure 6.6: Intensity APS for the smooth halo component (dashed blue line) and substructures (black line and bands). The smooth contribution has been obtained according to table 6.1 for the Aquarius simulation. The bands depict the uncertainty due to the presence of substructures. The average is shown as a black line while the gray bands refer to the 68%, 95% and 99% uncertainty bands as resulting from 500 realizations in the mass band $10^5 < M/\,\mathrm{M}_\odot < 10^{10}$ as explained in 2.2. The light blue band shows the fluctuation of the full set of realizations.

The fluctuation of the full set of realizations (depicted as a light blue band in Fig. 6.6) spans over several orders of magnitude, due to few very unlikely realizations that can depart much from the mean value. We further show in Fig. 6.6 the average and the 68%, 95% and 99% uncertainty bands as resulting from our MonteCarlo, computed by fitting for each ℓ the distribution of the C_ℓ with a log-normal function. We show in Fig. 6.7 the C_ℓ distribution for $\ell = 100$, together with its best fit function. The low value of the χ^2 that we find in all our fits, makes us confident that our distributions have statistically converged, at least to percent precision. While for high multipoles the uncertainty on the total APS is reduced to a few %, for $l \lesssim 100$ it can exceed one order of magnitude. Most massive subhalos, with masses $\gtrsim 10^8\,\mathrm{M}_\odot$, show the largest statistical fluctuations, due to their exiguous number.

In the present analysis we have not included any contribution from DM in extragalactic structures (see Appendix 6.A.1). In fact, as discussed in [649], the contribution from ex-

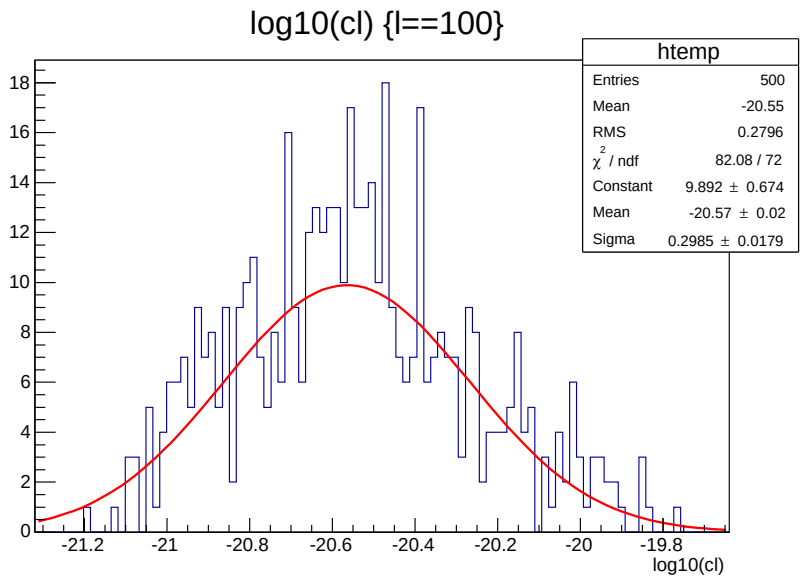

Figure 6.7: C_ℓ distribution for $\ell = 100$ fitted with a log-normal function.

tragalactic DM halos and subhalos that are not resolved by N-body simulations leads to a at least 2-order of magnitude uncertainty on the predicted level of the extragalactic energy spectrum, which may result as the dominant or the subdominant component of the total energy spectrum. Similarly, depending on how extragalactic (sub)structures are modelled, they can give a significant or a negligible contribution to the intensity APS.

4 Conclusions

We constructed the all-sky γ-ray maps from DM annihilation in the halo and subhalos of our galaxy. We modeled the DM distribution according to current N-body numerical simulations: galaxy g15784 part of the Making Galaxies in a Cosmological Context (MaGICC) programme and the analitical fits of the Aquarius simulation provided by [651]. We have not included any contribution from DM in extragalactic structures because they are affected by too many uncertainties.
We have then calculated the APS of the γ-ray flux from DM annihilation in the halo of our Galaxy. Indeed, the analysis of the uncertainties related to the anisotropies of the DM-induced emission done in sec. 3.1, was the main aim of this work. We computed the APS using the Healpix software, up to $\ell = 512$.

Since the computation of the APS to increasing larger multipoles requires exploring the DM distribution at small scales, possibly much smaller than the resolution of current numerical experiments, we first explored the APS computed for the smooth halo of the simulated galaxy g15784 fitted with an Einasto profile, in three different cases, where we set to zero the DM density profile in the central regions of the halo. We found that the extrapolation of the DM density profile clearly affects the APS at multipoles $l \gtrsim 10$.

We then compared the APS for both the smooth halo and subhalos of the same simulated galaxy, obtained by using three different fitting formulae: NFW, Einasto and MS profile. We showed in Fig. 6.5 the results. The different behavior of the main halo profiles at small scales affects the APS up to seven orders of magnitude at large multipoles ($l \sim 500$). Such a dependence of the angular power spectrum on the behavior of the DM profile at small scales could yield a significant hint about the shape of the DM density distribution in the central regions of the main halo of the galaxy, a region which can not be probed by current numerical simulations.

Finally, we evaluated the uncertainty due to the presence of substructures by performing several realizations of their distributions according to the analytical fits shown in section 2.2. We performed 500 realizations in the mass band $10^5 < \mathrm{M}/\,\mathrm{M}_\odot < 10^{10}$. In order to establish whether this amount of realizations was sufficient, we showed in Fig. 6.7 the distribution of values of the APS for the specific multipole $l = 100$ and we fitted it with a log-normal function, thus confirming the convergence of our procedure. We showed then in Fig. 6.6 the mean value of the APS as well as the 68%, 95% and 99% uncertainty bands calculated from our MonteCarlo realizations. While for high multipoles the uncertainty on the total APS shrinks to approximately few %, for $l \lesssim 100$ it can exceed one order of magnitude.

The analysis of the impact of these uncertainties on the computation of the APS plays an important role in understanding how much the assumptions that are usually made in the literature can affect the prediction of anisotropies in the γ-ray sky due to DM annihilation in the halo of our galaxy.

A comparison with the Fermi-LAT data or with the future data from CTA [425] is a prospect of update of the present work. A rigorous comparison requires a detailed study of the astrophysical sources though, and the application of a mask to the central regions of the galaxy. In the anisotropy analysis of the Fermi-LAT data indeed, the low galactic latitude region of $b < 30$ deg is masked in order to get rid of the galactic disk background.

Finally, the simulations considered in this work as well as in the related literature up to now are pure dissipationless DM simulations, run in a CDM setup. However, it is widely believed that the presence of baryons should affect the structure formation process. Indeed, cooling baryons play a role in the evolution of subhalos, by increasing the density of the central halo region in two ways: because of the extra mass associated with the inflow and because of the adiabatic contraction of the total mass distribution. This is valid for both the main halo and its subhalos, therefore it should be expected that subhalos formed within hydrodynamical simulations will experience a different tidal force. Omission of baryonic physics biases the DM-only simulations by overpredicting dwarf central densities. This effect, in turn, may overestimate the APS of the galactic gamma-ray emission. We are currently computing the APS for some galaxies simulated in a hydrodynamical setting.

In conclusion, the study of the energy spectrum and of the anisotropies are complementary methods to investigate the IGRB nature and consequently to test an eventual contribution

from DM. This two lines of investigation, along with a better characterization and removal of the galactic foreground, should be pursued.

6.A Appendix

6.A.1 Comments about the extra-galactic contribution

The extragalactic component of the APS is expected to be almost isotropic. Indeed, γ-rays emitted by DM annihilations in extragalactic halos and subhalos are in principle capable to reach us in the form of an isotropic contribution to the total γ-ray intensity and should therefore be included in the analysis of anisotropies. The main difference with respect to the galactic case is that on cosmologically large distances γ-rays can be absorbed by the interstellar medium while travelling to us. Common processes relevant to the absorption of energetic photons (MeVs - TeVs) in cosmological length scales are pair production on either baryonic matter or photon background (mainly composed by the CMB, the intergalactic stellar light and secondary IR radiation) and photon-photon scattering.

We shortly discuss the extragalactic contribution to the γ-ray flux. See Refs. [656,657] for a formal whole description.

We assume a standard homogeneous and isotropic cosmology, described by the metric:

$$ds^2 = c^2dt^2 - R^2(t)\left[dr^2 + S_k^2(r)d\Omega^2\right] \ , \tag{25}$$

where $d\Omega^2 = d\theta^2 + \sin^2\theta d\phi^2$ is the angular acceptance of a given detector. Moreover, we assume a flat geometry for the Universe, i.e. $k = 0$. The function $S_k(r)$ depends on the value of k, namely on the overall curvature of the Universe:

$$S_k(r) = \begin{cases} r, & \text{k=0;} \\ \arcsin r, & \text{k=+1;} \\ \text{arsinh}r, & \text{k=-1.} \end{cases} \tag{26}$$

At redshift z, $d\Omega$ and the radial increment dr determine the proper volume:

$$dV = \frac{[R_0 S_k(r)]^2 \, R_0}{(1+z)^3} dr d\Omega \ . \tag{27}$$

The number of photons emitted in this volume in the time interval dt and energy range (E, $E + dE$ is obtained by summing over all the sources in that volume. The corresponding number of photons dN_γ collected by a detector on earth with effective area dA during the time dt_0 and in the (redshifted) energy range (E_0, $E_0 + dE_0$), is equal to:

$$dN_\gamma = e^{-\tau(z,E_0)} \left[(1+z)^3 \int dM \, \frac{dn}{dM}(M,z) \, \frac{d\mathcal{N}_\gamma}{dE}(E,M,z)\right] \, \frac{dV \, dA}{4\pi[R_0 S_k(r)]^2} \, dE_0 \, dt_0 \ , \tag{28}$$

where dn/dM is the halo mass function, i.e. the comoving number density of bound objects that have mass M at redshift z.

The estimate of the diffuse extragalactic γ-ray flux due to the annihilation of DM particles that we observe at z = 0, is then obtained by summing over all contributions in the form in Eq. (28):

$$\begin{aligned} \frac{d\phi_{EG,\gamma}}{dE_0} &\equiv \frac{dN_\gamma}{dA\, d\Omega\, dt_0\, dE_0} \\ &= \frac{c}{4\pi} \int dz \frac{e^{-\tau_{EBL}(z,E_0)}}{H_0\, h(z)} \int dM\ \frac{dn}{dM}(M,z)\, \frac{d\mathcal{N}_\gamma}{dE}\left(E_0\,(1+z), M, z\right)\ . \end{aligned} \tag{29}$$

where the integration along the line of sight has been replaced by one over redshift, H_0 is the Hubble parameter, c is the speed of light and h depends on the cosmological model,

$$h(z) = \sqrt{\Omega_M (1+z)^3 + \Omega_\Lambda}. \tag{30}$$

$\frac{d\mathcal{N}_\gamma}{dE}$ is the differential energy spectrum for the number of γ-rays emitted, per unit of time, in a generic halo of mass M located at redshift z. The exponential factor refers to the photon absorption from pair production due to the interactions of the photons with the extragalactic background light (EBL) along the l.o.s. through the the optical depth τ_{EBL}.

The role of substructures can be encoded in the cosmological boost factor B(z), defined as $\mathrm{B(z)} = 1 + \langle\delta(\mathrm{z})^2\rangle$, where $\delta = \rho/\bar{\rho} - 1$ is the overdensity. To evaluate the boost factor, it is necessary to make some assumptions about the DM halos distribution, for example it is possible to assume that the matter distribution in the Universe is a superposition of DM halos. Depending on the values of the parameters entering the modelling of the halos distribution, the boost factor can change up to three orders of magnitude, especially at low redshift. Overall, its typical values range between 1 (at large redshift) and 10^6 (at redshift z=0).

CONCLUSIONS AND OUTLOOK

This thesis has been constructed along two lines of research: the phenomenology of SUSY GUT models, and the search for DM in the γ-ray sky. Besides the unavoidable study of the literature concerning the topics presented in the previous Chapters, the work has been carried out both with analytical and numerical tools, such as SARAH, SPheno, Toolbox, CalcHep, Micromegas, ROOT and Healpix. In this chapter we will summarize the main results achieved.

In the first part of the thesis we discussed the phenomenology of four basic SUSY SO(10) GUT models. We studied the leading-log RGE evolution of the MSSM soft SUSY breaking parameters for four different GUT models with mSugra boundary conditions. Although all the settings were based on the unified $SO(10)$ gauge group, they differ at the level of intermediate scale symmetry groups and/or particle content below the GUT scale. The extra gauge groups and/or beyond MSSM fields change the evolution of the soft parameters with respect to the basic mSugra expectation. The invariant mass combinations we considered are especially suited to uncover the effects of beyond-mSugra physics on the SUSY spectra. Remarkably, while invariants contain only a logarithmic dependence on the new physics scales, their behavior is *qualitatively* different in different models. Therefore, we argued that the RGE invariants may be good model discriminators.

We then studied low scale seesaw models with a sneutrino LSP. We considered two possibilities: models with the MSSM gauge group and either a linear or inverse seesaw and a model with the gauge group $SU(3)_c \times SU(2)_L \times U(1)_{B-L} \times U(1)_R$ and an inverse seesaw. Sneutrinos can be the DM in both cases, fulfilling all known experimental bounds. While inverse and linear seesaw lead to different results for LFV, in general, they give similar DM phenomenology.

Then we investigated the properties of DM in a generic context, keeping only the assumption that DM is in the form of WIMPs. In particular, we studied the prospects for DM indirect searches with γ-rays, notably exploiting the latest results of the Fermi-LAT satellite.
We considered the measurements of the isotropic γ-ray background made by the Fermi-LAT satellite and we explored possible non-negligible diffuse contributions from standard astrophysical sources. Assuming that all the residual IGRB is due to DM annihilation in the

halo of our galaxy, we set conservative upper limits on the DM annihilation cross section. Moreover, the bounds on $\langle \sigma v \rangle$ have been interpreted in terms of Sommerfeld enhancement of the annihilation cross section, inferring a lower limit on the mass of the force mediator, depending on the coupling and the velocity of DM particles.

Further information about the origin of the IGRB can be inferred by analizing the fluctuations on small angular scales. We have discussed two kinds of uncertainties related to the study of the APS from galactic DM annihilation: first, computing the power spectrum at $l \gtrsim 100$ requires to extrapolate the DM profile to scales below the resolution of current numerical simulations. Second, different spatial distributions of substructures can lead to different APS.
For this purpose, we have considered N-body simulations of MW-sized DM galactic halos. We found that the extrapolation of the DM density profile clearly affects the APS at multipoles $l \gtrsim 10$. Finally, we evaluated the uncertainty due to the presence of substructures by performing 500 realizations of their distributions. While for high multipoles the uncertainty on the total APS shrinks to approximately few %, for $l \lesssim 100$ it can exceed one order of magnitude.

In conclusion, in this doctoral thesis we have dealt with different aspects of the phenomenology of new physics beyond the SM. Notably we focused on two still unresolved problems of the SM, neutrino oscillations and DM. With this aim in mind we have exploited the interplay between the study of new theoretical models and the analysis of recent experimental results. In particular, we have seen that SUSY SO(10) GUT models show an interesting phenomenology which can be studied with the higher center-of-mass energy run at LHC or with a future linear collider. Moreover, we showed that SUSY models capable of accomodating neutrino masses through low-energy scale seesaws can also provide a good DM candidate, the sneutrino. Finally, we investigated indirect detection of DM as an additional method to test its nature. The good sensitivity of the Fermi-LAT telescope offers a unique tool to identify DM signals in the γ-ray sky.

The steady progress of experimental techniques, both regarding accelerators and direct/indirect DM searches will allow to shed further light on the scenarios that we have studied in this thesis, and hopefully to finally get to a correct description of how neutrino masses are generated as well as to identify the particle physics nature of DM.

ACKNOWLEDGEMENTS

First of all I acknowledge financial support from the EU Network grant UNILHC PITN-GA-2009-237920.

This thesis is somehow a summary of the work I've been carrying on in these three years of PhD in Valencia. My efforts behind the writing of this thesis have always been supported by many people, which I would like to acknowledge here in these few lines.

First and foremost, my warmest thanks go to my supervisor Martin Hirsch. He indeed gave me the opportunity of learning many interesting physics concepts and of working on intellectually stimulating research topics. I'm really thankful to him, as an adviser, because he has always dispensed thoughtful advices that have been always helpful to me. I also consider Martin a great scientist, who has never failed to impress; his physics knowledge is really wide and versatile, as he always demonstrated whenever I asked him a question or an explanation. Next, I would like to thank my second supervisor, Fiorenza Donato. I'm grateful to her too for introducing me to another very stimulating physics topic. Although being far, she always assisted me and gave me many useful suggestions. I'm also very grateful to her for her kindness and support during my stay in Torino. Last but definitely not least, Jose Valle. Besides being an outstanding physicist, I must say that he is really a nice person and a great group leader. He always takes much care of his students and postdocs and really works hard in order to keep the group very active. I'm very thankful to him for having given me the chance of being part of the AHEP group.

I then would like to thank those that I collaborated with to produce some of the work summarized in this manuscript. Michal Malinsky, who I repute a real expert of GUT theories. During our collaboration, he taught me many concepts about group theory and grand unification, therefore I must thank him warmly. Francesca Calore, who I repute a friend more than a collaborator, and who shared with me joys and pains of the work. She has always been a reference point for my PhD, since our academic paths have proceeded jointly. Luca Maccione, whom I want to thank for being so kind and helpful during my visit in Munich, and for many useful physics discussions that we have had. Finally, Mattia di Mauro, who also shared with me and Francesca many joys and pains related to our work, under the common fate of being PhD students.

Next thanks go to the referees of my thesis: Asmaa Abada, David Cerdeño, Joakim Edsjö, Nicolao Fornengo, Nuria Rius and Pierre Salati. I'm definetely grateful to them for having read this manuscript so carefully and for their suggestions and corrections.

I would then like to express gratitude to the past and present AHEPians that I met across my way, and that make AHEP group such a nice place to work. Sergio and Mariam, who gave me many valuable tips, Stefano, Laslo, Avelino, Fabio, Lucho, Eduardo, Carolina, Laura, Alma, Quim, Pablo, Cesar...even if I don't mention all of them, I'm thankful to everybody. I'm also very glad to have started such a nice friendship with some of the AHEPians: Roberto, Sofiane, David, Urbano. Thanks for sharing with me many happy and bad instants, the house, the tea after lunch, your weddings, dinners, beaches, swimming pools, dances and most of all lots of life stories.

I have been very fortunate to attend a number of conferences during the PhD years. I would like to thank the friends I have made during my travels for sharing with me those experiences and for having shown me how nice it is to be part of the physics community. Thanks Roberta, Ivano, Jacques, Ninetta, Francesco, Maria, Antonio, Nina, Valentina...

IFIC is a very stimulating institute where to work. I had met many people with whom I had interesting discussions, and shared nice circumstances: Lotfi, Vicen, Ebhe, Melahat, David, Mauricio, Adry, Elena, Francesca, Eleonora, Mike, Nancy, Nayeli, Maria, Alejandro, Mariana, Cris, Victoria, Leslie...without listing all the names, I just thank you all because you all are little pieces of the huge mosaic of friends that I met in Valencia, which anyway extends outside IFIC too.

However there are few friends that I want to thank personally. I'm endlessly grateful to them for filling the time between the support they constantly gave me and many incredible instants we spent together, with entertaining conversations. Gracias Diana, Ana, Mer y Nuria por vuestro apoyo y constante comprensión. Gracias por las paradas en el pasillo para contarnos pequeñas historias de vida, por los innumerables buenos momentos que he vivido con vosotras, las increíbles vacaciones en Mallorca, Oporto y Salamanca, las excursiones, los días de playa, las carreras en el Turia, las cenas de chicas, las rancheras cantadas, los bailes disfrutados, las muchísimas noches de alegría que tuvimos juntas y mucho más. Gracias por ser mis amigas, soy muy feliz de haberos conocido y de teneros. Os quiero mucho.
A very important thank must go to those friends, who unfortunately live far, but are always present. They support me like if we were living always in the same city. Grazie a Sara, Isa, Ilaria, Donutilla, Lauretta, Maria Chiara, Elibetta, Ale, Marco, Giusè, tutti gli altri amici di Torino così come Alessandra e le ballerine che sempre mi fanno sentire "a casa" ogni volta che torno a trovarli.
Nel contesto delle persone purtroppo lontante, un grazie molto più che speciale va a Marco. Per tanti motivi, ma soprattutto perchè le capre di solito i fogli della tesi se li mangiano, non li scrivono. È stato un duro lavoro convincerle del contrario.

The writing of this thesis would probably not have been the same, without an important aspect of my life in Valencia: circus. The friends that I met in the classes of aerial silks that I have been attending for the last two years play a very important role, because of the (indirect) support they have been giving me all the time. Gracias Estela por haberme enseñado a volar con las telas, por tús clases tan divertidas, y por la bonita experiencia del

Cabaret. ¡Me la pasè geníal, siempre! Gracias a Jana, Irene, Gabi, Jose Luis, por compartir conmigo quedadas teleras en el Turía, que he disfrutado un montón, así como muchos otros instantes felices, a Juan por preguntarme tantas veces sobre los agujeros negros que no hay en mi tesís, y a todos los otros amigos y compañeros del Espai que me hacen sentir como en una familia.

Ok, at this point, I am running out of words to thanks those people who are maybe the most important of all: my family. Actually no many words are necessary to express the gratitude I feel to them, who have always loved and supported me unconditionally. My parents, my grandma and my uncles. Without their psychological, economical and love support for sure I would not be where I am now. Grazie!

BIBLIOGRAPHY

[1] Valentina De Romeri, Martin Hirsch, and Michal Malinsky. Soft masses in SUSY SO(10) GUTs with low intermediate scales. *Phys.Rev.*, D84:053012, 2011, 1107.3412.

[2] Valentina De Romeri and Martin Hirsch. Sneutrino Dark Matter in Low-scale Seesaw Scenarios. *JHEP*, 1212:106, 2012, 1209.3891.

[3] Francesca Calore, Valentina De Romeri, and Fiorenza Donato. Conservative upper limits on WIMP annihilation cross section from Fermi-LAT γ-rays. *Phys.Rev.*, D85:023004, 2012, 1105.4230.

[4] S.L. Glashow. Partial Symmetries of Weak Interactions. *Nucl.Phys.*, 22:579–588, 1961.

[5] Abdus Salam and John Clive Ward. Electromagnetic and weak interactions. *Phys.Lett.*, 13:168–171, 1964.

[6] Steven Weinberg. A Model of Leptons. *Phys.Rev.Lett.*, 19:1264–1266, 1967.

[7] Steven Weinberg. The Making of the standard model. *Eur.Phys.J.*, C34:5–13, 2004, hep-ph/0401010.

[8] R. Davis. A review of the Homestake solar neutrino experiment. *Prog.Part.Nucl.Phys.*, 32:13–32, 1994.

[9] B.T. Cleveland, Timothy Daily, Jr. Davis, Raymond, et al. Measurement of the solar electron neutrino flux with the Homestake chlorine detector. *Astrophys.J.*, 496:505–526, 1998.

[10] K. Lande, B.T. Cleveland, R. Davis, et al. The Homestake solar neutrino program. *Nucl.Phys.Proc.Suppl.*, 77:13–19, 1999.

[11] Y. Fukuda et al. Solar neutrino data covering solar cycle 22. *Phys.Rev.Lett.*, 77:1683–1686, 1996.

[12] S. Fukuda et al. Solar B-8 and hep neutrino measurements from 1258 days of Super-Kamiokande data. *Phys.Rev.Lett.*, 86:5651–5655, 2001, hep-ex/0103032.

[13] S. Fukuda et al. Determination of solar neutrino oscillation parameters using 1496 days of Super-Kamiokande I data. *Phys.Lett.*, B539:179–187, 2002, hep-ex/0205075.

[14] M.B. Smy. A Unique oscillation solution to the solar neutrino problem? pages 40–49, 2002, hep-ex/0202020.

[15] Alan W.P. Poon. Review of solar and reactor neutrinos. *Int.J.Mod.Phys.*, A21:1855–1868, 2006, hep-ex/0509024.

[16] J.N. Abdurashitov et al. Measurement of the solar neutrino capture rate with gallium metal. *Phys.Rev.*, C60:055801, 1999, astro-ph/9907113.

[17] J.N. Abdurashitov et al. Solar neutrino flux measurements by the Soviet-American Gallium Experiment (SAGE) for half the 22 year solar cycle. *J.Exp.Theor.Phys.*, 95:181–193, 2002, astro-ph/0204245.

[18] W. Hampel et al. GALLEX solar neutrino observations: Results for GALLEX IV. *Phys.Lett.*, B447:127–133, 1999.

[19] M. Altmann et al. GNO solar neutrino observations: Results for GNO I. *Phys.Lett.*, B490:16–26, 2000, hep-ex/0006034.

[20] C.M. Cattadori. Update of solar neutrino interaction rate measurements from GNO at LNGS. *Nucl.Phys.Proc.Suppl.*, 110:311–314, 2002.

[21] Q.R. Ahmad et al. Direct evidence for neutrino flavor transformation from neutral current interactions in the Sudbury Neutrino Observatory. *Phys.Rev.Lett.*, 89:011301, 2002, nucl-ex/0204008.

[22] Q.R. Ahmad et al. Measurement of day and night neutrino energy spectra at SNO and constraints on neutrino mixing parameters. *Phys.Rev.Lett.*, 89:011302, 2002, nucl-ex/0204009.

[23] S.N. Ahmed et al. Measurement of the total active B-8 solar neutrino flux at the Sudbury Neutrino Observatory with enhanced neutral current sensitivity. *Phys.Rev.Lett.*, 92:181301, 2004, nucl-ex/0309004.

[24] B. Aharmim et al. Electron energy spectra, fluxes, and day-night asymmetries of B-8 solar neutrinos from measurements with NaCl dissolved in the heavy-water detector at the Sudbury Neutrino Observatory. *Phys.Rev.*, C72:055502, 2005, nucl-ex/0502021.

[25] John N. Bahcall, M.H. Pinsonneault, and Sarbani Basu. Solar models: Current epoch and time dependences, neutrinos, and helioseismological properties. *Astrophys.J.*, 555:990–1012, 2001, astro-ph/0010346.

[26] John N. Bahcall and Roger K. Ulrich. Solar Models, Neutrino Experiments and Helioseismology. *Rev.Mod.Phys.*, 60:297–372, 1988.

[27] John N. Bahcall and M.H. Pinsonneault. Standard solar models, with and without helium diffusion and the solar neutrino problem. *Rev.Mod.Phys.*, 64:885–926, 1992.

[28] John N. Bahcall, Aldo M. Serenelli, and Sarbani Basu. New solar opacities, abundances, helioseismology, and neutrino fluxes. *Astrophys.J.*, 621:L85–L88, 2005, astro-ph/0412440.

[29] John N. Bahcall, Sarbani Basu, Marc Pinsonneault, and Aldo M. Serenelli. Helioseismological implications of recent solar abundance determinations. *Astrophys.J.*, 618:1049–1056, 2005, astro-ph/0407060.

[30] G. Battistoni, E. Bellotti, C. Bloise, et al. THE NUSEX DETECTOR. *Nucl.Instrum.Meth.*, A245:277, 1986.

[31] M. Aglietta et al. Experimental study of atmospheric neutrino flux in the NUSEX experiment. *Europhys.Lett.*, 8:611–614, 1989.

[32] Mayly C. Sanchez et al. Measurement of the L/E distributions of atmospheric neutrinos in Soudan 2 and their interpretation as neutrino oscillations. *Phys.Rev.*, D68:113004, 2003, hep-ex/0307069.

[33] Christoph Berger et al. A Study of atmospheric neutrino oscillations in the FREJUS experiment. *Phys.Lett.*, B245:305–310, 1990.

[34] K. Daum et al. Determination of the atmospheric neutrino spectra with the Frejus detector. *Z.Phys.*, C66:417–428, 1995.

[35] R. Becker-Szendy, C.B. Bratton, D. Casper, et al. The Electron-neutrino and muon-neutrino content of the atmospheric flux. *Phys.Rev.*, D46:3720–3724, 1992.

[36] R. Becker-Szendy, C.B. Bratton, D. Casper, et al. Neutrino measurements with the IMB detector. *Nucl.Phys.Proc.Suppl.*, 38:331–336, 1995.

[37] M. Ambrosio et al. Measurement of the atmospheric neutrino induced upgoing muon flux using MACRO. *Phys.Lett.*, B434:451–457, 1998, hep-ex/9807005.

[38] K.S. Hirata et al. Observation of a small atmospheric muon-neutrino / electron-neutrino ratio in Kamiokande. *Phys.Lett.*, B280:146–152, 1992.

[39] Y. Fukuda et al. Atmospheric muon-neutrino / electron-neutrino ratio in the multiGeV energy range. *Phys.Lett.*, B335:237–245, 1994.

[40] Y. Fukuda et al. Measurement of a small atmospheric muon-neutrino / electron-neutrino ratio. *Phys.Lett.*, B433:9–18, 1998, hep-ex/9803006.

[41] Y. Fukuda et al. Study of the atmospheric neutrino flux in the multi-GeV energy range. *Phys.Lett.*, B436:33–41, 1998, hep-ex/9805006.

[42] Y. Ashie et al. Evidence for an oscillatory signature in atmospheric neutrino oscillation. *Phys.Rev.Lett.*, 93:101801, 2004, hep-ex/0404034.

[43] P. Adamson et al. Measurements of atmospheric neutrinos and antineutrinos in the MINOS Far Detector. *Phys.Rev.*, D86:052007, 2012, 1208.2915.

[44] G. Barr, T.K. Gaisser, and T. Stanev. FLUX OF ATMOSPHERIC NEUTRINOS. *Phys.Rev.*, D39:3532–3534, 1989.

[45] Vivek Agrawal, T.K. Gaisser, Paolo Lipari, and Todor Stanev. Atmospheric neutrino flux above 1-GeV. *Phys.Rev.*, D53:1314–1323, 1996, hep-ph/9509423.

[46] Morihiro Honda, T. Kajita, K. Kasahara, and S. Midorikawa. A New calculation of the atmospheric neutrino flux in a 3-dimensional scheme. *Phys.Rev.*, D70:043008, 2004, astro-ph/0404457.

[47] L.V. Volkova. Energy Spectra and Angular Distributions of Atmospheric Neutrinos. *Sov.J.Nucl.Phys.*, 31:784–790, 1980.

[48] M. Apollonio et al. Limits on neutrino oscillations from the CHOOZ experiment. *Phys.Lett.*, B466:415–430, 1999, hep-ex/9907037.

[49] K. Eguchi et al. First results from KamLAND: Evidence for reactor anti-neutrino disappearance. *Phys.Rev.Lett.*, 90:021802, 2003, hep-ex/0212021.

[50] T. Araki et al. Measurement of neutrino oscillation with KamLAND: Evidence of spectral distortion. *Phys.Rev.Lett.*, 94:081801, 2005, hep-ex/0406035.

[51] M.H. Ahn et al. Indications of neutrino oscillation in a 250 km long baseline experiment. *Phys.Rev.Lett.*, 90:041801, 2003, hep-ex/0212007.

[52] D.G. Michael et al. Observation of muon neutrino disappearance with the MINOS detectors and the NuMI neutrino beam. *Phys.Rev.Lett.*, 97:191801, 2006, hep-ex/0607088.

[53] P. Adamson et al. Measurement of Neutrino Oscillations with the MINOS Detectors in the NuMI Beam. *Phys.Rev.Lett.*, 101:131802, 2008, 0806.2237.

[54] P. Adamson et al. Improved search for muon-neutrino to electron-neutrino oscillations in MINOS. *Phys.Rev.Lett.*, 107:181802, 2011, 1108.0015.

[55] K. Abe et al. Indication of Electron Neutrino Appearance from an Accelerator-produced Off-axis Muon Neutrino Beam. *Phys.Rev.Lett.*, 107:041801, 2011, 1106.2822.

[56] M.H. Ahn et al. Measurement of Neutrino Oscillation by the K2K Experiment. *Phys.Rev.*, D74:072003, 2006, hep-ex/0606032.

[57] F.P. An et al. Observation of electron-antineutrino disappearance at Daya Bay. *Phys.Rev.Lett.*, 108:171803, 2012, 1203.1669.

[58] J.K. Ahn et al. Observation of Reactor Electron Antineutrino Disappearance in the RENO Experiment. *Phys.Rev.Lett.*, 108:191802, 2012, 1204.0626.

[59] A. Aguilar-Arevalo et al. Evidence for neutrino oscillations from the observation of anti-neutrino(electron) appearance in a anti-neutrino(muon) beam. *Phys.Rev.*, D64:112007, 2001, hep-ex/0104049.

[60] A.A. Aguilar-Arevalo et al. A Search for electron neutrino appearance at the $\Delta m^2 \sim 1\text{eV}^2$ scale. *Phys.Rev.Lett.*, 98:231801, 2007, 0704.1500.

[61] B. Pontecorvo. Mesonium and anti-mesonium. *Sov.Phys.JETP*, 6:429, 1957.

[62] B. Pontecorvo. Inverse beta processes and nonconservation of lepton charge. *Sov.Phys.JETP*, 7:172–173, 1958.

[63] B. Pontecorvo. Neutrino Experiments and the Problem of Conservation of Leptonic Charge. *Sov.Phys.JETP*, 26:984–988, 1968.

[64] F. Boehm and P. Vogel. Physics of massive neutrinos. 1992.

[65] C.W. Kim and A. Pevsner. Neutrinos in physics and astrophysics. *Contemp.Concepts Phys.*, 8:1–429, 1993.

[66] Samoil M. Bilenky, C. Giunti, and W. Grimus. Phenomenology of neutrino oscillations. *Prog.Part.Nucl.Phys.*, 43:1–86, 1999, hep-ph/9812360.

[67] Carlo Giunti. Neutrino Flavor States and Oscillations. *J.Phys.*, G34:R93–R109, 2007, hep-ph/0608070.

[68] Alessandro Strumia and Francesco Vissani. Neutrino masses and mixings and... 2006, hep-ph/0606054.

[69] Evgeny Kh. Akhmedov and Alexei Yu. Smirnov. Paradoxes of neutrino oscillations. *Phys.Atom.Nucl.*, 72:1363–1381, 2009, 0905.1903.

[70] Samoil Bilenky. Introduction to the physics of massive and mixed neutrinos. *Lect.Notes Phys.*, 817:1–255, 2010.

[71] Ziro Maki, Masami Nakagawa, and Shoichi Sakata. Remarks on the unified model of elementary particles. *Prog.Theor.Phys.*, 28:870–880, 1962.

[72] J. Schechter and J.W.F. Valle. Neutrino Masses in SU(2) x U(1) Theories. *Phys.Rev.*, D22:2227, 1980.

[73] J. Beringer et al. Review of Particle Physics (RPP). *Phys.Rev.*, D86:010001, 2012.

[74] L. Wolfenstein. Neutrino Oscillations in Matter. *Phys.Rev.*, D17:2369–2374, 1978.

[75] S.P. Mikheev and A. Yu. Smirnov. Resonance Amplification of Oscillations in Matter and Spectroscopy of Solar Neutrinos. *Sov.J.Nucl.Phys.*, 42:913–917, 1985.

[76] M.C. Gonzalez-Garcia, P.C. de Holanda, Carlos Pena-Garay, and J.W.F. Valle. Status of the MSW solutions of the solar neutrino problem. *Nucl.Phys.*, B573:3–26, 2000, hep-ph/9906469.

[77] D.V. Forero, M. Tortola, and J.W.F. Valle. Global status of neutrino oscillation parameters after Neutrino-2012. *Phys.Rev.*, D86:073012, 2012, 1205.4018.

[78] Y. Abe et al. Indication for the disappearance of reactor electron antineutrinos in the Double Chooz experiment. *Phys.Rev.Lett.*, 108:131801, 2012, 1112.6353.

[79] P.A.R. Ade et al. Planck 2013 results. XVI. Cosmological parameters. 2013, 1303.5076.

[80] M. Costanzi Alunno Cerbolini, B. Sartoris, Jun-Qing Xia, et al. Constraining neutrino properties with a Euclid-like galaxy cluster survey. 2013, 1303.4550.

[81] A. Gando et al. Measurement of the double-β decay half-life of ^{136}Xe with the KamLAND-Zen experiment. *Phys.Rev.*, C85:045504, 2012, 1201.4664.

[82] M. Auger et al. Search for Neutrinoless Double-Beta Decay in ^{136}Xe with EXO-200. *Phys.Rev.Lett.*, 109:032505, 2012, 1205.5608.

[83] A. Gando et al. Limit on Neutrinoless $\beta\beta$ Decay of Xe-136 from the First Phase of KamLAND-Zen and Comparison with the Positive Claim in Ge-76. *Phys.Rev.Lett.*, 110(6):062502, 2013, 1211.3863.

[84] Stefan. Schonert et al. The GERmanium Detector Array (GERDA) for the search of neutrinoless beta beta decays of Ge-76 at LNGS. *Nucl.Phys.Proc.Suppl.*, 145:242–245, 2005.

[85] M. Agostini et al. Results on neutrinoless double beta decay of 76Ge from GERDA Phase I. 2013, 1307.4720.

[86] A. Osipowicz et al. KATRIN: A Next generation tritium beta decay experiment with sub-eV sensitivity for the electron neutrino mass. Letter of intent. 2001, hep-ex/0109033.

[87] Gianfranco Bertone, Dan Hooper, and Joseph Silk. Particle dark matter: Evidence, candidates and constraints. *Phys.Rept.*, 405:279–390, 2005, hep-ph/0404175.

[88] P.A.R. Ade et al. Planck 2013 results. I. Overview of products and scientific results. 2013, 1303.5062.

[89] Douglas Clowe, Marusa Bradac, Anthony H. Gonzalez, et al. A direct empirical proof of the existence of dark matter. *Astrophys.J.*, 648:L109–L113, 2006, astro-ph/0608407.

[90] David M. Wittman, J. Anthony Tyson, David Kirkman, Ian Dell'Antonio, and Gary Bernstein. Detection of weak gravitational lensing distortions of distant galaxies by cosmic dark matter at large scales. *Nature*, 405:143–149, 2000, astro-ph/0003014.

[91] J. Anthony Tyson, Greg P. Kochanski, and Ian P. Dell'Antonio. Detailed mass map of CL0024+1654 from strong lensing. *Astrophys.J.*, 498:L107, 1998, astro-ph/9801193.

[92] Aaron D. Lewis, David A. Buote, and John T. Stocke. Chandra observations of Abell 2029: The Dark matter profile at <0.01 R(VIR) in an unusually relaxed cluster. *Astrophys.J.*, 586:135–142, 2003, astro-ph/0209205.

[93] Alexey Vikhlinin, A. Kravtsov, W. Forman, et al. Chandra sample of nearby relaxed galaxy clusters: Mass, gas fraction, and mass-temperature relation. *Astrophys.J.*, 640:691–709, 2006, astro-ph/0507092.

[94] Steven W. Allen, August E. Evrard, and Adam B. Mantz. Cosmological Parameters from Observations of Galaxy Clusters. *Ann.Rev.Astron.Astrophys.*, 49:409–470, 2011, 1103.4829.

[95] Karsten Jedamzik and Maxim Pospelov. Big Bang Nucleosynthesis and Particle Dark Matter. *New J.Phys.*, 11:105028, 2009, 0906.2087.

[96] S. Gillessen, F. Eisenhauer, S. Trippe, et al. Monitoring stellar orbits around the Massive Black Hole in the Galactic Center. *Astrophys.J.*, 692:1075–1109, 2009, 0810.4674.

[97] P. Salucci, F. Nesti, G. Gentile, and C.F. Martins. The dark matter density at the Sun's location. *Astron.Astrophys.*, 523:A83, 2010, 1003.3101.

[98] Paul J. McMillan. Mass models of the Milky Way. *Mon.Not.Roy.Astron.Soc.*, 414:2446–2457, 2011, 1102.4340.

[99] Jo Bovy and Scott Tremaine. On the local dark matter density. *Astrophys.J.*, 756:89, 2012, 1205.4033.

[100] Silvia Garbari, Chao Liu, Justin I. Read, and George Lake. A new determination of the local dark matter density from the kinematics of K dwarfs. *Mon.Not.Roy.Astron.Soc.*, 425:1445, 2012, 1206.0015.

[101] Miguel Pato, Oscar Agertz, Gianfranco Bertone, Ben Moore, and Romain Teyssier. Systematic uncertainties in the determination of the local dark matter density. *Phys.Rev.*, D82:023531, 2010, 1006.1322.

[102] Riccardo Catena and Piero Ullio. A novel determination of the local dark matter density. *JCAP*, 1008:004, 2010, 0907.0018.

[103] F. Zwicky. Spectral displacement of extra galactic nebulae. *Helv.Phys.Acta*, 6:110–127, 1933.

[104] Max Tegmark et al. Cosmological parameters from SDSS and WMAP. *Phys.Rev.*, D69:103501, 2004, astro-ph/0310723.

[105] Jeremy L. Tinker, Erin S. Sheldon, Risa H. Wechsler, et al. Cosmological Constraints from Galaxy Clustering and the Mass-to-Number Ratio of Galaxy Clusters. *Astrophys.J.*, 745:16, 2012, 1104.1635.

[106] The Scientific programme of planck. 2006, astro-ph/0604069.

[107] E. Komatsu et al. Seven-Year Wilkinson Microwave Anisotropy Probe (WMAP) Observations: Cosmological Interpretation. *Astrophys.J.Suppl.*, 192:18, 2011, 1001.4538.

[108] J. Dunkley, R. Hlozek, J. Sievers, et al. The Atacama Cosmology Telescope: Cosmological Parameters from the 2008 Power Spectra. *Astrophys.J.*, 739:52, 2011, 1009.0866.

[109] J.E. Carlstrom, P.A.R. Ade, K.A. Aird, et al. The 10 Meter South Pole Telescope. *Publ.Astron.Soc.Pac.*, 123:568–581, 2011, 0907.4445.

[110] D.J. Fixsen, E.S. Cheng, J.M. Gales, et al. The Cosmic Microwave Background spectrum from the full COBE FIRAS data set. *Astrophys.J.*, 473:576, 1996, astro-ph/9605054.

[111] Andrew H. Jaffe et al. Cosmology from MAXIMA-1, BOOMERANG and COBE / DMR CMB observations. *Phys.Rev.Lett.*, 86:3475–3479, 2001, astro-ph/0007333.

[112] G. Hinshaw et al. Nine-Year Wilkinson Microwave Anisotropy Probe (WMAP) Observations: Cosmological Parameter Results. 2012, 1212.5226.

[113] Shaun Cole et al. The 2dF Galaxy Redshift Survey: Power-spectrum analysis of the final dataset and cosmological implications. *Mon.Not.Roy.Astron.Soc.*, 362:505–534, 2005, astro-ph/0501174.

[114] Will J. Percival et al. Baryon Acoustic Oscillations in the Sloan Digital Sky Survey Data Release 7 Galaxy Sample. *Mon.Not.Roy.Astron.Soc.*, 401:2148–2168, 2010, 0907.1660.

[115] M. Kowalski et al. Improved Cosmological Constraints from New, Old and Combined Supernova Datasets. *Astrophys.J.*, 686:749–778, 2008, 0804.4142.

[116] G. Bertone. *Particle Dark Matter : Observations, Models and Searches.* Cambridge University Press, 2010.

[117] C. Alcock et al. The MACHO project: Microlensing results from 5.7 years of LMC observations. *Astrophys.J.*, 542:281–307, 2000, astro-ph/0001272.

[118] P. Tisserand et al. Limits on the Macho Content of the Galactic Halo from the EROS-2 Survey of the Magellanic Clouds. *Astron.Astrophys.*, 469:387–404, 2007, astro-ph/0607207.

[119] Rabindra N. Mohapatra and Vigdor L. Teplitz. Mirror matter MACHOs. *Phys.Lett.*, B462:302–309, 1999, astro-ph/9902085.

[120] T. Lasserre. Not enough stellar mass machos in the galactic halo. *Astron.Astrophys.*, 355:L39–L42, 2000, astro-ph/0002253.

[121] Jaiyul Yoo, Julio Chaname, and Andrew Gould. The end of the MACHO era: limits on halo dark matter from stellar halo wide binaries. *Astrophys.J.*, 601:311–318, 2004, astro-ph/0307437.

[122] L. Wyrzykowski, J. Skowron, S. Kozłowski, et al. The OGLE view of microlensing towards the Magellanic Clouds - IV. OGLE-III SMC data and final conclusions on MACHOs. *MNRAS*, 416:2949–2961, October 2011, 1106.2925.

[123] Kris Sigurdson, Michael Doran, Andriy Kurylov, Robert R. Caldwell, and Marc Kamionkowski. Dark-matter electric and magnetic dipole moments. *Phys.Rev.*, D70:083501, 2004, astro-ph/0406355.

[124] Samuel D. McDermott, Hai-Bo Yu, and Kathryn M. Zurek. Turning off the Lights: How Dark is Dark Matter? *Phys.Rev.*, D83:063509, 2011, 1011.2907.

[125] Vernon Barger, Wai-Yee Keung, and Danny Marfatia. Electromagnetic properties of dark matter: Dipole moments and charge form factor. *Phys.Lett.*, B696:74–78, 2011, 1007.4345.

[126] George R. Blumenthal, S.M. Faber, Joel R. Primack, and Martin J. Rees. Formation of Galaxies and Large Scale Structure with Cold Dark Matter. *Nature*, 311:517–525, 1984.

[127] Kevork Abazajian. Linear cosmological structure limits on warm dark matter. *Phys.Rev.*, D73:063513, 2006, astro-ph/0512631.

[128] Alexey Boyarsky, Julien Lesgourgues, Oleg Ruchayskiy, and Matteo Viel. Lyman-alpha constraints on warm and on warm-plus-cold dark matter models. *JCAP*, 0905:012, 2009, 0812.0010.

[129] Stephane Colombi, Scott Dodelson, and Lawrence M. Widrow. Large scale structure tests of warm dark matter. *Astrophys.J.*, 458:1, 1996, astro-ph/9505029.

[130] Scott Dodelson. Modern cosmology. 2003.

[131] Kevork Abazajian, Eric R. Switzer, Scott Dodelson, Katrin Heitmann, and Salman Habib. The Nonlinear cosmological matter power spectrum with massive neutrinos. 1. The Halo model. *Phys.Rev.*, D71:043507, 2005, astro-ph/0411552.

[132] Pedro Colin, Vladimir Avila-Reese, and Octavio Valenzuela. Substructure and halo density profiles in a warm dark matter cosmology. *Astrophys.J.*, 542:622–630, 2000, astro-ph/0004115.

[133] Matteo Viel, Katarina Markovic, Marco Baldi, and Jochen Weller. The Non-Linear Matter Power Spectrum in Warm Dark Matter Cosmologies. *Mon.Not.Roy.Astron.Soc.*, 421:50–62, 2012, 1107.4094.

[134] Robert E. Smith and Katarina Markovic. Testing the Warm Dark Matter paradigm with large-scale structures. *Phys.Rev.*, D84:063507, 2011, 1103.2134.

[135] M. Viel, G.D. Becker, J.S. Bolton, and M.G. Haehnelt. Warm Dark Matter as a solution to the small scale crisis: new constraints from high redshift Lyman-alpha forest data. 2013, 1306.2314.

[136] Frank C. van den Bosch and Rob A. Swaters. Dwarf galaxy rotation curves and the core problem of dark matter halos. *Mon.Not.Roy.Astron.Soc.*, 325:1017, 2001, astro-ph/0006048.

[137] W.J.G. de Blok. The Core-Cusp Problem. *Adv.Astron.*, 2010:789293, 2010, 0910.3538.

[138] Joshua D. Simon and Marla Geha. The Kinematics of the Ultra-Faint Milky Way Satellites: Solving the Missing Satellite Problem. *Astrophys.J.*, 670:313–331, 2007, 0706.0516.

[139] Louis E. Strigari, James S. Bullock, Manoj Kaplinghat, et al. Redefining the Missing Satellites Problem. *Astrophys.J.*, 669:676–683, 2007, 0704.1817.

[140] G. S. Stinson, C. Brook, A. V. Macciò, et al. Making Galaxies In a Cosmological Context: the need for early stellar feedback. *MNRAS*, 428:129–140, January 2013, 1208.0002.

[141] Laurent Canetti, Marco Drewes, and Mikhail Shaposhnikov. Sterile Neutrinos as the Origin of Dark and Baryonic Matter. *Phys.Rev.Lett.*, 110(6):061801, 2013, 1204.3902.

[142] Edward W. Kolb, Daniel J.H. Chung, and Antonio Riotto. WIMPzillas! pages 91–105, 1998, hep-ph/9810361.

[143] Gary Steigman and Michael S. Turner. Cosmological Constraints on the Properties of Weakly Interacting Massive Particles. *Nucl.Phys.*, B253:375, 1985.

[144] Gerard Jungman, Marc Kamionkowski, and Kim Griest. Supersymmetric dark matter. *Phys.Rept.*, 267:195–373, 1996, hep-ph/9506380.

[145] Edward W. Kolb and Michael S. Turner. The Early universe. *Front.Phys.*, 69:1–547, 1990.

[146] Geraldine Servant and Timothy M.P. Tait. Is the lightest Kaluza-Klein particle a viable dark matter candidate? *Nucl.Phys.*, B650:391–419, 2003, hep-ph/0206071.

[147] Hsin-Chia Cheng, Jonathan L. Feng, and Konstantin T. Matchev. Kaluza-Klein dark matter. *Phys.Rev.Lett.*, 89:211301, 2002, hep-ph/0207125.

[148] R. D. Peccei and Helen R. Quinn. CP conservation in the presence of pseudoparticles. *Phys. Rev. Lett.*, 38:1440–1443, Jun 1977.

[149] Steven Weinberg. A New Light Boson? *Phys.Rev.Lett.*, 40:223–226, 1978.

[150] Jihn E. Kim. Light Pseudoscalars, Particle Physics and Cosmology. *Phys.Rept.*, 150:1–177, 1987.

[151] Leanne D. Duffy and Karl van Bibber. Axions as Dark Matter Particles. *New J.Phys.*, 11:105008, 2009, 0904.3346.

[152] Masahiro Kawasaki and Kazunori Nakayama. Axions : Theory and Cosmological Role. 2013, 1301.1123.

[153] Pierre Ramond. Dual Theory for Free Fermions. *Phys.Rev.*, D3:2415–2418, 1971.

[154] D.V. Volkov and V.P. Akulov. Is the Neutrino a Goldstone Particle? *Phys.Lett.*, B46:109–110, 1973.

[155] J. Wess and B. Zumino. Supergauge Transformations in Four-Dimensions. *Nucl.Phys.*, B70:39–50, 1974.

[156] Sidney R. Coleman and J. Mandula. ALL POSSIBLE SYMMETRIES OF THE S MATRIX. *Phys.Rev.*, 159:1251–1256, 1967.

[157] Rudolf Haag, Jan T. Lopuszanski, and Martin Sohnius. All Possible Generators of Supersymmetries of the s Matrix. *Nucl.Phys.*, B88:257, 1975.

[158] Eldad Gildener and Steven Weinberg. Symmetry Breaking and Scalar Bosons. *Phys.Rev.*, D13:3333, 1976.

[159] Georges Aad et al. Observation of a new particle in the search for the Standard Model Higgs boson with the ATLAS detector at the LHC. *Phys.Lett.*, B716:1–29, 2012, 1207.7214.

[160] Serguei Chatrchyan et al. Observation of a new boson at a mass of 125 GeV with the CMS experiment at the LHC. *Phys.Lett.*, B716:30–61, 2012, 1207.7235.

[161] Steven Weinberg. Implications of Dynamical Symmetry Breaking. *Phys.Rev.*, D13:974–996, 1976.

[162] Steven Weinberg. Implications of Dynamical Symmetry Breaking: An Addendum. *Phys.Rev.*, D19:1277–1280, 1979.

[163] Howard E. Haber and Ralf Hempfling. Can the mass of the lightest Higgs boson of the minimal supersymmetric model be larger than m(Z)? *Phys.Rev.Lett.*, 66:1815–1818, 1991.

[164] Yasuhiro Okada, Masahiro Yamaguchi, and Tsutomu Yanagida. Upper bound of the lightest Higgs boson mass in the minimal supersymmetric standard model. *Prog.Theor.Phys.*, 85:1–6, 1991.

[165] Y. Okada, Masahiro Yamaguchi, and T. Yanagida. Renormalization group analysis on the Higgs mass in the softly broken supersymmetric standard model. *Phys.Lett.*, B262:54–58, 1991.

[166] John R. Ellis, Giovanni Ridolfi, and Fabio Zwirner. Radiative corrections to the masses of supersymmetric Higgs bosons. *Phys.Lett.*, B257:83–91, 1991.

[167] John R. Ellis, Giovanni Ridolfi, and Fabio Zwirner. On radiative corrections to supersymmetric Higgs boson masses and their implications for LEP searches. *Phys.Lett.*, B262:477–484, 1991.

[168] K.G. Wilson and John B. Kogut. The Renormalization group and the epsilon expansion. *Phys.Rept.*, 12:75–200, 1974.

[169] Paul Langacker. Grand Unified Theories and Proton Decay. *Phys.Rept.*, 72:185, 1981.

[170] John R. Ellis, S. Kelley, and Dimitri V. Nanopoulos. Probing the desert using gauge coupling unification. *Phys.Lett.*, B260:131–137, 1991.

[171] A.J. Buras, John R. Ellis, M.K. Gaillard, and Dimitri V. Nanopoulos. Aspects of the Grand Unification of Strong, Weak and Electromagnetic Interactions. *Nucl.Phys.*, B135:66–92, 1978.

[172] S. Dimopoulos, S. Raby, and Frank Wilczek. Supersymmetry and the Scale of Unification. *Phys.Rev.*, D24:1681–1683, 1981.

[173] R.N. Mohapatra. Supersymmetric grand unification: An Update. pages 336–394, 1999, hep-ph/9911272.

[174] Stephen P. Martin. A Supersymmetry primer. 1997, hep-ph/9709356.

[175] M. Drees, R. Godbole, and P. Roy. Theory and phenomenology of sparticles: An account of four-dimensional N=1 supersymmetry in high energy physics. 2004.

[176] Hans Peter Nilles. Supersymmetry, Supergravity and Particle Physics. *Phys.Rept.*, 110:1–162, 1984.

[177] Howard E. Haber and Gordon L. Kane. The Search for Supersymmetry: Probing Physics Beyond the Standard Model. *Phys.Rept.*, 117:75–263, 1985.

[178] M.F. Sohnius. Introducing Supersymmetry. *Phys.Rept.*, 128:39–204, 1985.

[179] S. Ferrara, J. Wess, and B. Zumino. Supergauge Multiplets and Superfields. *Phys.Lett.*, B51:239, 1974.

[180] M. Dine. Supersymmetry and string theory: Beyond the standard model. 2007.

[181] S.J. Gates, Marcus T. Grisaru, M. Rocek, and W. Siegel. Superspace Or One Thousand and One Lessons in Supersymmetry. *Front.Phys.*, 58:1–548, 1983, hep-th/0108200.

[182] Manuel Drees. An Introduction to supersymmetry. 1996, hep-ph/9611409.

[183] Edward Witten. Dynamical Breaking of Supersymmetry. *Nucl.Phys.*, B188:513, 1981.

[184] Michael Dine and Ann E. Nelson. Dynamical supersymmetry breaking at low-energies. *Phys.Rev.*, D48:1277–1287, 1993, hep-ph/9303230.

[185] Kenzo Inoue, Akira Kakuto, Hiromasa Komatsu, and Seiichiro Takeshita. Aspects of Grand Unified Models with Softly Broken Supersymmetry. *Prog.Theor.Phys.*, 68:927, 1982.

[186] Luis E. Ibanez and Graham G. Ross. Low-Energy Predictions in Supersymmetric Grand Unified Theories. *Phys.Lett.*, B105:439, 1981.

[187] William J. Marciano and Goran Senjanovic. Predictions of Supersymmetric Grand Unified Theories. *Phys.Rev.*, D25:3092, 1982.

[188] A. Djouadi et al. The Minimal supersymmetric standard model: Group summary report. 1998, hep-ph/9901246.

[189] Savas Dimopoulos and Howard Georgi. Softly Broken Supersymmetry and SU(5). *Nucl.Phys.*, B193:150, 1981.

[190] Masaaki Kuroda. Complete Lagrangian of MSSM. 1999, hep-ph/9902340.

[191] D.J.H. Chung, L.L. Everett, G.L. Kane, et al. The Soft supersymmetry breaking Lagrangian: Theory and applications. *Phys.Rept.*, 407:1–203, 2005, hep-ph/0312378.

[192] L. Girardello and Marcus T. Grisaru. Soft Breaking of Supersymmetry. *Nucl.Phys.*, B194:65, 1982.

[193] Ali H. Chamseddine, Richard L. Arnowitt, and Pran Nath. Locally Supersymmetric Grand Unification. *Phys.Rev.Lett.*, 49:970, 1982.

[194] G.F. Giudice and R. Rattazzi. Theories with gauge mediated supersymmetry breaking. *Phys.Rept.*, 322:419–499, 1999, hep-ph/9801271.

[195] R. Barbier, C. Berat, M. Besancon, et al. R-parity violating supersymmetry. *Phys.Rept.*, 420:1–202, 2005, hep-ph/0406039.

[196] J. Abdallah et al. Searches for supersymmetric particles in e+ e- collisions up to 208-GeV and interpretation of the results within the MSSM. *Eur.Phys.J.*, C31:421–479, 2003, hep-ex/0311019.

[197] Jonathan L. Feng, Shufang Su, and Fumihiro Takayama. Supergravity with a gravitino LSP. *Phys.Rev.*, D70:075019, 2004, hep-ph/0404231.

[198] John R. Ellis, Keith A. Olive, Yudi Santoso, and Vassilis C. Spanos. Gravitino dark matter in the CMSSM. *Phys.Lett.*, B588:7–16, 2004, hep-ph/0312262.

[199] M. Bolz, A. Brandenburg, and W. Buchmuller. Thermal production of gravitinos. *Nucl.Phys.*, B606:518–544, 2001, hep-ph/0012052.

[200] Josef Pradler and Frank Daniel Steffen. Constraints on the Reheating Temperature in Gravitino Dark Matter Scenarios. *Phys.Lett.*, B648:224–235, 2007, hep-ph/0612291.

[201] M. Kawasaki and T. Moroi. Gravitino production in the inflationary universe and the effects on big bang nucleosynthesis. *Prog.Theor.Phys.*, 93:879–900, 1995, hep-ph/9403364.

[202] Luis E. Ibanez. The Scalar Neutrinos as the Lightest Supersymmetric Particles and Cosmology. *Phys.Lett.*, B137:160, 1984.

[203] John S. Hagelin, Gordon L. Kane, and S. Raby. Perhaps Scalar Neutrinos Are the Lightest Supersymmetric Partners. *Nucl.Phys.*, B241:638, 1984.

[204] Katherine Freese. Can Scalar Neutrinos Or Massive Dirac Neutrinos Be the Missing Mass? *Phys.Lett.*, B167:295, 1986.

[205] Toby Falk, Keith A. Olive, and Mark Srednicki. Heavy sneutrinos as dark matter. *Phys.Lett.*, B339:248–251, 1994, hep-ph/9409270.

[206] Mark W. Goodman and Edward Witten. Detectability of Certain Dark Matter Candidates. *Phys.Rev.*, D31:3059, 1985.

[207] R.N. Mohapatra and J.W.F. Valle. Neutrino Mass and Baryon Number Nonconservation in Superstring Models. *Phys.Rev.*, D34:1642, 1986.

[208] Evgeny K. Akhmedov, Manfred Lindner, Erhard Schnapka, and J.W.F. Valle. Dynamical left-right symmetry breaking. *Phys.Rev.*, D53:2752–2780, 1996, hep-ph/9509255.

[209] Evgeny K. Akhmedov, Manfred Lindner, Erhard Schnapka, and J.W.F. Valle. Left-right symmetry breaking in NJL approach. *Phys.Lett.*, B368:270–280, 1996, hep-ph/9507275.

[210] M. Hirsch, M. Malinsky, W. Porod, L. Reichert, and F. Staub. Hefty MSSM-like light Higgs in extended gauge models. *JHEP*, 1202:084, 2012, 1110.3037.

[211] Martin Hirsch, Werner Porod, Laslo Reichert, and Florian Staub. Phenomenology of the minimal supersymmetric $U(1)_{B-L} \times U(1)_R$ extension of the standard model. *Phys.Rev.*, D86:093018, 2012, 1206.3516.

[212] H. David Politzer. Reliable Perturbative Results for Strong Interactions? *Phys.Rev.Lett.*, 30:1346–1349, 1973.

[213] D.J. Gross and Frank Wilczek. Asymptotically Free Gauge Theories. 1. *Phys.Rev.*, D8:3633–3652, 1973.

[214] Gerard 't Hooft. Dimensional regularization and the renormalization group. *Nucl.Phys.*, B61:455–468, 1973.

[215] Vincent Lucas and Stuart Raby. GUT scale threshold corrections in a complete supersymmetric SO(10) model: Alpha-s (m(z)) versus proton lifetime. *Phys.Rev.*, D54:2261–2272, 1996, hep-ph/9601303.

[216] Tomas Blazek, Marcela S. Carena, Stuart Raby, and Carlos E.M. Wagner. A Global chi**2 analysis of electroweak data in SO(10) SUSY GUTs. *Phys.Rev.*, D56:6919–6938, 1997, hep-ph/9611217.

[217] Guido Altarelli, Ferruccio Feruglio, and Isabella Masina. From minimal to realistic supersymmetric SU(5) grand unification. *JHEP*, 0011:040, 2000, hep-ph/0007254.

[218] Radovan Dermisek, Arash Mafi, and Stuart Raby. SUSY GUTs under siege: Proton decay. *Phys.Rev.*, D63:035001, 2001, hep-ph/0007213.

[219] JoAnne L. Hewett and Thomas G. Rizzo. Low-Energy Phenomenology of Superstring Inspired E(6) Models. *Phys.Rept.*, 183:193, 1989.

[220] H. Georgi and S.L. Glashow. Unity of All Elementary Particle Forces. *Phys.Rev.Lett.*, 32:438–441, 1974.

[221] Toru Goto and Takeshi Nihei. Effect of RRRR dimension five operator on the proton decay in the minimal SU(5) SUGRA GUT model. *Phys.Rev.*, D59:115009, 1999, hep-ph/9808255.

[222] Hitoshi Murayama and Aaron Pierce. Not even decoupling can save minimal supersymmetric SU(5). *Phys.Rev.*, D65:055009, 2002, hep-ph/0108104.

[223] Harald Fritzsch and Peter Minkowski. Unified Interactions of Leptons and Hadrons. *Annals Phys.*, 93:193–266, 1975.

[224] T.E. Clark, Tzee-Ke Kuo, and N. Nakagawa. A SO(10) SUPERSYMMETRIC GRAND UNIFIED THEORY. *Phys.Lett.*, B115:26, 1982.

[225] C.S. Aulakh and Rabindra N. Mohapatra. IMPLICATIONS OF SUPERSYMMETRIC SO(10) GRAND UNIFICATION. *Phys.Rev.*, D28:217, 1983.

[226] Rabindra N. Mohapatra and B. Sakita. SO(2n) Grand Unification in an SU(N) Basis. *Phys.Rev.*, D21:1062, 1980.

[227] R. Slansky. Group Theory for Unified Model Building. *Phys.Rept.*, 79:1–128, 1981.

[228] K.S. Babu and R.N. Mohapatra. Predictive neutrino spectrum in minimal SO(10) grand unification. *Phys.Rev.Lett.*, 70:2845–2848, 1993, hep-ph/9209215.

[229] K. Matsuda, Y. Koide, T. Fukuyama, and H. Nishiura. How far can the SO(10) two Higgs model describe the observed neutrino masses and mixings? *Phys.Rev.*, D65:033008, 2002, hep-ph/0108202.

[230] Takeshi Fukuyama and Nobuchika Okada. Neutrino oscillation data versus minimal supersymmetric SO(10) model. *JHEP*, 0211:011, 2002, hep-ph/0205066.

[231] H.S. Goh, R.N. Mohapatra, and S. Nasri. SO(10) symmetry breaking and type II seesaw. *Phys.Rev.*, D70:075022, 2004, hep-ph/0408139.

[232] Borut Bajc, Goran Senjanovic, and Francesco Vissani. Probing the nature of the seesaw in renormalizable SO(10). *Phys.Rev.*, D70:093002, 2004, hep-ph/0402140.

[233] Bhaskar Dutta, Yukihiro Mimura, and R.N. Mohapatra. Neutrino masses and mixings in a predictive SO(10) model with CKM CP violation. *Phys.Lett.*, B603:35–45, 2004, hep-ph/0406262.

[234] Takeshi Fukuyama, Amon Ilakovac, Tatsuru Kikuchi, Stjepan Meljanac, and Nobuchika Okada. SO(10) group theory for the unified model building. *J.Math.Phys.*, 46:033505, 2005, hep-ph/0405300.

[235] K.S. Babu and Cosmin Macesanu. Neutrino masses and mixings in a minimal SO(10) model. *Phys.Rev.*, D72:115003, 2005, hep-ph/0505200.

[236] Stefano Bertolini, Luca Di Luzio, and Michal Malinsky. Seesaw Scale in the Minimal Renormalizable SO(10) Grand Unification. *Phys.Rev.*, D85:095014, 2012, 1202.0807.

[237] C. Arbelaez, R.M. Fonseca, M. Hirsch, and J.C. Romao. Supersymmetric SO(10) GUTs with sliding scales. 2013, 1301.6085.

[238] Charanjit S. Aulakh, Borut Bajc, Alejandra Melfo, Goran Senjanovic, and Francesco Vissani. The Minimal supersymmetric grand unified theory. *Phys.Lett.*, B588:196–202, 2004, hep-ph/0306242.

[239] Jogesh C. Pati and Abdus Salam. Lepton Number as the Fourth Color. *Phys.Rev.*, D10:275–289, 1974.

[240] R.N. Mohapatra and Jogesh C. Pati. A Natural Left-Right Symmetry. *Phys.Rev.*, D11:2558, 1975.

[241] G. Senjanovic and Rabindra N. Mohapatra. Exact Left-Right Symmetry and Spontaneous Violation of Parity. *Phys.Rev.*, D12:1502, 1975.

[242] Goran Senjanovic. Spontaneous Breakdown of Parity in a Class of Gauge Theories. *Nucl.Phys.*, B153:334, 1979.

[243] Rabindra N. Mohapatra and Jogesh C. Pati. Left-Right Gauge Symmetry and an Isoconjugate Model of CP Violation. *Phys.Rev.*, D11:566–571, 1975.

[244] S.F. King. Neutrino mass models. *Rept.Prog.Phys.*, 67:107–158, 2004, hep-ph/0310204.

[245] R.N. Mohapatra, S. Antusch, K.S. Babu, et al. Theory of neutrinos: A White paper. *Rept.Prog.Phys.*, 70:1757–1867, 2007, hep-ph/0510213.

[246] R.N. Mohapatra and A.Y. Smirnov. Neutrino Mass and New Physics. *Ann.Rev.Nucl.Part.Sci.*, 56:569–628, 2006, hep-ph/0603118.

[247] J.W.F. Valle. Neutrino physics overview. *J.Phys.Conf.Ser.*, 53:473–505, 2006, hep-ph/0608101.

[248] Hiroshi Nunokawa, Stephen J. Parke, and Jose W.F. Valle. CP Violation and Neutrino Oscillations. *Prog.Part.Nucl.Phys.*, 60:338–402, 2008, 0710.0554.

[249] Ettore Majorana. Theory of the Symmetry of Electrons and Positrons. *Nuovo Cim.*, 14:171–184, 1937.

[250] J. Schechter and J.W.F. Valle. Neutrinoless Double beta Decay in SU(2) x U(1) Theories. *Phys.Rev.*, D25:2951, 1982.

[251] Martin Hirsch, Sergey Kovalenko, and Ivan Schmidt. Extended black box theorem for lepton number and flavor violating processes. *Phys.Lett.*, B642:106–110, 2006, hep-ph/0608207.

[252] W. Konetschny and W. Kummer. Nonconservation of Total Lepton Number with Scalar Bosons. *Phys.Lett.*, B70:433, 1977.

[253] T.P. Cheng and Ling-Fong Li. Neutrino Masses, Mixings and Oscillations in SU(2) $\times$ U(1) Models of Electroweak Interactions. *Phys.Rev.*, D22:2860, 1980.

[254] Rabindra N. Mohapatra and Goran Senjanovic. Neutrino Mass and Spontaneous Parity Violation. *Phys.Rev.Lett.*, 44:912, 1980.

[255] Rabindra N. Mohapatra and Goran Senjanovic. Neutrino Masses and Mixings in Gauge Models with Spontaneous Parity Violation. *Phys.Rev.*, D23:165, 1981.

[256] Robert Foot, H. Lew, X.G. He, and Girish C. Joshi. SEESAW NEUTRINO MASSES INDUCED BY A TRIPLET OF LEPTONS. *Z.Phys.*, C44:441, 1989.

[257] Steven Weinberg. Baryon and Lepton Nonconserving Processes. *Phys.Rev.Lett.*, 43:1566–1570, 1979.

[258] Ernest Ma. Pathways to naturally small neutrino masses. *Phys.Rev.Lett.*, 81:1171–1174, 1998, hep-ph/9805219.

[259] Peter Minkowski. mu $\to$ e gamma at a Rate of One Out of 1-Billion Muon Decays? *Phys.Lett.*, B67:421, 1977.

[260] Murray Gell-Mann, Pierre Ramond, and Richard Slansky. COMPLEX SPINORS AND UNIFIED THEORIES. *Conf.Proc.*, C790927:315–321, 1979, 1306.4669.

[261] George Lazarides, Q. Shafi, and C. Wetterich. Proton Lifetime and Fermion Masses in an SO(10) Model. *Nucl.Phys.*, B181:287–300, 1981.

[262] David G. Cerdeno and Anne M. Green. Direct detection of WIMPs. 2010, 1002.1912.

[263] A.K. Drukier, K. Freese, and D.N. Spergel. Detecting Cold Dark Matter Candidates. *Phys.Rev.*, D33:3495–3508, 1986.

[264] Z. Ahmed et al. Search for Weakly Interacting Massive Particles with the First Five-Tower Data from the Cryogenic Dark Matter Search at the Soudan Underground Laboratory. *Phys.Rev.Lett.*, 102:011301, 2009, 0802.3530.

[265] Z. Ahmed et al. Dark Matter Search Results from the CDMS II Experiment. *Science*, 327:1619–1621, 2010, 0912.3592.

[266] Z. Ahmed et al. Results from a Low-Energy Analysis of the CDMS II Germanium Data. *Phys.Rev.Lett.*, 106:131302, 2011, 1011.2482.

[267] R. Agnese et al. Dark Matter Search Results Using the Silicon Detectors of CDMS II. *Phys.Rev.Lett.*, 2013, 1304.4279.

[268] G. Angloher, M. Bauer, I. Bavykina, et al. Results from 730 kg days of the CRESST-II Dark Matter Search. *Eur.Phys.J.*, C72:1971, 2012, 1109.0702.

[269] C.E. Aalseth et al. Results from a Search for Light-Mass Dark Matter with a P-type Point Contact Germanium Detector. *Phys.Rev.Lett.*, 106:131301, 2011, 1002.4703.

[270] C.E. Aalseth, P.S. Barbeau, J. Colaresi, et al. Search for an Annual Modulation in a P-type Point Contact Germanium Dark Matter Detector. *Phys.Rev.Lett.*, 107:141301, 2011, 1106.0650.

[271] E. Armengaud et al. Final results of the EDELWEISS-II WIMP search using a 4-kg array of cryogenic germanium detectors with interleaved electrodes. *Phys.Lett.*, B702:329–335, 2011, 1103.4070.

[272] H. Kraus, M. Bauer, I. Bavykina, et al. EURECA: The European future of dark matter searches with cryogenic detectors. *Nucl.Phys.Proc.Suppl.*, 173:168–171, 2007.

[273] R. Bernabei et al. First results from DAMA/LIBRA and the combined results with DAMA/NaI. *Eur.Phys.J.*, C56:333–355, 2008, 0804.2741.

[274] D. Yu. Akimov, G.J. Alner, H.M. Araujo, et al. The ZEPLIN-III dark matter detector: instrument design, manufacture and commissioning. *Astropart.Phys.*, 27:46–60, 2007, astro-ph/0605500.

[275] J. Angle et al. First Results from the XENON10 Dark Matter Experiment at the Gran Sasso National Laboratory. *Phys.Rev.Lett.*, 100:021303, 2008, 0706.0039.

[276] E. Aprile et al. Dark Matter Results from 100 Live Days of XENON100 Data. *Phys.Rev.Lett.*, 107:131302, 2011, 1104.2549.

[277] E. Aprile et al. Dark Matter Results from 225 Live Days of XENON100 Data. *Phys.Rev.Lett.*, 109:181301, 2012, 1207.5988.

[278] E. Behnke et al. Improved Spin-Dependent WIMP Limits from a Bubble Chamber. *Science*, 319:933–936, 2008, 0804.2886.

[279] G.J. Alner, H. Araujo, A. Bewick, et al. The DRIFT-II dark matter detector: Design and commissioning. *Nucl.Instrum.Meth.*, A555:173–183, 2005.

[280] Andre Rubbia. ArDM: A Ton-scale liquid Argon experiment for direct detection of dark matter in the universe. *J.Phys.Conf.Ser.*, 39:129–132, 2006, hep-ph/0510320.

[281] R. Brunetti et al. Warp liquid argon detector for dark matter survey. *New Astron.Rev.*, 49:265–269, 2005, astro-ph/0405342.

[282] D.S. Akerib et al. The Large Underground Xenon (LUX) Experiment. *Nucl.Instrum.Meth.*, A704:111–126, 2013, 1211.3788.

[283] Paul L. Brink et al. Beyond the CDMS-II dark matter search: SuperCDMS. *eConf*, C041213:2529, 2004, astro-ph/0503583.

[284] Richard W. Schnee et al. The SuperCDMS Experiment. 2005, astro-ph/0502435.

[285] Elena Aprile. The XENON1T Dark Matter Search Experiment. 2012, 1206.6288.

[286] R. Bernabei, P. Belli, S. d'Angelo, et al. Dark Matter investigation by DAMA at Gran Sasso. 2013, 1306.1411.

[287] R. Bernabei, P. Belli, V. Landoni, et al. New limits on WIMP search with large-mass low-radioactivity NaI(Tl) set-up at Gran Sasso. *Phys.Lett.*, B389:757–766, 1996.

[288] R. Bernabei, Pierluigi Belli, F. Cappella, et al. Dark matter particles in the Galactic halo: Results and implications from DAMA/NaI. *Int.J.Mod.Phys.*, D13:2127–2160, 2004, astro-ph/0501412.

[289] R. Bernabei et al. New results from DAMA/LIBRA. *Eur.Phys.J.*, C67:39–49, 2010, 1002.1028.

[290] R. Bernabei, P. Belli, F. Cappella, et al. Final model independent result of DAMA/LIBRA-phase1. 2013, 1308.5109.

[291] R. Bernabei, P. Belli, F. Montecchia, et al. Searching for WIMPs by the annual modulation signature. *Physics Letters B*, 424:195–201, April 1998.

[292] R. Bernabei, P. Belli, F. Montecchia, et al. On a further search for a yearly modulation of the rate in particle Dark Matter direct search. *Physics Letters B*, 450:448–455, March 1999.

[293] R. Bernabei, P. Belli, R. Cerulli, et al. Search for WIMP annual modulation signature: results from DAMA/NaI-3 and DAMA/NaI-4 and the global combined analysis. *Physics Letters B*, 480:23–31, May 2000.

[294] R. Agnese et al. Silicon Detector Results from the First Five-Tower Run of CDMS II. *Phys.Rev.D*, 2013, 1304.3706.

[295] D. Yu. Akimov, H.M. Araujo, E.J. Barnes, et al. WIMP-nucleon cross-section results from the second science run of ZEPLIN-III. *Phys.Lett.*, B709:14–20, 2012, 1110.4769.

[296] O. Buchmueller, R. Cavanaugh, A. De Roeck, et al. Supersymmetry in Light of 1/fb of LHC Data. *Eur.Phys.J.*, C72:1878, 2012, 1110.3568.

[297] O. Buchmueller, R. Cavanaugh, D. Colling, et al. Implications of Initial LHC Searches for Supersymmetry. *Eur.Phys.J.*, C71:1634, 2011, 1102.4585.

[298] Marco Farina, Duccio Pappadopulo, Alessandro Strumia, and Tomer Volansky. Can CoGeNT and DAMA Modulations Be Due to Dark Matter? *JCAP*, 1111:010, 2011, 1107.0715.

[299] Mads T. Frandsen, Felix Kahlhoefer, Christopher McCabe, Subir Sarkar, and Kai Schmidt-Hoberg. Resolving astrophysical uncertainties in dark matter direct detection. *JCAP*, 1201:024, 2012, 1111.0292.

[300] Patrick J. Fox, Joachim Kopp, Mariangela Lisanti, and Neal Weiner. A CoGeNT Modulation Analysis. *Phys.Rev.*, D85:036008, 2012, 1107.0717.

[301] Chris Kelso, Dan Hooper, and Matthew R. Buckley. Toward A Consistent Picture For CRESST, CoGeNT and DAMA. *Phys.Rev.*, D85:043515, 2012, 1110.5338.

[302] Joachim Kopp, Thomas Schwetz, and Jure Zupan. Light Dark Matter in the light of CRESST-II. *JCAP*, 1203:001, 2012, 1110.2721.

[303] C. Savage, G. Gelmini, P. Gondolo, and K. Freese. Compatibility of DAMA/LIBRA dark matter detection with other searches. *JCAP*, 0904:010, 2009, 0808.3607.

[304] Juan Herrero-Garcia, Thomas Schwetz, and Jure Zupan. Astrophysics independent bounds on the annual modulation of dark matter signals. *Phys.Rev.Lett.*, 109:141301, 2012, 1205.0134.

[305] James M. Cline, Zuowei Liu, and Wei Xue. An optimistic CoGeNT analysis. *Phys.Rev.*, D87:015001, 2013, 1207.3039.

[306] Christoph Weniger. A Tentative Gamma-Ray Line from Dark Matter Annihilation at the Fermi Large Area Telescope. *JCAP*, 1208:007, 2012, 1204.2797.

[307] Joseph Silk, Keith A. Olive, and Mark Srednicki. The Photino, the Sun and High-Energy Neutrinos. *Phys.Rev.Lett.*, 55:257–259, 1985.

[308] S. Desai et al. Search for dark matter WIMPs using upward through-going muons in Super-Kamiokande. *Phys.Rev.*, D70:083523, 2004, hep-ex/0404025.

[309] C. Rott, T. Tanaka, and Y. Itow. Enhanced Sensitivity to Dark Matter Self-annihilations in the Sun using Neutrino Spectral Information. *JCAP*, 1109:029, 2011, 1107.3182.

[310] E. Aslanides et al. A deep sea telescope for high-energy neutrinos. 1999, astro-ph/9907432.

[311] J. Ahrens et al. Sensitivity of the IceCube detector to astrophysical sources of high energy muon neutrinos. *Astropart.Phys.*, 20:507–532, 2004, astro-ph/0305196.

[312] J. Ahrens et al. Icecube - the next generation neutrino telescope at the south pole. *Nucl.Phys.Proc.Suppl.*, 118:388–395, 2003, astro-ph/0209556.

[313] M. Ambrosio et al. Limits on dark matter WIMPS using upward going muons in the MACRO detector. *Phys.Rev.*, D60:082002, 1999, hep-ex/9812020.

[314] E. Andres, P. Askebjer, S.W. Barwick, et al. The AMANDA neutrino telescope: Principle of operation and first results. *Astropart.Phys.*, 13:1–20, 2000, astro-ph/9906203.

[315] T. Tanaka et al. An Indirect Search for WIMPs in the Sun using 3109.6 days of upward-going muons in Super-Kamiokande. *Astrophys.J.*, 742:78, 2011, 1108.3384.

[316] M.G. Aartsen et al. Search for dark matter annihilations in the Sun with the 79-string IceCube detector. *Phys.Rev.Lett.*, 110:131302, 2013, 1212.4097.

[317] G. Wikstrom and J. Edsjo. Limits on the WIMP-nucleon scattering cross-section from neutrino telescopes. *JCAP*, 0904:009, 2009, 0903.2986.

[318] K. Clark and D.F. Cowen. IceCube/DeepCore and IceCube/PINGU: Prospects for few-GeV scale ν physics in the ice. *Nucl.Phys.Proc.Suppl.*, 233:223–228, 2012.

[319] D. Jason Koskinen. IceCube-DeepCore-PINGU: Fundamental neutrino and dark matter physics at the South Pole. *Mod.Phys.Lett.*, A26:2899–2915, 2011.

[320] K. Abe, T. Abe, H. Aihara, et al. Letter of Intent: The Hyper-Kamiokande Experiment — Detector Design and Physics Potential —. 2011, 1109.3262.

[321] Pierre Salati. Indirect and direct dark matter detection. *PoS*, CARGESE2007:009, 2007.

[322] S.W. Barwick et al. Measurements of the cosmic ray positron fraction from 1-GeV to 50-GeV. *Astrophys.J.*, 482:L191–L194, 1997, astro-ph/9703192.

[323] M. Aguilar et al. Cosmic-ray positron fraction measurement from 1 to 30-GeV with AMS-01. *Phys.Lett.*, B646:145–154, 2007, astro-ph/0703154.

[324] Oscar Adriani et al. An anomalous positron abundance in cosmic rays with energies 1.5-100 GeV. *Nature*, 458:607–609, 2009, 0810.4995.

[325] M. Ackermann et al. Measurement of separate cosmic-ray electron and positron spectra with the Fermi Large Area Telescope. *Phys.Rev.Lett.*, 108:011103, 2012, 1109.0521.

[326] V. Barger, Wai Yee Keung, D. Marfatia, and G. Shaughnessy. PAMELA and dark matter. *Phys.Lett.*, B672:141–146, 2009, 0809.0162.

[327] Lars Bergstrom, Torsten Bringmann, and Joakim Edsjo. New Positron Spectral Features from Supersymmetric Dark Matter - a Way to Explain the PAMELA Data? *Phys.Rev.*, D78:103520, 2008, 0808.3725.

[328] Patrick J. Fox and Erich Poppitz. Leptophilic Dark Matter. *Phys.Rev.*, D79:083528, 2009, 0811.0399.

[329] Marco Cirelli and Alessandro Strumia. Minimal Dark Matter predictions and the PAMELA positron excess. *PoS*, IDM2008:089, 2008, 0808.3867.

[330] Marco Cirelli, Mario Kadastik, Martti Raidal, and Alessandro Strumia. Model-independent implications of the e+-, anti-proton cosmic ray spectra on properties of Dark Matter. *Nucl.Phys.*, B813:1–21, 2009, 0809.2409.

[331] Marco Cirelli and James M. Cline. Can multistate dark matter annihilation explain the high-energy cosmic ray lepton anomalies? *Phys.Rev.*, D82:023503, 2010, 1005.1779.

[332] Ilias Cholis, Lisa Goodenough, Dan Hooper, Melanie Simet, and Neal Weiner. High Energy Positrons From Annihilating Dark Matter. *Phys.Rev.*, D80:123511, 2009, 0809.1683.

[333] N. Arkani-Hamed, D. P. Finkbeiner, T. R. Slatyer, and N. Weiner. A theory of dark matter. *Phys. Rev. D*, 79(1):015014–+, January 2009, 0810.0713.

[334] John David March-Russell and Stephen Mathew West. WIMPonium and Boost Factors for Indirect Dark Matter Detection. *Phys.Lett.*, B676:133–139, 2009, 0812.0559.

[335] Ilias Cholis, Douglas P. Finkbeiner, Lisa Goodenough, and Neal Weiner. The PAMELA Positron Excess from Annihilations into a Light Boson. *JCAP*, 0912:007, 2009, 0810.5344.

[336] Peng-fei Yin, Qiang Yuan, Jia Liu, et al. PAMELA data and leptonically decaying dark matter. *Phys.Rev.*, D79:023512, 2009, 0811.0176.

[337] Maxim Pospelov and Adam Ritz. Astrophysical Signatures of Secluded Dark Matter. *Phys.Lett.*, B671:391–397, 2009, 0810.1502.

[338] O. Adriani, G.C. Barbarino, G.A. Bazilevskaya, et al. A new measurement of the antiproton-to-proton flux ratio up to 100 GeV in the cosmic radiation. *Phys.Rev.Lett.*, 102:051101, 2009, 0810.4994.

[339] Marco Cirelli and Gaelle Giesen. Antiprotons from Dark Matter: Current constraints and future sensitivities. *JCAP*, 1304:015, 2013, 1301.7079.

[340] Carmelo Evoli, Ilias Cholis, Dario Grasso, Luca Maccione, and Piero Ullio. Antiprotons from dark matter annihilation in the Galaxy: astrophysical uncertainties. *Phys.Rev.*, D85:123511, 2012, 1108.0664.

[341] F. Donato, D. Maurin, P. Brun, T. Delahaye, and P. Salati. Constraints on WIMP Dark Matter from the High Energy PAMELA $\bar{p}/p$ Data. *Phys. Rev. Lett.*, 102(7):071301–+, February 2009, 0810.5292.

[342] Daniel Feldman, Zuowei Liu, and Pran Nath. PAMELA Positron Excess as a Signal from the Hidden Sector. *Phys.Rev.*, D79:063509, 2009, 0810.5762.

[343] Masahiro Ibe, Hitoshi Murayama, and T.T. Yanagida. Breit-Wigner Enhancement of Dark Matter Annihilation. *Phys.Rev.*, D79:095009, 2009, 0812.0072.

[344] Wan-Lei Guo and Yue-Liang Wu. Enhancement of Dark Matter Annihilation via Breit-Wigner Resonance. *Phys.Rev.*, D79:055012, 2009, 0901.1450.

[345] Arnold J. W. Sommerfeld. **Uber die Beugung und Bremsung der Elektronen**. *Annalen der Physik*, 403, 1931.

[346] Massimiliano Lattanzi and Joseph Silk. **Can the WIMP annihilation boost factor be boosted by the Sommerfeld enhancement?** *Phys. Rev. D*, 79:083523, 2009. 0812.0360v2.

[347] Junji Hisano, Sh. Matsumoto, and Mihoko M. Nojiri. Explosive dark matter annihilation. *Phys. Rev. Lett.*, 92:1–5, 2004. 037216v1.

[348] Roberto Iengo. Sommerfeld enhancement: general results from field theory diagrams. *JHEP*, 0905:024:1–14, 2009. 0902.0688.

[349] J. Zavala, M. Vogelsberger, T. R. Slatyer, A. Loeb, and V. Springel. *accepted for publication in Phys. Rev. D*, 2011, 1103.0776.

[350] Dan Hooper, Pasquale Blasi, and Pasquale Dario Serpico. Pulsars as the Sources of High Energy Cosmic Ray Positrons. *JCAP*, 0901:025, 2009, 0810.1527.

[351] Hasan Yuksel, Matthew D. Kistler, and Todor Stanev. TeV Gamma Rays from Geminga and the Origin of the GeV Positron Excess. *Phys.Rev.Lett.*, 103:051101, 2009, 0810.2784.

[352] Stefano Profumo. Dissecting cosmic-ray electron-positron data with Occam's Razor: the role of known Pulsars. *Central Eur.J.Phys.*, 10:1–31, 2011, 0812.4457.

[353] D. Grasso et al. On possible interpretations of the high energy electron-positron spectrum measured by the Fermi Large Area Telescope. *Astropart.Phys.*, 32:140–151, 2009, 0905.0636.

[354] Ilias Cholis and Dan Hooper. Dark Matter and Pulsar Origins of the Rising Cosmic Ray Positron Fraction in Light of New Data From AMS. 2013, 1304.1840.

[355] M. Aguilar et al. First Result from the Alpha Magnetic Spectrometer on the International Space Station: Precision Measurement of the Positron Fraction in Primary Cosmic Rays of 0.5-350 GeV. *Phys.Rev.Lett.*, 110(14):141102, 2013.

[356] Lars Bergstrom, Torsten Bringmann, Ilias Cholis, Dan Hooper, and Christoph Weniger. New limits on dark matter annihilation from AMS cosmic ray positron data. 2013, 1306.3983.

[357] F. Donato, D. Maurin, P. Brun, T. Delahaye, and P. Salati. Constraints on WIMP Dark Matter from the High Energy PAMELA $\bar{p}/p$ data. *Phys.Rev.Lett.*, 102:071301, 2009, 0810.5292.

[358] Mathias Garny, Alejandro Ibarra, and David Tran. Constraints on Hadronically Decaying Dark Matter. *JCAP*, 1208:025, 2012, 1205.6783.

[359] Torsten Bringmann. Antiproton and Radio Constraints on the Dark Matter Interpretation of the Fermi Gamma Ray Observations of the Galactic Center. 2009, 0911.1124.

[360] David G. Cerdeno, Timur Delahaye, and Julien Lavalle. Cosmic-ray antiproton constraints on light singlino-like dark matter candidates. *Nucl.Phys.*, B854:738–779, 2012, 1108.1128.

[361] Fiorenza Donato, Nicolao Fornengo, and Pierre Salati. Anti-deuterons as a signature of supersymmetric dark matter. *Phys.Rev.*, D62:043003, 2000, hep-ph/9904481.

[362] S.A.I. Mognet, T. Aramaki, N. Bando, et al. The Prototype GAPS (pGAPS) Experiment. 2013, 1303.1615.

[363] N. Fornengo, L. Maccione, and A. Vittino. Dark matter searches with cosmic antideuterons: status and perspectives. 2013, 1306.4171.

[364] J. A. R. Cembranos, A. de La Cruz-Dombriz, A. Dobado, R. A. Lineros, and A. L. Maroto. Photon spectra from WIMP annihilation. *Phys. Rev. D*, 83(8):083507, April 2011, 1009.4936.

[365] Torsten Bringmann, Lars Bergstrom, and Joakim Edsjo. New Gamma-Ray Contributions to Supersymmetric Dark Matter Annihilation. *JHEP*, 0801:049, 2008, 0710.3169.

[366] Marco Cirelli, Pasquale D. Serpico, and Gabrijela Zaharijas. Bremsstrahlung gamma rays from light Dark Matter. 2013, 1307.7152.

[367] Marco Cirelli. Indirect Searches for Dark Matter: a status review. *Pramana*, 79:1021–1043, 2012, 1202.1454.

[368] A. Morselli, B. Canadas, and V. Vitale. The Indirect Search for Dark Matter from the centre of the Galaxy with the Fermi LAT. *Nuovo Cim.*, C034N3:311–316, 2011, 1012.2292.

[369] R.M. Crocker, N.F. Bell, C. Balazs, and D.I. Jones. Radio and gamma-ray constraints on dark matter annihilation in the Galactic center. *Phys.Rev.*, D81:063516, 2010, 1002.0229.

[370] Dan Hooper and Tim Linden. On The Origin Of The Gamma Rays From The Galactic Center. *Phys.Rev.*, D84:123005, 2011, 1110.0006.

[371] Dan Hooper, Chris Kelso, and Farinaldo S. Queiroz. Stringent and Robust Constraints on the Dark Matter Annihilation Cross Section From the Region of the Galactic Center. *Astropart.Phys.*, 46:55–70, 2013, 1209.3015.

[372] A. Abramowski et al. Search for a Dark Matter annihilation signal from the Galactic Center halo with H.E.S.S. *Phys.Rev.Lett.*, 106:161301, 2011, 1103.3266.

[373] Louis E. Strigari, Savvas Michael Koushiappas, James S. Bullock, et al. The Most Dark Matter Dominated Galaxies: Predicted Gamma-ray Signals from the Faintest Milky Way Dwarfs. 2007, 0709.1510.

[374] Alex Geringer-Sameth and Savvas M. Koushiappas. Exclusion of canonical WIMPs by the joint analysis of Milky Way dwarfs with Fermi. *Phys.Rev.Lett.*, 107:241303, 2011, 1108.2914.

[375] M. Ackermann et al. Constraining Dark Matter Models from a Combined Analysis of Milky Way Satellites with the Fermi Large Area Telescope. *Phys.Rev.Lett.*, 107:241302, 2011, 1108.3546.

[376] Tesla E. Jeltema, John Kehayias, and Stefano Profumo. Gamma Rays from Clusters and Groups of Galaxies: Cosmic Rays versus Dark Matter. *Phys.Rev.*, D80:023005, 2009, 0812.0597.

[377] Anders Pinzke, Christoph Pfrommer, and Lars Bergstrom. Prospects of detecting gamma-ray emission from galaxy clusters: cosmic rays and dark matter annihilations. *Phys.Rev.*, D84:123509, 2011, 1105.3240.

[378] Jiaxin Han, Carlos S. Frenk, Vincent R. Eke, Liang Gao, and Simon D.M. White. Evidence for extended gamma-ray emission from galaxy clusters. 2012, 1201.1003.

[379] Andrew W. Strong, Igor V. Moskalenko, and Olaf Reimer. Diffuse continuum gamma-rays from the galaxy. *Astrophys.J.*, 537:763–784, 2000, astro-ph/9811296.

[380] Timur Delahaye, Armand Fiasson, Martin Pohl, and Pierre Salati. The GeV-TeV Galactic gamma-ray diffuse emission I. Uncertainties in the predictions of the hadronic component. *Astron.Astrophys.*, 531:A37, 2011, 1102.0744.

[381] J.A. Hinton. The Status of the H.E.S.S. project. *New Astron.Rev.*, 48:331–337, 2004, astro-ph/0403052.

[382] T.C. Weekes, H. Badran, S.D. Biller, et al. VERITAS: The Very energetic radiation imaging telescope array system. *Astropart.Phys.*, 17:221–243, 2002, astro-ph/0108478.

[383] F. Aharonian et al. H.E.S.S. observations of the Galactic Center region and their possible dark matter interpretation. *Phys.Rev.Lett.*, 97:221102, 2006, astro-ph/0610509.

[384] Kevork N. Abazajian and J. Patrick Harding. Constraints on WIMP and Sommerfeld-Enhanced Dark Matter Annihilation from HESS Observations of the Galactic Center. *JCAP*, 1201:041, 2012, 1110.6151.

[385] F. Aharonian et al. Discovery of very-high-energy gamma-rays from the galactic centre ridge. *Nature*, 439:695–698, 2006, astro-ph/0603021.

[386] : F. Aharonian. Observations of the Sagittarius Dwarf galaxy by the H.E.S.S. experiment and search for a Dark Matter signal. *Astropart.Phys.*, 29:55–62, 2008, 0711.2369.

[387] A. Abramowski et al. H.E.S.S. constraints on Dark Matter annihilations towards the Sculptor and Carina Dwarf Galaxies. *Astropart.Phys.*, 34:608–616, 2011, 1012.5602.

[388] A. Abramowski et al. H.E.S.S. observations of the globular clusters NGC 6388 and M 15 and search for a Dark Matter signal. *Astrophys.J.*, 735:12, 2011, 1104.2548.

[389] A. Abramowski et al. Search for photon line-like signatures from Dark Matter annihilations with H.E.S.S. *Phys.Rev.Lett.*, 110:041301, 2013, 1301.1173.

[390] K. Kosack et al. TeV gamma-ray observations of the galactic center. *Astrophys.J.*, 608:L97–L100, 2004, astro-ph/0403422.

[391] V.A. Acciari et al. VERITAS Search for VHE Gamma-ray Emission from Dwarf Spheroidal Galaxies. *Astrophys.J.*, 720:1174–1180, 2010, 1006.5955.

[392] E. Aliu et al. VERITAS Deep Observations of the Dwarf Spheroidal Galaxy Segue 1. *Phys.Rev.*, D85:062001, 2012, 1202.2144.

[393] J.S. Perkins. VERITAS Observations of the Coma Cluster of Galaxies. *AIP Conf.Proc.*, 1085:569–572, 2009, 0810.0302.

[394] R. Enomoto et al. Design study of CANGAROO-III, stereoscopic imaging atmospheric Cherenkov telescopes for sub-TeV gamma-ray. *Astropart.Phys.*, 16:235–244, 2002, astro-ph/0107578.

[395] E. Lorenz. Status of the 17-m MAGIC telescope. *New Astron.Rev.*, 48:339–344, 2004.

[396] D.J. Thompson, D.L. Bertsch, C.E. Fichtel, et al. Calibration of the Energetic Gamma-Ray Experiment Telescope (EGRET) for the Compton Gamma-Ray Observatory. *Astrophys.J.Suppl.*, 86:629–656, 1993.

[397] S.D. Hunter, D.L. Bertsch, J.R. Catelli, et al. EGRET observations of the diffuse gamma-ray emission from the galactic plane. *Astrophys.J.*, 481:205–240, 1997.

[398] W. de Boer, C. Sander, V. Zhukov, A.V. Gladyshev, and D.I. Kazakov. Egret excess of diffuse galactic gamma rays as tracer of dark matter. *Astron.Astrophys.*, 444:51, 2005, astro-ph/0508617.

[399] A.A. Abdo et al. The Spectrum of the Isotropic Diffuse Gamma-Ray Emission Derived From First-Year Fermi Large Area Telescope Data. *Phys.Rev.Lett.*, 104:101101, 2010, 1002.3603.

[400] W.B. Atwood et al. The Large Area Telescope on the Fermi Gamma-ray Space Telescope Mission. *Astrophys.J.*, 697:1071–1102, 2009, 0902.1089.

[401] A.A. Abdo et al. Observations of Milky Way Dwarf Spheroidal galaxies with the Fermi-LAT detector and constraints on Dark Matter models. *Astrophys.J.*, 712:147–158, 2010, 1001.4531.

[402] M. Ackermann et al. Constraints on the Galactic Halo Dark Matter from Fermi-LAT Diffuse Measurements. *Astrophys.J.*, 761:91, 2012, 1205.6474.

[403] M. Ackermann, M. Ajello, A. Allafort, et al. Constraints on Dark Matter Annihilation in Clusters of Galaxies with the Fermi Large Area Telescope. *JCAP*, 1005:025, 2010, 1002.2239.

[404] A.A. Abdo, M. Ackermann, M. Ajello, et al. Fermi LAT Search for Photon Lines from 30 to 200 GeV and Dark Matter Implications. *Phys.Rev.Lett.*, 104:091302, 2010, 1001.4836.

[405] M. Ackermann et al. Fermi LAT Search for Dark Matter in Gamma-ray Lines and the Inclusive Photon Spectrum. *Phys.Rev.*, D86:022002, 2012, 1205.2739.

[406] Search for Gamma-ray Spectral Lines with the Fermi Large Area Telescope and Dark Matter Implications. 2013, 1305.5597.

[407] Dan Hooper and Lisa Goodenough. Dark Matter Annihilation in The Galactic Center As Seen by the Fermi Gamma Ray Space Telescope. *Phys.Lett.*, B697:412–428, 2011, 1010.2752.

[408] Dan Hooper. The Empirical Case For 10 GeV Dark Matter. *Phys.Dark Univ.*, 1:1–23, 2012, 1201.1303.

[409] Alexey Boyarsky, Denys Malyshev, and Oleg Ruchayskiy. A comment on the emission from the Galactic Center as seen by the Fermi telescope. *Phys.Lett.*, B705:165–169, 2011, 1012.5839.

[410] Kevork N. Abazajian. The Consistency of Fermi-LAT Observations of the Galactic Center with a Millisecond Pulsar Population in the Central Stellar Cluster. *JCAP*, 1103:010, 2011, 1011.4275.

[411] Meng Su, Tracy R. Slatyer, and Douglas P. Finkbeiner. Giant Gamma-ray Bubbles from Fermi-LAT: AGN Activity or Bipolar Galactic Wind? *Astrophys.J.*, 724:1044–1082, 2010, 1005.5480.

[412] Dan Hooper, Douglas P. Finkbeiner, and Gregory Dobler. Possible evidence for dark matter annihilations from the excess microwave emission around the center of the Galaxy seen by the Wilkinson Microwave Anisotropy Probe. *Phys.Rev.*, D76:083012, 2007, 0705.3655.

[413] Philipp Mertsch and Subir Sarkar. Fermi gamma-ray 'bubbles' from stochastic acceleration of electrons. *Phys.Rev.Lett.*, 107:091101, 2011, 1104.3585.

[414] Jiaxin Han, Carlos S. Frenk, Vincent R. Eke, et al. Constraining Extended Gamma-ray Emission from Galaxy Clusters. *Mon.Not.Roy.Astron.Soc.*, 427:1651–1665, 2012, 1207.6749.

[415] Torsten Bringmann, Xiaoyuan Huang, Alejandro Ibarra, Stefan Vogl, and Christoph Weniger. Fermi LAT Search for Internal Bremsstrahlung Signatures from Dark Matter Annihilation. *JCAP*, 1207:054, 2012, 1203.1312.

[416] Elmo Tempel, Andi Hektor, and Martti Raidal. Fermi 130 GeV gamma-ray excess and dark matter annihilation in sub-haloes and in the Galactic centre. *JCAP*, 1209:032, 2012, 1205.1045.

[417] Arvind Rajaraman, Tim M.P. Tait, and Daniel Whiteson. Two Lines or Not Two Lines? That is the Question of Gamma Ray Spectra. *JCAP*, 1209:003, 2012, 1205.4723.

[418] Meng Su and Douglas P. Finkbeiner. Strong Evidence for Gamma-ray Line Emission from the Inner Galaxy. 2012, 1206.1616.

[419] Meng Su and Douglas P. Finkbeiner. Double Gamma-ray Lines from Unassociated Fermi-LAT Sources. 2012, 1207.7060.

[420] Andi Hektor, Martti Raidal, and Elmo Tempel. An evidence for indirect detection of dark matter from galaxy clusters in Fermi-LAT data. *Astrophys.J.*, 762:L22, 2013, 1207.4466.

[421] Alexey Boyarsky, Denys Malyshev, and Oleg Ruchayskiy. Spectral and spatial variations of the diffuse gamma-ray background in the vicinity of the Galactic plane and possible nature of the feature at 130 GeV. 2012, 1205.4700.

[422] N. Mirabal. The Dark Knight Falters. *Mon.Not.Roy.Astron.Soc.*, 429:L109, 2013, 1208.1693.

[423] Andi Hektor, Martti Raidal, and Elmo Tempel. Double gamma-ray lines from unassociated Fermi-LAT sources revisited. 2012, 1208.1996.

[424] Felix Aharonian, Dmitry Khangulyan, and Denis Malyshev. Cold ultrarelativistic pulsar winds as potential sources of galactic gamma-ray lines above 100 GeV. 2012, 1207.0458.

[425] M. Doro et al. Dark Matter and Fundamental Physics with the Cherenkov Telescope Array. *Astropart.Phys.*, 43:189–214, 2013, 1208.5356.

[426] A.M. Galper, O. Adriani, R.L. Aptekar, et al. Status of the GAMMA-400 Project. *Adv.Space Res.*, 51:297–300, 2013, 1201.2490.

[427] Karsten Jedamzik. Big bang nucleosynthesis constraints on hadronically and electromagnetically decaying relic neutral particles. *Phys.Rev.*, D74:103509, 2006, hep-ph/0604251.

[428] Junji Hisano, Masahiro Kawasaki, Kazunori Kohri, Takeo Moroi, and Kazunori Nakayama. Cosmic Rays from Dark Matter Annihilation and Big-Bang Nucleosynthesis. *Phys.Rev.*, D79:083522, 2009, 0901.3582.

[429] Junji Hisano, Masahiro Kawasaki, Kazunori Kohri, and Kazunori Nakayama. Positron/Gamma-Ray Signatures of Dark Matter Annihilation and Big-Bang Nucleosynthesis. *Phys.Rev.*, D79:063514, 2009, 0810.1892.

[430] S. Galli, F. Iocco, G. Bertone, and A. Melchiorri. CMB constraints on dark matter models with large annihilation cross section. *Phys. Rev. D*, 80(2):023505–+, July 2009, 0905.0003.

[431] S. Galli, F. Iocco, G. Bertone, and A. Melchiorri. Updated CMB constraints on dark matter annihilation cross sections. *Phys. Rev. D*, 84(2):027302–+, July 2011, 1106.1528.

[432] Tracy R. Slatyer, Nikhil Padmanabhan, and Douglas P. Finkbeiner. CMB Constraints on WIMP Annihilation: Energy Absorption During the Recombination Epoch. *Phys.Rev.*, D80:043526, 2009, 0906.1197.

[433] Marco Cirelli, Fabio Iocco, and Paolo Panci. Constraints on Dark Matter annihilations from reionization and heating of the intergalactic gas. *JCAP*, 0910:009, 2009, 0907.0719.

[434] Douglas P. Finkbeiner, Silvia Galli, Tongyan Lin, and Tracy R. Slatyer. Searching for Dark Matter in the CMB: A Compact Parameterization of Energy Injection from New Physics. *Phys.Rev.*, D85:043522, 2012, 1109.6322.

[435] Gert Hutsi, Jens Chluba, Andi Hektor, and Martti Raidal. WMAP7 and future CMB constraints on annihilating dark matter: implications on GeV-scale WIMPs. *Astron.Astrophys.*, 535:A26, 2011, 1103.2766.

[436] Patrick J. Fox, Roni Harnik, Joachim Kopp, and Yuhsin Tsai. Missing Energy Signatures of Dark Matter at the LHC. *Phys.Rev.*, D85:056011, 2012, 1109.4398.

[437] Jessica Goodman, Masahiro Ibe, Arvind Rajaraman, et al. Constraints on Light Majorana dark Matter from Colliders. *Phys.Lett.*, B695:185–188, 2011, 1005.1286.

[438] Jessica Goodman, Masahiro Ibe, Arvind Rajaraman, et al. Constraints on Dark Matter from Colliders. *Phys.Rev.*, D82:116010, 2010, 1008.1783.

[439] Arvind Rajaraman, William Shepherd, Tim M.P. Tait, and Alexander M. Wijangco. LHC Bounds on Interactions of Dark Matter. *Phys.Rev.*, D84:095013, 2011, 1108.1196.

[440] Search for New Phenomena in Monojet plus Missing Transverse Momentum Final States using 10fb-1 of pp Collisions at sqrts=8 TeV with the ATLAS detector at the LHC. 2012.

[441] Search for new physics in monojet events in pp collisions at sqrt(s)= 8 TeV.

[442] Georges Aad et al. Search for dark matter candidates and large extra dimensions in events with a jet and missing transverse momentum with the ATLAS detector. *JHEP*, 1304:075, 2013, 1210.4491.

[443] Georges Aad et al. Search for squarks and gluinos with the ATLAS detector in final states with jets and missing transverse momentum using 4.7 fb^{-1} of $\sqrt{s} = 7$ TeV proton-proton collision data. *Phys.Rev.*, D87:012008, 2013, 1208.0949.

[444] Stephen P. Martin and Pierre Ramond. Sparticle Spectrum Constraints. *Phys.Rev.*, D48:5365–5375, 1993, hep-ph/9306314.

[445] J.A. Aguilar-Saavedra et al. TESLA: The Superconducting electron positron linear collider with an integrated x-ray laser laboratory. Technical design report. Part 3. Physics at an e+ e- linear collider. 2001, hep-ph/0106315.

[446] G. Weiglein et al. Physics interplay of the LHC and the ILC. *Phys.Rept.*, 426:47–358, 2006, hep-ph/0410364.

[447] Juan Antonio Aguilar-Saavedra, A. Ali, Benjamin C. Allanach, et al. Supersymmetry parameter analysis: SPA convention and project. *Eur.Phys.J.*, C46:43–60, 2006, hep-ph/0511344.

[448] G.A. Blair, W. Porod, and P.M. Zerwas. Reconstructing supersymmetric theories at high-energy scales. *Phys.Rev.*, D63:017703, 2001, hep-ph/0007107.

[449] G.A. Blair, W. Porod, and P.M. Zerwas. The Reconstruction of supersymmetric theories at high-energy scales. *Eur.Phys.J.*, C27:263–281, 2003, hep-ph/0210058.

[450] Philip Bechtle, Klaus Desch, Werner Porod, and Peter Wienemann. Determination of MSSM parameters from LHC and ILC observables in a global fit. *Eur.Phys.J.*, C46:533–544, 2006, hep-ph/0511006.

[451] Remi Lafaye, Tilman Plehn, Michael Rauch, and Dirk Zerwas. Measuring Supersymmetry. *Eur.Phys.J.*, C54:617–644, 2008, 0709.3985.

[452] Claire Adam, Jean-Loic Kneur, Remi Lafaye, et al. Measuring Unification. *Eur.Phys.J.*, C71:1520, 2011, 1007.2190.

[453] Y. Fukuda et al. Evidence for oscillation of atmospheric neutrinos. *Phys.Rev.Lett.*, 81:1562–1567, 1998, hep-ex/9807003.

[454] Nima Arkani-Hamed and Savas Dimopoulos. Supersymmetric unification without low energy supersymmetry and signatures for fine-tuning at the LHC. *JHEP*, 0506:073, 2005, hep-th/0405159.

[455] G.F. Giudice and A. Romanino. Split supersymmetry. *Nucl.Phys.*, B699:65–89, 2004, hep-ph/0406088.

[456] S. Abe et al. Precision Measurement of Neutrino Oscillation Parameters with KamLAND. *Phys.Rev.Lett.*, 100:221803, 2008, 0801.4589.

[457] Thomas Schwetz, M.A. Tortola, and Jose W.F. Valle. Three-flavour neutrino oscillation update. *New J.Phys.*, 10:113011, 2008, 0808.2016.

[458] Thomas Schwetz, Mariam Tortola, and J.W.F. Valle. Global neutrino data and recent reactor fluxes: status of three-flavour oscillation parameters. *New J.Phys.*, 13:063004, 2011, 1103.0734.

[459] T. Yanagida. KEK lectures. *ed. O. Sawada and A. Sugamoto*, 1979.

[460] Rabindra N. Mohapatra and Goran Senjanovic. Neutrino Mass and Spontaneous Parity Violation. *Phys.Rev.Lett.*, 44:912, 1980.

[461] J.N. Esteves, J.C. Romao, M. Hirsch, F. Staub, and W. Porod. Supersymmetric type-III seesaw: lepton flavour violating decays and dark matter. *Phys.Rev.*, D83:013003, 2011, 1010.6000.

[462] Carla Biggio and Lorenzo Calibbi. Phenomenology of SUSY SU(5) with type I+III seesaw. *JHEP*, 1010:037, 2010, 1007.3750.

[463] R.N. Mohapatra. UNIFICATION AND SUPERSYMMETRY. THE FRONTIERS OF QUARK - LEPTON PHYSICS. 1986.

[464] Mirjam Cvetic and Jogesh C. Pati. N=1 SUPERGRAVITY WITHIN THE MINIMAL LEFT-RIGHT SYMMETRIC MODEL. *Phys.Lett.*, B135:57, 1984.

[465] Ravi Kuchimanchi and R.N. Mohapatra. No parity violation without R-parity violation. *Phys.Rev.*, D48:4352–4360, 1993, hep-ph/9306290.

[466] Charanjit S. Aulakh, Karim Benakli, and Goran Senjanovic. Reconciling supersymmetry and left-right symmetry. *Phys.Rev.Lett.*, 79:2188–2191, 1997, hep-ph/9703434.

[467] Charanjit S. Aulakh, Alejandra Melfo, Andrija Rasin, and Goran Senjanovic. Supersymmetry and large scale left-right symmetry. *Phys.Rev.*, D58:115007, 1998, hep-ph/9712551.

[468] Joachim Kopp, Manfred Lindner, Viviana Niro, and Thomas E.J. Underwood. On the Consistency of Perturbativity and Gauge Coupling Unification. *Phys.Rev.*, D81:025008, 2010, 0909.2653.

[469] Swarup Kumar Majee, Mina K. Parida, Amitava Raychaudhuri, and Utpal Sarkar. Low intermediate scales for leptogenesis in SUSY SO(10) GUTs. *Phys.Rev.*, D75:075003, 2007, hep-ph/0701109.

[470] Michal Malinsky, J.C. Romao, and J.W.F. Valle. Novel supersymmetric SO(10) seesaw mechanism. *Phys.Rev.Lett.*, 95:161801, 2005, hep-ph/0506296.

[471] P.S. Bhupal Dev and R.N. Mohapatra. TeV Scale Inverse Seesaw in SO(10) and Leptonic Non-Unitarity Effects. *Phys.Rev.*, D81:013001, 2010, 0910.3924.

[472] Search for high-mass dilepton resonances in 20 fb^{-1} of pp collisions at $\sqrt{s} = 8$ tev with the atlas experiment. Technical Report ATLAS-CONF-2013-017, CERN, Geneva, Mar 2013.

[473] K. Nakamura et al. Review of particle physics. *J.Phys.*, G37:075021, 2010.

[474] Georges Aad et al. Search for high mass dilepton resonances in pp collisions at $\sqrt{s} = 7$ TeV with the ATLAS experiment. *Phys.Lett.*, B700:163–180, 2011, 1103.6218.

[475] Lorenzo Basso, Alexander Belyaev, Stefano Moretti, Giovanni Marco Pruna, and Claire H. Shepherd-Themistocleous. Z' discovery potential at the LHC in the minimal $B - L$ extension of the Standard Model. *Eur.Phys.J.*, C71:1613, 2011, 1002.3586.

[476] A. Ferrari, Johann Collot, M-L. Andrieux, et al. Sensitivity study for new gauge bosons and right-handed Majorana neutrinos in pp collisions at $s = 14$-TeV. *Phys.Rev.*, D62:013001, 2000.

[477] S.N. Gninenko, M.M. Kirsanov, N.V. Krasnikov, and V.A. Matveev. Detection of heavy Majorana neutrinos and right-handed bosons. *Phys.Atom.Nucl.*, 70:441–449, 2007.

[478] Matthew R. Buckley and Hitoshi Murayama. How can we test seesaw experimentally? *Phys.Rev.Lett.*, 97:231801, 2006, hep-ph/0606088.

[479] M. Hirsch, S. Kaneko, and W. Porod. Supersymmetric seesaw type. II. LHC and lepton flavour violating phenomenology. *Phys.Rev.*, D78:093004, 2008, 0806.3361.

[480] Martin Hirsch, Laslo Reichert, and Werner Porod. Supersymmetric mass spectra and the seesaw scale. *JHEP*, 1105:086, 2011, 1101.2140.

[481] Luis Lavoura, Helmut Kuhbock, and Walter Grimus. Charged-fermion masses in SO(10): Analysis with scalars in 10+120. *Nucl.Phys.*, B754:1–16, 2006, hep-ph/0603259.

[482] Martin Heinze and Michal Malinsky. Flavour structure of supersymmetric SO(10) GUTs with extended matter sector. *Phys.Rev.*, D83:035018, 2011, 1008.4813.

[483] Renato M. Fonseca, Michal Malinsky, Werner Porod, and Florian Staub. Running soft parameters in SUSY models with multiple U(1) gauge factors. *Nucl.Phys.*, B854:28–53, 2012, 1107.2670.

[484] John R. Ellis, Keith A. Olive, Yudi Santoso, and Vassilis C. Spanos. Phenomenological constraints on patterns of supersymmetry breaking. *Phys.Lett.*, B573:162–172, 2003, hep-ph/0305212.

[485] Stephen P. Martin and Michael T. Vaughn. Two loop renormalization group equations for soft supersymmetry breaking couplings. *Phys.Rev.*, D50:2282, 1994, hep-ph/9311340.

[486] Claude Amsler et al. Review of Particle Physics. *Phys.Lett.*, B667:1–1340, 2008.

[487] Werner Porod. SPheno, a program for calculating supersymmetric spectra, SUSY particle decays and SUSY particle production at e+ e- colliders. *Comput.Phys.Commun.*, 153:275–315, 2003, hep-ph/0301101.

[488] W. Porod and F. Staub. SPheno 3.1: Extensions including flavour, CP-phases and models beyond the MSSM. *Comput.Phys.Commun.*, 183:2458–2469, 2012, 1104.1573.

[489] F. Staub. SARAH. 2008, 0806.0538.

[490] Florian Staub. From Superpotential to Model Files for FeynArts and CalcHep/CompHep. *Comput.Phys.Commun.*, 181:1077–1086, 2010, 0909.2863.

[491] Florian Staub. Automatic Calculation of supersymmetric Renormalization Group Equations and Self Energies. *Comput.Phys.Commun.*, 182:808–833, 2011, 1002.0840.

[492] Howard Baer, Vernon Barger, Andre Lessa, and Xerxes Tata. Discovery potential for SUSY at a high luminosity upgrade of LHC14. *Phys.Rev.*, D86:117701, 2012, 1207.4846.

[493] Howard Baer, Vernon Barger, Andre Lessa, and Xerxes Tata. SUSY discovery potential of LHC14 with $0.3 - 3\ ab^{-1}$: A Snowmass whitepaper. 2013, 1306.5343.

[494] Howard Baer, Vernon Barger, Peisi Huang, et al. Leaving no stone unturned in the hunt for SUSY naturalness: A Snowmass whitepaper. 2013, 1306.3148.

[495] Takehiko Asaka, Koji Ishiwata, and Takeo Moroi. Right-handed sneutrino as cold dark matter. *Phys.Rev.*, D73:051301, 2006, hep-ph/0512118.

[496] Takehiko Asaka, Koji Ishiwata, and Takeo Moroi. Right-handed sneutrino as cold dark matter of the universe. *Phys.Rev.*, D75:065001, 2007, hep-ph/0612211.

[497] Ki-Young Choi and Osamu Seto. A Dirac right-handed sneutrino dark matter and its signature in the gamma-ray lines. *Phys.Rev.*, D86:043515, 2012, 1205.3276.

[498] Shrihari Gopalakrishna, Andre de Gouvea, and Werner Porod. Right-handed sneutrinos as nonthermal dark matter. *JCAP*, 0605:005, 2006, hep-ph/0602027.

[499] Francesca Borzumati and Yasunori Nomura. Low scale seesaw mechanisms for light neutrinos. *Phys.Rev.*, D64:053005, 2001, hep-ph/0007018.

[500] Zachary Thomas, David Tucker-Smith, and Neal Weiner. Mixed Sneutrinos, Dark Matter and the CERN LHC. *Phys.Rev.*, D77:115015, 2008, 0712.4146.

[501] Beranger Dumont, Genevieve Belanger, Sylvain Fichet, Sabine Kraml, and Thomas Schwetz. Mixed sneutrino dark matter in light of the 2011 XENON and LHC results. *JCAP*, 1209:013, 2012, 1206.1521.

[502] G. Belanger, M. Kakizaki, E.K. Park, S. Kraml, and A. Pukhov. Light mixed sneutrinos as thermal dark matter. *JCAP*, 1011:017, 2010, 1008.0580.

[503] Genevieve Belanger, Sabine Kraml, and Andre Lessa. Light Sneutrino Dark Matter at the LHC. *JHEP*, 1107:083, 2011, 1105.4878.

[504] Hye-Sung Lee, Konstantin T. Matchev, and Salah Nasri. Revival of the thermal sneutrino dark matter. *Phys.Rev.*, D76:041302, 2007, hep-ph/0702223.

[505] G. Belanger, J. Da Silva, and A. Pukhov. The Right-handed sneutrino as thermal dark matter in U(1) extensions of the MSSM. *JCAP*, 1112:014, 2011, 1110.2414.

[506] John March-Russell, Christopher McCabe, and Matthew McCullough. Neutrino-Flavoured Sneutrino Dark Matter. *JHEP*, 1003:108, 2010, 0911.4489.

[507] Frank Deppisch and Apostolos Pilaftsis. Thermal Right-Handed Sneutrino Dark Matter in the F(D)-Term Model of Hybrid Inflation. *JHEP*, 0810:080, 2008, 0808.0490.

[508] Chiara Arina and Nicolao Fornengo. Sneutrino cold dark matter, a new analysis: Relic abundance and detection rates. *JHEP*, 0711:029, 2007, 0709.4477.

[509] Priyotosh Bandyopadhyay, Eung Jin Chun, and Jong-Chul Park. Right-handed sneutrino dark matter in $\mathbf{U(1)}'$ seesaw models and its signatures at the LHC. *JHEP*, 1106:129, 2011, 1105.1652.

[510] David G. Cerdeno and Osamu Seto. Right-handed sneutrino dark matter in the NMSSM. *JCAP*, 0908:032, 2009, 0903.4677.

[511] David G. Cerdeno, Ji-Haeng Huh, Miguel Peiro, and Osamu Seto. Very light right-handed sneutrino dark matter in the NMSSM. *JCAP*, 1111:027, 2011, 1108.0978.

[512] C. Arina, F. Bazzocchi, N. Fornengo, J.C. Romao, and J.W.F. Valle. Minimal supergravity sneutrino dark matter and inverse seesaw neutrino masses. *Phys.Rev.Lett.*, 101:161802, 2008, 0806.3225.

[513] P.S. Bhupal Dev, Subhadeep Mondal, Biswarup Mukhopadhyaya, and Sourov Roy. Phenomenology of Light Sneutrino Dark Matter in cMSSM/mSUGRA with Inverse Seesaw. *JHEP*, 1209:110, 2012, 1207.6542.

[514] Zhaofeng Kang, Jinmian Li, Tianjun Li, Tao Liu, and Jinmin Yang. Asymmetric Sneutrino Dark Matter in the NMSSM with Minimal Inverse Seesaw. 2011, 1102.5644.

[515] Haipeng An, P.S. Bhupal Dev, Yi Cai, and R.N. Mohapatra. Sneutrino Dark Matter in Gauged Inverse Seesaw Models for Neutrinos. *Phys.Rev.Lett.*, 108:081806, 2012, 1110.1366.

[516] Shaaban Khalil, Hiroshi Okada, and Takashi Toma. Right-handed Sneutrino Dark Matter in Supersymmetric B-L Model. *JHEP*, 1107:026, 2011, 1102.4249.

[517] Lorenzo Basso, Ben O'Leary, Werner Porod, and Florian Staub. Dark matter scenarios in the minimal SUSY B-L model. *JHEP*, 1209:054, 2012, 1207.0507.

[518] Valentina De Romeri. Right Handed Sneutrino Dark Matter in Inverse and Linear seesaw scenarios. 2012, 1209.1465.

[519] G. Belanger, F. Boudjema, A. Pukhov, and A. Semenov. MicrOMEGAs 2.0: A Program to calculate the relic density of dark matter in a generic model. *Comput.Phys.Commun.*, 176:367–382, 2007, hep-ph/0607059.

[520] G. Belanger, Neil D. Christensen, A. Pukhov, and A. Semenov. SLHAplus: a library for implementing extensions of the standard model. *Comput.Phys.Commun.*, 182:763–774, 2011, 1008.0181.

[521] Florian Staub, Thorsten Ohl, Werner Porod, and Christian Speckner. A Tool Box for Implementing Supersymmetric Models. *Comput.Phys.Commun.*, 183:2165–2206, 2012, 1109.5147.

[522] M. Hirsch, H.V. Klapdor-Kleingrothaus, and S.G. Kovalenko. B-L violating masses in softly broken supersymmetry. *Phys.Lett.*, B398:311–314, 1997, hep-ph/9701253.

[523] Yuval Grossman and Howard E. Haber. Sneutrino mixing phenomena. *Phys.Rev.Lett.*, 78:3438–3441, 1997, hep-ph/9702421.

[524] M. Hirsch, T. Kernreiter, J.C. Romao, and Albert Villanova del Moral. Minimal Supersymmetric Inverse Seesaw: Neutrino masses, lepton flavour violation and LHC phenomenology. *JHEP*, 1001:103, 2010, 0910.2435.

[525] Georges Aad et al. Observation of a new particle in the search for the Standard Model Higgs boson with the ATLAS detector at the LHC. *Phys.Lett.*, B716:1–29, 2012, 1207.7214.

[526] Serguei Chatrchyan et al. Observation of a new boson at a mass of 125 GeV with the CMS experiment at the LHC. *Phys.Lett.*, B716:30–61, 2012, 1207.7235.

[527] M.Z. Akrawy et al. A Study of coherence of soft gluons in hadron jets. *Phys.Lett.*, B247:617–628, 1990.

[528] O. Adriani et al. Search for isosinglet neutral heavy leptons in Z0 decays. *Phys.Lett.*, B295:371–382, 1992.

[529] P. Abreu et al. Search for new phenomena using single photon events in the DELPHI detector at LEP. *Z.Phys.*, C74:577–586, 1997.

[530] P. Achard et al. Search for heavy isosinglet neutrino in e^+e^- annihilation at LEP. *Phys.Lett.*, B517:67–74, 2001, hep-ex/0107014.

[531] P.S. Bhupal Dev, Roberto Franceschini, and R.N. Mohapatra. Bounds on TeV Seesaw Models from LHC Higgs Data. *Phys.Rev.*, D86:093010, 2012, 1207.2756.

[532] Pier Paolo Giardino, Kristjan Kannike, Martti Raidal, and Alessandro Strumia. Is the resonance at 125 GeV the Higgs boson? *Phys.Lett.*, B718:469–474, 2012, 1207.1347.

[533] Search for resonances in the dilepton mass distribution in pp collisions at sqrt(s) = 8 tev. Technical Report CMS-PAS-EXO-12-015, CERN, Geneva, 2012.

[534] Georges Aad et al. Search for high-mass resonances decaying to dilepton final states in pp collisions at s**(1/2) = 7-TeV with the ATLAS detector. *JHEP*, 1211:138, 2012, 1209.2535.

[535] Search for squarks and gluinos with the atlas detector using final states with jets and missing transverse momentum and 5.8 fb^{-1} of $\sqrt{s}$=8 tev proton-proton collision data. Technical Report ATLAS-CONF-2012-109, CERN, Geneva, Aug 2012.

[536] Interpretation of searches for supersymmetry. Technical Report CMS-PAS-SUS-11-016, CERN, Geneva, 2012.

[537] Arcadi Santamaria. Masses, mixings, Yukawa couplings and their symmetries. *Phys.Lett.*, B305:90–97, 1993, hep-ph/9302301.

[538] J.A. Casas and A. Ibarra. Oscillating neutrinos and muon to e, gamma. *Nucl.Phys.*, B618:171–204, 2001, hep-ph/0103065.

[539] D.V. Forero, S. Morisi, M. Tortola, and J.W.F. Valle. Lepton flavor violation and non-unitary lepton mixing in low-scale type-I seesaw. *JHEP*, 1109:142, 2011, 1107.6009.

[540] P.F. Harrison, D.H. Perkins, and W.G. Scott. Tri-bimaximal mixing and the neutrino oscillation data. *Phys.Lett.*, B530:167, 2002, hep-ph/0202074.

[541] Francesca Borzumati and Antonio Masiero. Large Muon and electron Number Violations in Supergravity Theories. *Phys.Rev.Lett.*, 57:961, 1986.

[542] M. Hirsch, F. Staub, and A. Vicente. Enhancing $l_i \to 3l_j$ with the Z^0-penguin. *Phys.Rev.*, D85:113013, 2012, 1202.1825.

[543] Asmaa Abada, Debottam Das, Avelino Vicente, and Cedric Weiland. Enhancing lepton flavour violation in the supersymmetric inverse seesaw beyond the dipole contribution. *JHEP*, 1209:015, 2012, 1206.6497.

[544] D. Larson, J. Dunkley, G. Hinshaw, et al. Seven-Year Wilkinson Microwave Anisotropy Probe (WMAP) Observations: Power Spectra and WMAP-Derived Parameters. *Astrophys.J.Suppl.*, 192:16, 2011, 1001.4635.

[545] A. Bottino, F. Donato, N. Fornengo, and S. Scopel. Size of the neutralino nucleon cross-section in the light of a new determination of the pion nucleon sigma term. *Astropart.Phys.*, 18:205–211, 2002, hep-ph/0111229.

[546] E. Aprile et al. Analysis of the XENON100 Dark Matter Search Data. 2012, 1207.3458.

[547] E. Aprile et al. Implications on Inelastic Dark Matter from 100 Live Days of XENON100 Data. *Phys.Rev.*, D84:061101, 2011, 1104.3121.

[548] Serguei Chatrchyan et al. Search for heavy Majorana neutrinos in $\mu^+\mu^+[\mu^-\mu^-]$ and $e^+e^+[e^-e^-]$ events in pp collisions at $\sqrt{s} = 7$ TeV. *Phys.Lett.*, B717:109–128, 2012, 1207.6079.

[549] Search for majorana neutrino production in pp collisions at sqrt(s)=7 tev in dimuon final states with the atlas detector. Technical Report ATLAS-CONF-2012-139, CERN, Geneva, Sep 2012.

[550] J. Diemand, M. Kuhlen, P. Madau, et al. Clumps and streams in the local dark matter distribution. *Nature*, 454:735–738, 2008, 0805.1244.

[551] Joachim Stadel, Doug Potter, Ben Moore, et al. Quantifying the heart of darkness with GHALO - a multi-billion particle simulation of our galactic halo. 2008, 0808.2981.

[552] Volker Springel, Jie Wang, Mark Vogelsberger, et al. The Aquarius Project: the subhalos of galactic halos. *Mon.Not.Roy.Astron.Soc.*, 391:1685–1711, 2008, 0809.0898.

[553] George R. Blumenthal, S.M. Faber, Ricardo Flores, and Joel R. Primack. Contraction of Dark Matter Galactic Halos Due to Baryonic Infall. *Astrophys.J.*, 301:27, 1986.

[554] Michael Gustafsson, Malcolm Fairbairn, and Jesper Sommer-Larsen. Baryonic Pinching of Galactic Dark Matter Haloes. *Phys.Rev.*, D74:123522, 2006, astro-ph/0608634.

[555] P. Young. Numerical models of star clusters with a central black hole. I - Adiabatic models. *"Astrophys.J."*, 242:1232–1237, December 1980.

[556] Oleg Y. Gnedin, Andrey V. Kravtsov, Anatoly A. Klypin, and Daisuke Nagai. Response of dark matter halos to condensation of baryons: Cosmological simulations and improved adiabatic contraction model. *Astrophys.J.*, 616:16–26, 2004, astro-ph/0406247.

[557] Michael Kuhlen, Mark Vogelsberger, and Raul Angulo. Numerical Simulations of the Dark Universe: State of the Art and the Next Decade. *Phys.Dark Univ.*, 1:50–93, 2012, 1209.5745.

[558] Joel R. Primack. Cosmology: small scale issues revisited. *New J.Phys.*, 11:105029, 2009, 0909.2247.

[559] F. Governato, A. Zolotov, A. Pontzen, et al. Cuspy No More: How Outflows Affect the Central Dark Matter and Baryon Distribution in Lambda CDM Galaxies. *Mon.Not.Roy.Astron.Soc.*, 422:1231–1240, 2012, 1202.0554.

[560] J. F. Navarro, C. S. Frenk, and S. D. M. White. *Astrophys. J.*, 462:563, 1996.

[561] Ben Moore, Fabio Governato, Thomas R. Quinn, Joachim Stadel, and George Lake. Resolving the structure of cold dark matter halos. *Astrophys.J.*, 499:L5, 1998, astro-ph/9709051.

[562] J. Einasto. On constructing models of stellar systems. V. The binomial model. *Publications of the Tartu Astrofizica Observatory*, 36:414–441, 1968.

[563] J. Einasto and U. Haud. Galactic models with massive corona. I - Method. II - Galaxy. *"Astronomy and Astrophysics"*, 223:89–106, October 1989.

[564] Julio F. Navarro, Eric Hayashi, Chris Power, et al. The Inner structure of Lambda-CDM halos 3: Universality and asymptotic slopes. *Mon.Not.Roy.Astron.Soc.*, 349:1039, 2004, astro-ph/0311231.

[565] K.G. Begeman, A.H. Broeils, and R.H. Sanders. Extended rotation curves of spiral galaxies: Dark haloes and modified dynamics. *Mon.Not.Roy.Astron.Soc.*, 249:523, 1991.

[566] John N. Bahcall and R.M. Soneira. The Universe at faint magnetidues. 2. Models for the predicted star counts. *Astrophys.J.Suppl.*, 44:73–110, 1980.

[567] A. Burkert. The Structure of dark matter halos in dwarf galaxies. *IAU Symp.*, 171:175, 1996, astro-ph/9504041.

[568] O. Adriani, G. C. Barbarino, G. A. Bazilevskaya, et al. An anomalous positron abundance in cosmic rays with energies 1.5-100GeV. *Nature*, 458:607–609, April 2009, 0810.4995.

[569] O. Adriani, G. C. Barbarino, G. A. Bazilevskaya, et al. A statistical procedure for the identification of positrons in the PAMELA experiment. *Astropart. Phys.*, 34:1–11, August 2010, 1001.3522.

[570] A. A. Abdo, M. Ackermann, M. Ajello, et al. Measurement of the Cosmic Ray $e^+ + e^-$ Spectrum from 20GeV to 1TeV with the Fermi Large Area Telescope. *Phys. Rev. Lett.*, 102(18):181101–+, May 2009, 0905.0025.

[571] F. Aharonian, A. G. Akhperjanian, G. Anton, et al. Probing the ATIC peak in the cosmic-ray electron spectrum with H.E.S.S. *Astron. Astrophys.*, 508:561–564, December 2009, 0905.0105.

[572] O. Adriani, G. C. Barbarino, G. A. Bazilevskaya, et al. New Measurement of the Antiproton-to-Proton Flux Ratio up to 100 GeV in the Cosmic Radiation. *Phys. Rev. Lett.*, 102(5):051101–+, February 2009, 0810.4994.

[573] O. Adriani et al. PAMELA results on the cosmic-ray antiproton flux from 60 MeV to 180 GeV in kinetic energy. *Phys. Rev. Lett.*, 105:121101, 2010, 1007.0821.

[574] A. A. Abdo, M. Ackermann, M. Ajello, et al. The Spectrum of the Isotropic Diffuse Gamma-Ray Emission derived from first-year Fermi Large Area Telescope Data. *Phys. Rev. Lett.*, 104:101101, 2010, 1002.3603.

[575] W. Mitthumsiri. *Fermi Symposium, Rome*, 2011.

[576] T. Delahaye, J. Lavalle, R. Lineros, F. Donato, and N. Fornengo. Galactic electrons and positrons at the Earth: new estimate of the primary and secondary fluxes. *Astron. Astrophys.*, 524:A51, December 2010, 1002.1910.

[577] D. Hooper, P. Blasi, and D. Serpico. Pulsars as the sources of high energy cosmic ray positrons. *JCAP*, 1:25–+, January 2009, 0810.1527.

[578] M. Cirelli, R. Franceschini, and A. Strumia. Minimal Dark Matter predictions for galactic positrons, anti-protons, photons. *Nuclear Phys. B*, 800:204–220, September 2008, 0802.3378.

[579] L. Bergström, T. Bringmann, and J. Edsjö. New positron spectral features from supersymmetric dark matter: A way to explain the PAMELA data? *Phys. Rev. D*, 78(10):103520–+, November 2008, 0808.3725.

[580] I. Cholis, L. Goodenough, D. Hooper, M. Simet, and N. Weiner. *Phys. Rev. D*, 80:123511, 2009.

[581] A. A. Abdo, M. Ackermann, M. Ajello, et al. Observations of Milky Way Dwarf Spheroidal Galaxies with the Fermi-Large Area Telescope Detector and Constraints on Dark Matter Models. *Astrophys. J.*, 712:147–158, March 2010, 1001.4531.

[582] M. Ackermann, M. Ajello, A. Allafort, et al. Constraints on dark matter annihilation in clusters of galaxies with the Fermi large area telescope. *JCAP*, 5:25–+, May 2010, 1002.2239.

[583] A. A. Abdo, M. Ackermann, M. Ajello, et al. Constraints on cosmological dark matter annihilation from the Fermi-LAT isotropic diffuse gamma-ray measurement. *JCAP*, 4:14–+, April 2010.

[584] A. A. Abdo, M. Ackermann, M. Ajello, et al. Fermi Large Area Telescope Search for Photon Lines from 30 to 200 GeV and Dark Matter Implications. *Phys. Rev. Lett.*, 104(9):091302–+, March 2010, 1001.4836.

[585] Marco Cirelli, Paolo Panci, and Pasquale D. Serpico. Diffuse gamma ray constraints on annihilating or decaying Dark Matter after Fermi. *Nucl. Phys.*, B840:284–303, 2010, 0912.0663.

[586] Eric J. Baxter and Scott Dodelson. A Robust Approach to Constraining Dark Matter from Gamma-Ray Data. *Phys.Rev.*, D83:123516, 2011, 1103.5779.

[587] Beatriz B. Siffert, Angelo Limone, Enrico Borriello, Giuseppe Longo, and Gennaro Miele. Radio emission from dark matter annihilation in the Large Magellanic Cloud. *Mon. Not. Roy. Astron. Soc.*, 410:2463–2471, 2011, 1006.5325.

[588] A. Abramowski et al. H.E.S.S. constraints on Dark Matter annihilations towards the Sculptor and Carina Dwarf Galaxies. *Astropart.Phys.*, 34:608–616, 2011, 1012.5602.

[589] The Fermi-LAT Collaboration: M. Ackermann, M. Ajello, A. Albert, et al. Constraining dark matter models from a combined analysis of Milky Way satellites with the Fermi-LAT. *ArXiv e-prints*, August 2011, 1108.3546.

[590] A. A. Abdo et al. Fermi Large Area Telescope First Source Catalog. *Astrophys. J.*, 188:405, 2010.

[591] A. A. Abdo, M. Ackermann, M. Ajello, et al. The Fermi-LAT High-Latitude Survey: Source Count Distributions and the Origin of the Extragalactic Diffuse Background. *Astrophys. J.*, 720:435–453, September 2010, 1003.0895.

[592] A. A. Abdo, M. Ackermann, M. Ajello, et al. The First Fermi Large Area Telescope Catalog of Gamma-ray Pulsars. *Astrophys. J. Suppl.*, 187:460–494, April 2010, 0910.1608.

[593] B. D. Fields, V. Pavlidou, and T. Prodanovic. Cosmic Gamma-Ray Background from Star-Forming Galaxies. *Astrophys. J. Lett.*, 722:L199, 2010, 1003.3647.

[594] O. Kalashev, D. Semikoz, and G. Sigl. Ultrahigh energy cosmic rays and the GeV-TeV diffuse gamma-ray flux. *Phys. Rev. D*, 79:063005, 2009.

[595] Y. Inoue, T. Totani, and Y. Ueda. *Astrophys. J.*, 672:L5, 2008.

[596] Y. Inoue and T. Totani. *Astrophys. J.*, 702:523, 2009.

[597] A. A. Abdo, M. Ackermann, M. Ajello, et al. Fermi Large Area Telescope Observations of Misaligned Active Galactic Nuclei. *Astrophys. J.*, 720:912–922, September 2010.

[598] L. Stawarz and T. M. Kneiske. Kiloparsec-Scale Jets in FR I Radio Galaxies and the gamma-ray Background. *Astrophys. J.*, 637:693–698, 2006.

[599] Y. Inoue. Contribution of the Gamma-ray Loud Radio Galaxies Core Emissions to the Cosmic MeV and GeV Gamma-Ray Background Radiation. *ArXiv e-prints*, March 2011, 1103.3946.

[600] Troung Le and Charles D. Dermer. Gamma Ray Bursts predictions for the Fermi gamma ray space telescope. *Astrophys. J.*, 700:1026–1033, 2009.

[601] T. A. Thompson, E. Quataert, and E. Waxman. The Starburst Contribution to the Extra-Galactic Gamma-Ray Background. *Astrophys. J.*, 654:219–225, 2006.

[602] P. Blasi, S. Gabici, and G. Brunetti. Gamma rays from clusters of galaxies. *Int. J. Mod. Phys.*, A22:681–706, 2007.

[603] R. C. Berrington and C. D. Dermer. *Astrophys. J.*, 594:709, 2003.

[604] C. Pfrommer et al. *MNRAS*, 385:1211, 2008.

[605] U. Keshet, E. Waxman, A. Loeb, et al. Gamma-Rays from Intergalactic Shocks. *Astrophys. J.*, 585:128–150, 2003.

[606] S. Gabici and P. Blasi. The gamma ray background from large scale structure formation. *Astropart. Phys.*, 19:679–689, 2003.

[607] P. Sreekumar et al. EGRET Observations of the Extragalactic Gamma Ray Emission. *Astrophys. J.*, 494:523, 1998.

[608] Floyd W. Stecker and Tonia M. Venters. Components of the Extragalactic Gamma Ray Background. *Astrophys.J.*, 736:40, 2011, 1012.3678.

[609] C. A. Faucher-Giguere and A. Loeb. The Pulsar Contribution to the Gamma-Ray Background. *JCAP*, 1001:005, 2010.

[610] J. M. Siegal-Gaskins, R. Reesman, V. Pavlidou, S. Profumo, and T. P. Walker. Anisotropy Constraints on Millisecond Pulsars in the Diffuse Gamma Ray Background. *ArXiv e-prints*, November 2010, 1011.5501.

[611] A. A. Abdo et al. *Science*, 325:848, 2009.

[612] R. Makiya et al. *Astrophys. J.*, 728:158, 2011, 1005.1390.

[613] V. Berezinsky, A. Gazizov, M. Kachelriess, and S. Ostapchenko. Fermi-LAT restrictions on UHECRs and cosmogenic neutrinos. *Phys. Lett. B*, 695:13, 2010, 1003.1496.

[614] H.-U. Bengtsson, P. Salati, and J. Silk. Quark flavours and the γ-ray spectrum from halo dark matter annihilations. *Nuclear Phys. B*, 346:129–148, December 1990.

[615] L. Bergström, P. Ullio, and J. H. Buckley. Observability of gamma rays from dark matter neutralino annihilations in the Milky Way halo. *Astropart. Phys.*, 9:137–162, August 1998, 9712318.

[616] A. Bottino, F. Donato, N. Fornengo, and S. Scopel. Indirect signals from light neutralinos in supersymmetric models without gaugino mass unification. *Phys. Rev. D*, 70:015005, 2004, 0401186.

[617] N. Fornengo, L. Pieri, and S. Scopel. Neutralino annihilation into γ rays in the Milky Way and in external galaxies. *Phys. Rev. D*, 70(10):103529–+, November 2004, 0407342.

[618] R. Lineros. *private communications*, 2011.

[619] J. F. Navarro, E. Hayashi, C. Power, et al. The inner structure of ΛCDM haloes - III. Universality and asymptotic slopes. *MNRAS*, 349:1039–1051, April 2004, 0311231.

[620] S. Cassel. Sommerfeld factor for arbitrary partial wave processes. *Journal of Physics G Nuclear Physics*, 37(10):105009–+, October 2010, 0903.5307.

[621] Jonathan L.Feng, Manoj Kaplinghat, and Hai-Bo Yu. **Sommerfeld enhancement for thermal relic dark matter**. *Phys. Rev. D*, 82:083525, 2010. 1005.4678v1.

[622] Brant Robertson and Andrew Zentner. Dark Matter Annihilation Rates with Velocity-Dependent Annihilation Cross Sections. *Phys.Rev.*, D79:083525, 2009, 0902.0362.

[623] Stefano Profumo, Kris Sigurdson, and Marc Kamionkowski. **What mass are the smallest protohaloes?** *Phys. Rev. Lett.*, 97:1–5, 2006. 0603373v1.

[624] Marc Kamionkowski and Stefano Profumo. Early Annihilation and Diffuse Backgrounds in Models of Weakly Interacting Massive Particles in Which the Cross Section for Pair Annihilation Is Enhanced by 1/v. *Phys. Rev. Lett.*, 101:261301, 2008, 0810.3233.

[625] Anne M. Green, Stefan Hofmann, and Dominik J. Schwarz. The power spectrum of SUSY-CDM on sub-galactic scales. *Mon. Not. Roy. Astron. Soc.*, 353:L23, 2004, astro-ph/0309621.

[626] A. Loeb and M. Zaldarriaga. Small-scale power spectrum of cold dark matter. *Phys. Rev. D*, 71(10):103520–+, May 2005, arXiv:astro-ph/0504112.

[627] Stefan Hofmann, Dominik J. Schwarz, and Horst Stoecker. Damping scales of neutralino cold dark matter. *Phys.Rev.*, D64:083507, 2001, astro-ph/0104173.

[628] Xue-lei Chen, Marc Kamionkowski, and Xin-min Zhang. Kinetic decoupling of neutralino dark matter. *Phys.Rev.*, D64:021302, 2001, astro-ph/0103452.

[629] C. Schmid, D. J. Schwarz, and P. Widerin. Amplification of cosmological inhomogeneities by the QCD transition. *Phys. Rev. D*, 59(4):043517–+, February 1999, arXiv:astro-ph/9807257.

[630] Junji Hisano et al. Cosmological constraints on dark matter models with velocity-dependent annihilation cross section. *Phys. Rev.*, D83:123511, 2011, 1102.4658.

[631] Torsten Bringmann, Francesca Calore, Mattia Di Mauro, and Fiorenza Donato. Constraining dark matter annihilation with the isotropic γ-ray background: updated limits and future potential. 2013, 1303.3284.

[632] Shin'ichiro Ando, Eiichiro Komatsu, Takuro Narumoto, and Tomonori Totani. Angular power spectrum of gamma-ray sources for GLAST: Blazars and clusters of galaxies. *Mon.Not.Roy.Astron.Soc.*, 376:1635–1647, 2007, astro-ph/0610155.

[633] Shin'ichiro Ando and Vasiliki Pavlidou. Imprint of Galaxy Clustering in the Cosmic Gamma-Ray Background. *Mon.Not.Roy.Astron.Soc.*, 400:2122, 2009, 0908.3890.

[634] Jennifer M. Siegal-Gaskins, Rebecca Reesman, Vasiliki Pavlidou, Stefano Profumo, and Terry P. Walker. Anisotropies in the gamma-ray sky from millisecond pulsars. *Mon.Not.Roy.Astron.Soc.*, 415:1074S, 2011, 1011.5501.

[635] M. Ackermann et al. Anisotropies in the diffuse gamma-ray background measured by the Fermi LAT. *Phys.Rev.*, D85:083007, 2012, 1202.2856.

[636] Shin'ichiro Ando. Can dark matter annihilation dominate the extragalactic gamma-ray background? *Phys.Rev.Lett.*, 94:171303, 2005, astro-ph/0503006.

[637] Shin'ichiro Ando and Eiichiro Komatsu. Anisotropy of the cosmic gamma-ray background from dark matter annihilation. *Phys.Rev.*, D73:023521, 2006, astro-ph/0512217.

[638] Shin'ichiro Ando, Eiichiro Komatsu, Takuro Narumoto, and Tomonori Totani. Dark matter annihilation or unresolved astrophysical sources? Anisotropy probe of the origin of cosmic gamma-ray background. *Phys.Rev.*, D75:063519, 2007, astro-ph/0612467.

[639] A. Cuoco, S. Hannestad, T. Haugbolle, et al. The Signature of Large Scale Structures on the Very High Energy Gamma-Ray Sky. *JCAP*, 0704:013, 2007, astro-ph/0612559.

[640] Alessandro Cuoco, Jacob Brandbyge, Steen Hannestad, Troels Haugboelle, and Gennaro Miele. Angular Signatures of Annihilating Dark Matter in the Cosmic Gamma-Ray Background. *Phys.Rev.*, D77:123518, 2008, 0710.4136.

[641] Marco Taoso, Shin'ichiro Ando, Gianfranco Bertone, and Stefano Profumo. Angular correlations in the cosmic gamma-ray background from dark matter annihilation around intermediate-mass black holes. *Phys.Rev.*, D79:043521, 2009, 0811.4493.

[642] Jennifer M. Siegal-Gaskins. Revealing dark matter substructure with anisotropies in the diffuse gamma-ray background. *JCAP*, 0810:040, 2008, 0807.1328.

[643] Mattia Fornasa, Lidia Pieri, Gianfranco Bertone, and Enzo Branchini. Anisotropy probe of galactic and extra-galactic Dark Matter annihilations. *Phys.Rev.*, D80:023518, 2009, 0901.2921.

[644] Jennifer M. Siegal-Gaskins and Vasiliki Pavlidou. Robust identification of isotropic diffuse gamma rays from Galactic dark matter. *Phys.Rev.Lett.*, 102:241301, 2009, 0901.3776.

[645] Shin'ichiro Ando. Gamma-ray background anisotropy from galactic dark matter substructure. *Phys.Rev.*, D80:023520, 2009, 0903.4685.

[646] Jesus Zavala, Volker Springel, and Michael Boylan-Kolchin. Extragalactic gamma-ray background radiation from dark matter annihilation. *Mon.Not.Roy.Astron.Soc.*, 405:593, 2010, 0908.2428.

[647] Alejandro Ibarra, David Tran, and Christoph Weniger. Detecting Gamma-Ray Anisotropies from Decaying Dark Matter: Prospects for Fermi LAT. *Phys.Rev.*, D81:023529, 2010, 0909.3514.

[648] A. Cuoco, A. Sellerholm, J. Conrad, and S. Hannestad. Anisotropies in the Diffuse Gamma-Ray Background from Dark Matter with Fermi LAT: a closer look. *Mon.Not.Roy.Astron.Soc.*, 414:2040–2054, 2011, 1005.0843.

[649] Mattia Fornasa, Jesus Zavala, Miguel A. Sanchez-Conde, et al. Characterization of Dark-Matter-induced anisotropies in the diffuse gamma-ray background. 2012, 1207.0502.

[650] Volker Springel, Simon D.M. White, Adrian Jenkins, et al. Simulating the joint evolution of quasars, galaxies and their large-scale distribution. *Nature*, 435:629–636, 2005, astro-ph/0504097.

[651] Lidia Pieri, Julien Lavalle, Gianfranco Bertone, and Enzo Branchini. Implications of High-Resolution Simulations on Indirect Dark Matter Searches. *Phys.Rev.*, D83:023518, 2011, 0908.0195.

[652] K. M. Górski, E. Hivon, A. J. Banday, et al. HEALPix: A Framework for High-Resolution Discretization and Fast Analysis of Data Distributed on the Sphere. *Astrophys.J.*, 622:759–771, April 2005, astro-ph/0409513.

[653] Anne M. Green, Stefan Hofmann, and Dominik J. Schwarz. The First wimpy halos. *JCAP*, 0508:003, 2005, astro-ph/0503387.

[654] Torsten Bringmann. Particle Models and the Small-Scale Structure of Dark Matter. *New J.Phys.*, 11:105027, 2009, 0903.0189.

[655] Rene Brun and Fons Rademakers. Root - an object oriented data analysis framework. *Nucl. Inst. and Meth. in Phys. Res. A*, 389:81–86, 1997.

[656] Piero Ullio, Lars Bergstrom, Joakim Edsjo, and Cedric G. Lacey. Cosmological dark matter annihilations into gamma-rays - a closer look. *Phys.Rev.*, D66:123502, 2002, astro-ph/0207125.

[657] M. Fornasa, L. Pieri, G. Bertone, and E. Branchini. Anisotropy probe of galactic and extra-galactic Dark Matter annihilations. *Phys. Rev. D*, 80:023518, 2009, 0901.2921.